

Bioactive Silica and Titania Coatings on Implant Materials

Von der Naturwissenschaftlichen Fakultät der
Gottfried Wilhelm Leibniz Universität Hannover

zur Erlangung des Grades
Doktorin der Naturwissenschaften
(Dr. rer. nat.)

genehmigte Dissertation

von

Natalja Wendt, M. Sc.

2018

Referent: Prof. Dr. Peter Behrens

Korreferent: Prof. Dr. Peter Paul Müller

Tag der Promotion: 09.07.2018

Abstract

A major goal of the current research on implants is the generation of a sustainable positive interaction of the implant with the body, accompanied by minimal side effects. Hence, the focus of many studies lies on the integration of implants in the surrounding tissue, often supported by implant-associated drug delivery, thus reducing the need for systemic medication usually associated with strong side effects. When the surface of an implant is bioinert or bioincompatible due to its physical or chemical properties, this can be improved by a suitable coating. Such coatings change the surface properties chemically and/or structurally. Additionally, they can provide reservoirs for an implant-associated drug delivery.

This thesis focusses on the development of bioactive silica and titania coatings on different types of implant materials like polymers, bioglasses or metals. These systems were chosen with regard to applications on middle ear or cochlea implants. The thesis was carried out as a part of the D1 project in the Collaborative Research Centre 599 “*Sustainable bioresorbable and permanent implants of metallic and ceramic materials*” of the German Research Foundation and of the Cluster of Excellence “*Hearing4all*”.

The first part of the thesis presents comprehensive investigations on the properties of periodic mesoporous organosilica (PMO) coatings as a novel biomaterial. PMOs are materials with a high surface area and structured mesopores that can be synthesized by condensation and hydrolysis from organosilica precursors in combination with structure-directing agents. PMO coatings on implant materials have not been studied so far. In this work, it was demonstrated that PMO coatings could store and release large amounts of active substances like the antibiotic ciprofloxacin and the neuroprotective agent rolipram. Furthermore, cell culture experiments showed that PMO coatings were cytocompatible and could influence the cell growth positively.

The second part of the thesis deals with the functionalization of PEEK (polyether ether ketone) surfaces. The polymer PEEK possesses favourable properties for application as a biomaterial and can, for example, be applied in middle ear prostheses. However, although PEEK is biocompatible, it is also bioinert. Hence, for some applications as an implant material, its surface has to be functionalized before implantation. The objective of the present work was to coat PEEK with differently modified titania films by the dip-coating method to produce mechanically stable thin films. The developed coatings were based either on super-hydrophilic porous titania and or on titania modified with titania nanoparticles. They displayed excellent results in cell culture tests and led to an enhanced cell compatibility of the PEEK material.

Keywords: bioactive coatings, periodic mesoporous organosilica, titania, thin films, polyether ether ketone, drug delivery system, biocompatibility

Kurzzusammenfassung

Heutzutage liegt die optimale Funktion eines Implantats nicht nur darin bestimmte Körperfunktionen zu übernehmen, die Forschung ist bemüht um eine nachhaltige Interaktion des Implantats mit dem Körper mit den kleinstmöglichen Nebenwirkungen. Zu den Schwerpunkten der Forschungsarbeiten gehören die Integration von Implantatmaterialien in das umliegende Gewebe sowie die Reduktion an systemischer Medikation, die Entzündungen vermeiden soll. Ist die Oberfläche des Materials aufgrund ihrer physikalischen bzw. chemischen Eigenschaften bioinert oder bioinkompatibel, so kann dies mittels einer geeigneten Beschichtung geändert werden. Dabei kann die funktionelle Beschichtung nicht nur bioaktive Moleküle tragen, sondern auch strukturell oder chemisch die Oberfläche verändern.

Die vorliegende Dissertation beschäftigt sich mit der Entwicklung von bioaktiven Beschichtungen auf Silica- und Titandioxidbasis auf Implantatmaterialien wie Polymeren, Metallen und Biogläsern, die den Einheilungsprozess z.B. von Mittelohrprothesen oder Cochlea-Implantaten unterstützen sollen. Die Dissertation wurde im Rahmen des Teilprojekts D1 des Sonderforschungsbereichs 599 „*Zukunftsfähige bioresorbierbare und permanente Implantate aus metallischen und keramischen Werkstoffen*“ der Deutschen Forschungsgemeinschaft und des Exzellenzclusters „*Hearing4all*“ durchgeführt.

Im Rahmen der vorliegenden Arbeit wurden zum einen neuartige periodisch mesoporöse Organosilica- (PMO) Beschichtungen entwickelt. Die PMOs sind Materialien mit einer großen Oberfläche und gleichmäßig angeordneten Mesoporen, die durch Kondensation und Hydrolyse aus Organosilica-Prekursoren und strukturdirigierenden Agentien erhalten werden. Die Beschichtung von Implantatmaterialien mit dieser Stoffklasse ist bislang wenig etabliert, bietet jedoch dank der organischen Moleküle im Silica-Gerüst eine Vielzahl an Modifikationsmöglichkeiten. Im Rahmen dieser Arbeit wurden Beschichtungen auf permanenten Implantaten untersucht, in denen Wirkstoffe, wie das Antibiotikum Ciprofloxacin und das Neuroprotektivum Rolipram eingelagert wurden. Es konnte gezeigt werden, dass die PMO-Schichten ein hohes Einlagerungsvolumen haben und auch eine hohe Menge an Wirkstoffen wieder freisetzen können. In den abschließenden Zellkulturstudien wurde gezeigt, dass die PMO-Schichten sehr gut cytotokompatibel sind und das Zellwachstum positiv beeinflussen können.

Der zweite Teil der Dissertation beschäftigt sich mit der Funktionalisierung von PEEK-Oberflächen (Polyetheretherketon). Das Polymer PEEK soll hierbei als Material für Mittelohrprothesen zum Einsatz kommen. Da das Polymer zwar biokompatibel aber bioinert ist, muss dessen Oberfläche im Hinblick auf manche Implantatanwendungen zuvor funktionalisiert werden. Im Rahmen der Arbeit wurde die Oberfläche direkt mit unterschiedlichen Titandioxidfilmen beschichtet. Es wurde gezeigt, dass die Schichten mittels des Dip-Coatings auf die PEEK-Oberfläche aufgebracht werden konnten und auf dieser auch mechanisch stabil waren. Die entwickelten Beschichtungen auf Basis von superhydrophilem porösem sowie mit Nanopartikeln modifiziertem Titandioxid zeigten sehr gute Ergebnisse in den Zellkulturuntersuchungen und führten zu einer deutlichen Steigerung der Zellkompatibilität der PEEK-Materialien.

Stichpunkte: Bioaktive Beschichtungen, Periodisch mesoporöse Organosilica, Titandioxid, Dünnschichten, Polyetheretherketon, Medikamentenfreisetzungssysteme, Biokompatibilität

Table of Contents

Abstract.....	I
Kurzzusammenfassung	II
Table of Contents.....	III
Abbreviations.....	VII
1. Introduction.....	1
2. General Background	6
2.1 Physiology of Hearing	6
2.2 Implants in Otology	9
2.2.1 Middle Ear Prosthesis	9
2.2.2 Cochlea Implant	14
2.3 Polymeric Biomaterials as Medical Implants	17
2.4 Polyether Ether Ketone (PEEK)	18
2.4.1 Biocompatibility of PEEK.....	21
2.4.2 Bioactive Functionalisation of PEEK.....	23
2.5 Titania and Inorganic-Organic Silica Materials.....	26
2.5.1 Titania Films in Biomedical Applications	26
2.5.2 Silica-Based Mesoporous Organic-Inorganic Materials.....	27
2.5.3 Periodic Mesoporous Organosilica (PMO).....	32
2.5.4 PMOs for Biomedical Applications.....	36
2.6 Dip-Coating	39
2.7 Antibiotics and Neuroprotective Substances	43
2.7.1 Ciprofloxacin	43
2.7.2 Brain-Derived Neurotrophic Factor.....	46
2.7.3 Rolipram	47
2.8 Controlled Drug Delivery	48

Table of Contents

2.9 Influence of Surface Properties on Cell Adhesion.....	50
3. Preparation of Materials.....	51
3.1 Cleaning of the Substrates	51
3.2 Preparation of Titania Thin Films on PEEK Substrates	52
3.3 Preparation of Silica-Based Mesoporous Organic-Inorganic Coatings	54
3.4 Modification of Phenyl-PMO with Sulfonate Groups.....	55
3.5 Drug Loading and Release Procedures	57
3.5.1 Drug Loading and Release of Ciprofloxacin	57
3.5.2 Drug Loading and Release of Rolipram	59
4. Analytical Methods.....	62
4.1 Physisorption Measurements	62
4.2 Ellipsometry.....	65
4.3 Scanning Electron Microscopy	68
4.4 Transmission Electron Microscopy	69
4.5 Nanoindenter Analysis.....	70
4.6 Water Contact Angle Measurements	71
4.7 Förster Resonance Electron Transfer.....	72
4.8 Thermogravimetric Analysis	73
4.9 Ultraviolet/Visible Light (UV-Vis) Photometry.....	74
4.10 Infrared Spectroscopy	75
4.11 X-ray Diffraction	75
4.12 Cell Culture Tests	76
4.12.1 Cell Culture Tests on PMO Coatings	77
4.12.2 Cytocompatibility Tests of Titania-Coated PEEK.....	80
4.12.3 Antibacterial Activity Tests for Phenyl-PMO Coatings	81
5. Results and Discussion I.....	83

5.1 Characterisation of PMO Particles	83
5.2 Characterisation of PMO Coatings	89
5.2.1 Spectroscopic, Diffractometric and Microscopic Analysis of PMO Coatings	90
5.2.2 Krypton Sorption Measurements of the PMOs Coatings	99
5.2.3 Ellipsometric Measurements.....	103
5.2.4 Stiffness of PMO Coatings	106
5.2.5 Sulfonation of Phenyl-PMO Coatings	107
5.2.6 Wettability of PMO Coatings	109
5.2.7 Stability of PMOs under Cell Culture Conditions	110
5.3 Drug Loading and Release.....	112
5.3.1 Loading of Ciprofloxacin.....	112
5.3.2 Release of Ciprofloxacin	114
5.3.3 Examination of Ciprofloxacin Release by Foerster Resonance Energy Transfer.....	118
5.3.4 Release of Rolipram.....	126
5.4 Antibacterial Activity of Ciprofloxacin-Loaded Phenyl-PMO Coatings	128
5.5 Cell Culture Tests on PMO Coatings	131
5.5.1 Cytocompatibility Tests of PMO Coatings.....	131
5.5.2 Examination of Brain-Derived Neurotrophic Factor Producing Cells on Phenyl-PMO Coating.....	138
5.5.3 Spiral Ganglion Cell Culture Investigations of PMO Coatings Loaded with Bioactive Molecules	140
5.6 Summary and Outlook.....	145
6. Results and Discussion II.....	149
6.1 Characterisation of Thin Titania Films on PEEK.....	149
6.2 Mechanical Stability Studies of Titania Films.....	154

Table of Contents

6.3 Chemical Stability Studies of Titania Films	155
6.4 Cytocompatibility Tests of Titania-Coated PEEK.....	157
6.5 Summary and Outlook	162
7. Conclusions.....	164
8. References.....	166
9. Supporting Information.....	180
10. Appendix.....	187
Danksagung	187
List of Publications	189
Curriculum Vitae	192

Abbreviations

%	percent
°	degree
µg	microgram
Å	Angstrom
a.u.	atomic units
acac	acetyl acetone
Ar	argon
as	as synthesized
BDNF	brain-derived neurotrophic factor
BET	BRUNNER, EMMETT, TELLER
BJH	BARETT, JOYNER, HALENDA
BTEB	1,4-bis(triethoxysilyl)benzene
BTEBp	4,4- bis(triethoxysilyl)biphenyl
C	Celsius
ca	calcined
cAMP	cyclic adenosine monophosphate
CCP	cell culture plastic
CFX	ciprofloxacin
CI	cochlea implant
cm	centimetre
CMC	critical micelle concentration
CTAB	Cetyltrimethylammoniumbromid
CTAC	Cetyltrimethylammoniumchlorid
<i>d</i>	day
DEA	diethanol amine
DFT	density functional theory
DMEM	Dulbecco's Modified Eagle's Medium
e.g.	<i>exempli gratia</i> , for example
EISA	evaporation-induced self-assembly
<i>et al.</i>	<i>et alii</i> , and other
EtOH	ethanol
eV	electronvolt
FCS	fetal calf serum
FRET	Förster resonance energy transfer
FTIR	Fourier transformed infrared spectroscopy
g	gram
GPa	gigapascal

Abbreviations

HA	hydroxyapatite
HCl	hydrochloric acid
HUVEC	human umbilical vein endothelial cells
I	intensity
i.e.	<i>id est</i> , that means
Kr	Krypton
λ	wave length
L	litre
LDH	layer doubled hydroxide
m	meter
M	molar (concentration)
min	minute
mL	millilitre
mM	millimolar
MPS	mesoporous
N	Nitrogen
n	amount of substance
NaOH	sodium hydroxide
ng	nanogram
NK	negative control
Nm	Newton meter
OTAB	octyltrimethylammonium bromide
OTAC	octyltrimethylammonium chloride
<i>p</i>	pressure
Pa	Pascal
PBS	phosphate buffered saline
PEEK	polyether ether ketone
PEG	polyethylene glycol
PK	positive control
PMMA	poly(methyl methacrylate)
PMO	periodic mesoporous organosilica
PORP	particular ossicular chain reconstructive prosthesis
RP	rolipram
rpm	round per meter
s	second
S_{BET}	BET surface, specific surface
SDA	stricture-directing agent
SEM	scanning electron microscope
SFB	special research fields

Si	silicon
SNG	spiral ganglion neuron
STD	standard
T	temperature
<i>t</i>	thickness
<i>t</i>	time
TCP	tricalcium phosphate
TEM	transmission electron microscope
TEOS	tetraethyl orthosilicat
TGA	thermogravimetric analysis
TiO ₂	titania
TORP	total ossicular chain reconstructive prosthesis
<i>V</i>	volume
<i>v</i>	speed
XRD	X-Ray diffraction

1. Introduction

Nowadays, as life expectancy progressively increases, the need for sustainable implants grows. Implants not only have the purpose of taking over the failed body functions throughout the lifetime; moreover, they have to fulfil further requirements like excellent biointegration and inhibited bacterial growth. The interaction between the surface of an implant and the surrounding tissue is a crucial factor for its efficiency in the human body. If the implant surface is bioinert or bioincompatible, this property can be changed by establishing bioactive coatings.

These coatings must possess some crucial characteristics. First of all, the coatings have to be biocompatible without provoking foreign-body reactions or negative immune response. Second, they should have antibacterial properties to fight or inhibit inflammation after implantation. Furthermore, especially for bone-replacing implants, osteoconductive and osteoinductive features are essential. Hence, the coatings should induce the adhesion of osteoblasts and excite them to proliferate. Finally, the coatings have to be mechanically stable without detachment from the implant surface under physiological stress.^[1]

In the present thesis, two different coatings are evaluated regarding their bioactivity, cytocompatibility, antibacterial efficacy and chemical properties. On the one hand, periodic mesoporous organosilica coatings are examined as a possible novel biomaterial for applications involving controlled drug-release systems. On the other hand, different titania coatings on PEEK are evaluated concerning their osteoconductive properties.

In general, the development of drug delivery systems is a field of great interest. There is a need to improve the effectiveness, maximise therapeutic activity, minimise side effects, increase bioavailability and control the release rate for these systems. Therefore, a suitable material has to be developed with sufficient storage volume and the controlled release behaviour of drugs.^[2] These two aspects can be combined with the development of implant-associated drug delivery systems, relying on the release of a drug from a surface coating, which also attenuates the surface properties.

Porous silica nanoparticles and mesoporous silica thin films have become one of the most promising materials as drug delivery systems, because they offer a high surface area, uniform porous structure with well-defined and tunable pore sizes as well as a good biocompatibility.^[2-4] Our group has already successfully introduced mesoporous

1. Introduction

silica films as a novel type of coating, which allows functionalisation and local drug delivery from implants.^[3-7] Within this thesis, the next step of our research was to apply and investigate periodic mesoporous organosilicas (PMOs, Figure 1 right) as bioactive coatings on implants. These coatings offer a variety of useful characteristics for biomedical applications and are more versatile due to their hybrid composition. Correspondingly, the chemical, physical and mechanical properties of the PMO coatings can be finally adjusted by the chemistry of the organic bridging groups in the precursors.^[8,9]

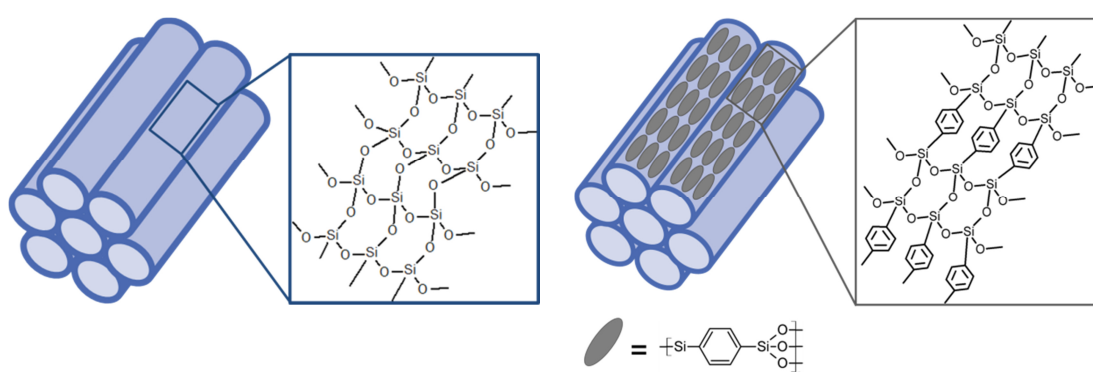


Figure 1: Comparison between a nanoporous silica (**left**) and periodic mesoporous organosilica (PMO) material (**right**).

The periodic mesoporous organosilicas were first described as ordered hybrid mesoporous materials containing homogeneously distributed organic groups in the silica network in 1999.^[10,11] This class of mesoporous material contains both organic and inorganic units in the pore walls. Here, the organic moieties replace a part of the siloxane bridges. The comparison between a porous silica network and a phenyl-PMO is displayed in Figure 1. PMOs offer a well-ordered pore structure, high surface areas and large pore volumes, hydrophobic nature and various chemically reactive sites.^[12,13] The main advantage of the PMOs versus nanoporous silicas is that a first chemical modification is already incorporated inside the pore walls. The presence of organic linkers in the framework has consequences for the rigidity or the flexibility of the material depending on the organic moiety and general structural properties. By contrast, nanoporous silicas can only be modified by co-condensation or post-grafting. Hence, the added functional groups reduce the pore diameter and pore volume and present a steric hindrance for guest molecules like enzymes or drugs.^[8,13] To date, a wide range of

organic-bridged silsesquioxane precursors have been used for the synthesis of PMOs, covering the field of the alkylenes, alkenylenes, aromatic groups as well as more complex moieties, e.g. with urea units in the organic linkers. The large variety of the organic bridging groups incorporated in the PMO precursors nowadays enables the choice of an optimal one for the desired functionality or application. In addition to the precursors exhibiting active sites, co-condensation of the bissilylated bridged organosilanes and monosilylated coupling agents is also possible, resulting in bifunctional PMOs with inert bridging groups and active functional groups located in the mesopores.^[13] This synthesis provides even more options for the modification of PMO materials.

The synthesis of PMOs is similar to that of nanostructured mesoporous M41S-type materials, displayed in Figure 2. For the synthesis of both material groups, various structure-directing agents (SDAs) like surfactants can be applied under acidic, neutral or basic conditions. PMO materials can also be deposited as thin films on substrates by dip-, spin- or drop-coating,^[14,15] as is the case for the thoroughly investigated silica coatings.

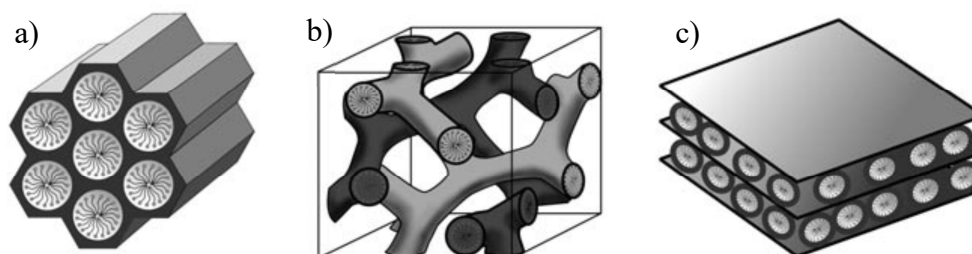


Figure 2: Different structures of mesoporous M41S materials: a) MCM-41 (2D hexagonal), b) MCM-48 (cubic) and c) MCM-50 (lamellar), taken from HOFFMANN *et al.*^[8]

The emphasis in this work lies on developing phenylene- and biphenylene-bridged PMO thin films. These aromatic-bridged PMOs were chosen due to their amenability for modification by different accesses, namely the modification of the phenylene ring as well as the binding of silanes to remaining reactive silanol groups of the silica network. The possibility of direct chemical modification of the organic bridging groups in the pore walls is an important advantage of the PMOs. Especially unsaturated bridging moieties – e.g. ethenylene groups – or, like in our case, aromatic ones, offer various possibilities. For example, for the purpose of binding positively charged drugs (such as

the antibiotic ciprofloxacin), the modification of the pore walls with sulfonate groups has been proven favourable.^[3,16] Moreover, the hydrophobic moieties in the walls of the PMOs positively influence the storage of many drugs, as most drugs contain non-polar domains in their structure.

In the first part of the present thesis, comprehensive investigations on the properties of PMO films as novel coatings for biomedical implants are presented. Apart from basic characterisation, the research focus is on mechanical properties, cytocompatibility as well as the loading and release of the substances ciprofloxacin and rolipram. Sol-gel methods were applied to generate the PMO coatings by dip-coating in the presence of the organic-inorganic silica precursors 1,4-bis(triethoxysilyl)benzene (BTEB) and 4,4-bis(triethoxysilyl)biphenyl (BTEBp). Most results were obtained for the phenyl-PMO coatings, as the first successful results concerning the specific surface area and drug loading were gathered with the BTEB precursor. Later, the BTEBp precursor was examined and used in the thin film synthesis. In a second step, the modification of phenyl-PMO with sulfonic acid groups was performed by grafting to increase the amount of the loaded antibiotic ciprofloxacin by electrostatic interactions. The excellent cell compatibility was accompanied by a high uptake of the antibiotic ciprofloxacin and the drug rolipram. A controlled release of both substances could be achieved for about 14 days. For ciprofloxacin, the efficacy of the release system was confirmed using bacterial cultures. Furthermore, the effect of PMO surfaces on gene-modified fibroblasts that produce the brain-derived neurotrophic factor (BDNF) as well as on spiral ganglion neurons was studied, with generally positive results. Hence, this novel biomaterial possesses many favourable properties for the application as an implant coating.

In the second part of the present thesis, different titania coatings were applied on the bioinert polymer polyether ether ketone (PEEK). This is a promising lightweight polymer material for medical implants, especially in the field of spinal, trauma and orthopaedic implantology. Due to its tunable mechanical properties, PEEK may hold interest in other areas like dentistry and otolaryngology (e.g. ossicular implants). As PEEK is a bioinert material, the emphasis of the work lies on the application of thin titania coatings to provoke a cytocompatible character of the implant material. A simple sol-gel method was applied to prepare chemically and mechanically stable as well as

cytocompatible titania coatings on commercially available PEEK substrates. Three different titania coatings were investigated: plain titania films, titania films with added titania nanoparticles and titania films prepared with additives, which cause the formation of nanoparticles during the synthesis. Cytocompatibility tests with fibroblasts and osteoblast progenitor cells demonstrated an enhanced cell adhesion and cell proliferation on the titania films compared to native PEEK samples. Overall, the plain titania coatings showed the most favourable combination of properties and appeared to be most promising for the further development of implant materials, especially to enhance the osteointegration of PEEK implants.

2. General Background

This chapter provides an overview of the general background for a basic comprehension of the presented thesis. First, the anatomy of the ear and the audio impression are presented, followed by the medical treatment of the ear with middle ear prosthesis or a cochlea implant due to hearing loss. Furthermore, periodic mesoporous organosilica (PMO) itself, the different options for modification as well as the application of PMOs as biomaterials are explained. A brief introduction to the polymeric biomaterials used as medical implants with a detailed view on the modified polymer polyether ether ketone (PEEK) is offered. The impact on the cytocompatibility of titania-coated implants follows. Finally, different active substances and materials are presented that can improve the bioactivity of implants.

2.1 Physiology of Hearing

One of the basic forms for human communication is related to hearing and speaking. This is crucial for contact with other humans and integration into social life. Therefore, the function of the ear holds special relevance for hearing itself and language development, especially during early childhood. Besides hearing ability, the inner ear is also responsible for the sense of balance. Hence, a healthy ear holds extensive importance in everyday life. However, when the ear becomes ill or an inherent dysfunction is given, it can be remedied by an inner or middle ear implant, dependent on the disability.

The anatomy of the ear is complex. In the following, it is divided into different parts (Figure 3), namely the peripheral and the central part. The peripheral part is the outer, middle and inner ear as well as *Nervus vestibulocochlearis*, which is divided into the auditory and the balance nerve. The central part of the ear includes the auditory pathway, which is responsible for the stimulus processing, the central part of the facial nerve, (*Nervus facialis*) which reaches the inner ear, and the vestibular pathway, which is responsible for the sense of balance. The peripheral part of the ear is responsible for the audio processing of sounds and speech and forwards the audio impression to the central system.^[17,18]

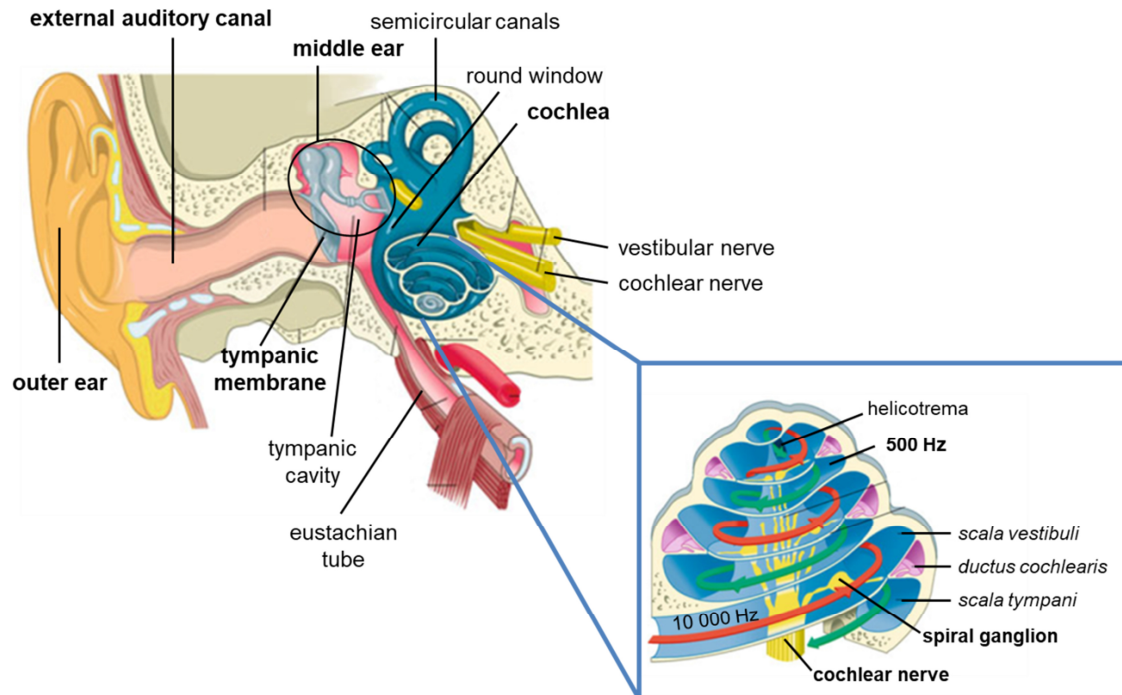


Figure 3: Overview of the outer, middle and inner ear with an enlarged extract of the cochlea, adopted from LENARZ and BOENNINGHAUS 2012.^[17]

The upper picture of Figure 3 displays an overview of the ear structure. The outer ear with the pinna and the external auditory canal is made of cartilage, whereby only the inner part of the auditory canal is bordered by bone. The funnel-shaped tympanic membrane lies at the end of the external auditory canal where the middle ear starts. The middle ear includes the ossicles in the inflated tympanic cavity. The tympanic cavity is linked by the Eustachian tube to the nose and throat area for pressure compensation of the middle ear. The Eustachian tube is also vulnerable to the transfer of viruses and bacteria to the middle ear, which can cause an otitis media. The pressure compensation towards the middle ear is important at varying air pressure to enable the vibration of the tympanic membrane and transition of this vibration to the ossicles. The auditory ossicles comprise three mucus-covered small bones named the malleus, incus and stapes, which are fixed to the tympanic membrane and flexibly anchored to the round window. The inner ear filled with liquid lies after the round window. In the inner ear, the cochlea can be found, entwined two-and-a-half times around its own axis and liable for audio procession. The vestibular labyrinth responsible for the balance sense can also be found in the inner ear.^[17-19]

2. General Background

The cochlea can be divided into three parts: the *Scala vestibuli*, which transmits the sound to the lower frequencies in the upper cochlea; the *Scala tympani*, transmitting the sound back to the lower frequencies; and the *Ductus cochlearis*, incorporating the sensory cells named hair cells, which are divided in one row of inner hair cells and three rows of outer hair cells (compare Figure 4). The hair cells are bound over synapses to the dendrites of the spiral ganglion neurons (SGNs), which merge into *Ganglion spirale cochleae* and converge to the auditory nerve (*Nervus cochlearis*). From the auditor nerve, the stimuli are passed to the auditory pathway of the central part and processed in the brain to sense perception.^[17,20]

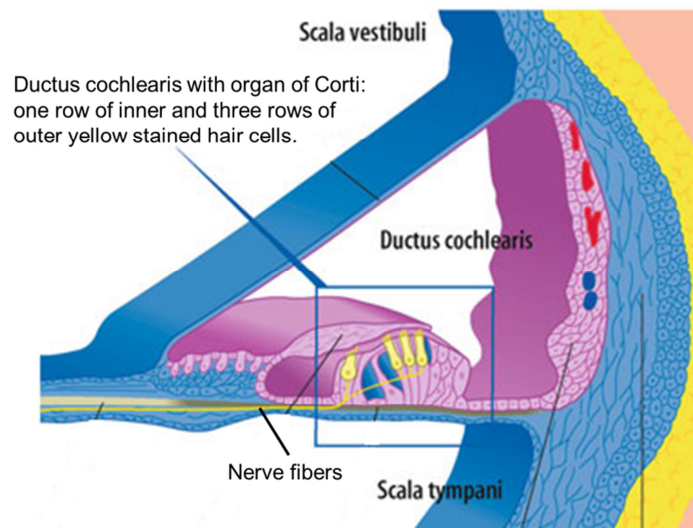


Figure 4: Magnification of the *Ductus cochlearis* with a better insight into the hair cells, adopted from LENARZ and BOENNINGHAUS 2012.^[17]

The percipience of the soundwave in the outer ear is the first step of the information processing whereby the audio impression stands at the end. The human ear is able to perceive and transform soundwaves in a frequency range between 20 Hz and 16000 Hz, whereby different tone pitches can be differed.^[19] The soundwaves are periodic air pressure fluctuations that are detected by the pinna. Subsequently, they are transmitted through the auditory canal to the tympanic membrane, which starts to swing and transduces the vibration to the ossicles in such a way. The transformation of the air pressure fluctuation into mechanic swinging causes a change of the impedance from the air-filled middle ear to the liquid-filled inner ear. The amplification of the sound in the middle ear is important for the efficient transmission of the soundwave through the

liquid in the inner ear (perilymph). Since the surface area of the tympanic membrane (60 mm^2) is larger compared to the oval window (3 mm^2), the sound is amplified before it reaches the perilymph.^[21] The travelling wave in the perilymph is induced by the vibrations of the ossicles and passes through the basilar membrane to the helicotrema in the cochlea. At a certain frequency in the *Scala vestibuli*, the wave brakes and stimulates the sensory hair at this place (see Figure 4). When the sensory hairs are stimulated, the mechanic energy is transferred into chemical signals. The hair cells are induced and forward the chemical signals to the SGNs, which in turn induce the action potential in the auditor nerve. The transformation of impulses in auditory impression and directional hearing is conducted in the central auditory pathway and the brain.^[17,18,22]

2.2 Implants in Otology

There are various reasons for using implants in the ear, the most prominent of which are infections, innate deafness or high exposure to noise. Problems can occur in the inner ear as well as the middle ear or the central auditory system and they are sometimes difficult to explain. Nevertheless, many patients can be helped by employing implants, dependent on the illness of the inner or the middle ear. Although most patients carrying an auditory implant have problems differing single sounds when it is too noisy – e.g. when many are voices talking at the same time or music is played – they enjoy taking part in the social life without severe disabilities. The project D1 within the SFB 599 focused on the improvement of middle ear prosthesis and the excellence cluster *Hearing4all* focused on cochlea prosthesis. These two are described in further detail in the following.

2.2.1 Middle Ear Prosthesis

Diseases of the Middle Ear

When the function of the middle ear and the ossicles is impaired, the sound transmission to the inner ear is no longer possible, whereby a so-called conductive hearing loss results.^[23] A chronic *otitis media* or a cholesteatoma can lead to the loss of ossicles. A chronical inflammation like *otitis media* is caused by bacteria like *Pseudomonas aeruginosa*, *Staphylococcus aureus* or *Streptococcus pneumoniae*.^[24] During an

2. General Background

infection, the air-filled space of the middle ear is filled with a liquid caused by invaded bacteria leading to an interrupted sound transmission. In most cases, the inflammation can be healed by antibiotics. In a few severe cases, the inflammation becomes chronic and can destroy the ossicles or their transmission function.^[17] When the middle ear loses its function, the hearing decreases by about 26 dB, which does not lead to complete deafness.^[21,23] Another common disease of the middle ear is otosclerosis. The bone that surrounds the middle ear is restructured, leading to an immobility of the stapes due to ossification.^[25]

Cholesteatoma are rampant epithelial cells of the middle ear mucosa accompanied by a bacterial attack, which can lead to an infection. This infection can engage the ossicles and destroy them (Figure 5). This disease can only be healed through the surgical removal of all affected tissue and subsequent treatment with an antibiotic like ciprofloxacin.^[18,24] One possible therapy is the implantation of a middle ear prosthesis, replacing the lost ossicles as shown in Figure 6.

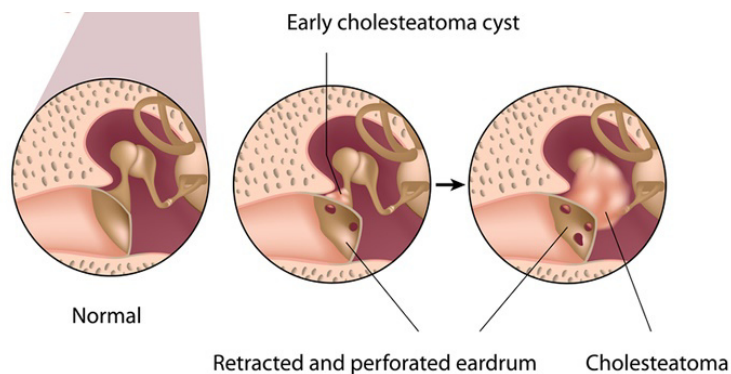


Figure 5: Cholesteatoma impacted middle ear, from ref. [26].

Types of Middle Ear Prosthesis

Different types of middle ear prosthesis are possible. When only the incus is missing or has to be replaced, a so-called *partial ossicular replacement prosthesis* (PORP) is inserted. As shown in Figure 6 c), this implant is placed between the malleus – which is still in contact with the tympanic membrane – and stapes to restore the mechanic sound conduction. When all ossicles are removed or only the malleus is retained, then the implant is called a *total ossicular replacement prosthesis* (TORP) and it is attached to the round window.^[27] The project D1 within SFB 599 tried to improve such PORP or

TORP implants in various ways during the runtime of the project. The methods are described in the following sections.

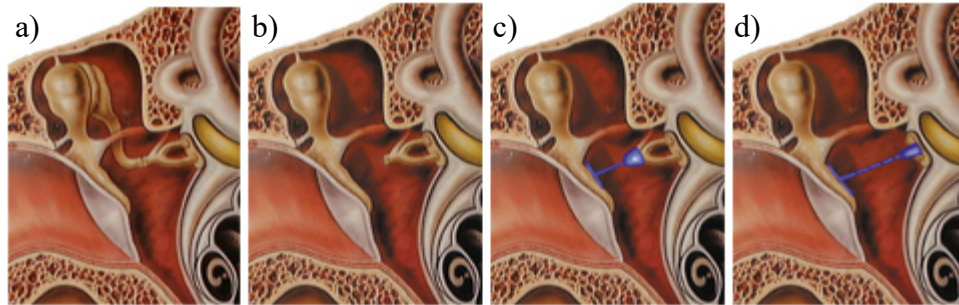


Figure 6: Middle ear implant for replacement of ossicles. a) intact ossicular chain, b) missing incus, c) incus replaced by Partial Ossicular Replacement Prosthesis (PORP) when stapes is still intact, d) Total Ossicular Replacement Prosthesis (TORP) replacing incus and stapes. From ref. [27].

Another type of middle ear implants is one that is attached directly at the ossicles, as displayed in Figure 7 (middle). It is called a bone-anchored hearing aid (BAHA) and can be used instead of a conventional hearing aid, if this cannot be applied due to medical reasons or chronic ear canal inflammation, as well as for sensorineural hearing loss. This implant converts the sound in mechanical vibrations and stimulates the ossicles conducting the signals to the cochlea. The receiver of the electric signals that is attached to the ossicles is called a floating mass transducer. The floating mass transducer can even replace the ossicles and is attached directly to the round window, thus stimulating the cochlea.^[23]

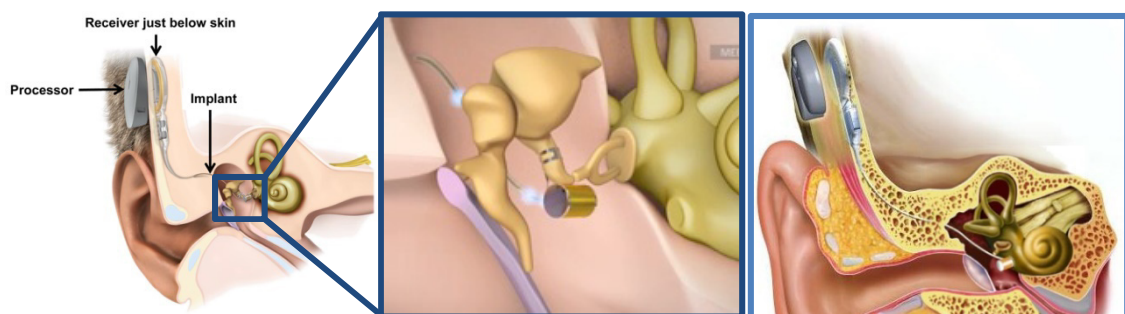


Figure 7: Vibrant SOUNDBRIDGE (BAHA) as a middle ear prosthesis. **Left:** The sound is transmitted by the processor, which is placed at the outer side of the bone, to the receiver, below the skin, and transformed into electrical signals. **Middle:** The signals are conducted to the floating mass transducer (FMT) itself, which is attached to the incus, so that the stiff ossicles are moved. **Right:** FMT can also replace the ossicles and be attached directly to the round window. From MED-EL.^[23]

Improvement of Middle Ear Implant Materials

The crucial properties for materials for PORP or TORP are stiffness and lightweight for the best possible sound transmission. Furthermore, the material should be biocompatible and stable in the physiological environment. The disease of the middle ear and the destruction of the ossicles determine what shape and material the prosthesis have to be. Bioactive materials like bones or cartilage and biodegradable ceramics like glass ceramics or hydroxyapatite dissolve in a chronically inflamed middle ear. Using bioinert materials like metals or aluminium oxide may cause foreign-body reactions and thus rejection of the implant. An inflammation-free middle ear accepts many materials employed for the prosthesis. Here, the main required properties are non-toxicity and tissue-compatibility.^[28] Subsequently, the main problem is the displacement of the prosthesis in the middle ear. Hence, the list of alloplastic materials used for passive middle ear implants is long, including various metals like titanium, gold or steel, as well as plastics like Teflon® or ceramics like glass ceramics, hydroxyapatite and Bioverit®, which was examined intensively in SFB 599.^[18,28] Bioverit® (Figure 8 left) is sometimes used for middle ear implants. The advantages of the material are the possibility of implantation into inflamed tissue, the inhibition of growth of some bacteria and a large surface that can be used for modification.^[18,29] A recently presented study for the application of polyether etherketone material as TORP offered promising results. The advantages of PEEK TORP (Figure 8 right) are the light weight of the polymeric material, the adjustable hardness and the production of TORP in a high number by micro-injection moulding, while the major disadvantage is the bioinertness of PEEK. This will be discussed in another chapter.

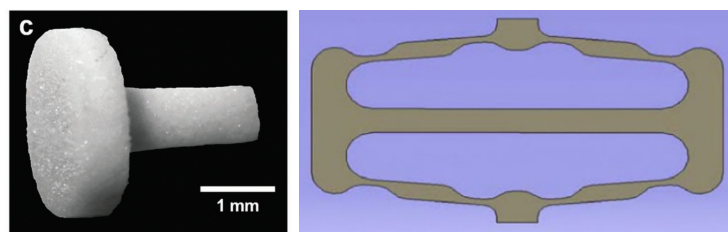


Figure 8: Left: Bioverit® prosthesis that is widely used to replace infected or impaired ossicles, from ref. [4]. Right: Schematic picture of a TORP made of PEEK by micro-injection moulding, from ref. [30].

A huge field of research exists aiming to improve the technology, shape, materials and functionalisation of the middle ear implants. Hence, in the following only the results collected inside the SFB 599 are summarised, whereas the full list can be found in [31]. One of the main emphases was the fixation of the TORP in the middle ear. LENSING *et al.* examined prosthesis made of magnesium, which provide a better fixation of the prosthesis to the stapes as magnesium appears to be osteoconductive.^[32,33] Indeed, magnesium degraded too quickly and thus was not suitable as a permanent TORP implant.^[34] EHLERT *et al.* pursued another approach,^[6] whereby Bioverit® prosthesis (Figure 8) were coated with thin mesoporous silica (MPS) films and subsequently modified with amino groups and BMP-2, a bone morphogenetic protein. Only the end of the stem was treated with BMP-2 for immobilisation of the TORP to the stapes.

Within the SFB 599, the coating with MPS thin films was examined intensively and evaluated in many *in-vitro* and *in-vivo* experiments.^[3-7,25,35-40] The present thesis evaluates the periodic mesoporous organosilica as an alternative coating on implant materials. Due to their chemistry, the PMOs are promising candidates in this research field. The MSP coating has the advantage that it is biocompatible and offers a lot of space for loading of active substances. After a reconstructive surgery of the middle ear, the patient is treated systemically with antibiotics – often ciprofloxacin – to suppress an inflammation.^[24,28] As the middle ear is an air-filled space, the drug transport and efficacy is reduced here. Hence, a high dose of antibiotics has to be given to achieve an antibacterial effect. A high amount of the given antibiotics is transported to other organs, leading to undesired side effects. EHLERT *et al.* have shown a possible drug release of the antibiotic ciprofloxacin from the MPS coating on the Bioverit®.^[3] The modification of the coating with sulfonic acid groups led to a higher amount of loaded ciprofloxacin. The functionalisation of the coating with steric hindering molecules bis(trimethoxysilyl)hexane and 1,3-di-n-octyl-tetramethyldisilazane provoked a reasonably controlled release. Without the large molecules, only a burst release could be achieved. *In-vivo* studies on infected middle ear in rabbit models proved that the MPS coatings were biocompatible^[5,38] and a high initial dose of the antibiotic was necessary to kill all of the bacteria. Subsequently, small doses of the drug prevented a new infection. The burst release – as achieved in sulfonated MPS coatings – was preferred over a slow and controlled release with the additional modifications.^[37]

2. General Background

Further approaches for antibacterial coatings were layer double hydroxides (LDHs) on Bioverit® loaded with ciprofloxacin^[41,42] and silver-loaded mesoporous as well as dense silica coatings.^[18,35]

2.2.2 Cochlea Implant

Partial or full hearing loss can occur due to sensorineural hearing loss when the sensory cells (hair cells) in the cochlea are missing inherently or damaged. This type of hearing loss is often permanent and cannot be solved by a hearing aid. Mild or moderate sensorineural hearing loss occurs when only the outer hair cells are impaired. Such a type of deafness can be treated with a hearing aid or middle ear implants like the BAHA. When the hair cells at the base of cochlea are impacted and the high frequencies can no longer be differed, it is called partial deafness. Therefore, a combined electric and acoustic stimulation can be used to help the patient.^[23] The full loss of sensorineural hearing is called severe or profound deafness and is caused by noise exposure, meningitis or exists inherently. Hereby, all hair cells are involved and stimulus conduction is no longer possible. The sound waves are not transformed in action potentials and transferred to the hearing nerve. In this case, a cochlea implant can help to regain the auditory impression by directly stimulating the spiral ganglion neurons through electrical impulses and transmitting the registered sound to the auditory nerve.^[43] Such implants can already be used for children from the age of 12 months with innate sensorineural hearing loss. Some parts of the electrode have to be replaced over the course of time when the children grow.^[23,43]

The cochlea implant is built up of an external part comprising a microphone, transmitting coil and the sound processor as well as an inner part with the cochlea electrode, counter electrode and receiver coil. A schematic (left) and real (right) picture of the cochlea implant is displayed in Figure 9.

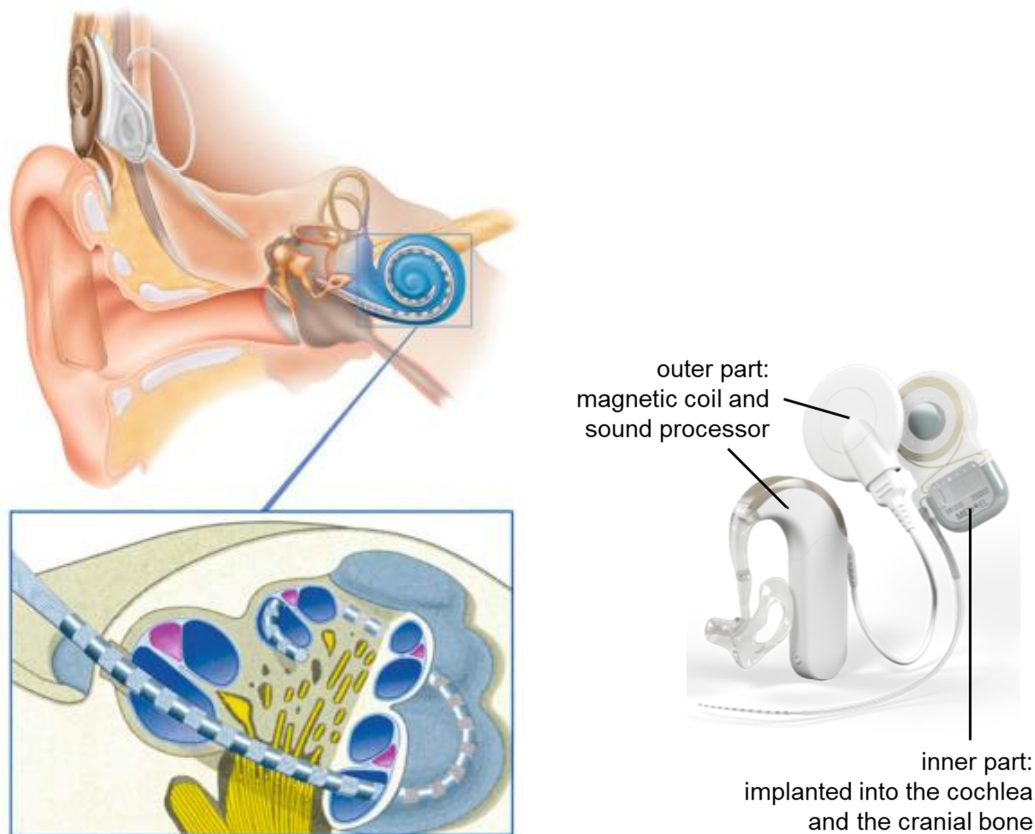


Figure 9: **Left:** Construction of a cochlea electrode and insertion in the cochlea, from ref. [17]. **Right:** Real cochlea electrode from MED-EL with an outer part with magnetic coil and sound processor and the inner part with cochlea electrode and receiver coil, from ref. [23].

The receiver coil is implanted in the bone behind the ear in a prepared bone gap, whereby the electrode is inserted through a small hole into the inaugurated inner ear.^[44] The sound processor with the microphone is placed externally behind the ear. Furthermore, the audio processor is also placed externally towards the receiver coil and is responsible for the translation of the auditory information in electrical impulses by radio waves. The implanted receiver decodes the electric impulses of the sound processor and transfers them to single contacts on the cochlea electrode itself, which is inserted into the cochlea. The necessary energy for this process in the implant is also transmitted from the sound processor transcutaneous. The flexible cochlea electrode has up to 22 platinum contacts (depending on the manufacturer), which are connected by platinum iridium alloy wires among each other and the receiver coil. The electrode is embedded in medical silicone with gaps for the contacts.^[18] The electrode is inserted in the *Scala tympani*. It stimulates the SGNs or dendrites by electrical impulses and causes

the action potential for stimulation of the auditory nerve. As the electrode contacts are located equidistant in the *Scala tympani*, they stimulate different parts of the basilar membrane and associated spiral ganglion neurons. Hence, the temporary structure of acoustic information is transferred due to the stimulation rate at every contact.^[17,19] Since the number of electrode contacts is limited and only few sections of the cochlea can be stimulated, the speech and sound comprehension is restricted. Especially the stimulation at lower frequencies is not possible, as the electrode does not reach the upper regions of the cochlea. Nonetheless, the technique is not sufficiently developed for the integration of more contacts on the electrode and manufacturing of more delicate and usable electrode structures.

The improvement of the cochlea implant is ongoing to achieve the best auditory impression and integrate patients in daily life. Scientists have been working on the cochlea implant for over 40 years. In the following, especially the interaction between the electrode itself and the surrounded tissue is regarded. Nevertheless, the improvement of the sound processor, the transmitter and receiver as well as electrode materials is also important for the best result provided to the patient. Many interdisciplinary projects are working on this issue. This thesis was integrated in one of them, excellence cluster *Hearing4all*. The list of publications on several topics related to the cochlea implant originated from this project can be found in [45].

One important research topic is the contact between the electrode and the nerve, and thus the location of the electrode in the cochlea. The distance between the electrode and the nerve should be as small as possible. With existing technology and materials, this cannot be realised for all areas of the cochlea. There are sectors where the electrode is located far away from the hair cells and SGNs at about 2.3 nm. This is too far for a qualitative transmission of electrical signals to the neurons.^[46,47] The electrical signal transmitted by the single electrode contact scatters and causes stimulation of adjacent regions, blurring the audio impression. Hence, higher electrical impulses are needed to stimulate the SGNs.

There are several approaches to overcome the poor communication between the electrode and the SGNs. STIEGHORST *et al.* published a study on self-bending electrode shafts due to swelling.^[48] The actuator was positioned eccentrically in a silicone hydrogel blend. Through the uptake of perilymph, the electrode bended and hugged the

cochlea.^[49,50] An important problem is also the degeneration of the SGNs due to the missing inner hair cells. The lower the amount of the SGNs, the poorer the signal transportation to the nerve.^[18] Hence, the growth of the SGNs and their dendrites should be increased or rather the degeneration should be stopped. Many studies report routes for a better interaction of dendrites of the SGNs with structured or coated electrodes.^[51–53] Moreover, the delivery of neuroprotective factors like brain-derived neurotrophic factor (BDNF) or drugs like rolipram from coatings or the silicone itself is examined. Both substances – rolipram and BDNF – are under suspicion to improve the proliferation of SGNs. A project within the excellence cluster *Hearing4all* dealt with chemically modified surfaces for the delivery of substances with neuroprotective effect, such as porous platinum or carbon nanotubes.^[45,54] A functionalisation of the electrode on a biological basis was evaluated by WARNECKE *et al.*^[55] They seeded gene-modified murine fibroblasts on structured silicone surfaces. The fibroblasts expressed BDNF, which had a positive effect on the survival rate of SGNs *in vitro*. KRANZ *et al.* could show that the application of rolipram and BDNF led to a three-time higher survival rate of SGNs compared to rolipram alone.^[56] Another strategy within the project was the structuring of the silicone of the electrode or embedding of dexamethasone to reduce fibroblasts.^[57,58]

In the present thesis, the influence of PMO coatings on the production of BDNF and the delivery of rolipram from the porous network is examined. The impact on survival of the spiral ganglion neurons was investigated and is summarised in section 5.5.3 Spiral Ganglion Cell Culture Investigations of PMO Coatings Loaded with Bioactive Molecules. It was planned to apply the PMO coatings, whether on the platinum electrodes or the silicone, to improve the interaction of the electrode with the SGNs.

2.3 Polymeric Biomaterials as Medical Implants

Already in the 1960s, synthetic polymers were used to replace sterilised metal utensils as disposable items to prevent infections in clinics. From then onwards, the use of polymers in the medical field has progressively increased. Soon, polymers were applied in long-term intracorporal devices like catheters and sewing materials and replaced metal implants in some applications.^[59] The range of polymers employed in the medical field includes synthetic, natural and biodegradable polymers, which are used in various

2. General Background

applications. Two types of applications have to be distinguished, namely short-term intracorporal cheap disposable items like catheters or long-term implants. The latter remain in the body for a long time and are exposed to chemical processes and mechanical strain. A major advantage of polymers in contrast to metal or glass is their simple and cheap production in a large quantity and variable design possibilities. By means of extrusion, injection, compression or blow molding, it is possible to create nearly all shapes of polymer samples using a template.

During recent years, many synthetic processes have been developed to produce biocompatible polymeric materials with the desired physical, chemical and biological features. This was attained by designing special chain segments or functional groups. Nevertheless, it is also possible to chemically modify an existing material installing functional groups or biomolecules as well as surface coatings.^[60] Certain characteristics of the medical grade polymers – especially their hydrophilicity or hydrophobicity, multifunctional groups or biodegradation – influence the interactions with the surrounding cells *in vivo*.^[61]

Many polymers that are used nowadays in the medical field were primarily developed for other purposes. Polyether ether ketone (PEEK) was originally synthesised for high temperature-resistant cable insulation. It has found its way quickly into other industrial areas – including in the medical field – due to its excellent mechanical and chemical properties.

2.4 Polyether Ether Ketone (PEEK)

Polyether ether ketone (PEEK) belongs to the family of polyaryl ether ketones (PAEK). It is semicrystalline with a maximal degree of crystallinity of 48%. It is a thermoplastic with a polymeric unit, as shown in Figure 10. In dependence of the manufacturing process, the temperature and the cooling rate, the crystallinity of PEEK varies.^[62]

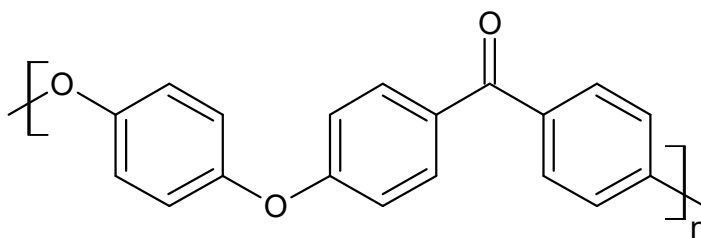


Figure 10: Monomer unit of the polymer polyether ether ketone (PEEK).

Polyaryl ether ketones are synthesised by alkylation of bisphenol salts. Polyether ether ketone is prepared by a polycondensation of 4,4-difluorobenzophenone and hydroquinone at 320 °C using potassium carbonate as catalyst (Figure 11).^[63]

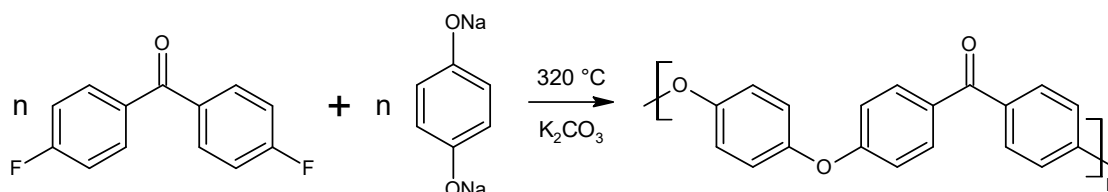


Figure 11: Reaction of the synthesis for PEEK.^[63]

PEEK is processed mainly by extrusion or injection molding. Very small samples for medical applications like dental implants can be produced using micro-injection molding. Given that PEEK can be processed without further additives, it is an ideal polymeric material for medical implants.

PEEK was successfully synthesised by Imperial Chemical Industries (ICI) in 1978 and commercialised in 1981. Initially, PEEK was used as high temperature-resistant cable isolation material. However, due to its excellent thermal and chemical stability, strong mechanical properties even at high temperatures as well as the easy processing, PEEK is applied in various industrial sectors. Among others, it is often used in the electronics, oil production, automotive and chemical industries. Especially due to its hardness and toughness, PEEK is a good alternative to metal.^[64] For this reason, PEEK implants can be found in different medical applications like orthopaedics, prosthetics, oral, thorax and vascular surgery.^[65,66]

PEEK is a semicrystalline thermoplastic polymer with a melting temperature of 334 °C and a glass transition temperature of 143 °C. Therefore, it is a high-temperature thermoplastic.^[62] Due to its chemical structure, PEEK has excellent chemical and mechanical properties such as chemical resistance against most acids and solvents as well as sterilisation processes, resistance to radiation, good thermal stability, low flammability and radiolucency.^[67–70] These properties can be explained by its resonance-stabilised chemical structure, as shown in Figure 10. The electrons in the aryl rings are delocalised within the macromolecule, making the material relatively stable against chemical influences. PEEK degrades only in strong oxidising acids like

2. General Background

concentrated sulfuric acid or fuming nitric acid. After dissolving PEEK in these acids, it can be regained by precipitation in water as sulfonic^[71] or nitro^[72] modified polymer.

PEEK also shows excellent resistance towards sterilisation, which is an important property of polymers used as medical implants. Treated in superheated steam for 500 cycles at 134 °C, PEEK does not change its structure or properties.^[73]

As-synthesised PEEK exhibits an elastic modulus in the range of 3 to 4 GPa. However, due to its good compatibility with reinforcing agents like glass or carbon fibres, the elastic modulus and other mechanical properties of PEEK can be adjusted to meet the requirements.^[74,75] Bare PEEK material shows signs of fatigue in products caused by continuous stress and temperature changes. Cracks occur and spread linearly through the whole material. PEEK reinforced with carbon fibres (CFR-PEEK composites) can be tailored to match the modulus of cortical bone (18 GPa) or even of Ti alloys (110 GPa). Metallic implants have a significantly higher elastic modulus than bones, and thus stress-shielding effects can occur during the healing after implantation. Metallic implant takes over the most mechanical stress and relieves the bone, which causes a degeneration of the bone substance over the years and leads to loosening of the implant. Hence, PEEK has become one of the leading high-performance polymers, which can replace metallic implant materials like titanium. The main applications lie in the field of dentistry, orthopaedics and trauma surgery (see Figure 12).^[76-78]

The inconvenient properties of PEEK also have to be considered. PEEK implants are not very flexible as the glass transition point lies clearly over the application temperature (37 °C). This is advantageous for the applications shown in Figure 12, but adverse for implants where flexibility is needed. A more crucial disadvantage is the bioinertness of PEEK. In many applications, where the cell to implant contact is inalienable – for instance, dental implants with necessary osseointegration – this disadvantage has to be considered and improved. Case studies on this inconvenient property are described below.

There are four grades of PEEK materials depending on the processing method, additives and purity of the final product.^[64,67,73] The first one cannot be employed in contact with blood or human tissue. The second one is admitted for a short contact with human tissue, such as surgical equipment. The third one can be used in the human body for an elongated time of less than 30 days, while only the fourth grade is admitted for long-

term use as a permanent implant. During recent years increasingly more fourth grade PEEK materials have been commercialised. The leading manufacturer of implant grade PEEK is Invibio® with its product PEEK-OPTIMA®.

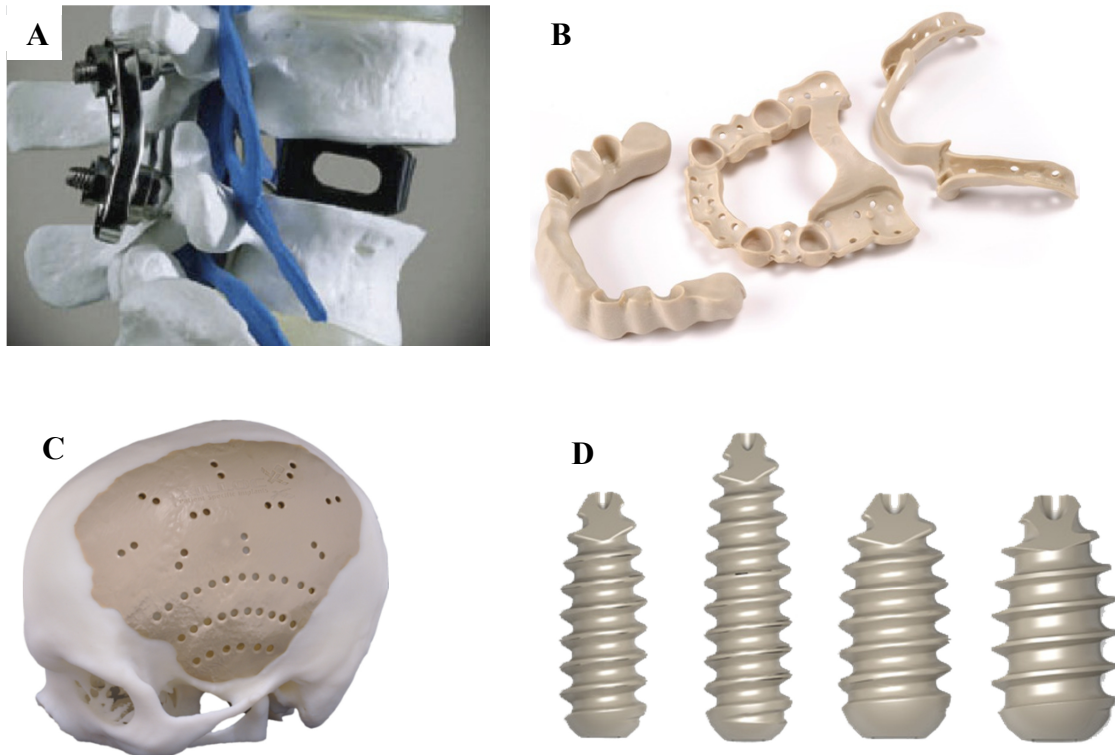


Figure 12: Examples of PEEK implants. A: Spinal disc replacement made of CFR-PEEK.^[64] B: Dental implants made of PEEK-OPTIMA® from Invibio®, the leading manufacturers for implant grade PEEK.^[79] C: Cranial plate for maintenance with patient-specific implants.^[80] D: Interface screws made of PEEK-OPTIMA®.^[81]

2.4.1 Biocompatibility of PEEK

The first studies concerning the biocompatibility of PEEK started in the late-1980s, stating excellent biocompatibility for PEEK and CFR-PEEK *in vivo*^[82] and *in vitro*^[77]. A material is biocompatible when it does not show any negative effects on the surrounding tissue.^[64] Bioinert materials – including PEEK – do not interact with the surrounding tissue, either negatively or positively. A bioactive material is one that shows specific biophysical, biochemical or physicochemical interactions with the surrounding tissue. Bioactive materials can affect the formation of new body tissue and – for example – an adhesion of osteoblasts to the implant for an optimal growth.^[83]

2. General Background

The first *in-vitro* biocompatibility studies were performed on carbon fibre-reinforced PEEK (CFR-PEEK) in 1990 by WENZ *et al.*^[77] For the cell culture studies, mouse fibroblasts were seeded on PEEK with 30% of carbon fibres. After 120 h, the lactate dehydrogenase (LDH) activity was examined, whereby CFR-PEEK showed a high *in-vitro* cytocompatibility in a direct cell contact as well as in extraction tests. HUNTER *et al.*^[84] explored the adhesion and proliferation of osteoblasts and fibroblasts on PEEK. Cell strains of murine fibroblasts and osteoblasts as well as fibroblasts from a human pulmonary tissue were seeded on PEEK and as references on titanium, Co-Cr-alloy and UHMW polyethylene substrates. The titanium sample showed the best proliferation results for fibroblasts, while UHMWPE substrates were the worst. PEEK samples revealed results comparable to the titanium. By contrast, the osteoblasts showed no differences in the adherence to various examined surfaces. This study verified that PEEK has no negative effects on the adhesion and proliferation of osteoblasts and fibroblasts.

The first *in-vivo* studies to examine the biocompatibility of PEEK were already carried out in 1987 by WILLIAMS *et al.*^[82] In this study, implants of bare PEEK and CFR-PEEK were inserted subcutaneously in rabbits and intramuscular in rats. Over an incubation period of 30 weeks, an encapsulation of the PEEK implants was observed. WILLIAMS evaluated the PEEK implants as biocompatible and appropriate for implantation due to the simple unspecific foreign-body reaction without further negative interaction between the implants and the tissue. Another study by JOCKISCH *et al.*^[85] confirmed WILLIAMS' results. The intramuscular implantation of CFR-PEEK samples and the fixation of a canine femur with CFR-PEEK plates revealed an unspecific foreign-body reaction, as well as a healing of the femur. Further cell culture studies with fibroblasts and osteoblasts confirmed the favourable cytocompatibility of pure PEEK as well as carbon and glass fibre-reinforced PEEK.^[70,86,87] Investigations on intramuscular implantation and systemic intracutaneous toxicity indicated no negative side effects.^[88]

All studies performed on the interaction of PEEK implants with cells as well as soft and hard animal tissues show that PEEK and its composites are biocompatible. However, they are still bioinert and exhibit only limited interactions with surrounding tissues, especially with bone. This can be traced back to the chemically-inert, hydrophobic character of PEEK, which hinders proteins from adsorbing on PEEK surfaces.^[89]

Instead, the contact of bone with a PEEK implant can cause the appearance of foreign-body granuloma since the bone is unable to bond to the material. This reaction can lead to loosening and rejection of the implant and infections of the surrounding body tissue.^[85]

A first study has recently been published reporting severe infectious complications after the application of PEEK dental implants.^[90] In three case studies, the patients lost their implants due to severe infections after implantation. A number of teeth were replaced in the jaw by a bridge holding containing PEEK implants, while only one implant was inserted as a screw. In all cases, osseointegration did not take place and the implants had to be replaced. The conclusion was that not only patient-dependent factors like oral hygiene influence the osseointegration, but also the limited knowledge on properties of PEEK in implantology. Although PEEK has been sufficiently evaluated through *in-vitro* and *in-vivo* studies, reliable clinical long-term studies are required to estimate the biocompatibility of PEEK in implantology. For long-term applications, the bioinert PEEK surface has to be modified for better interactions of a PEEK implant and the surrounding body tissue.

2.4.2 Bioactive Functionalisation of PEEK

In order to extend the applicability of PEEK, it is necessary to improve the healing process around PEEK implants and provide better integration with surrounding tissues, i.e. to lend the material a bioactive character. An excellent state-of-the-art review was published by MA and TANG.^[91] At present, two major strategies exist to improve the biocompatibility of PEEK: the surface modification of PEEK implants and the preparation of PEEK composites, thus changing the bulk material. However, mixing PEEK with other materials could have detrimental effects on its mechanical properties. In Table 1, all reported strategies for improving the bioactivity of PEEK are gathered. As is evident, there have been many attempts to modify PEEK and change its bioinertness. The most promising approaches involve the modification with hydroxyapatite, which was applied as a filler in PEEK bulk material as well as a coating. Furthermore, the modification with titania is a promising strategy. Many coating techniques have already been tested, although most of them are expensive and

2. General Background

difficult to apply on complex structures. Dip-coating is a possible solution for this problem.

Table 1: Overview of used and reported strategies to improve the bioactivity of PEEK, according to MA and TANG.^[91]

Composite preparation	Physical treatment	Chemical treatment
Fillers used: hydroxyapatite β -tricalcium phosphate bioglass calcium silicat titania	accelerated neutral atom beam Plasma treatment with: O_2 , N_2/O_2 , CH_4/O_2 , O_2/Ar NH_4 , NH_4/Ar , H_2/Ar	sulfonation hydroxylation
Surface modification		
Technique: radio frequency plasma immersion ion implantation cold spray technique magnetron sputtering arc ion plating ionic plasma deposition electronic beam deposition vacuum plasma spraying physical vapour deposition spin coating aerosol deposition	Coatings: hydroxyapatite titanium titania diamond like carbon tert-butoxid	

Bioactive PEEK Composites

The best-evaluated PEEK composites are those with hydroxyapatite (HA) and β -tricalcium phosphate (β -TCP). The most common manufacturing process is injection molding. Some samples were also manufactured by laser sintering as three-dimensional PEEK-HA scaffolds for tissue engineering.^[92]

The drawback of HA and β -TCP PEEK composites is the weak interaction of the fillers within the PEEK matrix, in contrast to carbon or glass fibre composites. The higher the

number of fine-dispersed HA particles embedded in the PEEK matrix, the higher the tensile modulus and microhardness, but the lower the tensile strength and strain to fracture.^[93] Further examined PEEK composites were those with different sized titania nanoparticles^[94] and PEEK/ β -TCP/TiO₂ composites.^[94]

Most studies on enhancing the biocompatibility of PEEK deal with enhancing the osteoconductivity of PEEK composites. Hence, common PEEK fillers are all well-known osteoconductive materials, especially hydroxyapatite. All investigated PEEK-HA composites showed a satisfactory biocompatibility without toxic side effects and improved ingrowth in bone. The enhanced binding of PEEK-HA composite implants to the bone was provided by the bone-like apatite layer on the surfaces of the former. The apatite layer is formed *in vivo* after implantation of bioactive-modified PEEK composites.^[64] Invibio® already released a clinically-tested PEEK-OPTIMA™ HA Enhanced Polymer for trauma and orthopaedics surgery exhibiting excellent results in osteoconductivity, long-term implantation and mechanical properties of these implants.^[95]

Bioactive Surface Modification of PEEK

Another way to improve the bioactivity of PEEK is to modify the PEEK surface; for example, through plasma treatment or by coating the surface, without changing the bulk material. The treatment of PEEK with ammonia, nitrogen or oxygen plasma leads to a roughening of the surface and introduces polar groups like hydroxyl or amino groups, leading to a good adhesion of mouse fibroblasts and osteoblasts.^[96-99]

The HA-coated PEEK is very well investigated similar to PEEK-HA composites. Commercially-accessible orthopaedic implants are coated with hydroxyapatite by HA plasma spray. Here, very fine hydroxyapatite powder is applied on the PEEK substrate. The physical properties of PEEK remains, while the bioactivity of the implants crucially enhances.^[100,101] The HA coating can also be applied via a sol-gel process, exhibiting similar good biocompatibility results.^[102] Various studies have demonstrated that hydroxyapatite affects enhanced osteoconductivity, bioactivity and is considerably biocompatible.^[91]

COOK and RUST-DAWICKI^[103] applied a thin titanium film on cylindrical CFR-PEEK implants by plasma vapour deposition. They implanted titanium-coated and bare CFR-

PEEK cylinders into the femur of dogs to estimate the contact between the bone and the implant. Histologically, this study showed that the bone-building ability around the titanium-coated samples was much stronger compared to the bare CRF-PEEK samples. In another study, PEEK implants were coated first with titanium and afterwards with hydroxyapatite. After implantation, the hydroxyapatite was resorbed by the surrounding body tissue and a bone-to-implant contact conducted by titanium was achieved.^[64]

The first studies for titania-coated PEEK were published by TSOU.^[104] PEEK was coated with titanium dioxide (rutile/anatase) by the arc ion plating (AIP) technique. These coatings exhibited good adherence to the PEEK substrate (as verified with an adhesive tape test) and a high corrosion resistance in aqueous NaCl and SBF (simulated body fluid) solutions. The surfaces showed superior biocompatibility with osteoblast precursor cells compared to uncoated samples.^[104-106] A recently-published study (2016) by SHIMIZU and co-workers presented the first *in-vivo* and *in-vitro* results for titania-coated PEEK samples by simple dip-coating from a sol-gel solution.^[107] In order to enhance the bond between the coating and the PEEK, the latter was treated with O₂ plasma to generate reactive groups or sandblasted to increase surface roughening prior to coating. Subsequently, the coated samples were treated with an acid to increase the formation of apatite between the rabbit tibia (used animal model) and titania-coated PEEK. The *in-vivo* and *in-vitro* results showed a clearly-enhanced bone-bonding ability and excellent cytocompatibility of coated PEEK compared to the pure PEEK samples. The pre-treatment with O₂ plasma or sand blasting had no impact on the performance of the coatings. Similar *in-vitro* results were attained in the present thesis.

2.5 Titania and Inorganic-Organic Silica Materials

2.5.1 Titania Films in Biomedical Applications

In general, metallic titanium has become the leading metallic material in implant technology. Its exceeding bio- and especially osseocompatibility can be traced back to the properties of titanium oxide. A layer of native amorphous titanium dioxide a few nanometers in thickness is formed onto the surface of metallic titanium when it is in contact with air or aqueous solutions.^[108] In such an oxidic environment, the hydroxyl groups represent active sites for the nucleation of calcium phosphate as the first step in bone building. In human serum, the density of hydroxyl groups is even enhanced and

thus the formation of new bone tissue around an implant is stimulated.^[109] Thereby, titania surfaces have an excellent cytocompatibility with an enhanced adhesion and proliferation for osteogenic cells. However, titanium is used in various implantological applications. Due to the negatively-charged titania surface at a pH of 7.4 (e.g. blood), the thrombocytes cannot bind to it and the blood clotting around the implant is inhibited. This is very favourable because the thrombosis and the inflammation risk is reduced.^[64]

In order to provide the advantageous properties of titania on other implant materials, the latter can be titania-coated by chemical vapour deposition, sputtering or – as applied recently – arc ion plating (AIP).^[104] However, these techniques are laborious, expensive and difficult to apply on implants with a complex geometry. In addition to the gas phase-based techniques, there are also coating methods using a liquid phase; for example, the sol-gel technique. From sols, coatings can be applied homogeneously on samples with complex shapes, using different techniques such as dip, spray or spin coating. The film thickness as well as the composition, topography and morphology of a coating can be aligned by adjusting different variables like the temperature, humidity and composition of the sol.^[110]

There are two problems with the sol-gel process, the first of which is the weak interactions between the coating and the substrate. This can be improved by roughening the surface of the sample or through a chemical modification with e.g. hydroxyl groups. The other problem is the possible cracking of the coating while drying when the film contracts. This can be reduced by the mixture of the sol and the atmospheric conditions while drying.^[111]

2.5.2 Silica-Based Mesoporous Organic-Inorganic Materials

Porous silica materials with high specific surface areas and large pore volumes have been examined intensively from the early-1990s onwards. The main research fields are adsorption, gas storage, catalysis, sensor technique and biomedical applications like the delivery of active substances.

Mesoporous Silica

A milestone was the development of M41S silica materials by the Mobil Oil Company with about 15 Å large ordered pores in 1992. This materials class has a high specific surface, an ordered porous system and a dense pore width distribution with pore sizes in a range of 2 – 10 nm. The most prominent representatives are MCM-41, MCM-48 and MCM-50, as shown in Figure 13.^[112,113] Mesoporous silica can be applied as (nano)particles in the biomedical field and has already been intensively investigated by our group.^[114–116] As thin films, it is dip- or spin-coated on implant materials, which have also been evaluated profoundly in many projects.^[3,4,6,7,35–39]

The application of ionic surfactants as structure-directing agents was one of the most important innovations. The long-chained alkyltrimethyl ammonium chalcogenides (CTAX, X = Cl or Br) form lyotropic liquid crystalline phases. Through the addition of silica precursors, ordered mesoporous composites are obtained. Subsequently, the templates (SDAs) are removed by extraction or calcination, leaving ordered mesoporous silica materials. Two different routes for the formation mechanism have to be differed, as shown in Figure 13.

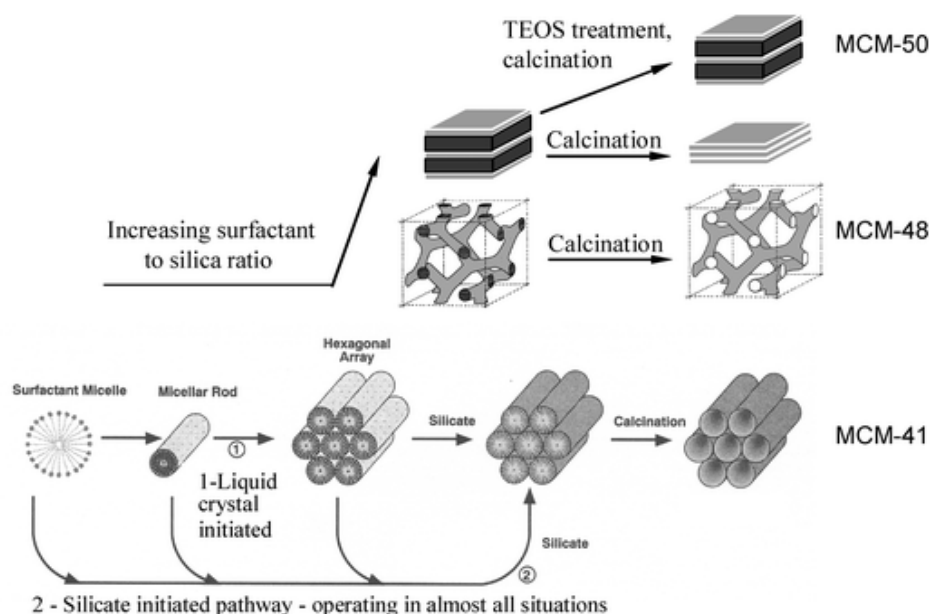


Figure 13: Formation of mesoporous silica materials by two different template mechanisms with structure-directing agents. (1) Liquid crystal-initiated reaction with first formation of the hexagonal array and afterwards condensation of silicate around it. (2) Cooperative liquid crystal mechanism, where the silicate is initially involved in building the hexagonal network. Depending on the silica-to-surfactant ratio, MCM-41 (hexagonal porous network), MCM-48 (cubic mesopores) or MCM-50 (lamellar structure) are formed.^[8,117]

On the one hand, there is the true liquid crystal template mechanism (Figure 13, 1). This route is followed when the concentration of the surfactant molecules is sufficiently high to form – under certain conditions such as temperature and pH value – lyotropic liquid crystalline phases without the presence of an organosilica precursor, common tetraethyl (TEOS) or tetramethyl (TMOS) orthosilicate. On the other hand, the cooperative self-organisation of a liquid crystalline phase with hexagonal, cubic or lamellar structure can be observed at low concentrations of the surfactant when the organosilicate precursor is already added (Figure 13, 2).^[118,119]

Such a synthesis can be varied by replacing the surfactant by a triblock copolymer, like the commonly-used Pluronic® F-127 or Pluronic® P123 and Brij® polymers, as structure-directing agents. In an acidic environment, the SBA silica structures are formed with larger pores and different structured pore systems.^[8] Moreover, in this work triblock copolymers Pluronic® F-127 and Pluronic® P123 were used in an acidic synthesis solution, since they form larger micelles and hence larger pores after extraction. A picture of both micelles is shown in Figure 14.

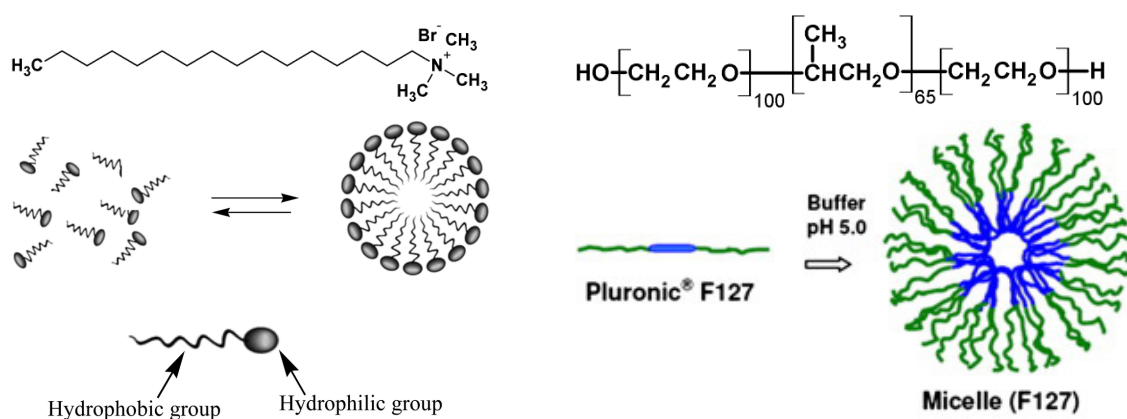


Figure 14: Formation of micelles from CTAB (left) and from Pluronic® F-127 (right). Both can be applied in the synthesis of mesoporous silica materials under different environments, giving different porous structures.^[120,121]

CTAB forms 2 – 3 nm large micelles, and hence smaller pores in the structure. A triblock copolymer like Pluronic® F-127 forms larger micelles due to larger alkyl chains. Pluronic® F-127 has the formula displayed in Figure 14 (right) and a PEO₁₀₀–PPO₆₅–PEO₁₀₀ polymeric structure, where PEO is poly(ethylene oxide) and PPO poly(propylene oxide). Pluronic® P123 is similar, but it has a slightly lower

molecular weight and the polymeric structure of PEO₂₀–PPO₇₀–PEO₂₀. Amphiphilic Pluronic® molecules form dependent on the temperature, pH value and concentration of self-aggregating micelles with the hydrophobic PPO inside (Figure 14 blue) and the hydrophilic PEO on the outside (Figure 14 green) of the micelle.^[122]

Many studies have investigated the combination of the advantages of inorganic silica materials and organic components bond to this framework. Since silica materials are thermally and mechanically very stable, although their chemistry is restricted towards many applications, whereby a modification or functionalisation with further groups is mandatory to unfold the full potential of this materials class. Through modification with organic substances, the polarity of the pore surface is changed and opens possibilities for applications like catalysis, chromatography as well as biochemical or biomedical use.^[8] The synthesis of porous organic-inorganic hybrid materials can be performed in various ways. So-called grafting is a post-modification of the open-porous silica materials. A simultaneous condensation of a silica and organosilica precursor is called co-condensation. The material prepared of organic-bridged one-component organosilane precursor – where the organic moieties are embedded in the pore walls – is called periodic mesoporous organosilica (PMO).

Grafting of Mesoporous Silica

The mesoporous silica surface can be modified by grafting with organosilanes. The organosilanes types of (R'O)₃SiR are mainly used, whereby R is the functional group and an alcohol is mainly separated during the reaction (see Figure 15). Chlorosilanes ClSiR₃ or silazanes HN(SiR₃)₂ are seldom chosen. Many functionalisation options of porous silica can be performed by the variation of the rest R. This type of modification has the advantage that the porous structure of the basic material usually remains unchanged. A disadvantage of this method is the risk of shrinkage of the pore entrance when the grafting molecules react at the entrance of the pore. Hence, the diffusion of further organosilane molecules into the pore is hindered and the functionalisation is not homogeneous. When the rest R molecules are very large, even pore blocking can occur, i.e. only the pore entrance and the outer surface of the material is modified.^[8]

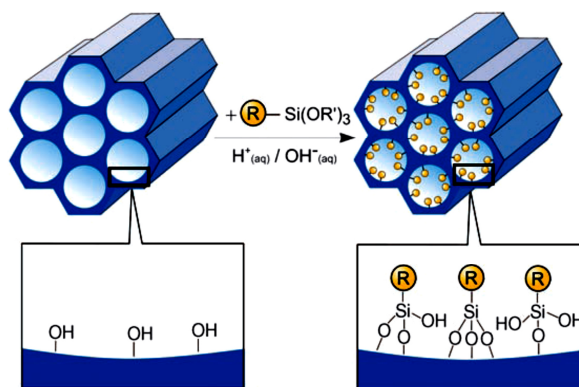


Figure 15: Grafting of pure mesoporous silica with terminal organosilanes, where R is the organic functional group, from ref. [8].

Thin films modified by post-grafting with different organic groups have been investigated in the medical field. Our workgroup was able to modify thin mesoporous silica coatings with sulfonic acid groups to bind more antibiotic ciprofloxacin in the coating.^[3] Another approach was the functionalisation with amino groups to immobilise the protein BMP-2.^[6]

Co-condensation of Mesoporous Silica

Another modification route is the co-condensation of tetraalkoxysilanes like TEOS or TMOS $[(RO)_4Si]$ with terminal trialkoxyorganosilanes $[(R'O)_3SiR]$ in the presence of structure-directing agents (Figure 16).

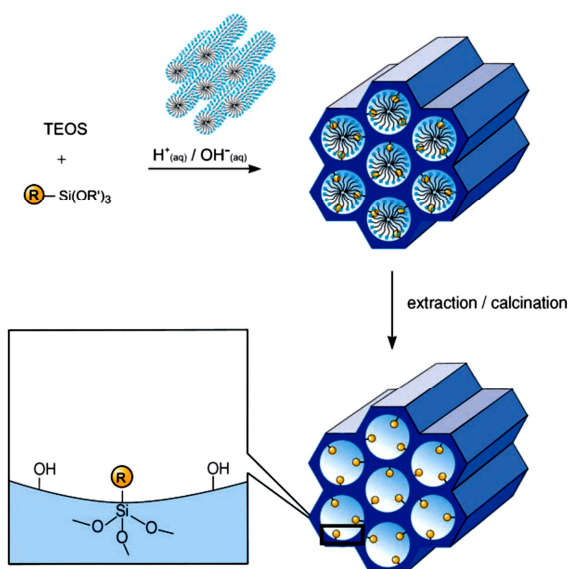


Figure 16: Co-condensation of tetraethyl organosilane (TEOS) with $(R'O)_3SiR$ for synthesis of modified mesoporous silica with organic groups.^[8]

During this synthesis, mesostructured silica materials are formed with organic moieties bound covalently in the pore walls and protruding into the pore itself. The pore-blocking effect is not a problem during co-condensation. Furthermore, the organic groups are distributed more homogeneously in the material, in contrast to grafting. However, this modification route has also some disadvantages. For instance, if the amount of the trialkoxyorganosilane is too high, above 40 mol%, the mesoscopic order of the structure decreases and only non-structured reaction products are obtained. Furthermore, the number of the functional groups in the final material is reduced compared to the precursor as homo-condensation cannot be properly suppressed. The pore width, pore volume and the specific surface area are also smaller due to the organic groups that protrude into the pore interior. Using this modification method, the SDA cannot be removed by calcination but primarily by extraction to ensure that the organic groups remain undamaged. This is more critical compared to the PMOs where the organic moieties are bound directly in the pore walls.

2.5.3 Periodic Mesoporous Organosilica (PMO)

The synthesis of organic-inorganic hybrid materials obtained by hydrolysis and condensation from sol-gel solutions with $(R'O)_3Si-R-Si_3(OR')$ as an organosilica precursor was already known in the mid-1990s.^[123] In contrast to post- or *in-situ*-modified silica phases, these hybrid materials have the organic moieties covalently bound in the three-dimensional network of the silica matrix. The organic moieties are homogeneously allocated in the silica network. The described materials are often received as aerogels with a high thermal stability and high surface areas. However, the porous structure is often not ordered with a wide pore size distribution.^[8]

In 1999, the first successful synthesis of the periodic mesoporous organosilica (PMO) was published simultaneously by three different groups.^[11,124,125] The same concept as for mesoporous structured silica materials was applied to obtain the ordered PMOs. Structure-directing surfactants and bisilylated organosilica precursors were mixed and precipitated in a sol-gel process, as shown in Figure 17. These materials had homogeneously-spread integrated organic moieties in the silica framework with a well-ordered porous structure, high specific surface area and a narrow pore size distribution.

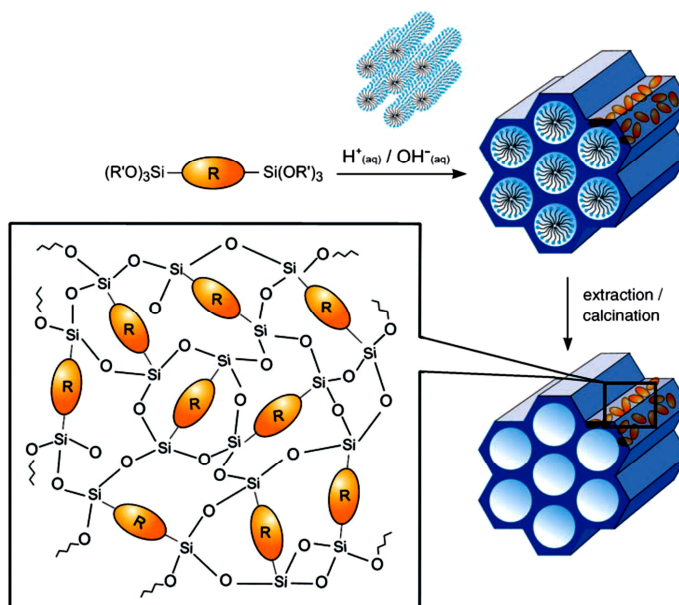


Figure 17: General synthesis method for the preparation of bissilylated organic-bridged mesoporous organosilica (PMO), taken from HOFFMANN *et al.*^[8]

Initially, the synthesis of the PMOs was performed using an ionic structure-directing agent CTAB or CTAC (cetyltrimethylammonium bromide or chloride) as well as OTAB or OTAC (octyltrimethylammonium bromide or chloride). INAGAKI *et al.* were among the first to synthesise a PMO by mixing 1,2-bis(trimethoxysilyl)ethane (BTME) with OTAC under basic conditions.^[124] Around the same time, OZIN *et al.*^[11] as well as STEIN^[125] and co-workers independently published a synthesis of an ethenylene bridged PMO under basic conditions with CTAB as SDA. OZIN modified the ethene-PMO with bromide to demonstrate the presence of intact ethenylene moieties in the two-dimensional hexagonal pore structures. By contrast, STEIN synthesised a material with a higher specific surface but smaller pores and a worm-like structure rather than an ordered two-dimensional hexagonal. In the same year, YOSHINA-ISHII *et al.* were able to synthesise the first PMO material with aromatic moieties.^[126] They applied 1,4-bis(trimethoxysilyl)benzene (BTEB) and 2,5-bis(trimethoxysilyl)thiophen (BTET) in the presence of CTAB as SDA under basic conditions. Unfortunately, these conditions led to cleavage of the Si–C bonds and fully-separated organic bridges. After changing to acidic conditions and the SDA hexadecylpyridinium chloride, they obtained well-structured products with stable organic bridges. A few years later, INAGAKI *et al.* synthesised aromatic PMOs with crystal-like pore walls in basic conditions with the

2. General Background

SDA OTAC.^[10] These PMOs had not only a well-structured periodic mesopores but also a crystal-like organisation of the organic bridges within the pore walls, as shown in Figure 18. KAPOOR *et al.* synthesised PMOs with a similar structure but a biphenylene bridge within the pore walls.^[127] They used 4,4-bis(triethoxysilyl)biphenyl as an organosilica precursor under basic conditions with OTAC as SDA. The biphenyl-PMO also displayed the crystal-like-oriented arrangement of the organic bridges in the pore walls. It is not completely clarified why these aromatic PMOs show the crystal-like organisation in contrast to ethylene- or methylene-bridged PMOs. One possible explanation is a high cooperative building process during the formation of micelles. MORELL *et al.* have shown a crystal-like arrangement of the biphenylene bridges parallel to the mesoscopic organisation of biphenyl-PMO itself by SAXS/XRD measurements.^[128] With the clear occurrence of reflections assigned to the formation of the mesoporous structure, the reflection for the crystallinity also occurs.

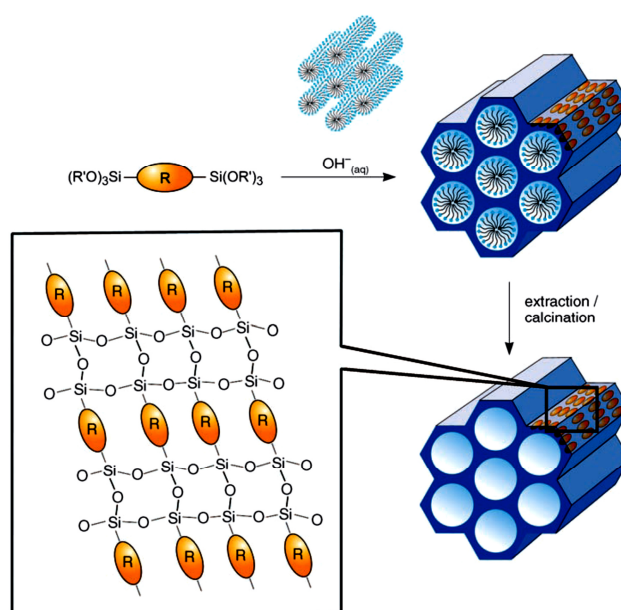


Figure 18: PMOs with well-ordered arrangement of organic bridges in the pore walls. This depiction is idealised, the organic linkers can be tilted. Nevertheless, they form crystal-like structures, from ref. [8].

Since the synthesis of PMOs with the ionic surfactants only provides pores in a range of 2 – 5 nm, the idea applying non-ionic surfactants was quickly implemented. As mentioned above, the non-ionic triblock copolymers P123, F127 or Brij56 can form pores up to 10 nm in diameter, as already shown by the synthesis of large mesoporous

silica materials like SBA-15 or FDU-1. MUTH *et al.* prepared an ethane-PMO under acidic conditions with Pluronic® P123 as SDA with pore diameters of 6.5 nm and a specific surface of $920 \text{ m}^2 \cdot \text{g}^{-1}$ in 2001. This material exhibited an analogous two-dimensional hexagonal structure as the SBA-15.^[129] One year later, GOTO and co-workers obtained the first phenyl-PMO under acidic conditions with Pluronic® F127.^[130] The well-structured material had a pore width of 7.4 nm and a specific area of $1030 \text{ m}^2 \cdot \text{g}^{-1}$ with a two-dimensional hexagonal symmetry. Unlike the phenyl-PMOs synthesised with an ionic surfactant, this phenyl-PMO had no crystal-like periodicity of the organic bridges in the pore walls. The reason could be the different chemistry of the SDA and the acidic rather than basic conditions, and hence a different building mechanism of the lyotropic phase.

Figure 19 shows the four possible pathways to synthesise different PMO materials.

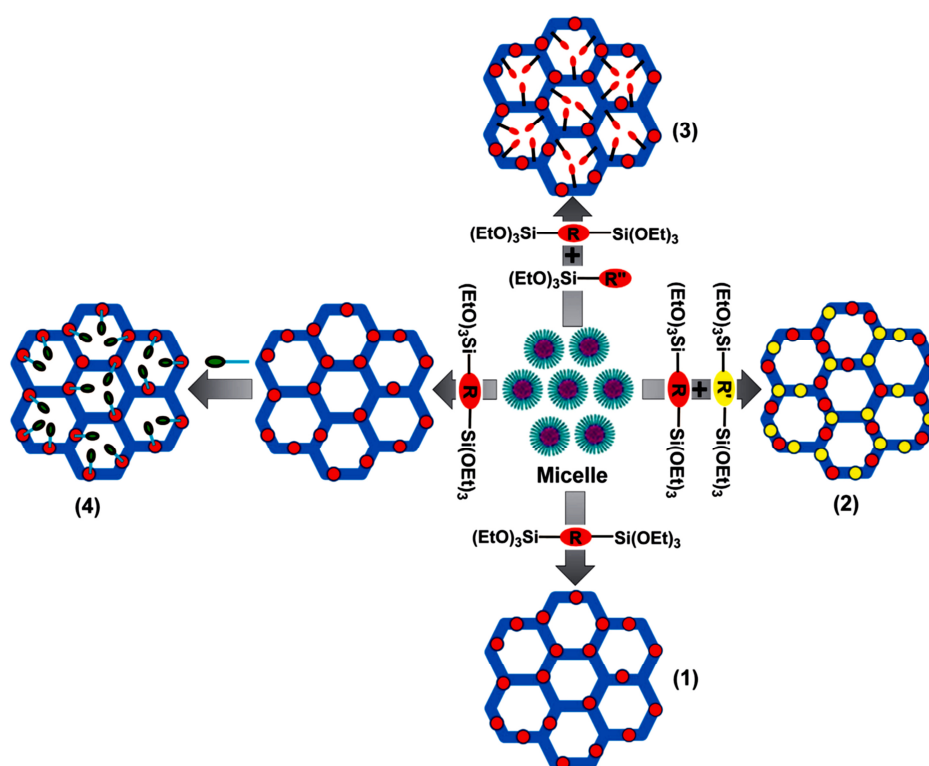


Figure 19: Different pathways for the preparation of PMOs. 1) PMO with a bisilylated precursor, 2) bisilylated precursors with two different organic bridges, 3) mix of mono- and bisilylated precursors and 4) PMO with a bisilylated precursor and following modification of the organic moiety. From ref. [131].

2. General Background

Besides the type of the SDA and the synthesis conditions, different organic moieties and their combination can be chosen to obtain a large variety of different PMOs. PMOs can be synthesised by applying only the bissilylated precursor, a mixture of two different bissilylated precursors with different organic bridges, a mixture of a mono- and a bissilylated precursors and finally the modification of the unsaturated bridges with different groups.

The PMO coatings examined in this thesis were prepared with the linkers shown in Figure 20. The phenyl-PMO coatings were prepared by using the precursor 1,4-bis(triethoxysilyl)phenyl (Figure 20 left). The biphenyl-PMO coatings were prepared by using the precursor 4,4-bis(triethoxysilyl)biphenyl (Figure 20 middle). The phenylene bridges were modified with sulfonic acid groups (Figure 20 right) according to the procedure described by CANCK *et al.*^[132]

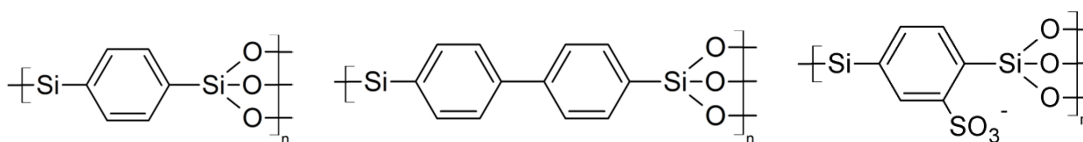


Figure 20: Left: Phenylene linker in PMO. Middle: Biphenylene linker in PMO. Right: Sulfonated phenylene linker in PMO.

2.5.4 PMOs for Biomedical Applications

Several studies examined PMO materials for possible biomedical applications. In most cases, nanoparticles or nanorods – overall PMO powders – were used in *in-vivo* and *in-vitro* investigations. PMOs were used as host materials for the adsorption or immobilisation of biomolecules like proteins, enzymes or peptides. The immobilisation of proteins follows three different pathways: covalent attachment, physical adsorption or encapsulation.^[133] The organic-inorganic nature of the PMO network is a perfect support for biomolecules due to different surface charge and hydrophobic properties compared to silica materials. PMOs can protect the immobilised enzymes and enhance their activity.^[134] The first protein immobilised on a PMO was cytochrome *c* on ethane-PMO as well as SBA-15 silica material. It was determined that between the cytochrome *c* and the SBA-15 electrostatic interactions were dominant, whereas between the ethane-PMO and cytochrome *c* hydrophobic interactions were enhanced.^[135] PARK *et al.* found that lysozyme adsorbed faster to phenyl- and biphenyl-PMOs compared to SBA-15 due

to the hydrophobic interaction. In addition, biphenyl-PMO had a higher adsorption capacity for the lysozyme owing to a greater hydrophobic character.^[136]

Besides their deployment as adsorbents of biomolecules, PMOs have been examined for intervene into the refolding process of proteins. WANG *et al.* reported about ethane-PMO that could entrap the unfolded denaturated proteins and assist their refolding by controlled release into the refolding buffer.^[137] This study suggested that the ethylene bridges interact with the hydrophobic parts of the protein lysozyme and bind them inside the pores. Through the insertion of polyethylene glycol (PEG) – which interacts with the silanol groups in the PMO walls – a controlled release of the proteins can be achieved. The released proteins are refolded to native proteins in the refolding buffer. The suggested mechanism is depicted in Figure 21. This study also claimed that due to the variety of precursors and organic linkers that could be inserted in a PMO wall, the PMO could be individually tailored for specific applications and proteins or enzymes.^[137]

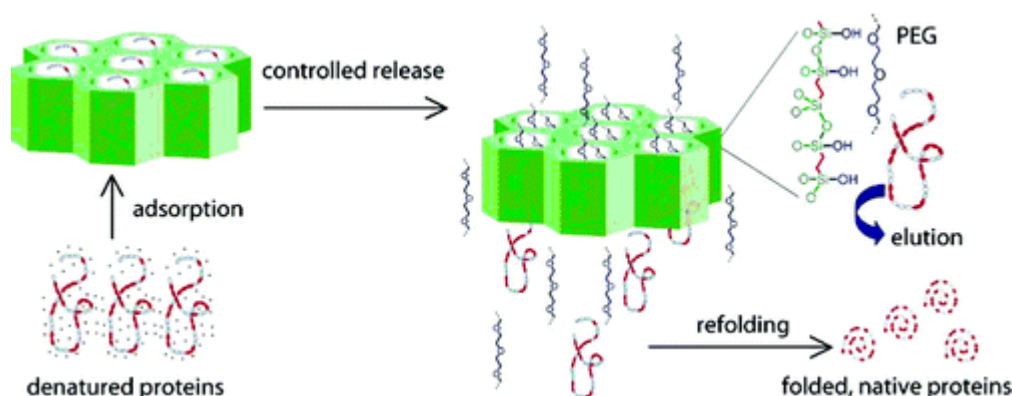


Figure 21: Protein refolding assisted by ethane-PMO. The unfolded proteins are entrapped in the mesopores. By using PEG, a controlled release of the entrapped denaturated protein lysozyme can be achieved, leading to high refolding yields. From ref. [137].

Besides the immobilisation of biomolecules, refolding of proteins and enzymatic support as biocatalysts in the form of lipase storage, PMOs have been intensively investigated as potential drug delivery systems.^[133] A wide range of materials like biodegradable polymers, hydrogels, LDHs or mesoporous silica materials have been evaluated as controlled drug delivery systems. Among these, silica-based mesoporous materials are promising ones as drug-release systems due to their large surface area,

tunable pore size, non-toxicity and excellent biocompatibility. Nevertheless, the hydrophilic silica pore walls sometimes have to be functionalised with organic groups to store more efficient hydrophobic drugs. The introduction of organic moieties seems to be a crucial factor for a sufficient loading with drugs resulting in higher loading capacities and slower release kinetics avoiding the burst release.^[133] As described above, the post-synthetic modification can lead to pore narrowing or the loss of functionalisation groups. By contrast, PMOs show a lower steric hindrance for host molecules with the advantage of embedded organic groups. The first study for controlled drug release from PMOs was published by LIN *et al.*^[2] They loaded the drug tetracycline in a hollow ethane-PMO and for comparison in mesoporous silica. They could show that the hollow PMO had the highest loading amount and the lowest release rate due to the strong hydrophobic van der Waals interactions. From then onwards, several drugs in different PMOs were examined regarding their release behaviour, including doxorubicin, tetracycline, captopril, 5-fluorocil and ibuprofen. In this thesis, the substances ciprofloxacin and rolipram are examined as model drugs. A good example for the influence of not only the hydrophobic interactions but also the electrostatic ones was given by Kao *et al.*^[138] They could show that the additional functionalisation with a carboxylic acid group led to even higher loading capacities and slower release rates of doxorubicin in a phenyl-PMO compared pure ethane- and phenyl-PMO. Another approach was followed by MOORTHY and co-workers, synthesising an amphoteric PMO for loading and release of hydrophobic and hydrophilic drugs simultaneously.^[139] Therefore, the PMO incorporated the ureylene and amidoxime moieties and were loaded with the drugs ibuprofen (hydrophobic) and 5-fluorocil (hydrophilic). The observed result was that the higher the hydrophobic properties of the PMO, the higher the loading capacity for both drugs. Furthermore, the materials had a higher affinity to the ibuprofen due to its hydrophobic character. The cytocompatibility investigations performed during this study revealed sufficient results for biocompatibility. The cancer cell treatment by the released 5-fluoracil was also successful.^[139]

As described above, there are several ideas for using PMOs in biomedical applications, although most focus on anti-cancer therapy. Hence, most studies on the cytocompatibility of PMOs are accompanied with anti-cancer investigations. The

studies on cytocompatibility or interactions with cells for PMOs published so far have stated a good biocompatibility and low toxicity.^[133] All studies found deal with PMO particles in different shapes as wires, rods or round nanoparticles. GUAN and co-workers showed that methane-PMO particles entered the HeLa cells and accumulated preferably in the perinuclear region without entering the nucleus.^[140] The tested concentrations were 4 – 125 $\mu\text{g} \cdot \text{mL}^{-1}$, whereby at the highest concentration only 25% of the cells died after 24 h. These values were comparable to those of the mesoporous silica nanoparticles. Another interesting approach was followed by CROISSANT *et al.*,^[141] who incorporated gold nanoparticles in phenyl- and ethane-PMOs in a one-pot synthesis. Subsequently, the drug doxorubicin was loaded into the PMO particles for simultaneous drug release and two-photon photodynamic therapy. KEHR *et al.* were able to show that cells could distinguish PMO particles due to their chirality.^[142] The chirality of the PMO particles was achieved by modification of the particles with D- or L-mannose amino acid. The first *in-vivo* results with PMO particles were shown by QIAN *et al.*^[143] The hollow phenyl-PMO particles were loaded with the anti-cancer drug paclitaxel and injected in mice. Through the application of ultrasound, the release of the drug was triggered, leading to an enhanced therapeutic efficiency.

To date, no *in-vivo* or *in-vitro* studies on PMO-coated implant materials or even sol-gel derived PMO films could be found. Hence, the results on the cytocompatibility of fibroblasts and osteoblasts on PMOs coatings as well as the survival rate of the spiral ganglion cells obtained in the present thesis are unique and have not been published thus far. Nevertheless, they are very promising, as described below.

2.6 Dip-Coating

The substrate is dipped into the dip-coating solution and after some remaining time in this solution it is withdrawn with a constant speed. Above the drying line, a layer of non-volatile species is formed on the substrate. The dip-coating process is schematically described in Figure 22.

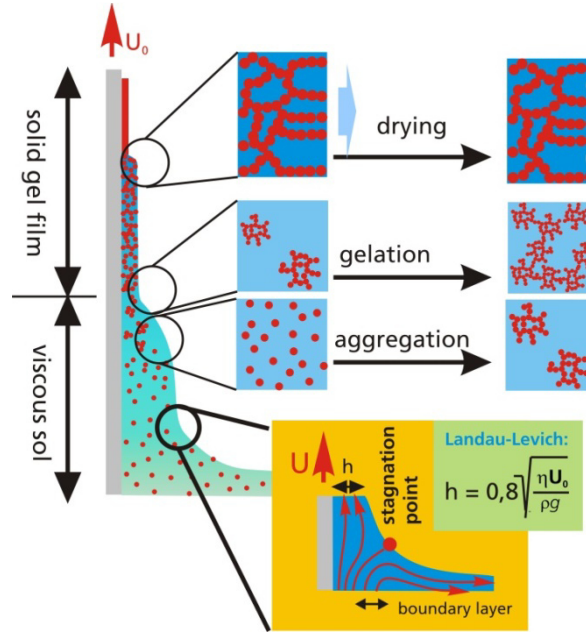


Figure 22: Dip-coating process from a sol-gel solution, from ref. [144].

Dip-coating is a very easy coating method with many advantages, like adjustable film thickness and optical properties, free choice of substrate with complex geometries and no waste of coating solution. However, there are also some disadvantages that have to be considered. For instance, sometimes the substrate has to be modified for a good adhesion of the coating when the surface tension of the solvent is too high or the zeta potential of the solution and substrate is similar. The thickness is difficult to control when ultra-thin films (< 20 nm) or ultra-thick films (> 1000 nm) are applied. Application on porous substrates like ITO or FTO is not easy due to the small structures. One of the main problems of coating itself is cracks caused by lateral tensile stress of the coating on the substrate during the subsequent drying process. This is especially valid for thick film or hard coatings, like ceramics.^[145] The most critical parameters of dip-coating are:

- withdrawal speed
- temperature of the solution
- temperature of the environment
- atmosphere, especially the humidity
- solvent and dilution of the solution.

During deposition of thin films from solutions containing surfactants, an evaporation-induced self-assembly (EISA) process takes place. Here, the solution contains a

structure-directing agent (SDA), a metal oxide precursor, the solvent and often an acid like hydrochloric acid. The concentration of the surfactant in the solution is usually below the critical micelle concentration. Hydrochloric acid adjusts the pH value around the isoelectric point of silica to stop further condensation of the inorganic phase during the coating process. When the substrate is withdrawn, the micelle formation starts at the stagnation point at the solution surface. The SDA molecules aggregate to form a liquid-crystal-like mesophase.^[146] By lifting the substrate, a faster evaporation of the solvent results, accompanied by a gelation. When the solvent is completely evaporated, the modulable steady state (MSS) occurs where the liquid phase is in equilibrium with the environment. The co-assembly of the micelles and inorganic building blocks is finally arranged depending on the relative humidity of the surrounding atmosphere. During the drying step, the condensation proceeds to form the final mesostructured film.^[146,147] The EISA process is schematically depicted in Figure 23.^[148]

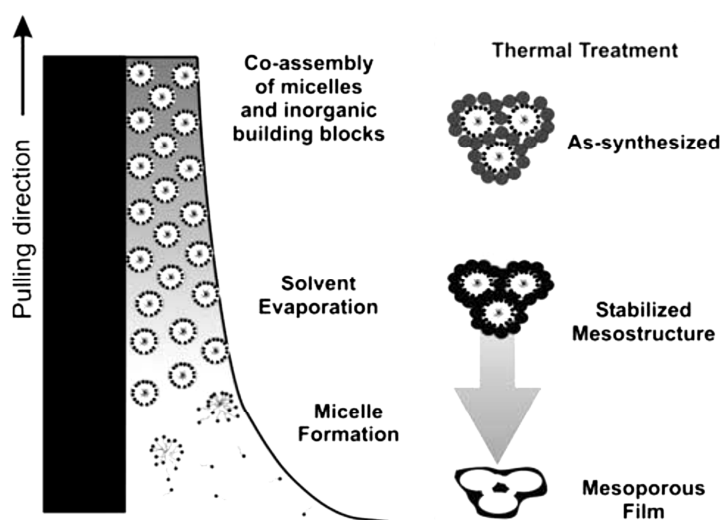


Figure 23: Schematic presentation of the evaporation-induced self-assembly (EISA) mechanism during the dip-coating process, picture taken from ref. [148].

In most cases, alcohols are used as solvents as their vapor pressure is high, and the solvent evaporates very quickly. Sometimes water is also used, albeit only for special solutions when alcohol as solvent cannot be applied. The withdrawal speed in the water-based solutions is low due to the slow evaporation. The Landau-Levich model is often taken to describe the film thickness. This equation is valid for a Newtonian and non-evaporating fluid. It predicts the thickness depending on the density, surface tension and

2. General Background

viscosity of the fluid.^[145] However, this model only describes few dip-coating processes as the most dip-coating solutions are non-Newtonian, caused by constant changes of their viscosity and surface tension due to evaporation processes. FAUSTINI *et al.* described two regimes for low and high withdrawal speeds, whereby both are shown in Figure 24.^[149] The capillarity regime is valid for low withdrawal speeds ($0.01 - 0.1 \text{ mm} \cdot \text{s}^{-1}$). The evaporation of the solvent becomes faster than the motion of the drying line at the three phases point. Hence, the upper part of the film is fed with solution by capillary forces leading to thicker films at lower speeds (Figure 24 left). By contrast, there is also the draining regime that is valid for high withdrawal speeds ($1 - 10 \text{ mm} \cdot \text{s}^{-1}$). This regime describes perfectly the Landau-Levich model. The non-evaporated liquid drains and the film is formed at the three-phase point. The faster the withdrawal speed, the thicker the film (Figure 24 right). Between these two regimes, the thin films are formed (up to 100 nm) at speeds between $0.1 - 1 \text{ mm} \cdot \text{s}^{-1}$. The balance of both regimes reigns here, as shown in Figure 24 (middle). In this picture, the impact of dilution is also shown, leading to thinner films and those of the temperature, enhancing the thickness at slower withdrawal speeds.

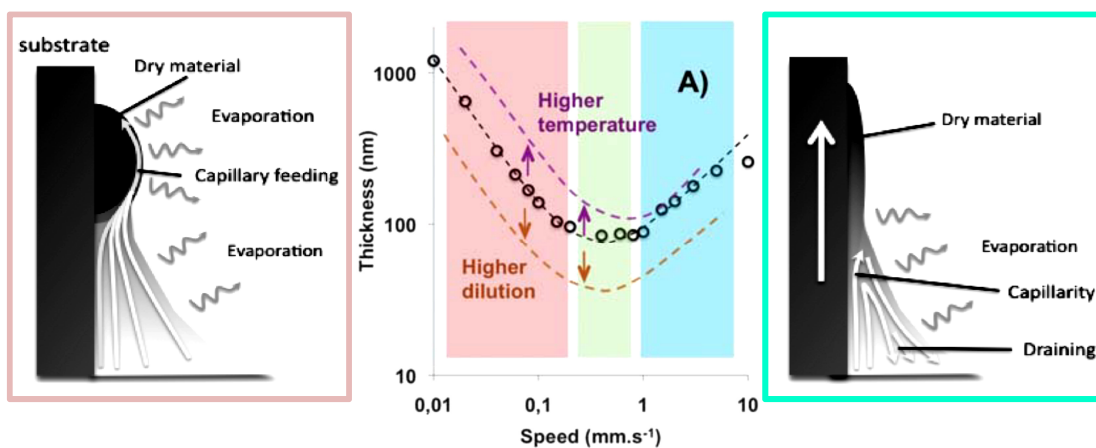


Figure 24: **Left:** Capillarity regime valid slow withdrawal speeds ($0.01 - 0.1 \text{ mm} \cdot \text{s}^{-1}$) for thicker coatings. **Right:** Draining regime valid for high withdrawal speeds ($1 - 10 \text{ mm} \cdot \text{s}^{-1}$). Both regimes were described by FAUSTINI *et al.*^[149]

2.7 Antibiotics and Neuroprotective Substances

Antibiotics

An antibiotic is a substance that inhibits or kills a microorganism. Nowadays, antibiotics are antimicrobial substances synthesised half- or full-synthetically or by gene technique. They are widely used for the treatment of infectious diseases and bacteria-induced inflammations. There are two ways of antibiotic effect: when bacteria are not killed but their growth is inhibited, it is called bacteriostatic; and when bacteria are killed, it is called bactericide. The choice of the operating principle depends on the desired effect and the bacterial stem. Hence, the antibacterial effect can be obtained by inhibition of ribosomal bacterial protein synthesis, DNA replication or folic acid formation. An antibiotic that is effective against a wide range of bacteria is called a broad-spectrum antibiotic.^[150] Normally, antibiotics are well tolerated and have a wide therapeutic range. The main side effects are allergies, dysfunction of the gut flora and mycosis. Especially long-term therapy can lead to a permanent and poor treatable malfunction of the gut flora. Antibiotics seldom have toxic side effects where organs are affected. Interactions with other drugs or medicaments can also occur during antibacterial therapy and have to be controlled by a doctor. Moreover, interactions with some dairy products have to be considered.^[151] The resistance of bacteria against antibiotics has occurred more often in recent years. There are bacterial stems that are no longer affected by antibiotics due to mutations. Nowadays, some bacteria developed that do not respond to any known antibiotics.^[152] For this reason, scientists are searching for further highly-efficient antibiotics. Often, after implantations the patients are systemically treated with antibiotics to prevent inflammations. However, the dosage of the drugs has to be sufficiently high to reach the related body parts. Hence, a local drug therapy at the related part where the implant was inserted is favourable to reduce the antibiotic dose and overload of the body with drugs. This is one goal of the present thesis, namely to develop effective drug-releasing coatings on implants.

2.7.1 Ciprofloxacin

Ciprofloxacin (Figure 25) is a synthetic antibiotic within the group of fluoroquinolones with a wide range of efficacy, including the bacterial stem of *Pseudomonas aeruginosa*, which is responsible for many infectious diseases. This drug was developed by Bayer in

2. General Background

1981. It shows excellent biocompatibility and bioavailability, good tissue penetrability as well as low toxic effects.^[153,154] Among other fluoroquinolones, ciprofloxacin is the most potent antibiotic and is 2 to 10 times more effective against *in-vitro*-tested *Escherichia coli* bacteria compared to other fluoroquinolones. It is especially effective against Gram-negative bacteria but also fighting Gram-positive bacteria to a certain extent.^[153,154]

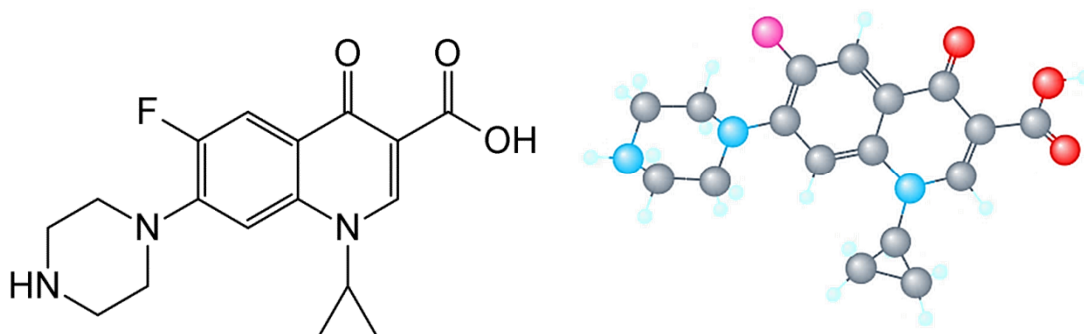


Figure 25: Molecular structure of ciprofloxacin. The blue nitrogen atoms, the red oxygen atoms and the violet fluoride atom are taken into account for the polar surface area of the antibiotic.^[155]

Ciprofloxacin is not only a broad-band antibiotic; moreover, it also gain attraction due to its anti-proliferative and apoptotic effect on several cancer cell lines.^[156] The therapy of prostate cancer proceeds positively by treatment with ciprofloxacin due to its limited toxic effects. There is less harmed tissue in comparison to standard chemotherapy.^[157,158] Besides the first attempts at cancer treatment by ciprofloxacin, this antibiotic is commonly used during cancer therapy as an effective medication for many severe infections.^[159]

Fluoroquinolones inhibit the topoisomerase II, referring to DNA gyrase. This is an enzyme needed for the replication of the bacterial DNA. DNA gyrase cuts the double-stranded DNA, introduces negative supercoils and subsequently reseals the ends. Quinolones interfere in bacterial DNA supercoiling by binding to topoisomerase II or IV. The double-stranded DNA breaks, resulting in cell death.^[160] This action mechanism is displayed in Figure 26.

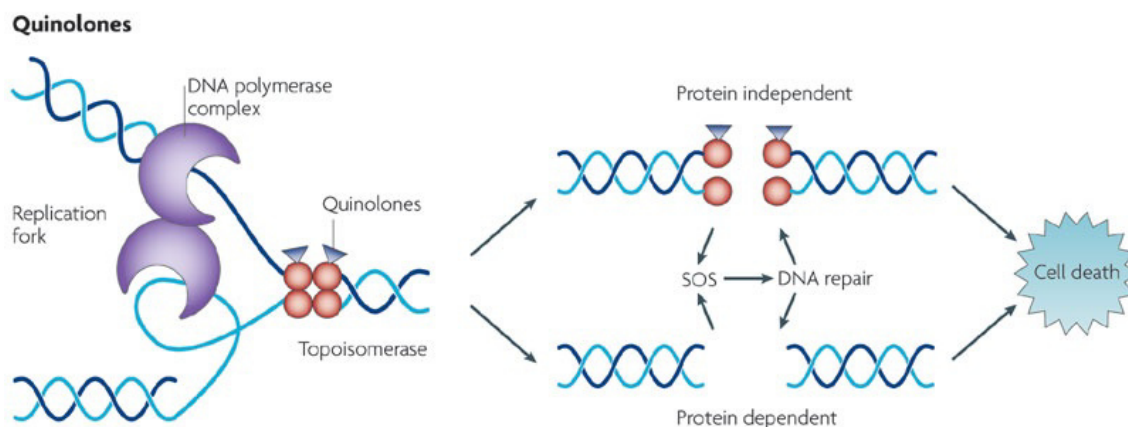


Figure 26: Mechanism of action of quinolones, to which ciprofloxacin belongs, showing cell death due to inhibiting the bacterial enzyme DNA gyrase, taken from [160].

Ciprofloxacin has a bioavailability of 70% after oral intake. It has a wide distribution in the body when applied systemically and can be found in the kidney, liver, gallbladder, prostate and lungs. It is excreted mainly unmetabolised in the urine and faeces. The predominant elimination route is through the gastrointestinal tract, sometimes accompanied by bile excretion with an elimination half-life of about 3 – 5 hours.^[161]

Chronic otitis media is often treated with the antibiotic ciprofloxacin.^[162,163] The local therapy with ciprofloxacin from mesoporous coatings was intensively studied within SFB 599. The lost ossicles were replaced by mesoporous silica coated Bioverit® implants in a rabbit study. The coatings were loaded with antibiotic ciprofloxacin. It could be shown that the inflammation caused by *Pseudomonas aeruginosa* was successfully fought by burst release of ciprofloxacin from the coatings. A retarded release did not have the same positive effect.^[3,4,34,36–38] In the present thesis, the CFX loading capacity of the PMOs is examined. It was expected that the organic moieties can bind more CFX in the porous structure.

Neuroprotective Substances

Neuroprotection means the protection of the nerve and brain cells against damage. Many substances have already been found that can help to prevent, stop or even regenerate such functional damage. It is especially interesting to stop the degeneration of nerve cells due to a disease, drug abuse or beginning dementia. Many substances acting neuroprotectively are natural or endogenous substances. The latter are patterns for drugs with maximal effect and minimal side effects.^[164]

2. General Background

A degeneration of the spiral ganglion neurons is observed when the hair cells are missing. For the best auditory impression, these cells are essential when a cochlea electrode is implanted.^[55] For the prevention of SNGs death, neuroprotective substances have to be applied to stabilise or even vitalise the SGNs. There are several neuroprotective mechanisms or influences known for effective neuroprotection. Estrogen seems to be one of the most effective substances with neurotrophic and neuroprotective actions and is involved in many neuroprotective mechanisms.^[165] Estrogen stops apoptosis of the damaged nerve cells. One of important nerve cell-impairing mechanisms is the oxidative stress with restriction of the mitochondria. Estrogen stabilises the function of mitochondria and acts neuroprotectively.^[166] In the research of neuroprotection, already about 400 substances are known that act neuroprotectively, some with great success and some with many side effects. Based on some studies performed previous in the SFB 599 and *Hearing4all*,^[55,56] the influence of the PMO coatings on the production of BDNF has been evaluated and the drug release of rolipram. Both agents are described in the following.

2.7.2 Brain-Derived Neurotrophic Factor

Brain-derived neurotrophic factor (BDNF) is one of the most important growth factors in the development of central nervous system and neuronal plasticity. The nervous system is able to help itself by local production of BDNF. It is formed where the injury or lack of oxygen in the brain or nervous system occurs. The production of BDNF is among others promoted by estrogen.^[167] As BDNF has a crucial impact on the function and plasticity of the brain, it is often applied in medication of psychiatric diseases and as a neurotrophic growth factor.^[168]

Neurotrophines are an important family of signalling molecules in the brain and nervous system. They are responsible for neuron growth, axon targeting, synaptic plasticity and maturity of synapsis during development.^[167] The first discovered neurotrophic factor was the nerve growth factor (NGF) in 1951 by LEVI-MONTALCINI^[169], followed by BDNF in 1982 by BARDE *et al.*^[170] and the neurotrophines 3^[171] and 4/5^[172], which had special trophic effects on neurons in the peripheral and central nervous system. In this row, BDNF is the best characterised – although not the oldest known – regarding its

effect on the synaptic plasticity, influence on neuron growth and especially its role in the treatment of psychiatric diseases.^[167]

BDNF is expressed as an initial protein called pro-BDNF, then cleaved into pro-BDNF (35 kDa) and afterwards in mature BDNF (14 kDa), as shown in Figure 27.^[173]

Pro-BDNF affects the central nervous system in a different way than mature BDNF and is thus independently important in the signalling pathway. Mature BDNF and pro-BDNF activate different intracellular pathways.^[167,168] BDNF acts as a signal for a decent axonal and dendritic growth. These effects are activated by several pathways and are not yet fully understood.^[174]

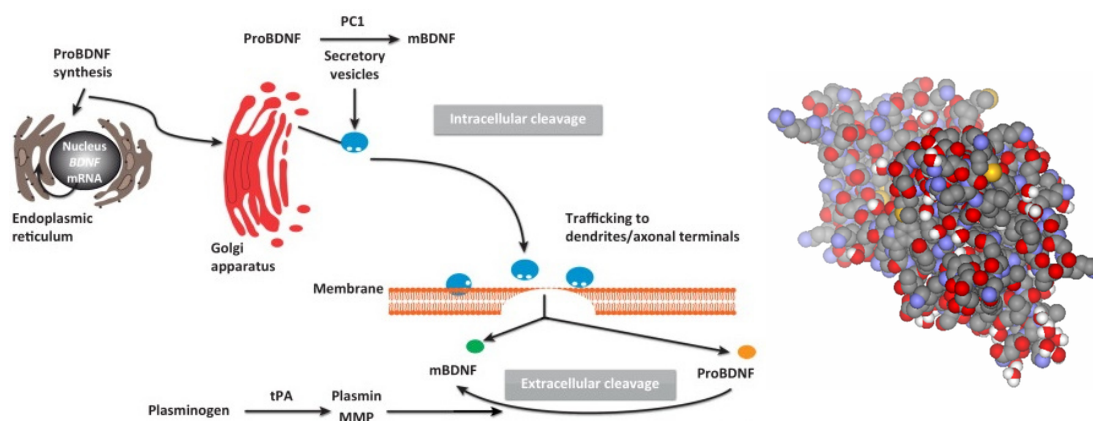


Figure 27: Left: Formation of pro-BDNF in the endoplasmic reticulum and its cleavage way down to mature BDNF (**Right**), taken from [175] and [176].

2.7.3 Rolipram

Rolipram (Figure 28) was developed in the early-1990s as a potential antidepressant, whereas later an inflammatory effect could be proven for this drug. Nowadays, rolipram is investigated in terms of its neuroprotective impact.^[177,178] Studies have shown that rolipram had only a narrow therapeutic window as an antidepressant, whereby excessive doses had negative side effects, among others on the gastrointestinal system.^[178]

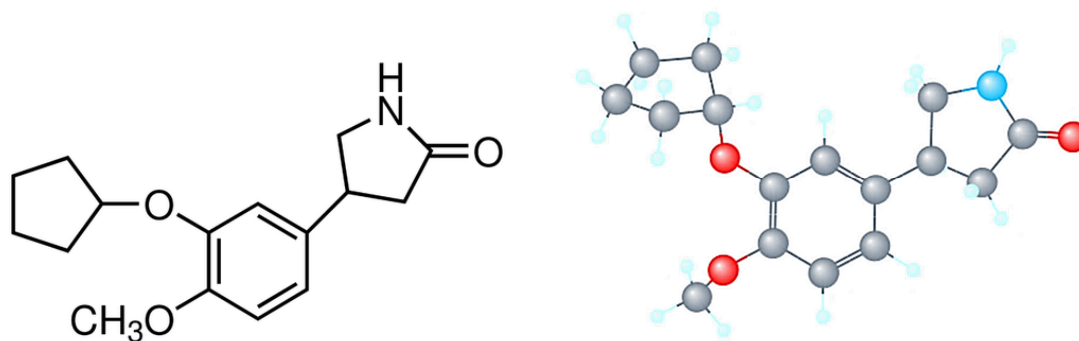


Figure 28: Molecular structure of rolipram. The blue nitrogen atom and the red oxygen atoms are taken into account for the polar surface area of the drug.^[155]

Rolipram inhibits phosphodiesterase 4 and increases the intracellular concentration of the regulatory cAMP (cyclic adenosine monophosphate). The increase in cAMP activates the cAMP response element-binding protein (CREB), which regulates many cellular functions by phosphorylation. This mechanism provokes neuroprotective effects and supports the axonal regeneration by enhanced expression of neuroprotective substances like BDNF.^[177,179,180]

An external systemic treatment with BDNF is not possible as BDNF is too large to pass the blood-brain barrier. Molecules with a PSA (polar surface area) less than 90 \AA^2 can pass this barrier and affect the receptors in the central nervous system.^[181] Molecules with a PSA smaller than 140 \AA^2 are able to permeate cell membranes.^[182] The polar surface area is a sum of all polar atoms and is often used in medicinal chemistry to evaluate the ability of drugs in terms of cell permeation. As rolipram with a PSA of 48 \AA^2 ^[155] is able to pass the blood-brain barrier, it can activate the intracellular cAMP that regulates the expression of BDNF.^[183–185] KRANZ *et al.* could prove in an *in-vitro* study that due to treatment of SGNs with rolipram (0.1 nM) and BDNF, 30% of neurons could survive.^[56] By contrast, treatment of SGNs only with BDNF or rolipram had reduced survival numbers. Hence, both substances were important for the protective effect on the SGNs.

2.8 Controlled Drug Delivery

Controlled drug delivery (CDD) is a versatile system for the local transportation of drugs to the targeted tissue. It is a possible alternative to the systemic drug therapy by oral, dermal or mucosal medication intake. Mesoporous silica is a very promising

material for drug delivery applications due its chemistry, biocompatibility and mesoporous network with a lot of space for loading of drugs.^[186] The size of the pores can be adapted to the size of the drug molecules to obtain the best release behaviour. Moreover, the functionalisation after the drug loading can control the release. Due to steric hindering groups, the release of a drug can be retarded, whereby the size of the capping molecule can control the release rate.^[3] PMOs offer a more adjusted storage system for CDD due to the organic moieties in the pore walls. Suitable organic groups can be chosen for particular drugs to achieve the best release behaviour without further modification. Furthermore, the organic bridges themselves lead to higher amounts of loaded drugs due to the non-polar chemical similarity.

It is possible to increase the amount of the loaded drug and control the release behaviour through modifications. Different release profiles are presented in Figure 29.

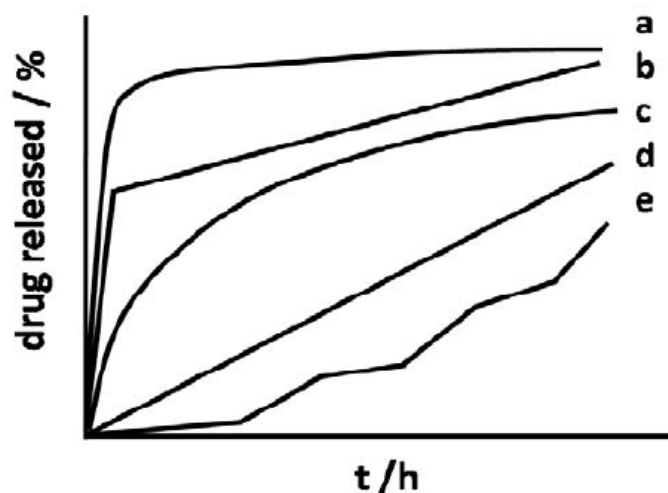


Figure 29: Release profiles for controlled drug delivery, adopted from [16].

Very often a burst release (Figure 29 a) can be observed for non-modified matrices where an initial high dose of a drug is released followed, by a very slow, barely-measurable release. This kind of profile is favourable when a high amount of a drug is needed; for instance, to fight severe inflammations. The small doses released later unfortunately have little therapeutic effect. Profile (b) can be favourable after surgeries when a high initial dose is needed to inhibit the first inflammation and subsequently smaller doses to suppress bacterial growth. Profile (c) describes the first-order kinetics dependent on the concentration of drugs in the porous system. The release is controlled

by dissolution or diffusion processes. A constant time-dependent release over a long time range is favourable but difficult to adjust (Figure 29 d). The release follows zero-order kinetics and is only time-dependent. Profile (e) represents a stimulus responsive drug delivery system. Here, the drug is released by changes of the surrounding of the drug delivery system; for example, the temperature, pH value or irradiation.^[16]

2.9 Influence of Surface Properties on Cell Adhesion

Several parameters crucially influence the cytocompatibility of materials. Besides the ambient conditions *in vitro* and *in vivo*, the surface structure and chemical functionalisation is also important for the specific interactions between cells and material. These properties determine the adhesion, proliferation and differentiation of the cells. The most important factors are as follows:^[187]

- Chemical structure and functional groups: fibronectin (a protein of the extracellular matrix that is responsible for the adhesion of the cells to the surface) binds preferentially to amino or hydroxyl modified surfaces.^[188]
- Hydrophily influences the adsorption of proteins to the surface. Many studies claim that the higher the hydrophily of the surface, the better that the cells adhere to the latter.^[189] By contrast, some authors^[190] could show that the water contact angle does not offer any evidence of cell proliferation. Hence, the influence of the hydrophily is discussed later in this thesis.
- The surface structure – especially on the nanoscopic scale – increases the surface of an implant and enhances the adhesion of cells. Best results have been achieved on surfaces structured with 28 nm and 58 nm large gold dots. Smaller dots of 10 nm were taken up by the cells, which caused inflammation and cell death.^[191]
- Surface energy in physiological media, like negatively-charged titania in blood, which reduces the thrombosis risk.^[64]

There are several methods to modulate the surface roughness, topography, energy and chemical structure. Commonly-used techniques are chemical etching, mechanical sandblasting, sputtering, laser ablation and structuring and functionalisation during the manufacturing of implants.

3. Preparation of Materials

In the experimental section, the syntheses performed are presented in detail. This contains the synthesis of mesoporous organosilica coatings and their modifications as well as the synthesis of mesoporous organosilica nanoparticles. The preparation of titania films as well as the dip-coating procedure of PEEK substrates are also described in the following. Furthermore, the loading procedure and release experiments with different drugs, the cell compatibility tests and the antibacterial procedures are presented. All chemicals were used without further purification.

3.1 Cleaning of the Substrates

Cleaning of the Glass Slides

As substrate material for the PMO, coatings glass slides (Glasbearbeitung Henneberg & Co., Martinroda, Germany) with dimensions of 9 mm x 10 mm x 0.95 mm and 9 mm x 20 mm x 0.95 mm, respectively, were used. The larger ones were scored as shown in Figure 30. This procedure was undertaken to prevent inhomogeneous dipping effects due to the mounting of the dipping device and edge effects on the lower end of the substrate. After the dipping and further production process, the small edges were broken off to maintain the homogeneous part of the coating. Prior to dip-coating, the glass slides were initially treated with acetone by ultrasonication for 15 min. Subsequently, they were cleaned in piranha acid ($\text{H}_2\text{SO}_4 : \text{H}_2\text{O}_2$ in a volume ratio of 3 : 2) for 2 hours, rinsed with water and ethanol and dried in air.



Figure 30: Scheme of scored glass slide.

Cleaning of PEEK Substrates

The cleaning procedure of the PEEK substrates was performed before coating with titania. As substrates, PEEK discs with a diameter of 1.1 cm were cut out from a

3. Preparation of Materials

15 x 15 x 0.1 cm PEEK sheet (Goodfellow GmbH, Bad Nauheim, Germany). Before coating, the PEEK discs were cleaned in an ultrasonic bath in absolute ethanol (Merck, Darmstadt, Germany) for 15 min, before being rinsed with absolute ethanol and dried in ambient air. This step was performed three times.

3.2 Preparation of Titania Thin Films on PEEK Substrates

Preparation of Plain Titania Film

The dip-coating solution for dense titania thin films was prepared in two steps: first, 3.33 mL titanium isopropoxide (TIP) was mixed with 20 mL n-butanol (solution A); and second, 2.58 mL acetic acid (HOAc) with 20 mL n-butanol (n-BuOH) (solution B). The molar ratio of the educts was TIP : HOAc : n-BuOH = 1 : 4 : 40. After stirring of both solutions for 15 min, solution B was slowly added to solution A. The resulting mixture was stirred at 40 °C for another 2 hours before dip-coating.^[192]

Preparation of Titania Thin Film with Added Titania Nanoparticles

The same dip-coating solution used for the dense titania films was prepared as described above. To 15 mL of this solution, 0.2 g commercially-available TiO₂ nanoparticles were added at a v/w ratio of solution : nanoparticles = 225 : 1 (15 mL : 0.2 g) and suspended in an ultrasonic bath for 15 min. Subsequently, 30 mL of the residual dip-coating solution was added to the suspension and stirred for 2 hours.^[193]

Preparation of Titania Film with Nanoparticles Formed In Situ

The dipping solution for porous titania films was synthesised in two steps, according to the synthesis presented by HUANG and co-workers.^[194] The first solution A was made by mixing 5 mL tetrabutyl titanate (TBT), 1 mL acetylacetone (acac) and 1.5 mL diethanolamine (DEA) with 45 mL of absolute ethanol (EtOH). For the second solution B, 0.5 mL 65% nitric acid (HNO₃) and 5 mL of ultrapure water were mixed with 5 mL absolute ethanol. The molar ratio of the educts was TBT : acac : DEA : HNO₃ : H₂O : EtOH = 1 : 0.7 : 1.1 : 0.8 : 19 : 59. Both solutions were stirred for 30 min, before solution B was slowly added to solution A. This mixture was stirred for 3 hours before dip-coating.^[194]

Dip-Coating of PEEK Substrates with Titania

The dip-coating procedure was performed using a Dip-Robot DR3 (Riegler & Kirstein GmbH, Berlin, Germany). The PEEK substrates were immersed into the dipping solution with a constant speed of $1 \text{ cm} \cdot \text{s}^{-1}$, stored in the solution for 60 s and then withdrawn with a constant speed of $0.02 \text{ cm} \cdot \text{s}^{-1}$ perpendicular to the surface of the solution. The substrates were dip-coated three times with intermittent drying step of 600 s in air before each immersion step. After coating, the samples with dense titania films and films containing nanoparticles were dried at $60 \text{ }^\circ\text{C}$ overnight. The porous titania films were dried at $90 \text{ }^\circ\text{C}$ overnight.

Mechanical and Chemical Stability of Titania Coatings

The interfacial adhesion of the films on the PEEK substrates was tested qualitatively with an adhesive tape test, using a standard Tesa® tape (Tesa Werk Hamburg GmbH, Hamburg, Germany). The tape was pressed onto the substrates by loading the titania coatings for 2 hours with a weight of one kilo.^[195,196] After pulling the tape off, the surface morphology of the remaining film was characterised by SEM measurements.

The stability of titania coatings in a simulated body environment and during the sterilisation process was tested with phosphate buffered saline solution (PBS) and ethanol. Therefore, titania-coated substrates were stored in 8 mL of PBS or 8 mL of ethanol, respectively, for 24 h, 48 h and one week at $37 \text{ }^\circ\text{C}$. Subsequently, $100 \text{ } \mu\text{L}$ of hydrochloric acid (2 M) was added to 3 mL of the recovered testing liquids.^[108,197] 0.5 mL chromotropic acid solution (0.11 g chromotropic acid dissolved in 20 mL of water, $0.013 \text{ mol} \cdot \text{L}^{-1}$) was added to the mixtures to form a red-violet Ti^{4+} -chromotropic complex. The extinction of the resulting solutions was measured at 470 nm by using an Eon Microplate Spectrophotometer (BioTek, Bad Friedrichshall, Germany).^[198] In order to determine the amount of dissolved titanium ions, a multi-point calibration was recorded. Therefore, a stock solution of titania ($5 \text{ } \mu\text{L}$ TIP, 5 mL EtOH and $50 \text{ } \mu\text{L}$ HCl) was prepared. This mixture was diluted with PBS in a volume ratio of 1 : 4 (stock solution 1 mL : PBS 4 mL) to record the calibration. Five drops of the chromotropic acid solution were added to every dilution to form the complex, which was determined by the UV-Vis measurement. At a concentration of $4 \cdot 10^{-7} \text{ mol} \cdot \text{L}^{-1}$, no signal for Ti^{4+} was detectable. The same procedure was performed to test the

stability of the coatings in ethanol. Here, the lowest detectable concentration was $5 \cdot 10^{-6} \text{ mol} \cdot \text{L}^{-1}$.

3.3 Preparation of Silica-Based Mesoporous Organic-Inorganic Coatings

Preparation of the PMO Layers with Phenylene Units on Glass Slides

Absolute ethanol was obtained from Merck (Darmstadt, Germany), while other chemicals were purchased from Sigma-Aldrich Chemie GmbH (Munich, Germany) and were used without further purification.

The synthesis was performed with some changes according to HAO *et al.*^[199] In general, periodic mesoporous organosilica layers were prepared by first dissolving 2.7 g of Pluronic® F-127 completely in 17 mL ethanol and 0.5 mL 2 M HCl at 40 °C for about 60 min. Subsequently, 2 mL of the siloxane precursor 1,4-bis(triethoxysilyl)benzene (BTEB) was added. The molar ratios of the dip-coating solution BTEB : Pluronic® F-127 : HCl : ethanol : H₂O were 1 : 0.04 : 0.20 : 57.79 : 5.11. The solution was stirred at 40 °C for about 2 hours before coating the specimens. The dip-coating procedure of the glass slides was performed by the layer-by-layer deposition robots DR3 (Riegler & Kirstein GmbH, Berlin, Germany). The substrates were immersed into the dipping solution at a constant speed of $1 \text{ cm} \cdot \text{s}^{-1}$, and then withdrawn at a constant speed of $0.1 \text{ cm} \cdot \text{s}^{-1}$ perpendicular to the surface of the solution. After coating, the samples were dried at 60 °C and subsequently at 120 °C overnight, followed by calcination at 350 °C in air for four hours with a heating rate of $1 \text{ °C} \cdot \text{min}^{-1}$. Some of the calcined coatings were additionally extracted in ethanol at 100 °C overnight to remove calcination residues – like carbon compounds – generated by the decomposition of Pluronic® F-127. Subsequently, each specimen was rinsed with ethanol and dried in air.

Preparation of the PMO Layers with Biphenylene Units on Glass Slides

The PMO layers with the biphenylene group were prepared in a similar manner. First, 2.21 g of Pluronic® F-127 was dissolved in 30 mL of ethanol and 0.5 mL 2 M HCl at 40 °C and stirred for about 60 min. Subsequently, the reaction mixture was cooled down to room temperature and 2 mL of 4,4-bis(triethoxysilyl)biphenyl (BTEBp) was added. Afterwards, the solution was stirred for a further 60 min before coating of the glass substrates. The molar ratio for the reaction mixture

BTEBp : Pluronic® F-127 : HCl : ethanol : H₂O was 1 : 0.04 : 0.23 : 117.61 : 5.89. The dip-coating and further procedures were performed in the same manner as described for the phenyl-PMO layers.

Preparation of Silica Coatings on Glass Slides

The synthesis of the silica coatings was first published by EHLERT *et al.*^[200] Silica coatings were prepared using two different SDAs, namely Pluronic® F-127 and Pluronic® P-123. The synthesis procedures for both coatings were equal. First, the respective SDA was dissolved in ethanol and distilled water, followed by the addition of HCl. After the SDA was completely dissolved, which took about 45 min, tetraethylorthosilicate (TEOS) was added to the mixture. Subsequently, the solution was stirred for 15 min to enable the hydrolysis of TEOS. The substrates were immersed into the dipping solution at a constant speed of 1 cm · s⁻¹, and then withdrawn at a constant speed of 0.1 cm · s⁻¹ perpendicular to the surface of the solution. After the coating procedure, the samples were dried at 60 °C overnight followed by calcination at 350 °C in air for 4 hours with a heating rate of 1 °C · min⁻¹. The molar ratio of the dipping solution with TEOS : Pluronic® F-127 : HCl : ethanol : H₂O was 1 : 0.0066 : 0.0067 : 22.62 : 4.65. For the other solution, the molar ratio of TEOS : Pluronic® P-123 : HCl : ethanol : H₂O was 1 : 0.013 : 0.06 : 48.79 : 26.53.

Preparation of PMO Particles

PMO particles were prepared by a simple evaporation process of the dipping solutions for the PMO coatings. Therefore, the dipping solutions were stored in a laboratory hood at room temperature to evaporate the solvents overnight. Subsequently, the resulting xerogels were dried at 120 °C for 24 h and calcined at 350 °C in air for 4 hours with a heating rate of 1 °C min⁻¹. The resulting powders were ground in a mortar and extracted in ethanol at 100 °C overnight to reduce residual decomposition products after the calcination.

3.4 Modification of Phenyl-PMO with Sulfonate Groups

The sulfonic acid modification was carried out according to de CANCK *et al.*^[132] To 130 mL of dichloromethane, 1.56 mL of chlorosulfonic acid was added and the mixture

3. Preparation of Materials

was cooled down to 0 °C before immersing the phenyl-PMO-coated glass slides. The solution was gently stirred for 24 h without renewing the ice bath. Subsequently, the glass slides were rinsed properly with water and dried at 110 °C for 6 h.

Quantification of Sulfonate Groups on Sulfonated Phenyl-PMO

The quantification of the sulfonate groups was carried out by staining the unmodified and sulfonated phenyl-PMO samples with methylene blue according to GHOSH *et al.*^[201] Figure 31 shows the reaction between the positively-charged amid group and the negatively-charged sulfonate group staining the material blue.

The methylene blue solution was prepared by dissolving 0.015 g of methylene blue chloride trihydrid in 0.5 L water ($c = 0.08 \text{ mmol} \cdot \text{L}^{-1}$). 50 mL of this deep blue solution was diluted with a further 50 mL of water ($c = 0.04 \text{ mmol} \cdot \text{L}^{-1}$). In this solution (0.04 M), five unmodified and five sulfonated phenyl-PMO-coated glass slides were immersed in separated vessels. After 12 h, the glass slides were removed and the absorption of the remained methylene blue solution was measured at 660 nm in the UV-Vis.

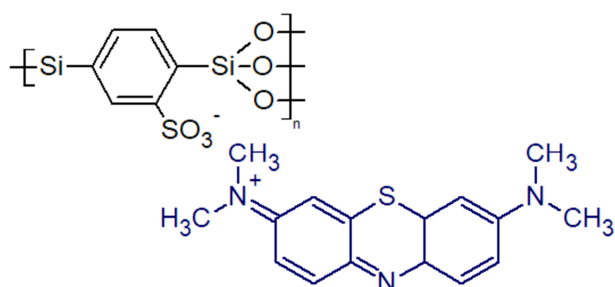
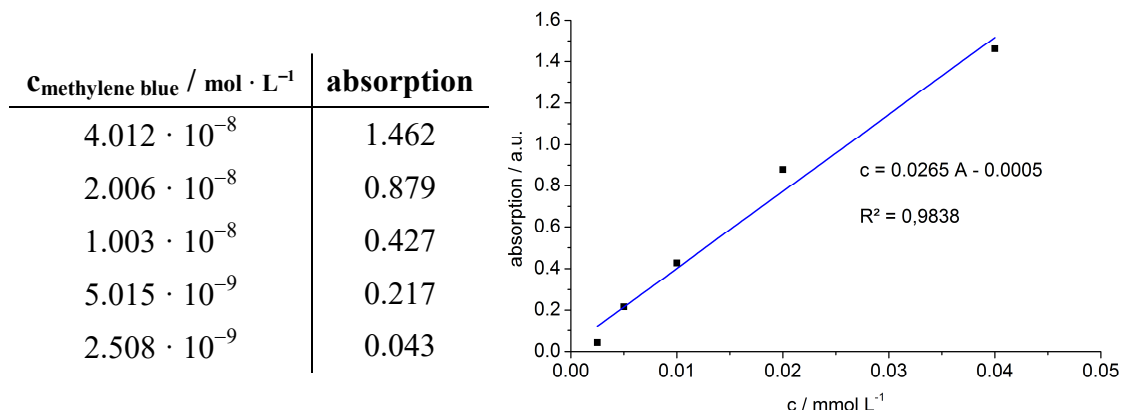


Figure 31: Electrostatic interaction between methylene blue and a sulfonated phenyl-PMO.

In order to determine the correct amount of attached methylene groups, a calibration was performed with various concentrations (see Table 2 and Figure 32). 300 μL of each solution was measured in a plate reader at the same wavelength. The number of the sulfonate groups attached to the phenyl-PMO was calculated by the difference of the absorbed methylene blue on sulfonate-modified PMO and the unmodified phenyl-PMO.

Table 2 and Figure 32: Calibration of the methylene blue solution in dependence of the concentration.

3.5 Drug Loading and Release Procedures

3.5.1 Drug Loading and Release of Ciprofloxacin

Loading of Ciprofloxacin

The drug-loading procedure with ciprofloxacin (CFX) of the PMO-coated substrates was carried out by storing the phenyl-PMO-coated glass slides, the additional sulfonate modified ones as well as the biphenyl-PMO-coated substrates in a 60 mM CFX solution. The CFX solution was prepared by dissolving 10 g (0.03 mol) of CFX in 300 mL of water, followed by reducing the pH value using a 2 M HCl until the solution turned yellow (pH \approx 2). Subsequently, the pH value was adjusted to pH 4 with a 1 M sodium hydroxide solution, whereby at this pH value the CFX solution proved most stable. The substrates were stored at pH 4 at 37 °C in this solution for four days.

After the drug-loading procedure, the slides were rinsed with water several times to wash off the highly concentrated CFX from the outer surface of the slides. Subsequently, the substrates were dried at 60 °C before being employed in further experiments.

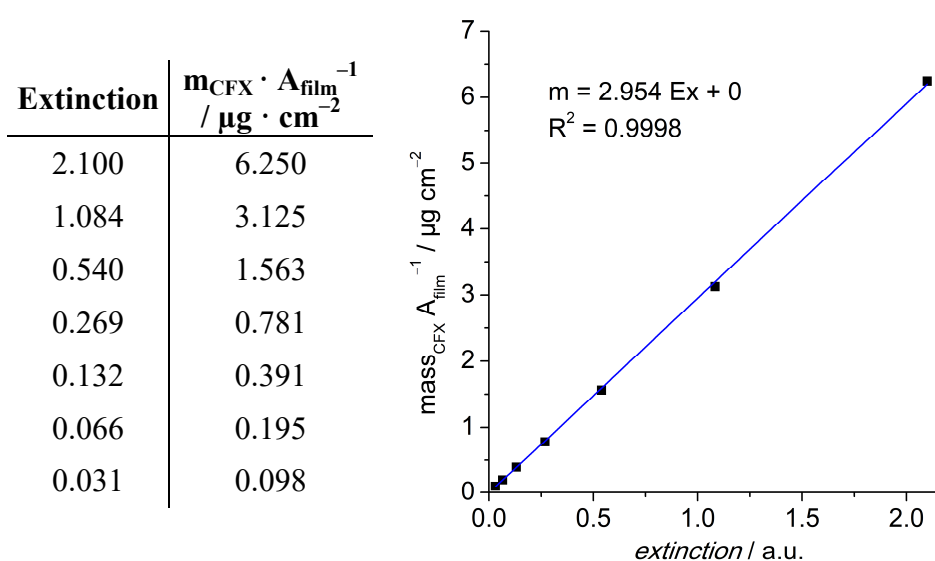
Release of Ciprofloxacin

The drug release experiments were performed by storing one drug-loaded substrate in 0.5 mL pre-warmed (37 °C) 0.01 M PBS solution (phosphate buffered saline) at 37 °C for 24 h. The substrates were transferred into fresh PBS solution once a day. On this occasion, the PBS solution was refreshed after every UV-Vis measurement to simulate the dynamic fluid conditions in the body. For statistical purposes, the experiments were

3. Preparation of Materials

performed with four glass slides simultaneously. The quantitative determination of the CFX in the solution was carried out on the Eon Microplate Spectrophotometer (BioTek Instruments, Winooski, US) measuring the supernatants at a wavelength of 275 nm. A calibration with different CFX concentrations was performed every time prior to the release experiments for a precise determination of the released amount of ciprofloxacin. An exemplary calibration is shown in Table 3 and Figure 33.

Table 3 and Figure 33: Exemplary calibration for the release of ciprofloxacin from the PMO coatings. The values are adjusted referring to the blank value of phenyl-PMO coating treated in PBS identically to the CFX-loaded samples.



The values for the extinction at the wavelength of 275 nm were always corrected by the blank value of parallel-measured pure PMO coatings. Pure PMO coatings – phenyl-PMO as well as biphenyl-PMO – were treated identically to the CFX-loaded samples. As the PMO coatings themselves, had a slight auto-fluorescence and were dissolving over time, the extinction values of these supernatants were chosen as blank values and were subtracted from the supernatants bearing CFX.

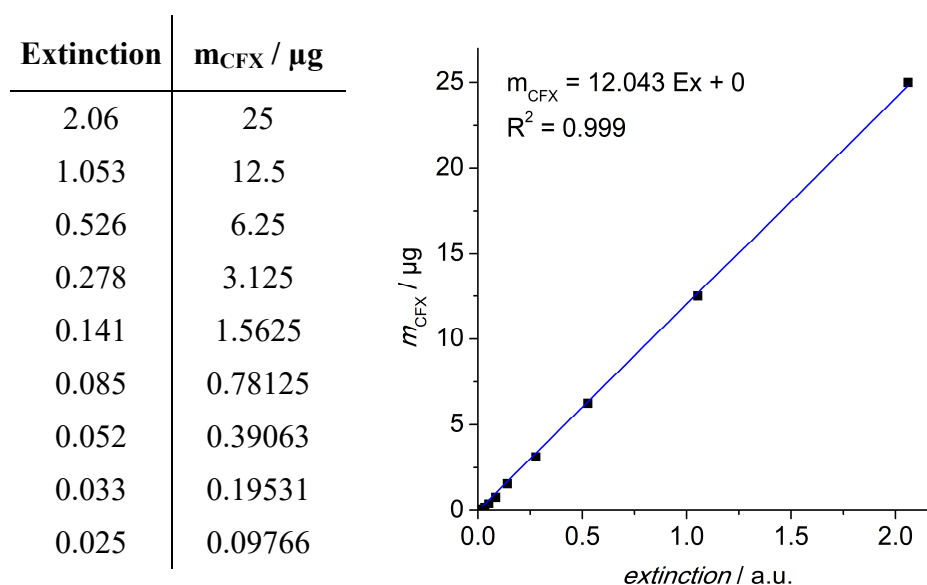
Determination of Stored Ciprofloxacin

The maximal amount of ciprofloxacin stored in the phenyl-PMO coatings was determined by dissolving the PMO coatings in 0.1 M sodium hydroxide solution. Phenyl-PMO-coated slides, sulfonated phenyl-PMO coating, CFX-loaded coating and

glass slides (reference) as well as solid CFX were stirred, respectively, in 0.1 M NaOH solution for 15 min. Subsequently, 100 μ L of the samples was measured on the Eon Microplate Spectrophotometer (BioTek Instruments, Winooski, US) at the wavelength of 200 – 800 nm to determine whether the NaOH solution itself or the phenyl- PMO coating have an impact on the fluorescence and can overlay the CFX signal.

In Table 4 and Figure 34, the calibration curve and values used for the CFX determination are shown.

Table 4 and Figure 34: Calibration for determination of CFX amount stored in different phenyl-PMO coatings.



The calibration for the determination of the stored CFX amount was performed by dissolving 0.003 g of CFX in 60 mL 0.1 M NaOH. The concentration series was recorded by diluting the stock solution 1:1 with 0.1 M NaOH.

3.5.2 Drug Loading and Release of Rolipram

Loading of Rolipram

Both coating types – the one with the phenylene unit and the one with the biphenylene unit – were loaded with rolipram. Therefore, 0.014 g (0.051 mmol) of rolipram was dissolved in 50 mL ethanol. In this 1 mM rolipram solution, eight substrates coated with phenyl- or biphenyl-PMO, respectively, were immersed (3.125 mL of rolipram solution

3. Preparation of Materials

per substrate). The solution with one substrate was covered with parafilm and stored at 37 °C for three days. After the loading procedure, the substrates were rinsed several times with water and dried at 37 °C overnight.

In addition, the PMO particles were also loaded with the drug rolipram. Therefore, 0.022 g (0.08 mmol) of rolipram was dissolved in 40 mL of ethanol, yielding a 2 mM solution of rolipram. In 10 mL of this rolipram solution, 0.4 g of PMO particles was dispersed. PMO particles were stirred in the rolipram solutions at 37 °C for 2 h before being transferred into centrifuge tubes and stored at 37 °C for two days. Subsequently, the particles were separated by centrifugation at 6000 rpm for 60 min, re-dispersed in 10 mL of water as a washing step, centrifuged again at 6000 rpm for 60 min and finally dried at 37 °C.

Release of Rolipram

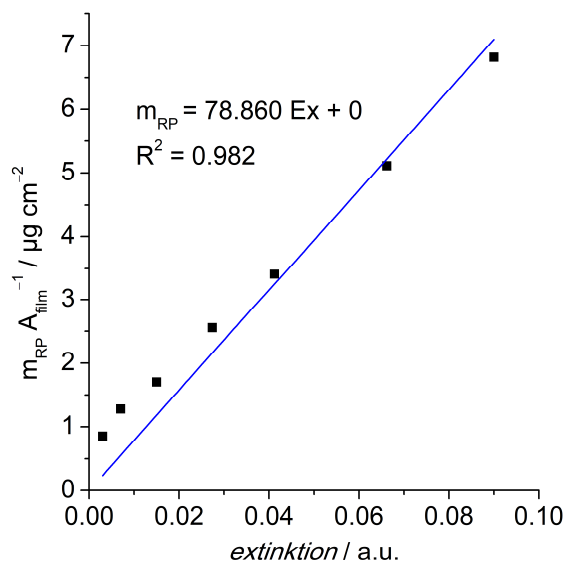
The rolipram release experiments were performed similar to those with ciprofloxacin. The coated glass substrates were stored at 37 °C in 0.5 mL of pre-warmed 0.01 M PBS solution. For statistical reasons, the experiments were performed with four glass slides simultaneously.

The release of rolipram from PMO powders was performed by dispersing 0.001 g of the PMO powder in 1 mL of pre-warmed 0.01 M PBS solution. After the release time of 24 h at 37 °C, the powders were centrifuged at 10300 rpm at 37 °C for 20 min, the supernatants were removed by decantation and replaced by fresh PBS. The PBS solutions in each release experiments were renewed every 24 h. The PBS solutions containing the released rolipram were measured at the wavelength of 280 nm on the Eon Microplate Spectrophotometer (BioTek Instruments, Winooski, US).

The amount of released rolipram was determined by a previously recorded calibration with different rolipram concentrations (see Table 5 and Figure 35). As already described in the previous chapter, the extinction values were also corrected by the blank values of the PMO coatings stored in PBS, as both PMO coatings were auto-fluorescent and dissolved over time.

Table 5 and Figure 35: Exemplary calibration for the release of rolipram from the PMO coatings. The values are adjusted referring to the blank value of phenyl-PMO coating treated in PBS identically to the rolipram-loaded samples.

Extinction	$m_{RP} \cdot A_{film}^{-1}$ / $\mu\text{g} \cdot \text{cm}^{-2}$
0.090	6.818
0.066	5.114
0.041	3.409
0.027	2.557
0.015	1.705
0.007	1.278
0.003	0.852



4. Analytical Methods

4.1 Physisorption Measurements

It is possible to analyse the specific BET (BRUNAUER, EMMETT and TELLER) surface area, pore volume and pore size distribution of porous materials by physisorption measurements. Prior to the actual measurement, it is necessary to outgaze the sample at high temperature and reduced pressure. Thus, it is important to ensure that the sample is stable under these conditions. The adsorptive adsorbs on the surface and in the pores of a sample and subsequently desorbs. The adsorbed gas volume is measured at predefined equilibrium points p/p_0 at isothermal conditions. The adsorption and desorption branch of an isotherm result from these points.

The isotherms can be classified in six different types, as shown in Figure 36 (left). Type I isotherms represent physisorption in microporous (pore size < 2.5 nm) solids with small external surfaces. Type II is typical for non-porous or macroporous substances and an unlimited monolayer-multilayer adsorption at p/p_0 near one. Point B represents the completion of the monolayer covering the surface, after which the multilayer adsorption starts. Type III is also valid for non-porous or macroporous substances, but there is no formation of monolayer visible. Gas molecules adsorb at active sites on the surface. For mesoporous adsorbents (2 – 50 nm), type IV isotherms are typical. An initial monolayer on the surface of the pore walls – comparable to type II isotherm – is followed by pore condensation behaviour. A liquid-like phase is formed at high p/p_0 during pore condensation. A plateau at the end of the isotherm with a variable length is characteristic for type IV isotherms. Sometimes capillary condensation is attended by a hysteresis, which is common for cylindrical pores with a pore width above 4 nm, assigned to type IV (a) isotherm. Adsorbents with smaller pores often show type IV (b) isotherms. When the adsorbent-adsorbate interactions are weak, type V isotherms are often seen. The stepwise type VI isotherm is measured for non-porous uniform surfaces with a layer-by-layer adsorption.^[202]

The type IV isotherm sometimes shows a hysteresis, depending on the adsorbate, adsorbent and the pore size. Six different hysteresis types can be differed, as shown in Figure 36 (right). Type H1 hysteresis is characteristic for materials with narrow pore sizes of uniform mesopores. Ink bottle pores with pore necks smaller than the pore

bodies also show a similar type H1 loop. Type H2 hysteresis describes the impact of the adsorbent in the porous network. H2 (a) hysteresis can be assigned to pore-blocking effects or cavitation-induced evaporation in narrow pore necks. By contrast, H2 (b) is common for pore-blocking with wider pore necks. Type H3 loops are sometimes measured for non-rigid porous systems of solids or macropores that are not fully filled with adsorbate. Type H4 hysteresis is similar to H3, but is often assigned to adsorption in microporous materials. Type H5 hysteresis is seldom found. Here, open and partially blocked pores are present.^[202]

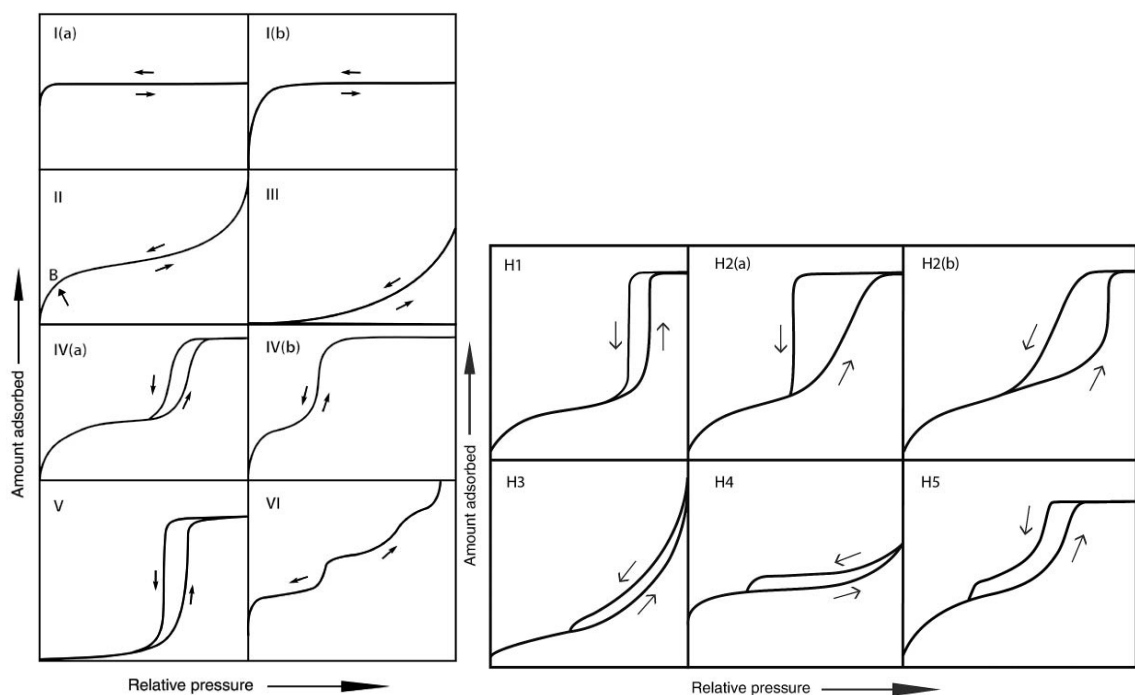


Figure 36: Left: Classification of physisorption isotherms. Right: Types of hysteresis loops. From [202].

The BET theory is used to determine the specific area of a porous system. It refers to multilayer adsorption with the assumption that gas molecules adsorb physically on a solid layer without limit. There is no interaction between the adsorbed layers and every position on the sample surface is equal, disregarding active sites. The scope for application of the BET analysis is given at the relative pressure values p/p_0 between 0.05 and 0.3 for mesopores (2 – 50 nm) and between 0.001 and 0.1 for micropores (< 2 nm).^[203]

The pore size distribution can be defined by using the BJH (BARRETT, JOYNER and HALENDA) method, where the KELVIN equation is modified. The KELVIN equation

predicts the pressures at which an adsorptive spontaneously condenses in a cylindrical pore. The theory describes capillary condensation in the pores with a hemispherical liquid-vapor meniscus and defined surface tension. The BJH theory approximates that the ratio of the core fluid radius and the pore radius is constant.^[204] However, given that this method is only valid for mesopores larger than 3 nm, only the data for $p/p_0 \geq 0.3$ can be considered.

Better and more accurate results are provided by the NLDFT (non-local density functional theory). It allows calculating sorption isotherms for pores with defined geometry based on intermolecular interactions. The so-called kernels give a calculated isotherm for a defined temperature, gas, adsorptive and pore geometry (e.g. N₂ at 77 K on silica, cylindrical/spherical pores, NLDFT adsorption model). This model isotherm is fitted to the experimental one and provides results not only for the pore size distribution but also for the pore volume and the specific area of a sample. However, the BJH method can underestimate the true pore size by up to 20 – 30%.

The choice of a gas depends on the sample and the desired information. Inert gases like nitrogen, argon or krypton are often used, because they show only little interactions with the most materials. Nitrogen is cheap and easily available, whereby it is used in most cases. However, a major disadvantage is the quadrupole moment of the diatomic nitrogen. It is possible that the diatomic nitrogen molecule adsorbs tilted to a surface covered, e.g. with hydroxyl groups. Accordingly, the possibility for misinterpretation of the BET results is very high and mistakes of up to 30% can occur. This problem does not emerge when argon is utilised, because it is a monoatomic gas and does not have a quadrupole moment. The specific interactions between the adsorbate and adsorbent are different in this case. In addition, argon has a smaller VAN DER WAALS radius and can resolve pore sizes up to 0.41 nm, while nitrogen is only able to determine pore diameters up to 0.5 nm. Rarely-used gases are CO₂ or H₂O, whereby CO₂ is utilised to determine ultra-micropores and H₂O to determine the wettability inside the pores of a material.

The characterisation of thin porous films is very difficult with the gases described above – argon or nitrogen – due to their high saturation pressure. Thin films are often only a few hundred nanometers thick. Hence, the device is unable to detect small pressure changes when only few gas atoms of argon or nitrogen adsorb to the very low surface

area of these films. As an alternative, krypton can be used at 77 K or 87 K as adsorptive. The saturation pressure of supercooled Kr with a value of 1.6 Torr at 77 K is much lower than that of nitrogen with 760 Torr at 77 K.^[205] Hence, Kr adsorption is much more sensitive as there are fewer Kr molecules in the measuring cell. Thus, the adsorption of few Kr molecules on the thin film surface can be recognised by the instrument much more precisely. Nowadays, this method is the most reliable for analysing surface areas down to 0.05 m².^[206] In order to determine surface areas by Kr, a temperature of 77 K and a saturation pressure of 1.6 Torr is recommended. However, for precise pore size distribution, a measurement at 87 K and a saturation pressure of 13 Torr is required. Pore sizes in a range of 1 – 9 nm can be resolved by this method. A vapour-to-liquid phase transition occurs close at the sublimation pressure of the bulk fluid at 87 K giving a direct relationship between the pore filling pressure and pore size.^[205,207] A typical isotherm course as well as the type of hysteresis obtained during Kr sorption measurement can provide important information about the porosity of the material, compared to Ar and N₂ sorption measurements. The pore size distribution received with Kr is calculated by a method developed by Quantachrome especially for this issue.

The krypton sorption measurements were performed with 10 to 20 PMO-coated glass samples with sizes of 0.9 x 1 x 0.1 cm at 87 K (supercooled Ar) with a saturation pressure of 13 Torr. The instrument used was Autosorb 1 from Quantachrome (Odelzhausen, Germany), while the evaluation software was ASiQwin. Since the mass of the coatings could not be weighed out, the values always referred to the outer film surface area. PMO powders were measured with nitrogen at 77 K and argon at 87 K with an Autosorb 3 from Quantachrome. All samples were outgassed at 100 °C for 24 h before measurements.

4.2 Ellipsometry

Ellipsometry is an analytical method for characterising thin films and material surfaces which was first utilised by PAUL DRUDE at the end of the 19th century. It is a spectral measurement method for determining dielectric material properties like the refractive index and permittivity as well as the film thickness.

During the ellipsometric measurements, a linear or circular polarised light beam is radiated onto the surface of a material. Due this interaction, the polarisation of this light beam changes depending on the characteristic material properties. The focused reflection of the light beam is polarised elliptically, as predicted by FRESNEL's and MAXWELL's equations (Figure 37).^[208] The polarisation state is described by the coefficients Δ and Ψ , whereby Δ stands for the polarisation-depending phase shift and Ψ represents the change of the amplitude of the incident electromagnetic wave.

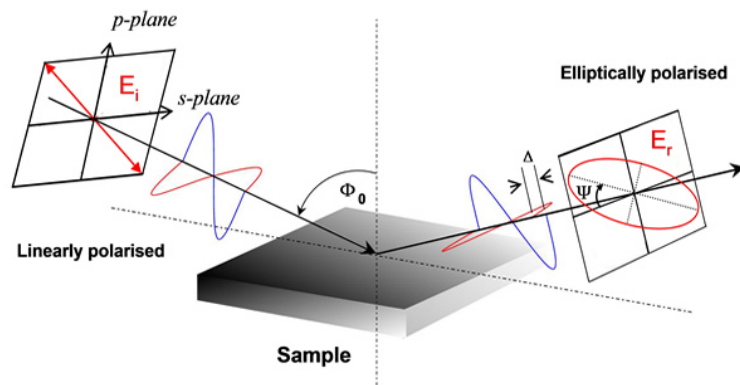


Figure 37: Schematic representation of the theory for ellipsometry and presentation of the p - and s -vectors. Taken from ref. [209].

The incident and the reflected beam form a common plane where both electromagnetic waves are described in one coordination system by two basis vectors s and p , which are perpendicular to each other. S -vector is the perpendicular one in the plane of incidence, whereas p -vector is the parallel one. In case of elliptic polarised light that is described by the two polarised waves, the amplitude in s and p direction and the phase δ between these waves is different.^[210]

Ellipsometry measures the phase δ of the incident (δ_i) and the reflected light beam δ_r . The difference between both δ is described by the phase shift Δ :

$$\Delta = \delta_i - \delta_r$$

In addition to the phase shift Δ , the amplitude Ψ can change between the incoming and outgoing electromagnetic wave. The change of the amplitude is given by the relation between the FRESNEL reflection coefficients r_p and r_s , which arise from linear polarised waves perpendicular to each other.

The advantage of ellipsometry is that it is a self-gauging method, where no reference is needed. It measures only relative and not absolute values. This method is less susceptible against ambient influences by determining two measuring parameters.^[210]

Both ellipsometric parameters Ψ and Δ are connected by the fundamental equation of ellipsometry:

$$\frac{\bar{r}_p}{\bar{r}_s} = \tan \Psi e^{i\Delta}$$

Both parameters – the amplitude Ψ and the phase shift Δ – are recorded during an ellipsometric measurement. The experimental data of the phase shift and amplitude can be fitted using parametrised models with specific fitting algorithms. The better the experimental curves and the calculated ones fit together, the higher the accuracy of the measurement. The calculated values provide data like refractive index, absorption coefficient and film thickness.

Depending on the film thickness, the Ψ and Δ curves show different numbers of peaks (Figure 38). The higher the thickness, the more peaks are visible in the curves. Thus, it is possible to estimate the thickness after regarding the curve progression.

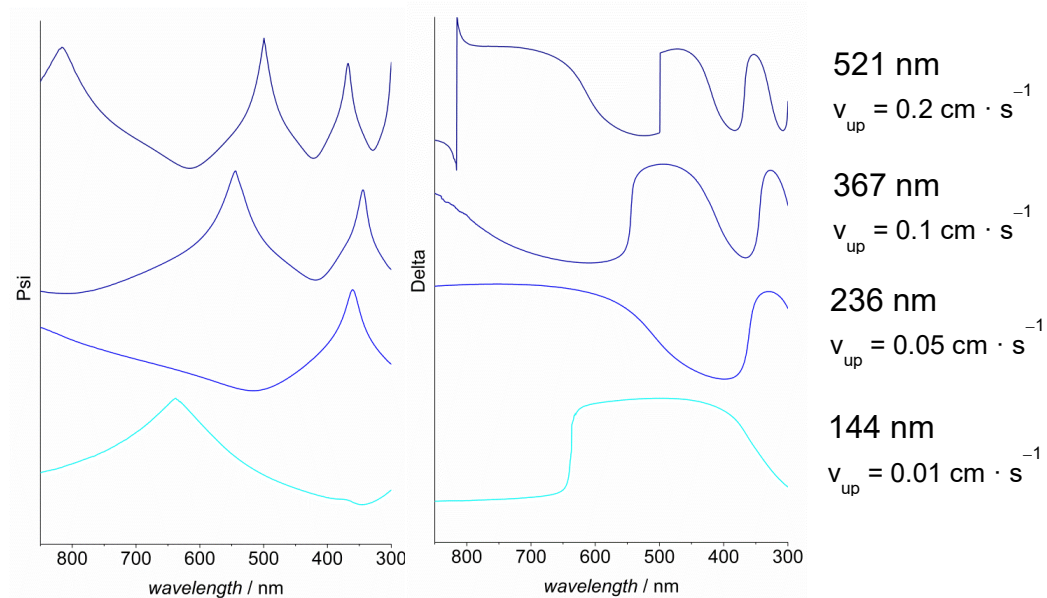


Figure 38: Ψ and Δ curves depending on the film thickness and withdrawal speed.

The measurements were performed with an ellipsometer SE 800 from Sentech (Berlin, Germany) and evaluated with the software SpectraRay 3 from Sentech. The PMO-

4. Analytical Methods

coated silicon wafers as well as titania-coated PEEK slides were measured without further sample preparation. The spectral range was set to 1.459 – 4.137 eV, the angle of incidence was 70.0° and the refractive index of the sample was defined at a wavelength of 632.8 nm. The following model (Table 6) was used for evaluation:

Table 6: Model used for evaluating the ellipsometric measurements.

Layer name	Dispersion formula	Fitted values
Air	Constant dispersion	No
Roughness	Effective medium approximation	Yes
PMO layer	Tauc-Lorentz	Yes
SiO₂	Cauchy	No
Si	File layer	No

The Cauchy dispersion is mainly used for transparent materials like dielectrics, e.g. SiO₂. The Tauc-Lorentz oscillator is often used to describe transparent dielectric materials with absorption in the short wavelength range. It comprises four parameters that must be set to calculate the refractive index. The values and data used are attached in the appendix.

4.3 Scanning Electron Microscopy

Scanning electron microscopy (SEM) is an analysis method where the sample surface is scanned under high vacuum using a high energetic electron beam. A map of the scanned area is received detecting either reflected electrons – so-called backscattered electrons – or weak bonded electrons detached from the sample surface, so-called secondary electrons. The number of secondary electrons depends on the sample composition, the topography of the sample and the orientation of the detector. The images provide information about surface structure, porosity and homogeneity of coatings or the morphology of crystals. The samples should be stable under reduced pressure and should preferably exhibit a certain level of electric conductivity. Especially samples with a high number of organic compounds can display charging effects resulting, in poor information. A scanning electron microscope can resolve structures down to a few

nanometers. In addition, many SEM feature an energy dispersive X-ray analysis (EDX) unit. Here, the sample is irradiated by a focused electron beam, which causes an X-ray radiation with an element specific wavelength. This method can be used to determine the chemical composition of a sample.

The SEM measurements were performed by KATHARINA NOLTE and DENNES NETHELROTH with a JOEL JSM-6700F (JOEL Ltd., Tokyo, Japan). The surface morphology was characterised by SEM using a field emission scanning microscope with an acceleration voltage of 2 kV and a working distance of 8 mm. Further SEM investigations and EDX analyses were carried out by BASTIAN HOPPE with a JOEL JSM-6610 (JOEL Ltd., Tokyo, Japan). Therefore, PMO-coated silicon wafers were attached on graphite adhesive pads and placed on a brass carrier. PMO powders were thoroughly ground and sprinkle on a graphite pad. The images were evaluated by the software ImageJ 1.47v (National Institutes of Health, USA).

4.4 Transmission Electron Microscopy

Transmission electron microscopy (TEM) can resolve nanostructures much more accurately with a higher resolution of down to 0.1 nm compared to SEM. The requirement is a sample thickness of about 100 nm as the electron beam must transmit this sample. An image is obtained by the interactions of the transmitted electrons with the specimen that are detected by a sensor like a CCD camera. This method effort also reduced pressure, an electron gun and electron lenses.

The phenyl-PMO coating on a glass slide was agglutinated with an epoxide resin, cut in thin slices and polished. The final thinning was performed with an argon ion beam to obtain electron transparent samples (30 – 70 nm) for investigating the phenyl-PMO layer in a cross-section manner. The subsequent TEM analysis was carried out by a field emission transmission electron microscope (FE-TEM) of the type JOEL JEM-2100F (JOEL Ltd., Tokyo, Japan), whereby this microscope was also used to record the scanning microscope (STEM) images. The measurements were performed by FRANK STEINBACH and evaluated by Prof. Dr. ARMIN FELDHOFF from the Institute for Physical Chemistry and Electrochemistry, LUH.

In order to gather more information about the porosity of the PMO coatings, they were scratched off the glass slides with a scalpel. The samples were dispersed in ethanol and

4. Analytical Methods

dropped on a copper grid, which was coated with a thin graphite film. The same procedure was carried out to examine PMO powders. The measurements were performed by Dr. ALEXANDRA SATALOV with a TEM Tecnai F20 S-Twin TEM from FEI (Hillsboro, USA). The images were evaluated by the software ImageJ.

4.5 Nanoindenter Analysis

It is possible to determine mechanical properties like hardness and elastic modulus (YOUNG's modulus) of thin coatings on the nanoscale by a nanoindenter. A diamond tip formed like a triangular pyramid with BERKOVICH geometry (Figure 39) is pressed into the sample surface with a define pressure and the mechanical parameters are recorded against the displacement into surface. Using the continuous stiffness measurement (CSM) technique, it is possible to measure the stiffness depending on the penetration depth for only a few nanometers. Due to this technique, the mechanical parameters of the substrate underneath do not influence the measurement results.

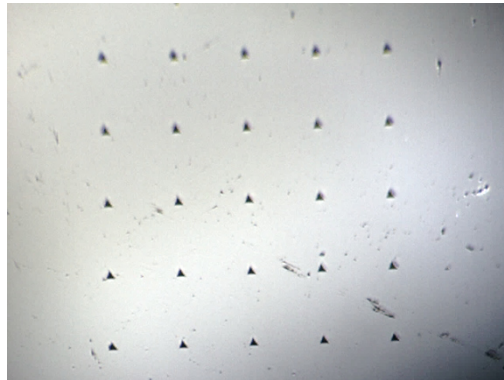


Figure 39: BERKOVICH tip of a nanoindenter pressed into a glass sample.

The diamond tip is pressed with an increasing force in a range of several $\text{mN} \cdot \text{s}^{-1}$ into the sample surface until the preset penetration depth is reached. The first contact of the indenter and the surface is only kind of elastic, so that the first values up to the first 10 nm are discarded. With increased force, the material undergoes a plastic deformation. The force is kept constant for 30 s to 240 s after reaching the preset penetration depth. During this phase, a viscous solidification is formed. The force, the penetration depth and the time are recorded during the measurement. From these parameters, the hardness and the elastic modulus can be calculated.^[211,212]

The nanoindentation tests were performed with an Agilent Nano Indenter G200 with the following extensions: CSM, Highload, LFM (Agilent Technologies, Santa Clara, USA). The maximal displacement into surface was 2000 nm. Prior to the measurements, no surface preparation was carried out and as reference cleaned glass slides were used. The results are an average of 25 measurement points from the film surface. The measurements were performed by DANIEL GOTTSCHALK from the Institute of Continuum Mechanics, Leibniz Universität Hannover.

4.6 Water Contact Angle Measurements

Contact angle measurements provide information about the interactions – like surface energy or the wettability – between a solid surface and a liquid, e.g. water. The contact angle characterisation was used to determine the hydrophilicity of the different PMO coatings regarding the different organic units within the structure, porosities and modifications.

The wettability of a surface can be described by the contact angle θ , which occurs at the three-phase point (solid/liquid/gaseous) when a droplet is settled on a solid surface. YOUNG's equation describes the relationship between the contact angle and the interfacial tension:

$$\sigma_s = \sigma_l \cos\theta + \gamma_{sl}$$

θ = contact angle

σ_l = liquid surface tension

σ_s = solid surface tension γ_{sl} = interfacial tension between solid and liquid

If water is used to determine the contact angle, there are three main types of wettability: if the contact angle is below 5°, the surface is strongly hydrophilic, whereas samples with a contact angle above 90° are hydrophobic and above 120° they are super hydrophobic. For interactions with cells, hydrophilic surfaces are desired.

The contact angles were measured with the instrument SurfTens Universal from OEG (Frankfurt/Oder, Germany) in a shadow projection. The medium was water. For the value of each layer, five to ten films were measured and averaged. Cleaned glass substrates were used as a reference.

4.7 Förster Resonance Electron Transfer

Förster resonance electron transfer (FRET) or fluorescence resonance transfer is a mechanism that describes the radiation-less energy transfer between two light-sensitive molecules. Through non-radiative dipole-dipole coupling, a donor fluorophore (chromophore) – in its excited state – transfers energy to an acceptor chromophore in dependence of the distance between them.

There are several preconditions for this effect.^[213,214] First, both coupling partners must match each other, which means that the emission band of the donor and the excitation band of the acceptor should overlap (Figure 40 a). To obtain a more effective energy transfer, it is necessary that the overlap of both curves is high. This has to be regarded when the fluorophores are chosen. The next precondition is the distance between the fluorophores (Figure 40 b).

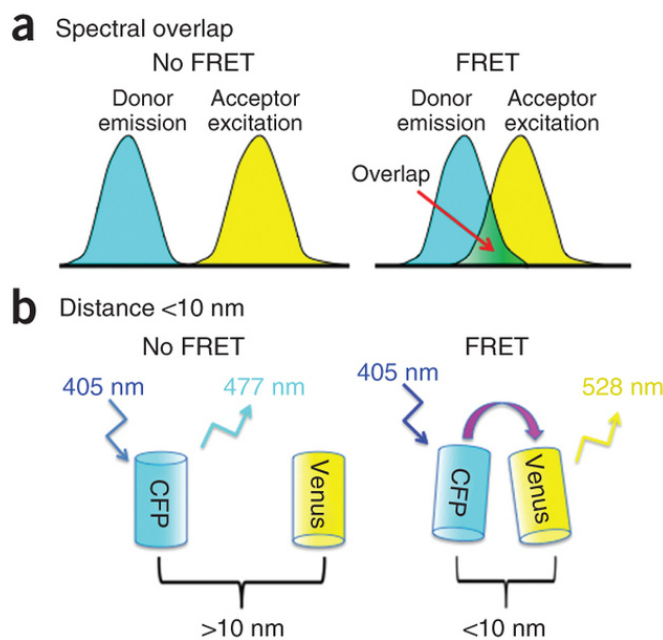


Figure 40: Preconditions for FRET: (a) Emission spectrum of the donor must overlap with the excitation spectrum of the acceptor. The higher the overlap, the more effective the FRET effect. (b) The distance between the donor (CFP) and the acceptor (Venus) must be less than 10 nm to observe the FRET effect.^[213] Image from ref. [215].

The distance is a crucial factor of the efficiency of the energy transfer and is inversely proportionally to the sixth power of the distance between the donor and acceptor. For the FRET effect, the near-field zone around the donor must have a value of

1 – 10 nm.^[214] This is why FRET analysis is often used in chemistry or biology to determine the distance between two molecules by measuring the FRET efficiency (spectroscopic ruler).^[216] Furthermore, the FRET donor should exhibit a high quantum yield and a high orientation factor, whereby the orientation factor describes the relative orientation of the transition dipole moments of the donor and acceptor.

FRET analysis is performed by measuring the fluorescence of the samples – whether solid or liquid – in a fluorescence spectrometer. The measured data are then summarised in an emission spectrum, where the fluorescence intensity is applied versus the wavelength. Depending on the chemical composition of the samples, the curves show various maxima, which is a hint for the FRET effect. The intensity of the fluorescence depends on the chemical structure of the sample and the solvent in the solutions.

PMO-coated glass substrates as well as ethanolic and aqueous solutions were analysed. The samples were fixed in a holder, the angle of the detector towards the sample could be adjusted. The coated glass slides were measured at an angle of 60°, the solutions at an angle of 90°. For phenyl-PMO-coated samples, the excitation wavelength was 272 nm and the emission was measured in a range of 290 – 550 nm. For the biphenyl-PMO samples, the excitation wavelength was 321 nm and the emission spectrum was recorded from 340 – 600 nm. The gap width of the beam was set to 5 nm, the signals were corrected regarding the wavelength of the spectrofluorometer and the dark current. Measurements were performed using a spectrofluorometer Fluoromax-4 from Horiba Ltd. (Kyoto, Japan). The evaluation was carried out using the software Origin 8.1 (OriginLab Corporation, Northampton, USA).

4.8 Thermogravimetric Analysis

During a thermogravimetric analysis, the change in sample mass depending on time or temperature is measured. The sample is placed on a micro balance and heated up with a certain heating rate dT/dt . The heating rate is a crucial factor for the accuracy of the analysis. The lower the heating rate, the better the resolution in the change of the sample mass and thus the quantification of the sample. A thermogram is typically measured between 25 °C and 1000 °C. During heating, several chemical and physical processes occur, like oxidation, reduction and decomposition as well as vaporisation and sublimation. A thermogram shows a stepped curve in which the turning point of each

step – extrapolated to the temperature axis – can be assigned to the decomposition temperature for each component of the material. The organic compounds are in general completely burned, whereby the inorganic compounds are left as residues.

The TG analysis was performed by a Simultaneous Thermal Analyser 429 from Netzsch (Selb, Germany) and evaluated with the software Proteus Thermal Analysis. The PMO powders were ground well and heated up to 1000 °C with a heating rate of 5 °C per minute. The measurements were performed by KATHARINA NOLTE and Dr. SERGEJ SPRINGER.

4.9 Ultraviolet/Visible Light (UV-Vis) Photometry

Photometric analysis is used to determine the quantitative concentration of dissolved substances as well as the absorption maxima. The sample is irradiated with electromagnetic waves in the range of ultraviolet and visible light, whereby the decrease of the intensity is measured. The concentration c of the absorbing substance is proportional to the measured extinction E_λ as described by the LAMBERT-BEER equation:

$$E_\lambda = \lg\left(\frac{I_0}{I}\right) = \varepsilon c d$$

E_λ = extinction at the wavelength λ ε = absorption coefficient

I_0 = intensity of the irradiated light c = concentration

I = intensity of the attenuated light d = path length of the light through the sample

The concentrations of the released substances previously loaded in PMO coatings were determined by measuring the supernatants. Therefore, the supernatants were transferred into 96-well plates, which were transparent for UV light and measured at the absorption maxima of the drugs. The absorption wavelength for ciprofloxacin was 275 nm and for rolipram it was 280 nm. 0.01 M PBS as well as unloaded pure PMO coatings and powders stored in PBS served as references. The measurements were carried out on an EON microplate spectrophotometer from BioTek (Winooski, USA). The evaluation was performed with the software GEN5 (BioTek, Winooski, USA).

4.10 Infrared Spectroscopy

Infrared (IR) spectroscopy can be used to characterise organic and inorganic solids, liquids and gases. Molecular vibrations and rotations in the sample are activated by the absorption of infrared light. Different functional groups show vibrations at characteristic energies at different wavelength and absorb the IR radiation only in a specific range. The whole measuring scale is between 200 cm^{-1} and 4000 cm^{-1} .

The infrared light is only absorbed when the electric dipole moment in a molecule can be changed and no centre of symmetry exists. These substances are called IR active: they are associated with a changing dipole. Symmetrical molecules with vibrations symmetrical to the centre of symmetry have a permanent dipole and are IR inactive.

The measurements of the PMO layers were performed via the ATR (attenuated total reflection) IR spectroscopy. Hereby, PMO-coated Si-Wafers were measured in a spectral range of $600 - 4000\text{ cm}^{-1}$. The ATR crystal of the instrument was used as a reference. The sample is pressed on the ATR crystal, typically a material with a high refractive index (e.g. silicon). The IR light passes through the ATR crystal and is partially absorbed by the sample. A typical penetration depth is between 0.5 and $2\text{ }\mu\text{m}$. The intensity of the reflected light is measured.

The PMO powders were measured in transmission mode, where a small amount of the sample is thoroughly ground with dry potassium bromide (KBr) and pressed with a hydraulic press to form KBr pellets. The reference for these measurements was a pure KBr pellet. The measuring range for the KBr mode was $400 - 4000\text{ cm}^{-1}$.

The IR samples were characterised by using a Fourier transformation IR spectrometer type Tensor 27 from Bruker (Billerica, USA). The spectra were evaluated with the instrument software OPUS 5.0 (Bruker) and the program Origin 8.1 (OriginLab Corporation, Northampton, USA).

4.11 X-ray Diffraction

X-ray diffraction can help to evaluate the structure of solid materials. With this method, the periodic structure of crystals or porous systems can be examined. The periodic texture of materials serves as a diffraction grating, where the X-ray beam is reflected and interferences occur. The resulting diffraction pattern can be described by BRAGG's equation, when the parameters of the crystal lattice satisfy the equation:

$$n \lambda = 2 d \sin \theta$$

n = positive integer d = interplanar distance
 λ = wavelength θ = scattering angle

The measurements are performed at constant wavelength. For this purpose, the sample is irradiated with K_{α} radiation, which can be monochromised by e.g. selective filtering metals. The diffracted radiation is then detected by a scintillation counter. Measured intensities are plotted against the scattering angle 2θ attaining typical X-ray diffraction pattern. The material is classified as amorphous or crystalline based on the resulting pattern. By indexing the reflections, information about the crystal lattice (hexagonal, cubic and other) is collected.^[217]

The PMO layers and titania-coated PEEK samples were measured on a θ - θ -diffractometer (STOE, Darmstadt, Germany) in reflection geometry. A sample was fixed in its position, the X-ray tube as well as the detector were moving around the sample. The reflected radiation was collected by a graphite secondary monochromator. The measuring range was $0.7 - 5.0^{\circ} 2\theta$, the step width was 0.01° and the step time was 2 s.

The PMO powders were characterised in transmission geometry by a StadiP-diffractometer (STOE, Darmstadt, Germany). Prior to the measurements, the samples were ground and placed in a StadiP sample holder between two X-ray foils. The 2θ measuring range was $0.5 - 5.0^{\circ}$ with a step width of 0.01° and a step time of 10 s. The evaluation was performed by the software WinXPow 1.1 (STOE, Darmstadt, Germany) and Origin 8.1 (OriginLab Corporation, Northampton, USA).

4.12 Cell Culture Tests

The evaluation of the cell compatibility on different un- and modified PMO coatings was performed by three different cooperation partners, namely Laser Zentrum Hannover (LZH), Hannover Medical School (MHH) and Helmholtz Centre for Infection Research in Braunschweig. It was crucial to investigate whether and how cells adhere and proliferate on PMO and titania surfaces. Furthermore, the antibacterial activity of ciprofloxacin-loaded PMO coatings was examined.

4.12.1 Cell Culture Tests on PMO Coatings

Cell Culture Tests on Phenyl-PMO Coatings with Fibroblasts and HUVEC

These cell culture tests were performed by Dr. SABRINA SCHLIE-WOLTER from the Laser Zentrum Hannover e. V., Hannover, Germany.

In order to test the biocompatibility of the prepared samples, cell culture tests with human fibroblasts and HUVEC (human umbilical vein endothelial cells) were performed. The fibroblasts were cultivated in Dulbecco's modified Eagle's medium (DMEM) supplemented with 10% fetal calf serum (FCS) and 1% antibiotics (Penicillin), while HUVEC were cultivated in endothelial growth basal medium (EBM-2). All media were purchased from Lonza (Basel, Switzerland). Prior to use, the samples were shortly washed with PBS and then sterilised under UV light for about 30 min. Glass slides served as a control and were treated in the same way. All samples were placed into a 24 well plate, which was then filled with 2 mL cell culture medium. Both cell lines were seeded onto the samples with a seeding cell density of $2.75 \cdot 10^4 \text{ cells} \cdot \text{mL}^{-1}$ for fibroblasts and $2.73 \cdot 10^5 \text{ cells} \cdot \text{mL}^{-1}$ for HUVEC, respectively. The cell density was determined by using a Fuchs-Rosenthal chamber.

Proliferation and Vitality of Fibroblasts and HUVEC

After 48 and 96 h cultivation time, the cells were trypsinized, collected and centrifuged. Trypsin was used to detach the cells from the cell culture dish. Trypsin is a serine protease that cleaves peptide chains at the carboxyl side of the amino acids lysin and argenin. Thus, only specific proteins are dissolved that hold the cells together. The chelating agent EDTA (ethylenediamin triacetate) complexes cations like Ca^{2+} , which stabilise the membrane proteins. This leads to a dissociation of the cell adhesion structures and separation of the cell layer to singular cells.^[218]

Subsequently, the cell density was determined to quantify the cell growth. Additionally, the cell suspension was stained using trypan blue to estimate the cell vitality. Vital cells do not take up trypanblue; rather, they appear white in front of a blue background. Only dead cells and those with a damaged cell membrane are stained deep blue by this dye. For a better comparison between the experiments, the quantified cell numbers ($\text{cells} \cdot \text{mL}^{-1}$) of vital and dead cells were normalised to the corresponding starting cell

density. Three independent measurements were performed. The results were given as average \pm standard error of mean.

Cell Morphology of Fibroblasts and HUVEC

After 24 h of cultivation time, the samples were fixed for 10 min with 4% formaldehyde. Staining with phalloidin-Atto for actin filaments and Hoechst 33342 for nuclei was performed at 37 °C for 1 h. Finally, the samples were washed with PBS and conserved for further analysis. Images of the stained cells were recorded with a Zeiss fluorescence microscope. The cell elongation – given as the ratio of cell length and cell width – was quantified using the ImageJ software. The results were obtained from 50 cells per treatment and presented as average \pm standard error of mean.

Cell Culture Tests with Fibroblasts on Phenyl- and Biphenyl-PMO Coatings

These cell culture tests were performed by JENNIFER SCHULZE at the Hannover Medical School (MHH, Hannover, Germany), Department of Otorhinolaryngology.

The cell type used was murine fibroblasts NIH3T3. The samples – glass as reference, phenyl-PMO and biphenyl-PMO coatings – were sterilised by UV light and transferred into a 24-well plate. Subsequently, 10,000 cells were added per well. The cell growth was monitored every day taking microscopic pictures. After 96 h, the samples were transferred into a new well plate to perform the neutral red uptake (NRU) test. This test is used to distinguish viable cells from the dead ones. Viable cells are able to incorporate and bind the dye neutral red in their lysosomes. After incubation with the neutral red-containing medium, the cells are washed and the acidified-extracted dye is measured by a spectrophotometer.^[219]

The NRU test was performed according to the following steps. First, neutral red stock solution was diluted 1 : 50 with Dulbecco's modified Eagle's medium (DMEM). From this dilution, 100 μ L was given to each well and incubated for 3 h at 37 °C. Afterwards, the dye solution was poured away, the cells were washed and fixed and treated with an acidified solution to extract the incorporated dye from the cells. Finally, the acidified solution with the released dye was measured in a spectrophotometer at 570 nm. The vitality of the cells was determined by the absorption at 570 nm with glass slides as a reference.

Influence of PMO and Mesoporous Silica Coatings on BDNF Production of Gene-Modified Fibroblasts

One goal was the usage of the PMO coatings on cochlea implants. Therefore, it was favourable to adhere brain-derived neurotrophic factor (BDNF)-producing cells on the surface of these coatings. BDNF improves the attachment of spiral ganglion cells to surfaces and thus provides a better interaction of the implant with the cochlea. These cell culture tests were performed by JENNIFER SCHULZE at the Hannover Medical School (MHH, Hannover, Germany), Department of Otorhinolaryngology.

First, the samples were sterilised by UV light for 20 min. Afterwards, native NIH3T3 murine fibroblasts (used as negative control) as well as gene-modified BDNF-producing NIH3T3 murine fibroblasts were seeded on the samples in a 24-well plate. Cell culture plastic was used as a positive control. 10^4 cells suspended in 100 μ L medium were placed in the middle of the each specimen. After 10 min, for the first adherence of the cells to the substrate, 400 μ L Dulbecco's modified Eagle's medium (DMEM) was added and the test setup was placed in an incubator at 37 °C and 5% CO₂ for 96 h. The cell growth was monitored every day by a fluorescence microscope.

The cells were counted in a hemocytometer (Neubauer Kammer) after 96 h to determine the cell number. Therefore, the cells were detached by 200 μ L of a trypsin/EDTA solution and incubated for 4 min at 37 °C. Subsequently, the cell suspension was diluted 1 : 2 with trypan blue and transferred into a hemocytometer for cell counting. The formula used for determining the cell number in one millilitre was:

$$(\text{counted cells} / \text{number of squares}) \times 10,000.$$

The supernatants from the cell culture test were frozen at 20 °C and subsequently applied to a murine BDNF ELISA kit (Boster biological technology Co., Ltd, Fremont) to determine the BDNF concentration. The BDNF ELISA kit was used according to recommendations of the manufacturer. This procedure was described by KATHARINA KRANZ *et al.*^[56]

Protective Effect of PMO Coatings Loaded with Rolipram on Spiral Ganglion Neurons

These cell culture tests were performed by JENNIFER SCHULZE at the Hannover Medical School (MHH, Hannover, Germany), Department of Otorhinolaryngology.

Spiral ganglion neurons (SGN) were attained from 30 cochleas of 15 Sprague Dawley rats. The cells were separated by a digestion solution with fetal calf serum and centrifuged at 6000 – 7000 rpm. Afterwards, the cells were washed with serum-free medium three times, and 1 mL of this medium was added to the cell suspension before cell counting. The serum-free medium contained 15 mL Panserin, 375 μL Hepes buffer, 275 μL PBS, 225 μL penicillin, 82.5 μL glucose-PBS solution, 35 μL insulin ($4 \text{ mg} \cdot \text{mL}^{-1}$) and 15 μL N2 supplement. 10 μL of cell suspension and 10 μL of trypanblue solution were mixed and filled into a hemocytometer. The total number of cells was determined by the mean of cell number in four squares of the counting chamber x dilution factor x volume (mL). 50 μL of the cell suspension and 50 μL of medium – with and without BDNF – were added to each well. The seeding control was fixed after 4 h, the remaining cells after 48 h. The cell fixation was performed by replacing the medium in the wells by a mixture of 100 μL methanol/acetone solution. The cells were fixed for 10 min, after which the methanol/acetone mixture was removed and the cells were washed with 150 μL PBS three times. Finally, a NRU staining was performed as described above to evaluate how many living SGN remained.

4.12.2 Cytocompatibility Tests of Titania-Coated PEEK

DR. BUSHRA RAIS from the Helmholtz Centre for Infection Research Braunschweig performed the cytocompatibility tests for titania-coated PEEK samples. Cell culture assays were performed using NIH3T3 (mouse fibroblasts) and MG63 (human osteosarcoma) cell lines. Prior to testing, all PEEK samples were washed with 70% ethanol and dried under laminar air flow. For every measurement, three samples per type were put in a 12-well plate and washed twice using Dulbecco's phosphate buffered saline (PBS) with a pH of 7.0. Polystyrene cell culture plates were used as a reference. After washing, the samples were pre-incubated in Dulbecco's Modified Eagle Medium (DMEM, Sigma, Germany) supplemented with 5% fetal calf serum (FCS, Biovest), 1% penicillin/streptomycin (Gibco, Germany) and 1% glutamine (Gibco, Germany) for two

days. Subsequently, MG63 and NIH3T3 cells were seeded at densities of $7.0 \cdot 10^4$ cells \cdot mL⁻¹ and $3.3 \cdot 10^4$ cells \cdot mL⁻¹, respectively. Cell cultures were incubated in a humidified atmosphere with 5% CO₂ in air at 37 °C (Labotect, C200).

The density and morphology of the cells were examined daily by visible light microscopy. When it reached an estimated cell density of 80% confluency, the cell supernatant was removed and cells were stained as follows. 8 μM of 5-(and 6)-carboxyfluorescein diacetate succinimidyl ester (CFSE, eBiosciences, Germany) were dissolved in PBS. Afterwards, the samples were incubated in 2 mL of CFSE solution for 15 minutes. Subsequently, this solution was removed and 2 mL DMEM without FCS was added. Finally, images were taken using a fluorescence detection microscope (Carl Zeiss, AX10). The images taken were electronically sharpened and cells were manually counted using the Image J software, version 1.47 (National Institutes of Health, USA).

4.12.3 Antibacterial Activity Tests for Phenyl-PMO Coatings

The antibacterial testing was performed by Dr. MUHAMMAD IMRAN RAHIM, Helmholtz Centre for Infection Research, Braunschweig, Germany.

Phenyl-PMO, sulfonated, CFX-loaded as well as sulfonated and CFX-loaded phenyl-PMO-coated samples and glass as a reference in triplicates were placed into a 24-well plate (Nunc, Denmark). 200 μL of PBS was added per well. The whole plate was placed at 37 °C in the presence of 5% CO₂ in a humidified cell culture incubator. 200 μL of PBS was collected from each well daily and replaced with fresh PBS for the time period of 15 days. The collected supernatants were stored at 4 °C.

A bioluminescent laboratory strain of *Pseudomonas aeruginosa* (PA01 CTX::lux) was used to investigate *in vitro* antibacterial activity of supernatants collected from discs. These bacteria are genetically transformed with lux operon, which makes them luminescent.^[220,221] The bacteria were spread on LB agar plates and incubated overnight. Later, to obtain fresh culture, they were grown as a suspension culture in LB until an OD₆₀₀ of 0.1 was obtained. 100 μL of supernatant collected from discs – each in triplicate – was placed into wells of 96-well plates with black background (100 μL of supernatant per well). Subsequently, 100 μL of bacterial culture suspension with an OD of 0.1 was poured directly into each well containing 100 μL of PBS. Plates containing supernatants and bacteria were incubated at 37 °C for 6 hours. The luminescence of the

4. Analytical Methods

bacteria was measured after 0, 4 and 6 hours with an IVIS®-200 *in-vivo* imaging system (Xenogen, USA). In order to assess the bacterial viability/survival, bacterial luminescence was measured with Living Image Software ® Version 2.6 (Xenogen). The luminescent intensity of each sample was measured as average radiation ($\text{p s}^{-1} \text{cm}^{-2} \text{r}^{-1}$). Bacterial luminescence can be used as an indicator to assess the bacterial growth and viability. All samples were analysed in triplicates. The data shown corresponds to the mean values \pm standard deviation.

5. Results and Discussion I

Evaluation of Periodic Mesoporous Organosilica (PMO) Coatings as a Novel Biomaterial

In this part, the obtained results are presented and discussed. First, the characteristics of the periodic mesoporous organosilica (PMO) coatings are introduced. Subsequently, the results of modification followed by drug loading with ciprofloxacin and rolipram are presented. Förster resonance energy transfer (FRET) as observation technique for release experiments is introduced and discussed in comparison with classic drug release experiments, after which the antibacterial tests are presented. Cell compatibility was one of the relevant factors for the usage of PMO coatings in biological systems and thus a special emphasis was set on cell culture tests.

5.1 Characterisation of PMO Particles

In the following, the analysis of phenyl- as well as biphenyl-PMO particles is presented and discussed. The particles were obtained by drying the dipping solution, calcination and finally grounding the xerogel. TGA measurements and IR analysis was performed employing PMO powders of phenyl- as well as biphenyl-PMO since the results obtained with PMO coatings (following in the chapters from 4.2) were difficult to analyse. Hence, the measurements with PMO powders provided more information.

Thermogravimetric Analysis of PMO Particles

Thermogravimetric analysis of the PMO particles was performed to characterise the different organic compounds and the inorganic residue of the PMOs. First, the decomposition temperature of the used structure-directing agent (SDA) Pluronic® F-127 was determined. Pluronic® F-127 decomposed completely at 305 °C, whereby the thermogram is shown in Figure 41. A mass loss of 100% was detected between 210 °C and 400 °C. Consequently, a calcination temperature of 350 °C was chosen to remove the SDA completely.

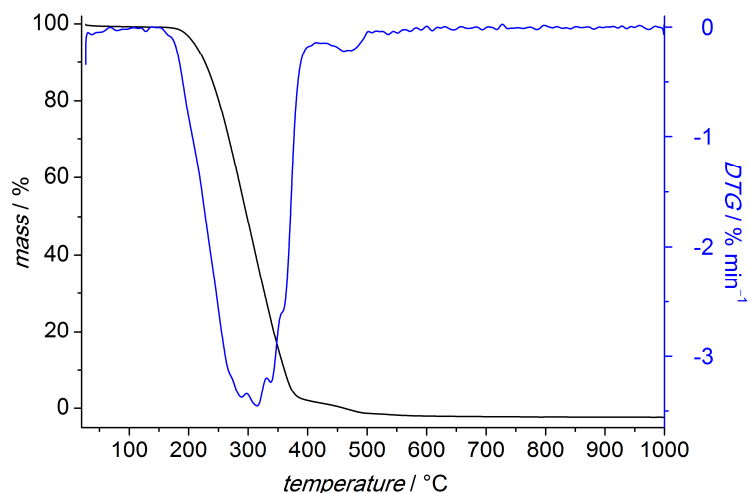


Figure 41: TG and DTG curves of Pluronic® F-127, the structure-directing agent used to obtain the porous PMO network.

It was important to ascertain whether the PMOs were stable at this temperature or the organic part in the framework decomposed like the SDA Pluronic® F-127. The thermogravimetric curves of the PMO particles (Figure 42) showed different decomposition behaviour depending on the organic unit. In all thermograms, the first range up to 125 °C was assigned to desorption of adsorbed solvent on the surface and in the pores of PMO particles. The second range indicated the decomposition of the organic unit. The phenylene group decomposed at 550 °C to 750 °C (Figure 42, top). The biphenylene group decomposed at temperatures from 455 °C to 745 °C (Figure 42, bottom). Hence, the decomposition temperature of the biphenylene units is slightly lower compared to the phenylene units. The phenylene and biphenylene units were burned to gaseous carbohydrates and vanished from the material. Since the decomposition temperatures of the regarded PMOs were above 400 °C, the calcination temperature of 350 °C was sufficiently high to remove the SDA and sufficiently low to maintain the organic groups intact in the framework.

The theoretically calculated inorganic residue of the phenyl-PMO was 66.7%. This implies that 33.3% of the material can be assigned to the organic part. Considering the organic part, the calculated values fitted very well to the measured ones. The value of the first step – depicting the amount of the absorbed solvent – was subtracted from the total mass of the sample. Subsequently, the measured data for the decomposition of the PMOs was recalculated, adjusted to the solvent-free values.

Looking at the phenyl-PMO, the measured percentage of the organic part fits perfectly to the calculated ones (Figure 42, top). In the TG measurement, 35.1% of the material was decomposed between 550 °C and 750 °C, which can clearly be assigned to the phenylene units. The silica part remained with a mass referring to 64.9%. The residual powder comprised silicon oxycarbides, which were coloured black due to the remaining carbon.

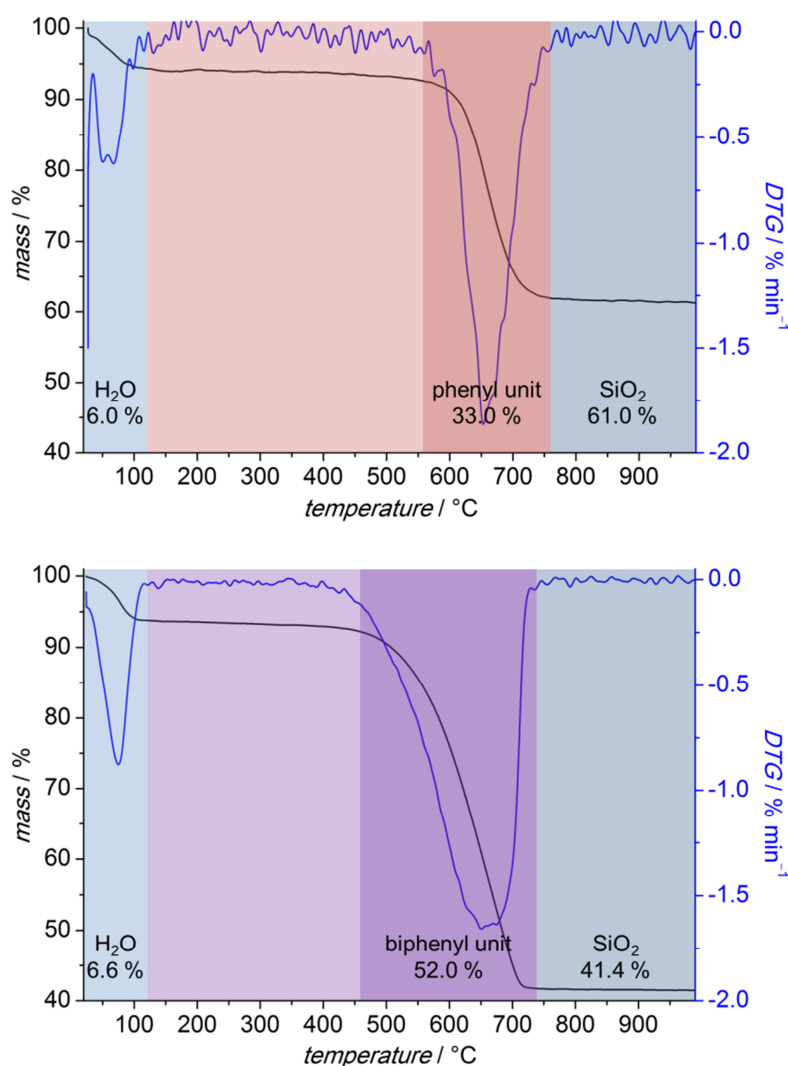


Figure 42: TG and DTG curves of calcined (**top**) phenyl- and (**bottom**) biphenyl-PMO powder prepared from the dip-coating solution.

Regarding the biphenyl-PMO, the measured values for the remaining silicon oxycarbides and decomposed biphenylene units correlate well with the calculated ones. The latter obtained for the decomposed biphenylene unit was 53.1%. The value for the

residue was 46.9%. These amounts also fitted well to the measured ones, with 55.7% for the biphenylene part and 44.3% for the black-coloured residue of silicon oxycarbides. The materials had a high thermal stability. The measured and calculated composition of the particles was consistent. On this basis, it was assumed that the desired phenyl- and biphenyl-PMO were synthesised without a decomposition of the organic units during calcination.

Infrared Spectra of PMO Particles

In addition to the thermogravimetric analysis, the PMO powders were also characterised by IR spectroscopic measurements. Therefore, the powders were mixed with KBr, pressed in a pellet form and measured in the transmission mode. The collected spectra are compared regarding the organic groups in the network. The results are summarised in Table 7. In Figure 43, the spectra of phenyl-PMO and biphenyl-PMO particles obtained by drying the dipping solution are compared.

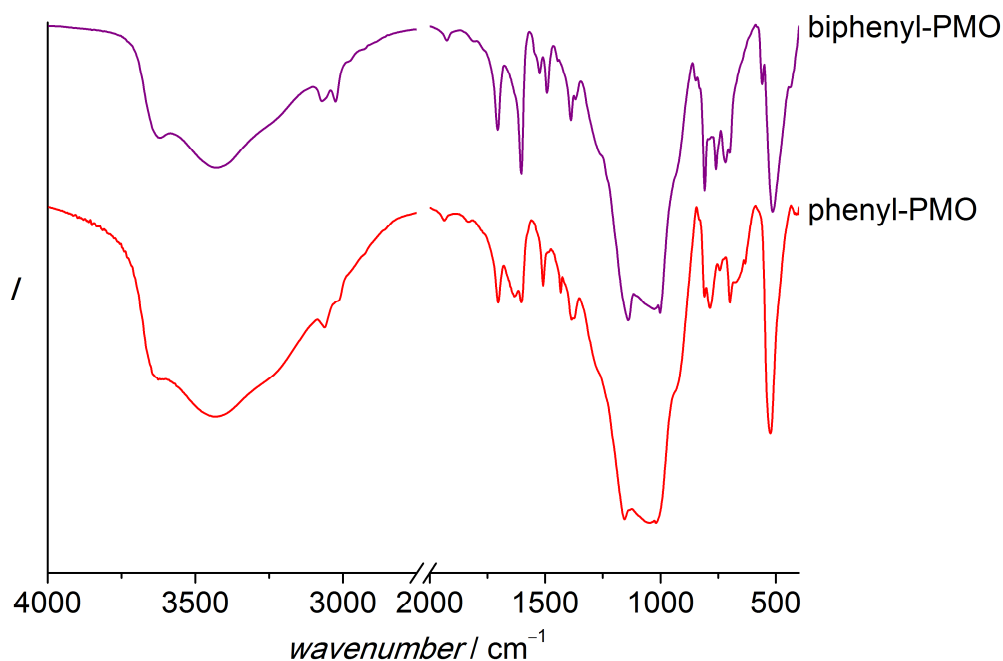


Figure 43: IR spectra of PMO powders synthesised from dipping solution.

Table 7: Summary of vibrations for phenyl-PMO and biphenyl-PMO powders and their assignment. The listed wavenumbers are given in the cm^{-1} unit.

biphenylene gel	phenylene gel	assignment	reference
3621	3636	$\nu(\text{Si-OH})$	[222]
3431	3433	$\nu(\text{Si-OH})$	[223]
3071	3064	$\nu(\text{ring-H})$	[224]
3026	3011	$\nu(\text{ring-H})$	[224]
1931	1939	$\nu(\text{ring})$	[224]
1706	1705	$\nu(\text{ring})$	[224]
	1630	asymm. $\nu(\text{ring})$	[224]
1605	1600	$\nu(\text{C=C})$	[225,226]
1523	1506	$\nu(\text{C=C})$	[225]
1493		$\nu(\text{C-C})$	[224]
1446	1434	$\nu(\text{C=C})$	[224,226]
1389	1385	$\delta(\text{C-H})$	[225]
1265	1280	symm. $\delta(\text{C-H})$	[223]
1140	1158	$\nu(\text{Si-O})$ or $\nu(\text{Si-Ph-Si})$	[225,226]
1030	1050	$\nu(\text{Si-O})$	[222]
845	835	$\delta(1,4\text{-substituted C-H})$	[224,225]
811	810	$\delta(\text{Si-O-Si})$	[222,225]
763	783	$\delta(\text{ring}), \text{Si-Ph}$	[226]
718		biphenyl-Si	[225]
698	696	symm. $\nu(\text{Si-C}), \text{Si-Ph}$	[225,226]
	663	$\delta(\text{Si-O-Si})$	[222]
560		biphenyl	[225]
513	525	$\delta(\text{Si-C})$	[225]
433		Si-O	[222,226]

The wide IR band between 3750 and 3100 cm^{-1} in all spectra could be assigned to the stretching vibrations of the silanol groups [Si-OH]. These bands were very prominent due to the enhanced hydrophilicity of the particles and the generation of hydroxyl groups by hydroxylation of the materials. Both small bands at 3064 cm^{-1} and 3012 cm^{-1} were characteristic for stretching vibrations between an aromatic ring and the bound

hydrogen.^[224] The signals around 1930 cm^{-1} and 1705 cm^{-1} in all spectra indicate an aromatic ring stretching vibrations and an asymmetric ring vibration found only in the phenyl-PMO spectra at 1630 cm^{-1} . These weak bands are overtone and combination vibrations, which are characteristic for aromatic molecules but also difficult to find in spectra. They can be overlapped by carbonyl bands.^[223] Further evidence for aromatic stretching vibration is a double bond between two carbons [C=C], which was found at 1600 cm^{-1} , 1512 cm^{-1} and 1434 cm^{-1} . A clear hint for the biphenylene group is given by the signal at a wavenumber of 1490 cm^{-1} . The symmetric stretching vibration between two carbon atoms is responsible for this signal. The absorption bands around 1380 cm^{-1} and 1270 cm^{-1} are assigned to the deformation vibration of a [C-H] bond. This is obvious for the hydrogen atoms bound to aromatic compounds. The band around 1150 cm^{-1} is difficult to associate. On the one hand, it is a possible [Si-O] stretching vibration, which is very typical at this wavenumber.^[225] On the other hand, in this region Si-phenyl-Si stretching vibrations can also occur.^[226] Both interpretations are possible for the analysed powders. The most prominent absorption band of all spectra is at 1150 cm^{-1} and can be assigned to the stretching vibration of the [Si-O] bonds. Around 840 cm^{-1} , an absorption band is located, caused by a deformation vibration of a 1,4-disubstituted [C-H] bond. This is obvious due to the binding of the phenylene ring with the first and the fourth carbon atom to the silicon atoms. The deformation vibration of the [Si-O-Si] bonds was found at 810 cm^{-1} . The band around 770 cm^{-1} is assigned to the framework vibration of the aromatic groups and the bond between a phenylene ring and a silicon atom,^[226] whereas the band at 717 cm^{-1} can only be found in the biphenyl-PMO spectrum and is assigned to the biphenyl-Si bond.^[225] The absorption band at 696 cm^{-1} was found again in all spectra and was caused by a symmetric stretching vibration between [Si-C]. The biphenylene group causes the small band at 560 cm^{-1} . Around 520 cm^{-1} , a very prominent band is shown, belonging to the deformation vibration of the [Si-C] bond.

The results of the IR measurements indicated a successful synthesis of both PMOs. The bands could be completely assigned to all important structural characteristics of these compounds. No band was found indicating a cleavage between the silicon atom and the organic group occurred during calcination. Moreover, the vibrations in the short

wavenumber region provided evidence of intact phenylene and biphenylene groups in the networks. Furthermore, it was conspicuous that the absorption bands of the aromatic rings and the bound hydrogen atoms obtained for the biphenyl-PMOs slightly shifted – by about 15 cm^{-1} – to lower values. By contrast, for the phenyl-PMO the wavenumbers of the bond between the aromatic ring and the silicon were higher.

Regarding the thermal analysis and the infrared spectroscopic measurements, it was obvious that the synthesised PMO particles and coatings were stable under thermal treatment up to $450\text{ }^{\circ}\text{C}$. Hence, the calcination temperature of $350\text{ }^{\circ}\text{C}$ affected the decomposition of the structure-directing agent Pluronic® F-127 but kept an intact [Si–C] bond. In conclusion, the calcination method is sufficient to remove the SDA and obtain the porous PMO network with organic bridges. In the literature, this evidence is also confirmed in other studies, showed by ^{29}Si NMR analysis.^[227,228] As is assumed, a few [Si–C] bonds were cleaved under the calcination treatment. Most remained intact, which was shown by the detection of signals in the IR spectra at 696 cm^{-1} ([Si–C] bond) and 840 cm^{-1} (1,4-disubstituted [C–H] bond).^[229]

However, ESQUIVEL et al. could show that some bonds between the phenylene group and the silicone atom were cleaved when the phenyl-PMO was calcined on air at temperatures above $400\text{ }^{\circ}\text{C}$.^[230] In nitrogen atmosphere fewer cleavages occurred, whereas in humidity the cleavages were promoted. This process leads to a terminal phenylene moiety and silanol group (compare Figure 44). A similar effect of annealing also observed ASEFA and co-workers for methylene-PMOs.^[231]

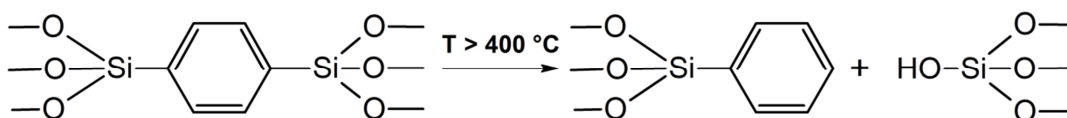


Figure 44: Cleavage of phenylene–Si bond at temperatures above $400\text{ }^{\circ}\text{C}$.^[230]

5.2 Characterisation of PMO Coatings

Periodic mesoporous organosilica coatings are an attractive alternative to the well-characterised and already widely-employed mesoporous silica coatings. PMOs offer wide application areas due to the organic units even without further functionalisation.

The characteristics of the PMO coatings containing phenylene and biphenylene groups are examined by various analytical methods and are discussed in the following.

5.2.1 Spectroscopic, Diffractometric and Microscopic Analysis of PMO Coatings

Infrared Spectrum of Phenyl-PMO Coating

As already discussed above, IR spectroscopy measurements were performed to investigate whether the SDA was successfully removed and the organic units remained unaffected after the calcination step. Possible by-products after calcination could be quinones due to the oxidation of the phenylene rings or the cleavage between silicon and carbon atoms in the oxidising atmosphere of air.

Due to the low film thickness and the deep penetration of IR radiation, only the signals of the substrate could be measured often. Most absorption bands in the fingerprint region could not be detected due to the measurement noise. A successful ATR-IR measurement of a phenyl-PMO coating is shown in Figure 45.

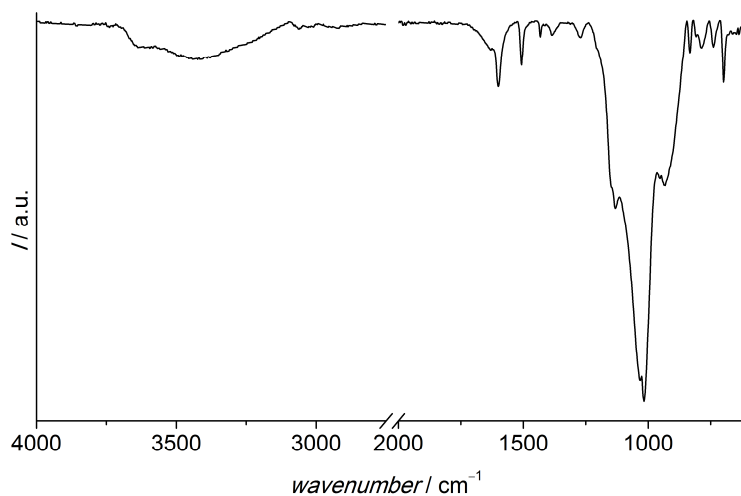


Figure 45: IR spectrum of the unmodified phenyl-PMO coating on silicon wafer measured in ATR-IR mode.

The full data of the spectrum is reported in Table 8. The most intensive bands in the spectrum were the [Si–O] and [Si–O–Si] stretching vibrations between 1250 cm^{-1} and 850 cm^{-1} , which belonged to the [Si–O] network of the PMO. The bending vibrations of the [Si–O–Si] units could be assigned to the IR bands at 806 cm^{-1} . Furthermore, the broad band between 3700 cm^{-1} and 3100 cm^{-1} refers to stretching vibrations of

[Si–OH], silanol groups.^[222] [Si–OH] bending vibrations are only visible as a shoulder and could be found at the wavenumber of 932 cm^{-1} overlapping with the [Si–O] band.^[225]

Table 8: Summary of vibrations for the phenyl-PMO film on silicon wafer and their assignment.

wavenumber / cm^{-1}	assignment	reference
3635	$\nu(\text{Si-OH})$	[222]
3058	$\nu(\text{ring-H})$	[224]
2929	$\nu(\text{C-H})$	[223]
1666	$\nu(\text{ring})$	[224]
1630	asymm. $\nu(\text{ring})$	[224]
1597	$\nu(\text{C=C})$	[224,225]
1510	$\nu(\text{C=C})$	[224,225]
1433	$\nu(\text{C=C})$	[224]
1380	$\delta(\text{C-H})$	[225]
1272	symm. $\delta(\text{C-H})$	[223]
1132	$\nu(\text{Si-O})$	[225]
1017	asymm. $\nu(\text{Si-O})$	[222]
932	$\delta(\text{Si-OH})$	[222,225]
831	$\delta(1,4\text{-substituted C-H})$	[224,225]
806	$\delta(\text{Si-O-Si})$	[222,225]
737	$\delta(\text{ring})$	[224,225]
696	symm. $\nu(\text{Si-C})$	[225]

There are typical bands in an IR spectrum, which can be clearly assigned to aromatic units found in a material. Regarding the IR analysis illustrated in Figure 45, the weak band at 3058 cm^{-1} is a hint for an aryl ring–H stretching vibration that could refer to the phenylene units in the PMO film. Between 2000 cm^{-1} and 1600 cm^{-1} , there are several overtone and combination vibrations, which are typical for aromatic compounds. These bands are located at 1666 cm^{-1} and 1630 cm^{-1} as well as the characteristic [C=C] stretching vibrations at 1597 cm^{-1} , 1510 cm^{-1} and 1433 cm^{-1} .^[224] A bending vibration of the ring is visible at 737 cm^{-1} . A characteristic band for 1,4-substituted phenylene–H groups is found at 831 cm^{-1} . Here, the [C–H] vibrations bend out of the plane and

influence each other. The coupling of the neighbored hydrogen atoms is responsible for these signals.^[224] A relatively prominent band can be found at 696 cm^{-1} . This signal is assigned to a stretching vibration between [Si–C] bonds. Due to the movement of all other molecules at the wavelength in the fingerprint region, the evidence for the [Si–C] coupling is vague. The identification of a [Si–C] bond by IR analysis is not easy and the results are often unconvincing.^[225]

Regarding the IR spectrum of the phenyl-PMO coating shown in Figure 45, it was concluded that the desired coating was successfully prepared. All signals were assigned to phenyl-PMO components. No by-products of the calcination like quinones were found. Typical IR bands for quinones are located at $1690 - 1660\text{ cm}^{-1}$ for [C=O] and at 1600 cm^{-1} for [C=C].^[223] As was difficult to prove that the bond between Si and C was not affected after the calcination, the signal monitored at 700 cm^{-1} could only be grade as a hint for its stability.

It was not possible to measure an IR spectrum of the biphenyl-PMO coatings. The intensities of the measured spectra were very low and difficult to analyse. Therefore, only the IR spectrum of the biphenyl-PMO powder is illustrated in the previous chapter.

Structural Analysis of PMO Coatings by X-Ray Diffraction

In addition to the chemical composition, the structural arrangement of the PMO coatings was investigated by X-ray diffraction (XRD). The periodic and repetitive arrangement of the pores in the nanometer range in the PMO coatings should lead to reflections in XRD pattern. The uncoated glass slides did not show any X-ray reflections due to the absence of any periodic arrangement in the glass. The phenyl-PMO film exhibits two reflections at 2θ values of 0.8° and 1.5° (Figure 46 left). The reason for the reflections is the electron density contrast between the empty cavities in the organosilica material after removing the organic structure-directing agent.^[232–234]

These reflections are difficult to assign to certain pore geometry like hexagonal or cubic. It is possible that the mesoporous films have a comparable structure like the mesoporous bulk material LMU-1.^[235] The most intensive reflection appears at $0.8^\circ 2\theta$, corresponding to a d -spacing of 11 nm. Such pore widths are supported by the TEM results shown in Figure 49.

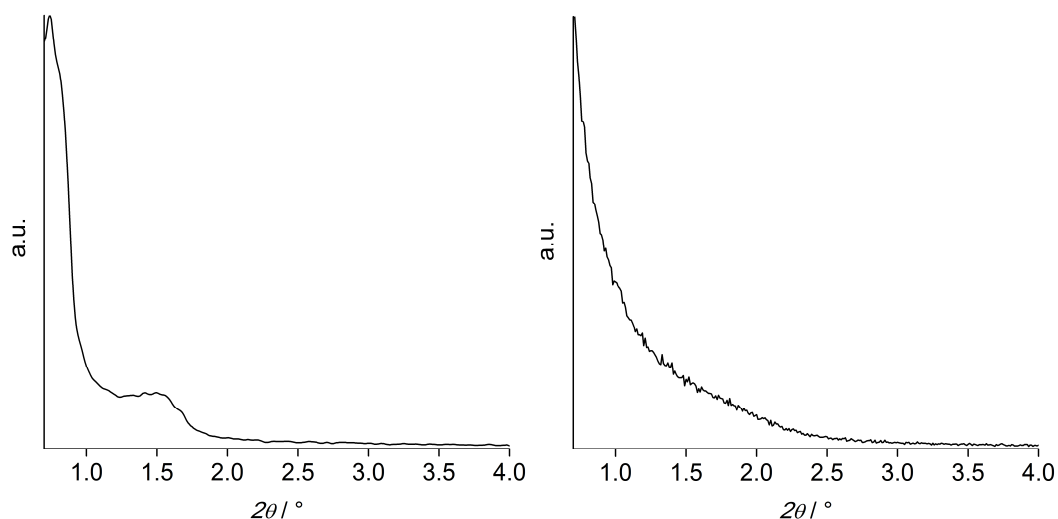


Figure 46: XRD pattern of **left)** phenyl-PMO and **right)** biphenyl-PMO film on a glass slide.

Contrary to the phenyl-PMO film, the biphenyl-PMO showed no reflections at all (Figure 46 right). One reason can be that there are no pores at all, although this contradicts the sorption and TEM measurements shown below. The missing reflections in the XRD pattern can be explained by the missing periodical structure. The disordered pore structure can have various reasons. On the one hand, it is possible that the solvent evaporated too quickly and the structure could not be formed so quickly. On the other hand, the rigidity of the biphenylene unit is high, which can lead to a disordered porous structure. The biphenylene unit with two aromatic rings is longer than the phenylene unit with one aromatic ring. The former is flexible along the longitudinal direction, e.g. rotations or changes of the bond angle between the aromatic rings can result.

Structural Investigations of PMOs by Scanning and Transmission Electron Microscopy

Scanning and transmission electron microscopy pictures were taken to characterise the surface and the pore structure of both PMOs films. The SEM pictures were taken without sputtering of the PMOs surface to avoid losing structural information. Admittedly, due to the high amount of organic material, charging effects in the samples occurred and led to a poor resolution at high magnification. On the one hand, the TEM pictures were taken in a cross-section manner to examine the overall porosity of the films over the whole film thickness. On the other hand, the films were scratched from

the substrate to also observe the overall porosity and periodicity of the pores in the coatings.

SEM and EDX Characterisation of Phenyl-PMO and Biphenyl-PMO Coatings

The SEM pictures of the phenyl-PMO coatings showed a smooth film on the macroscopic scale without any cracks and inhomogeneities (compare Figure 47 left). On the microscopic scale, the coating showed an open-porous outer surface of the PMO film (Figure 47 right). Pore openings were up to 10 nm large and were aligned parallel to each other, forming a pattern. The SEM pictures confirmed the existence of an open-porous phenyl-PMO film.

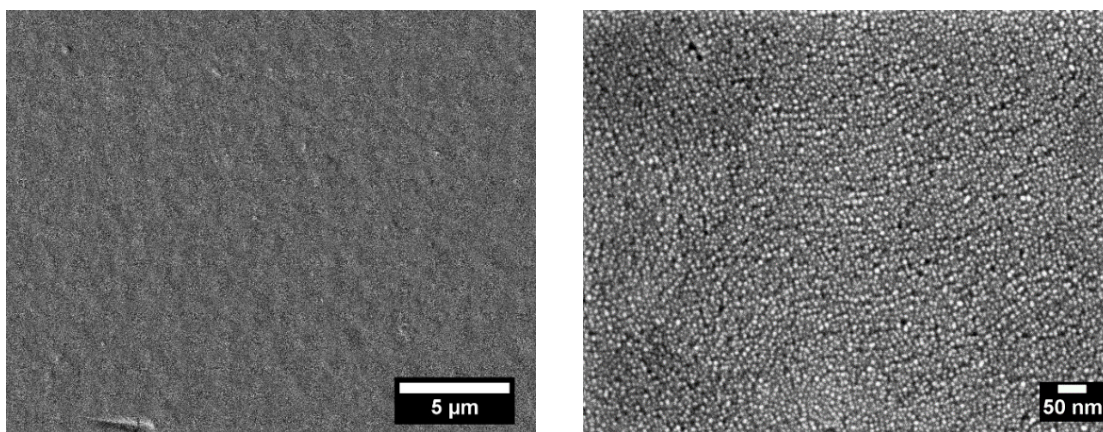


Figure 47: Scanning electron microscope images showing the surface of a native phenyl-PMO film. The right image reveals the open-porous structure of this coating.

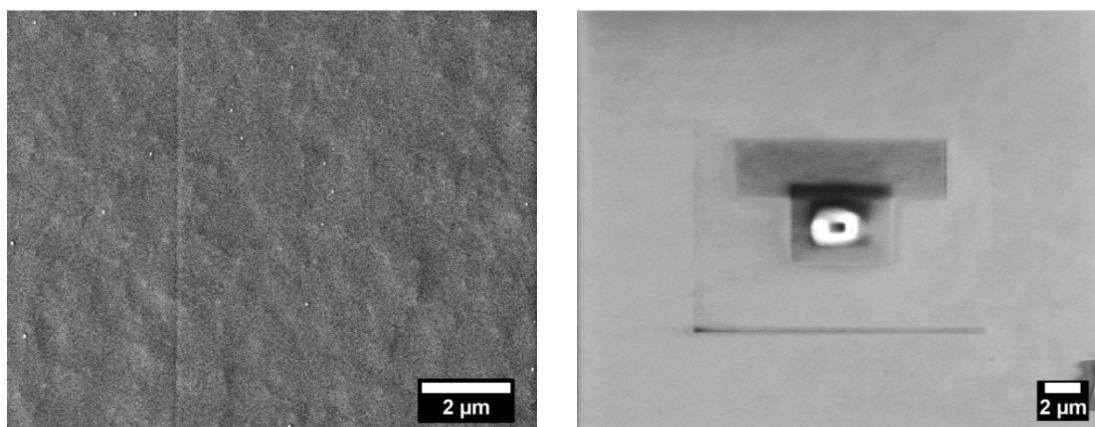


Figure 48: left: Scanning electron microscope image of the outer surface of a native biphenyl-PMO film. **right:** Strong charging effects of the biphenyl-PMO sample while SEM measurements. It was not possible to obtain high magnification pictures of the biphenyl-PMO coatings.

It was only possible to take a SEM image of the biphenyl-PMO in a low magnification (Figure 48 left) due to the high charging effects during SEM measurements (Figure 48 right). In this low magnification, a smooth and crack-free PMO film is visible, albeit without any evidence of pores.

TEM and EDX Characterisation of Phenyl-PMO and Biphenyl-PMO Coatings

TEM measurements were performed for better characterisation of the PMO coatings. They displayed the inner porous system of the phenyl-PMO and proved the porosity of the biphenyl-PMO.

The TEM pictures in a cross-section manner – recorded for the phenyl-PMO coating – clearly displayed the well-structured pore system (see Figure 49). These results confirmed the XRD measurements of the phenyl-PMO film shown in the section above. The XRD pattern (Figure 46 left) indicated an ordered porous system with a repeating distance of 11 nm. This could be validated by the TEM analysis. The ellipsometric measurements revealed a film thickness of about 360 nm, which was confirmed by the TEM measurements (Figure 49, left). The films have a regular porous structure with pore widths of about 9 nm and pores that are oriented nearly perpendicular to the substrate surface (Figure 49, right). However, these observations can only be made in inner areas of the coating. In the area directly connected to the substrate and at the top part of the coating, different structures can be found in the cross-section view. It is possible that these parallel-oriented pore channels proceed in other directions; for instance, parallel to the surface. Indeed, this could not be examined in a cross section as the pores vanished backwards in the image plane. Additionally, it is also possible that these areas at the top and bottom of the coating have an unstructured character, showing no aligned pore channels. Regarding the SEM and TEM examinations, it was concluded that the pores were open and accessible from the outer surface of the coatings. This is favourable for the loading and release of active agents like drugs or growth factors. Admittedly, the pores also showed a bottle-neck effect, which meant that the pore interior was larger compared to the pore exit. As shown in Figure 49 on the right, the external 50 nm of the coating had a disordered structure with narrow pore outcomes. This characteristic can be a disadvantage for loading the material with substances. Due to the narrow pore openings, a block can occur during the loading process. Hence, the

pore interior is only poorly available for substances since the drug molecules block the pores at the narrow pore neck. The exact values for the sizes of the pore necks and pore bodies were determined by krypton sorption measurements (section 5.2.2).

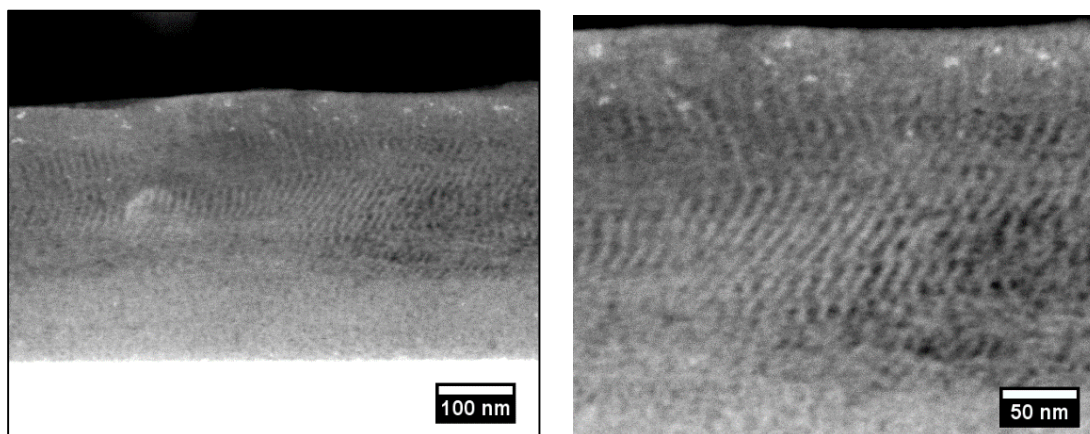


Figure 49: Transmission electron microscopy images in a cross section of a phenyl-PMO coating showing periodically-oriented mesopores with a size of approximately 9 nm. The pores were oriented perpendicularly to the substrate with pores open to the coating surface.

By means of EDX analysis of the TEM measurements, a homogeneous element distribution of carbon, oxygen and silicon in the phenyl-PMO layer could be detected. According to Figure 50, the red top layer is the epoxy resin for embedding the PMO sample, followed by a green layer in the middle comprising the phenyl-PMO with small red speckles of the carbon in the layer. The white layer below is the glass substrate.

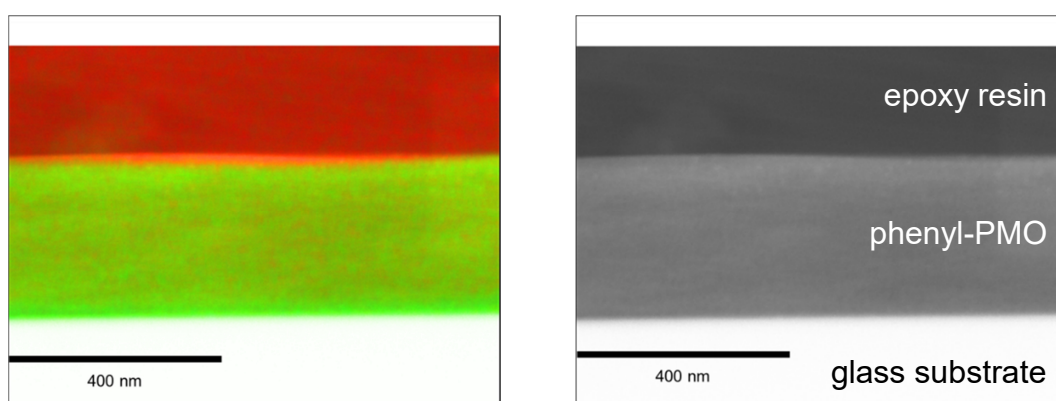


Figure 50: Coloured picture of the element distribution in the resin embedded phenyl-PMO coating on a glass substrate. The red layer was the resin, the green layer was phenyl-PMO and the white one was the epoxy resin.

Figure 51 supports determining the homogeneously-distributed elements such as carbon, oxygen and silicon in the phenyl-PMO coatings. Through a STEM dark field analysis, it was possible to visualise the element distributions of individual elements using Cu K_{α} radiation. The left picture of Figure 51 shows the carbon distribution in the examined area, the middle one shows the oxygen distribution and the right one the silicon distribution, all elementary compounds of the phenyl-PMO coatings. It shows that all three elements are well spread in the middle layer in all three images.

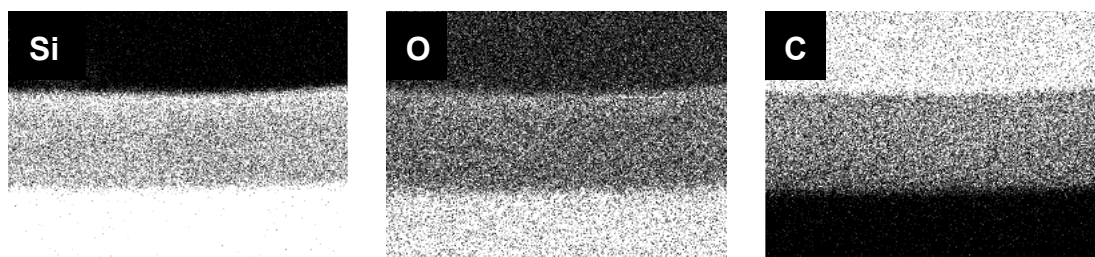


Figure 51: STEM dark field of the analysed sample area showing the individual element distribution of carbon, oxygen and silicon. Moreover, in these pictures the homogeneous distribution of the elements in the phenyl-PMO layer could be confirmed.

The EDX spectrum (attached in supporting information) of the investigated sample area approved the TEM pictures. The peaks of the elements silicon, oxygen and carbon had the highest intensity, indicating that these elements were the most common in the sample. Further determined elements were calcium, potassium, sodium, manganese, phosphor and chlorine, which are more a hint for a contamination during the sample preparation like embedding and polishing prior to the TEM measurement.

In order to determine the overall porosity of the PMO coatings, the films were scratched off. The scratched-off phenyl-PMO film show several hundred nanometer large domains of linearly-ordered pores (Figure 52 left). The domains are 50 to 100 nm large and indicate different orientations of the pores. Due to the scraped-off samples, the porosity of the whole PMO coating was approved, as pores could be found throughout the whole sample. Furthermore, a periodicity of the aligned phenylene-siloxane units can be observed (Figure 52 right) at certain spots. The distance between the singular lines is 0.24 nm, which corresponds to the diameter of a benzene ring. Nonetheless, the coatings showed more of an amorphous character, which was no disadvantage for the intended application.

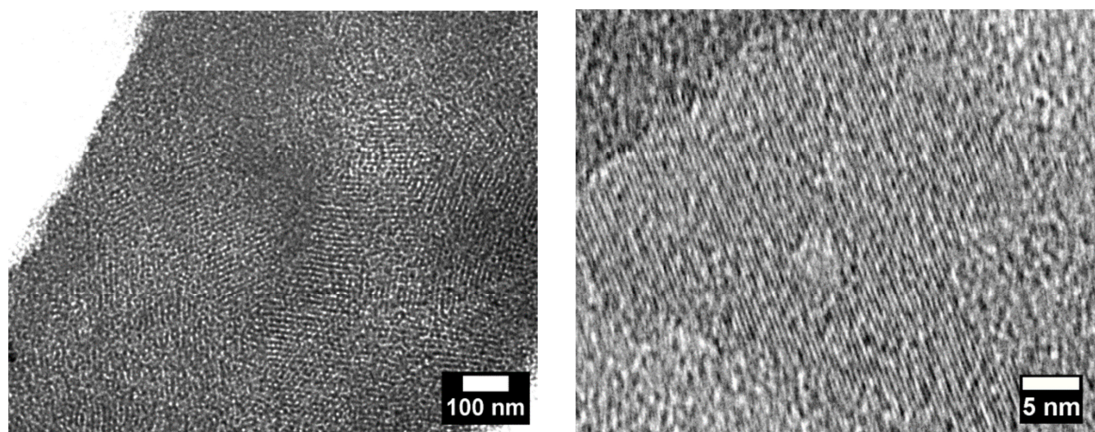


Figure 52: Transmission electron microscopy images of a scratched-off phenyl-PMO film that (left) indicated the porous domains of the coating. Taking a closer look (right), the straight aligned phenylene-siloxane units were also visible.

The TEM measurements of the biphenyl-PMO layer were very important, as the SEM analysis did not give a hint at the porosity of the coatings due to the high charging effects. The transmission electron microscope images of the scratched-off biphenyl-PMO coating (Figure 53) indicate that these coatings are porous, with a pore size of nearly 9 nm. The light grey areas in the picture can be assigned to the pores in the coating, while the darker areas are the PMO material itself. The darker the area in the picture (Figure 53 left), the thicker the sample in this area and the more layers that lie above each other. However, it was evident that the biphenyl-PMO coatings were denser compared to the phenyl-PMO coatings.

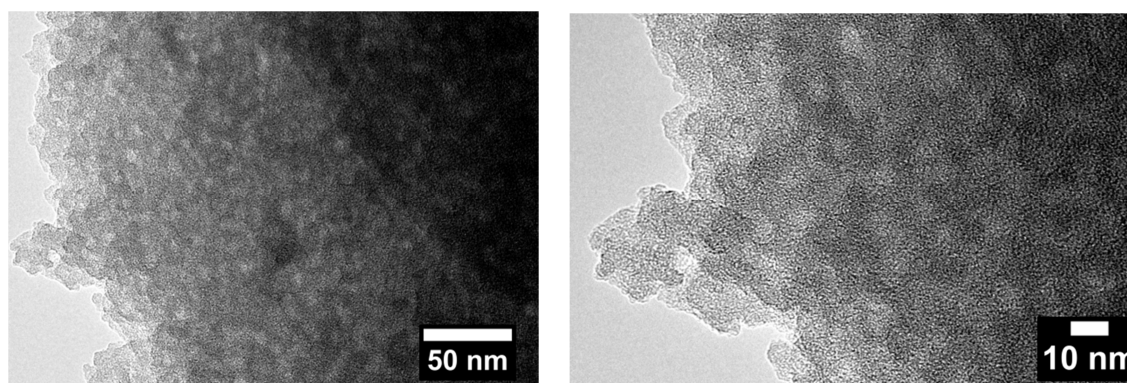


Figure 53: TEM images of a scratched-off biphenyl-PMO film showing the porous structure of the material.

The TEM analysis of the biphenyl-PMO material clearly showed that the samples had no structured pore system. The pores were irregularly distributed in the biphenyl-PMO coating. This also confirmed the X-ray diffraction pattern (Figure 46, right) of the PMO coating with no signals indicating a structured material. The pores had a diameter of 7 – 9 nm. From the various pore diameters and the absent structure of the porous system, it can be concluded that the larger biphenylene unit is very flexible. This led to a folding of the organic units in the structure and thus to the irregular and unstructured pore system. Furthermore, it was possible that the solvent evaporated very quickly during the dip-coating process and subsequent drying, which could hinder the forming of a more regular porous structure of the coatings. Nevertheless, the TEM analysis approved that both PMO coatings were porous, although the phenyl-PMO coating was more structured, containing more pores inside.

5.2.2 Krypton Sorption Measurements of the PMOs Coatings

Krypton sorption measurements were performed to determine the values for the specific surface areas, the pore volumes and the pore widths of the PMOs thin films. Both Kr isotherms of PMO coatings are of type IV with a hysteresis of type H2.^[203] This course is typical for capillary condensation in mesopores, which is valid for both PMO coatings. The course of the adsorption as well as the desorption branch of the isotherms reveal that these coatings have bottle-neck pores with a slim pore neck and a larger pore volume inside the film, showing a hysteresis type H2. This thesis is confirmed by the TEM images (Figure 49), depicting that the ca. 9 nm large pore interior merges in narrow pore necks at the film surface (ca. 50 nm of the film near the top of the film surface).

Native phenyl-PMO coatings had a specific surface area of about $460 \text{ cm}^2 \cdot \text{cm}^{-2}$ and a pore volume of $2.80 \cdot 10^{-5} \text{ cm}^3 \cdot \text{cm}^{-2}$, referring to the substrate surface (Figure 54). These values mean that the inner surface of the films is nearly 500 times larger than the outer surface, with 75% of free space in the coating. The specific surface area of the biphenyl-PMO films was $160 \text{ cm}^2 \cdot \text{cm}^{-2}$ and the pore volume was $1.30 \cdot 10^{-5} \text{ cm}^3 \cdot \text{cm}^{-2}$. In the case of biphenyl-PMO, the specific surface is 160 times larger than the outer surface and 60% of the coating is free space.

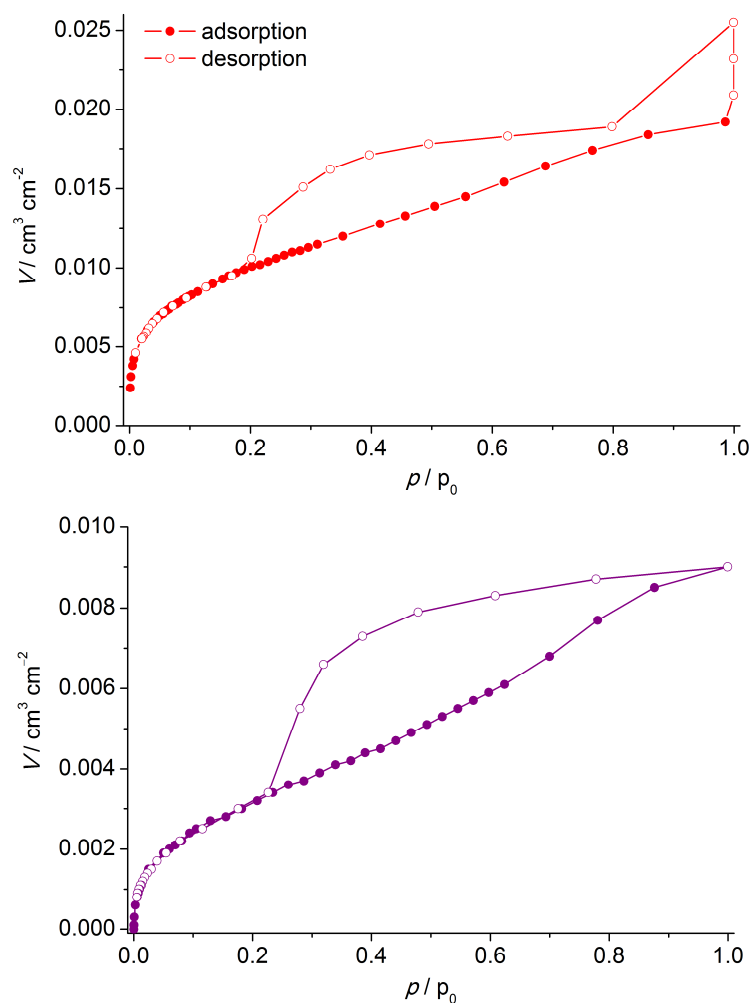


Figure 54: Krypton sorption measurement of **top**) phenyl-PMO and **bottom**) biphenyl-PMO showing an isotherm of type IV with a hysteresis of type H2.

In Figure 54 (left), a specificity of Kr isotherms is visible. At high pressures ($p/p_0 > 0.9$), the software is unable to precisely determine the pressure changes leading to an accumulation of the measuring points at $p/p_0 = 1.0$. For a better overview, the points at $p/p_0 > 0.9$ are removed in further isotherms.

Although the biphenyl-PMO coatings were only slightly thinner compared to the phenyl-PMO coatings, their specific surface as well as the pore volume was more than twice as low. These results fit well to the prior ones obtained by X-Ray diffraction and TEM. The porous structure of the biphenyl-PMOs is poorly developed due to the more flexible organic units. The flexibility of the biphenylene unit leads to a disordered porous material with a lower specific surface area and worse-accessible pores compared

to the phenyl-PMO. The main reason for this is that the biphenylene unit is longer and free in rotation and folding along the longitudinal axis.

In Figure 55, the comparison of three isotherms is illustrated depending on the film thickness of the phenyl-PMO. By means of the Krypton gas uptake and the isothermal course, it is clearly visible that the thinner the film thicknesses, the lower the specific surface areas of the coatings and the lower the pore volume. The hysteresis is also shrinking with decreasing film thicknesses. The isotherm of the 330 nm thick phenyl-PMO coating shows a typical H2 hysteresis for cylindrical and spherical mesopores. By contrast, the 142 nm thick phenyl-PMO coating shows a hysteresis with a course of a H4 slope, which is more typical for micro- and mesopores. The possible reason is the less-developed micelles during synthesis. When the coating is thin and the solvent evaporates very quickly, the micelles of Pluronic® F-127 cannot form a stable system. The pores are smaller and the material possesses low specific surface areas.

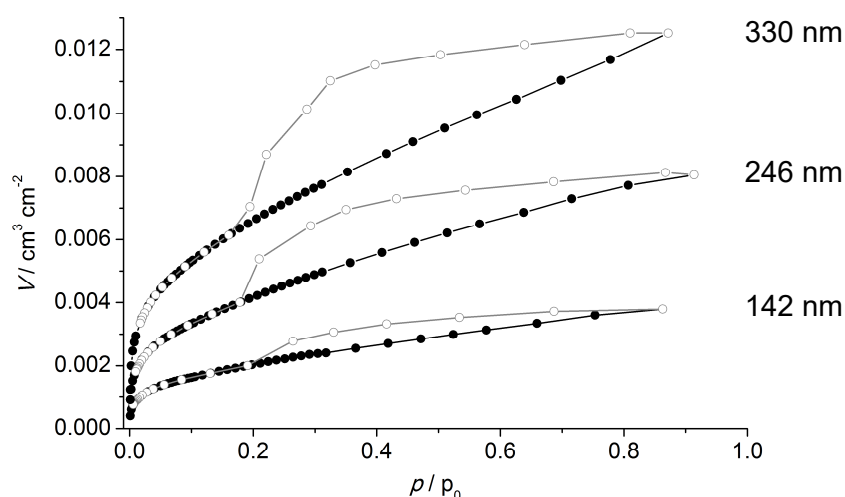


Figure 55: Krypton sorption measurement of phenyl-PMO coatings with different film thicknesses.

In Table 9, the values for the specific surface areas and the pore volumes determined from the isotherms in Figure 55 are listed. From these values, it is obvious that by doubling the film thickness the BET surfaces and the pore volumes are also nearly doubled. This confirms once again the choice of the thicker coatings for further applications for drug storage together with the fact that these thicker coatings are crack-free and stable.

5. Results and Discussion I

Table 9: Comparison of the values of the specific surface areas and the pore volumes of phenyl-PMO coatings depending on film thickness.

$t_{\text{PMO}} / \text{nm}$	$S_{\text{BET}} / \text{cm}^2 \cdot \text{cm}^{-2}$	pore volume / $\text{cm}^3 \cdot \text{cm}^{-2}$
142	129	$0.73 \cdot 10^{-5}$
246	266	$1.54 \cdot 10^{-5}$
330	415	$2.36 \cdot 10^{-5}$

The pore width distribution determined by Krypton measurements is displayed in Figure 56 (left), indicating pore widths of about 1.9 nm. However, from the TEM measurements (Figure 49), it is known that the pore sizes are about 9 – 10 nm. The Krypton sorption method can only resolve pore widths until 9 nm due to test conditions.^[205,236] Thus, it was not possible to determine the larger pores by Kr sorption measurements. This was valid for the most pore width distributions determined by Kr measurements leading to less meaningful curves. Figure 56 (right) shows a pore width distribution evaluated by Argon measurement. It reveals two maxima in the distribution at about 2.8 nm and 6.2 nm, correlating better with the results of TEM measurements.

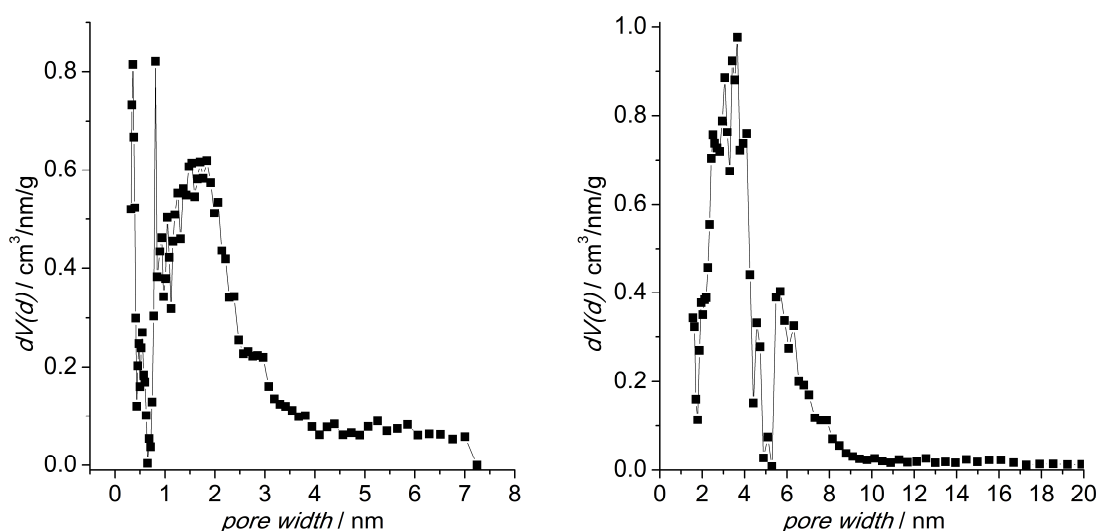


Figure 56: Pore width distribution of phenyl-PMO coating (**left**) evaluated by Kr sorption, (**right**) analysed by argon.

It is known from SBA-15 and KIT-6 materials that the large rod-like pores are interconnected by complementary small pores with about 2 nm in diameter. Such a pore

geometry is also conceivable for the PMO coatings, as their synthesis conditions are similar. This presumption is supported by the sorption measurements. The small pores are responsible for the steep slope at the beginning of the isotherms. The pore width distribution confirms this thesis.^[237–239]

Overall, materials with the present pore size have a high suitability for applications in drug loading and release systems. Given that most drugs are 2 – 4 nm in diameter, it is also favourable to have pores in the same range so that the drugs can enter the porous system. Furthermore, a high inner volume and a good accessible porous system are the perfect conditions for the loading of high amount of substances. However, the pores should also be sufficiently small to store the drugs, as larger pores lead to a very fast release of the gas molecules. Thus, pore sizes of about 8 nm – as found in the PMO coatings – are optimal for drug loading and release applications.

5.2.3 Ellipsometric Measurements

Ellipsometry was used as another characterisation method to determine the coating thickness of the PMO layers. This analysis could be performed very easily and quickly on the coated substrates without further preparation of the samples. Therefore, a Sentech ellipsometer and the software SpectraRay 3 (section 4.2) were used to calculate the film thickness by suitable models. This method was applied because the thickness determination by TEM analysis required very strong effort and was time-consuming. Nevertheless, both characterisation methods gave an equal value of the film thickness.

Due to the edge effects from dip-coating, only the middle of the sample was measured by ellipsometry to determine the film thickness. When the substrate was pulled out from the dip-coating solution, the sol drained off, causing a thicker film on the edges of the substrate due to the draining regime, shown as the yellow and violet parts of the coating in Figure 57. Only the film in the middle had a homogeneous thickness and could be considered for the film thickness determination. Consequently, the inhomogeneous parts of the coatings were cut-off and only the middle was used for further investigations.

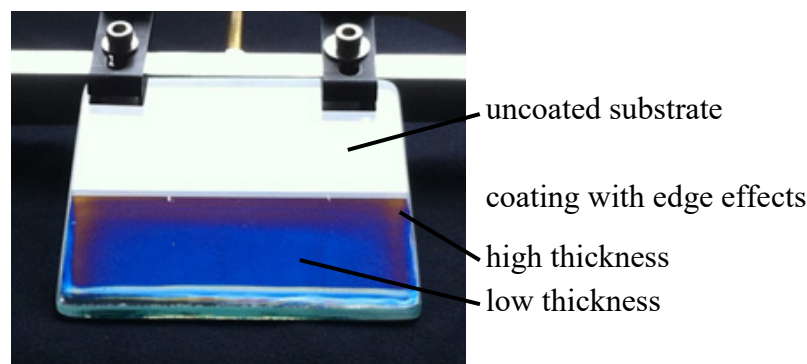


Figure 57: Edge effects caused by dip-coating.^[240] The edges that appear yellow and violet are caused by thicker coating than in the middle of the sample. The film thickness measured by ellipsometry was investigated in the middle of the coated substrates, where the thickness is homogeneous.

The thickness of the coatings could be adjusted by either the viscosity of the dip-coating solution or the withdrawal speed. In Table 10, such a correlation of increasing film thicknesses with an increasing withdrawal speed is gathered. This phenomenon can be explained by the longer time for which the draining solution is in contact with the dipping solution, as explained in section 2.6 Dip-Coating.

Table 10: Ellipsometric measured film thicknesses and refractive indexes of phenyl-PMO samples as-synthesised and calcined, depending on the withdrawal speed.

$v_{up} / \text{cm} \cdot \text{s}^{-1}$	film thickness t_{as} / nm	refractive index n_{as}	film thickness t_{ca} / nm	refractive index n_{ca}
0.01	340	1.669	142	1.366
0.05	525	1.579	246	1.374
0.10	667	1.542	330	1.357

In Table 10, the results of ellipsometric measurements are summarised, showing the different film thicknesses and refractive indexes depending on the withdrawal speed. The coating thickness and refractive index are displayed for as-synthesised films as well as after the calcination step when the structure-directing agent Pluronic® F127 is removed. During the calcination, the PMO films shrunk and the film thickness decreased nearly twofold. The SDA supported the structure of the coatings when it was still present in the pores. After burning the SDA out, the porous system in the coatings remained, but the material became more hard and brittle and shrunk to a certain amount. The shrinkage of sol-gel derived coatings caused by thermal treatment is a commonly-

observed phenomenon.^[241] The calcination step is performed not only to remove the SDA but also to achieve further condensation of the organosilica framework, thus making it more resistant to degradation. A consequence is an altering of the mesopores and a distortion of the porous system in a certain way.

Due to the calcination step, not only the thicknesses change but also the refractive index. The refractive indexes of the as-synthesised samples were higher compared to those after calcination. The as-synthesised coatings had a refractive index above 1.58, whereas the refractive index of the calcined samples declined to 1.36. Thus, the refractive index of the as-synthesised samples has a value comparable to the dense SiO₂ layer ($n = 1.52$) used in the fitting model. The lower the refractive index, the more porous the material (refractive index of air $n = 1.00$). The samples with higher refractive indices disclosed lower BET surfaces in sorption measurements and vice versa. Samples with lower refractive indices had higher BET surfaces. Certainly, there is not a direct correlation between the determined BET surfaces and the calculated refractive indexes, although a tendency can be recognised.

Table 11 compares the thicknesses and refractive indexes of the as-synthesised and calcined phenyl-PMO as well as biphenyl-PMO coatings dipped with a withdrawal speed of $0.1 \text{ cm} \cdot \text{s}^{-1}$.

Table 11: Ellipsometric measured film thickness and refractive index of PMO coatings as-synthesised and calcined at a withdrawal speed of $0.1 \text{ cm} \cdot \text{s}^{-1}$.

PMO	film thickness t_{as} / nm	refractive index n_{as}	film thickness t_{ca} / nm	refractive index n_{ca}
phenyl	643	1.515	387	1.351
biphenyl	339	1.551	270	1.325

At the same withdrawal speed, the phenyl-PMO coating is thicker than the biphenyl-PMO coating due to the lower viscosity of the dipping solution. Since the biphenyl-PMO dipping solution was only stable with a higher amount of the solvent ethanol, it was obvious that the coating solution was less viscous than the phenyl-PMO dipping solution. When the same amount of ethanol as in the phenyl-PMO dip-coating solution was applied in the biphenyl-PMO solution, after a short time the sol became opaque and particles began to precipitate. This is the reason why a higher amount of ethanol was

used for the biphenyl-PMO sol-gel coating. The shrinkage effect after calcination remained for both coatings. Calcined biphenyl-PMO films were nearly 40% thinner than the as-synthesised ones. The refractive index of the calcined biphenyl-PMO samples had nearly the same value as those of calcined phenyl-PMO samples.

Ellipsometry is a quick and reliable method to evaluate the film thickness and refractive index of PMOs coatings. It gives first hints on the porosity considering the refractive index and thus the quality of the coatings.

5.2.4 Stiffness of PMO Coatings

The nanoindenter measurements were performed by DANIEL GOTTSCHALK from Institute of Continuum Mechanics, Leibniz Universität Hannover. The purpose was to estimate the comparison between the Young's modulus (E) of mesoporous silica coatings and PMO coatings regarding the application of these on flexible substrates and implants. The results are displayed in Figure 58.

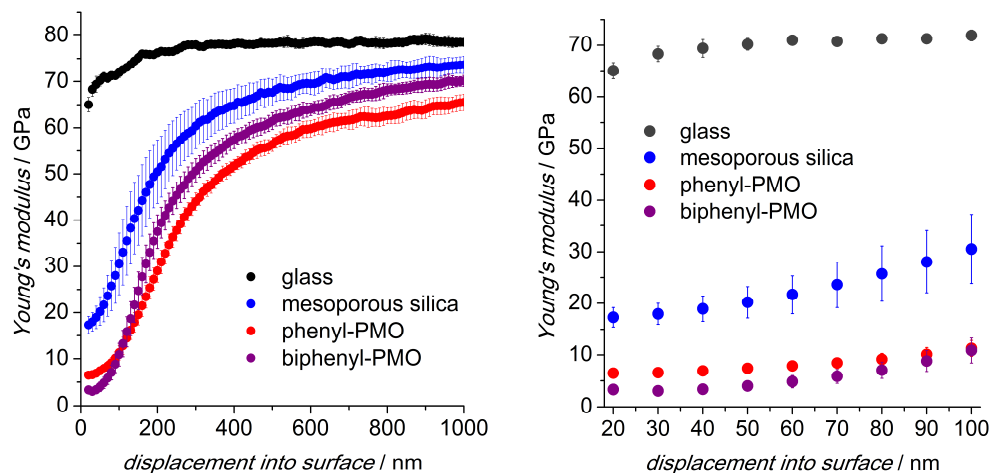


Figure 58: Nanoindenter measurements for determination of the Young's modulus (E) of a glass slide (GS), a mesoporous silica layer (MPS) and a PMO film (PMO). **right:** Magnification of the region between 10 – 100 nm to clearly define the Young's modulus of the coatings. The elasticity of PMOs coatings is higher compared to those of the mesoporous silica film.

The recorded curves can be divided into three parts. In the first part of the curves below 10 nm, the values for E are not accurate because in this region the contact between the nanoindenter tip and the coating surface is not well defined. Possible surface inhomogeneities and dirt have to be overcome on these first nanometers. The second

part between 10 – 60 nm can be considered as constant and thus defined as the Young's modulus of the coatings. The third part is the rest of the curve above 60 nm. Here, mixed properties of the substrate surface and coatings are measured.^[242] The more that the nanoindenter penetrates the samples, the closer the Young's modulus becomes to the value of pure glass slides, which have been used as a reference.

Looking at Figure 58 (right), it can be assumed that both PMOs coatings clearly have a lower Young's modulus than the silica coating. The mesoporous silica film has a Young's modulus of 18 GPa, whereas the phenyl-PMO coating has 6.6 GPa and the biphenyl-PMO has 3.3 GPa. The numbers for the Young's modulus of the measured materials are in the same order as found in the literature.^[243,244] The Young's modulus of mesoporous silica is – due to the porous network – lower than that of the glass slide. Nearly 50% of the coating is free space in contrast to the compact glass. Since the PMO coatings have a similar porous system as the mesoporous silica films and the first possess organic moieties in their structure, their Young's modulus is lower than that of silica. The phenylene and biphenylene groups – replacing a part of the siloxane bridges – make the material more flexible and softer compared to pure silica networks. Regarding these results, one can imagine that PMO coatings are favourable materials for applications on flexible materials as well as flexible implants like coronary stents or cochlea implants. However, in fact they are too brittle for applications on flexible devices. At high mechanical stresses – like they are applied on flexible implants – the PMO coatings would peel off. For applications on the surface of flexible devices, a Young's modulus around 0.05 GPa is needed.^[245]

5.2.5 Sulfonation of Phenyl-PMO Coatings

For an enhanced loading with a negatively-charged drug – for example, ciprofloxacin – the phenyl-PMO coatings were functionalised with positively-charged sulfonate groups.^[200] In order to determine the amount of these sulfonate groups, the modified films were stained with methylene blue and then examined in the UV-Vis spectrometer. The value for the bound sulfonate groups could be determined precisely based on the previously-performed calibration. The methylene blue molecules also attached to the non-polar phenylene groups in the phenyl-PMO. Hence, the number of sulfonate groups bound to the phenyl-PMO was determined by the difference of the adsorbed methylene

blue molecules on both materials. The assay gave a value of $1.032 \cdot 10^{16} \pm 1.0133 \cdot 10^{14}$ molecules per cm^2 of methylene blue adsorbed to the phenyl-PMO and $2.224 \cdot 10^{16} \pm 1.129 \cdot 10^{13}$ molecules per cm^2 adsorbed to the sulfonated phenyl-PMO. The difference is $1.192 \cdot 10^{16}$ molecules per cm^2 , which can be assigned to the sulfonate groups. The blue colour of the dye is very intensive. Hence, the different concentrations can be easily differentiated, as shown in Figure 59.

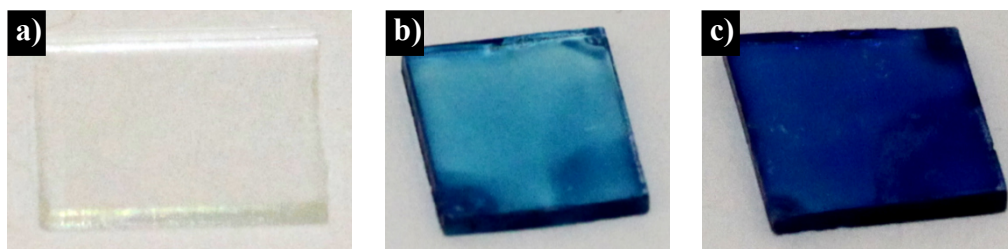


Figure 59: a) Native and methylene blue stained b) phenyl-PMO and c) sulfonated phenyl-PMO coatings.

Krypton sorption analysis confirmed the methylene blue results, as shown in Figure 60. The specific surface area of the sulfonated phenyl-PMO was lower with $380 \text{ cm}^2 \cdot \text{cm}^{-2}$ ($S_{\text{phenyl-PMO}} = 460 \text{ cm}^2 \cdot \text{cm}^{-2}$) as well as the pore volume with $2.46 \cdot 10^{-5} \text{ cm}^3 \cdot \text{cm}^{-2}$ ($PV_{\text{phenyl-PMO}} = 2.80 \cdot 10^{-5} \text{ cm}^3 \cdot \text{cm}^{-2}$). This indicates that the modification with sulfonic acid groups led to decreased specific surface area and pore volume of phenyl-PMO coatings.

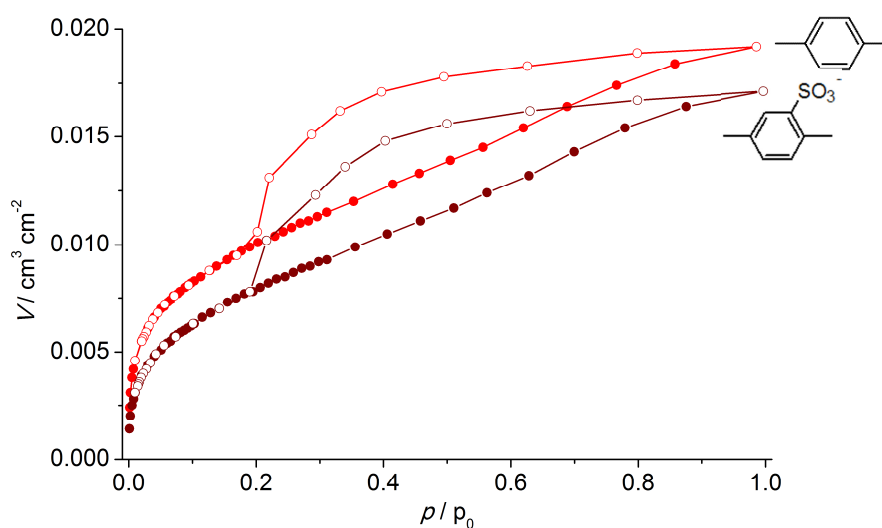


Figure 60: Krypton sorption measurements of unmodified and sulfonated phenyl-PMO displaying the lower specific surface area and lower pore volume of the sulfonated phenyl-PMO coatings.

5.2.6 Wettability of PMO Coatings

Water contact angle measurements were performed to estimate the wettability of the PMO films. The static water contact angle of PMOs coatings was compared to mesoporous silica films and cleaned glass slides (Figure 61). Regarding the rather hydrophilic MPS films (5°),^[7] phenyl-PMO (25°) and biphenyl-PMO (43°) coatings were clearly more hydrophobic. The uncoated glass slides showed a typical contact angle of 21° .

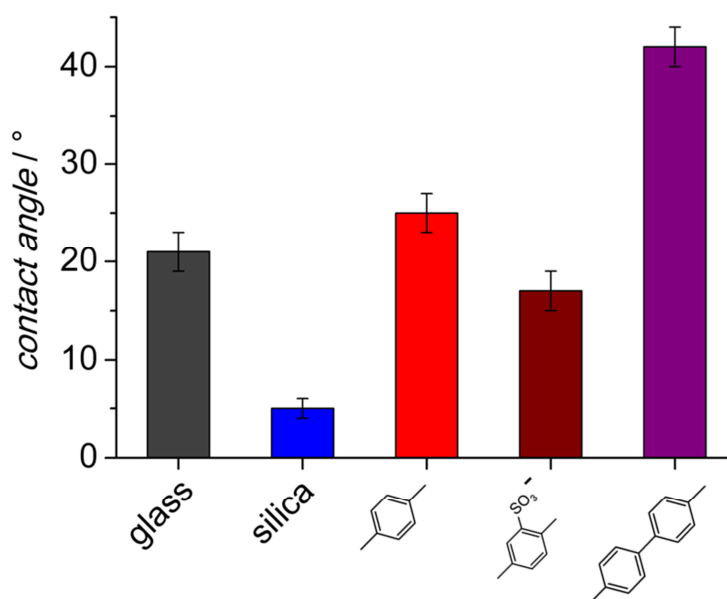


Figure 61: Water contact angle measurements of glass slides, mesoporous silica, phenyl-PMO, sulfonated phenyl-PMO and biphenyl-PMO coatings. PMO coatings revealed higher hydrophobicity compared to the mesoporous silica coatings.

The non-polar organic groups in the periodic mesoporous organosilica caused an increase of the water contact angle in a range of 20° to 25° . The low contact angle of the MPS coatings is induced by silanol groups and the porous system with a high surface area.^[246] It was shown that the surface topology – e.g. nanostructures or nanopores – affects the wettability of surfaces.^[247] Regarding PMO coatings, two effects compete with each other: the open pores at the surface of the coatings and the hydrophobic organic groups in the structure. The open porosity causes high wettability, whereas the organic groups reduce it again. However, the higher contact angle of the biphenyl-PMO film was not only influenced by the more hydrophobic biphenylene group; moreover, it

also had a less porous surface. The results of measured water contact angles shown above were contrary to some other investigations on the wettability of PMO films.^[248–250] Most PMOs coatings have a contact angle above 50°, with pores lying parallel to the substrate surface. These films have a low number of open pores on the outer film surface. This has a crucial effect on the wettability, given that only almost chemical properties influence the wettability of the PMO coating surfaces.

The sulfonate modification of the phenyl-PMO coatings was proven by a reduced contact angle, caused by the polar sulfonic acid groups. Due to this modification, the water contact angle decreased by 8° to a value of 17°. As the sulfonate group bind to the non-polar phenylene ring, its hydrophobic effect is lowered.

Due to the organic moieties in the silanol network, PMOs act more hydrophobically and thus are better suitable for the delivery of hydrophobic substances. Furthermore, the hydrophobic character of PMOs makes their porous structure more resistant against cell culture conditions, as shown in section 5.2.7. For better characterisation of the wettability inside of the porous PMO network, some water sorption measurements should be performed to confirm the results of the outer film surface.

5.2.7 Stability of PMOs under Cell Culture Conditions

The stability tests were carried out by immersing the PMO-coated glass substrates in cell culture medium where 10% of FSC and 1% of penicillin were added to simulate the cell culture test conditions. In order to indicate whether the coatings were stable under simulated body conditions, the films were investigated microscopy and XRD before and after immersion in the cell culture medium at 37 °C. Before storage under cell culture conditions (Figure 62 a), it is obvious that the native coating is homogeneous and even. After storage of the phenyl-PMO coatings in cell culture medium for 14 days (Figure 62 b), the coating looked corroded with slight peeling-off effects at the edges. Furthermore, the film thicknesses were inhomogeneous assigned by the different reflecting colours. This indicates that the phenyl-PMO coating is damaged during the storage conditions but remains almost completely on the glass slides.

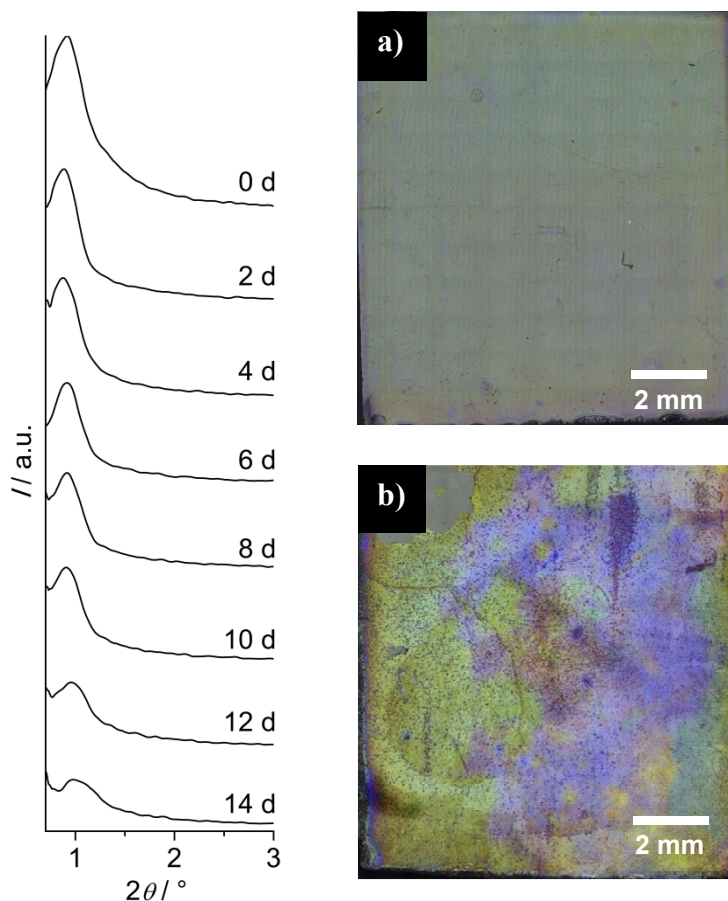


Figure 62: **Left:** X-ray diffraction pattern of phenyl-PMO layers on glass stored in cell culture medium with 10% of FSC and 1% penicillin. The structural stability of the coatings could be observed over 14 days. **Right:** Microscopy images of phenyl-PMO-coated glass slide before (a) and after (b) storage for 14 days under cell culture conditions. Looking at the top picture, it is obvious that the coating is corroded and starts to peel off from the glass slide. Furthermore, it shows different film thicknesses, which can be assigned to the different reflection colours.

Measuring the XRD pattern every 24 h, some structural rearrangement of the coatings could be observed. The intensity of the reflection at $0.9^\circ 2\theta$ – which can be assigned to mesopores – decreased and shifted slightly to higher 2θ values, accompanied with a broadening of the reflection within 14 days (Figure 62, left). This was due to a structural rearrangement of the porous system. Indeed, the ellipsometric measurements revealed that the film thickness slightly decreased in this time from 360 nm to 300 nm, but the coating remained on the glass slides. Regarding these results, it is obvious that the phenyl-PMO coating was influenced by the cell culture medium under *in-vitro* conditions. The layer thickness decreased while the coating partially dissolved. The

porous system was destroyed, possibly due to Ostwald ripening-type processes. A similar result was also observed for mesoporous silica films. Compared to the PMO coatings, they already lost the ordered porous structure after 24 h.^[6] The advanced stability of the phenyl-PMO coating under cell culture conditions is due to the organic moieties in the mesoporous structure. The network is more hydrophobic and more stable against aqueous solutions.

5.3 Drug Loading and Release

The loading and release ability of the phenyl- and biphenyl-PMO coatings was tested and evaluated regarding their suitability in local drug delivery applications. After implantation, it is important to combat the bacterial flora and assist during the healing process. Thus, a sufficient and immediate treatment with drugs is necessary. The requirement is a consistent release of drugs over a longer time. A benefit of such modified implants would be an immediate release of a higher drug amount after the implantation to suppress the first inflammation. The release kinetics are challenging to adjust due to complex simulation conditions of a living system.

The success of the loading procedure was tested not only by UV-Vis spectroscopy during release experiments but also prior by infrared spectroscopy and krypton sorption measurements. Additionally, Foerster resonance electron transfer (FRET) spectroscopy was also performed. This investigation had to clarify whether the loaded ciprofloxacin could be detected in the PMO coatings itself and the CFX release monitored in the coatings and not only indirectly in the release solutions.

5.3.1 Loading of Ciprofloxacin

Before the release experiments were carried out, the ciprofloxacin-loaded PMO films were examined by IR and Kr sorption measurements to estimate the successful loading of the drug. In Figure 63, the IR spectra of the pure phenyl-PMO film in comparison with the sulfonated and CFX-loaded ones are displayed. All spectra differ only in small details. The clear bands for the sulfonated PMO are overlapped by the very strong [Si–O] bands at about 1130 cm^{-1} and 1020 cm^{-1} , whereas only the strong band at about 900 cm^{-1} gives an evidence of a 1,2,4-trisubstituted phenylene ring. The CFX-loaded samples were also not easy to examine by IR spectroscopy. A new band at about

1710 cm^{-1} can be assigned to the carbonyl and carboxylic acid groups in CFX. Furthermore, bands for amino groups can be found at 1500 cm^{-1} and an enhanced band at 1630 cm^{-1} gives a hint for further present nitrogen species.

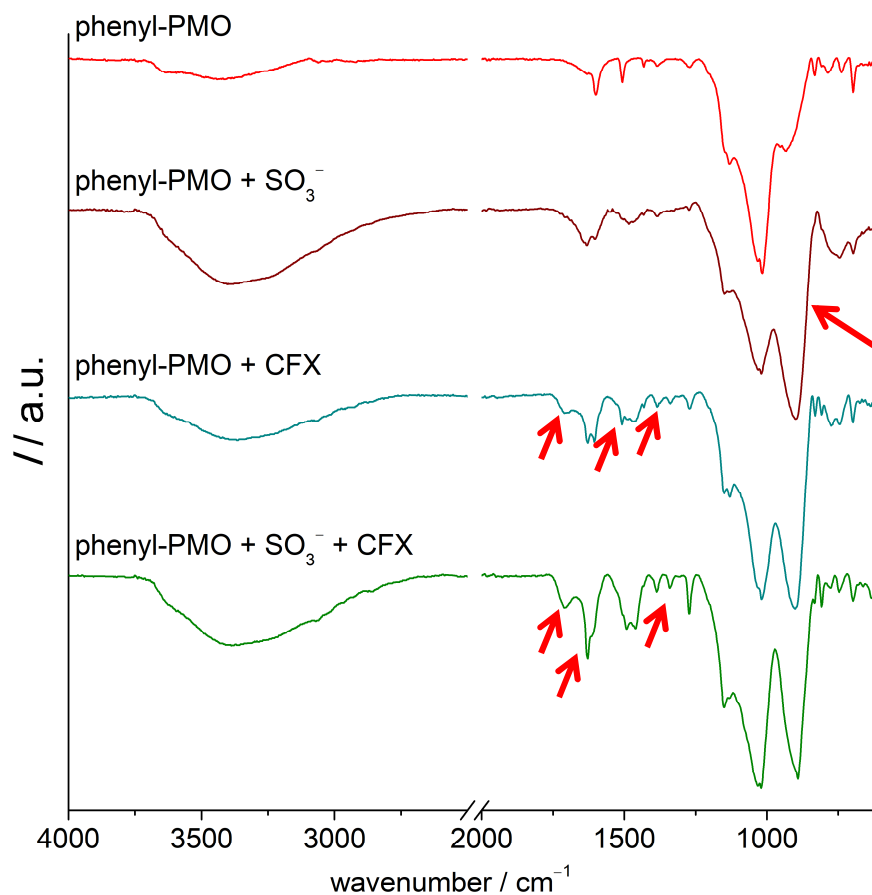


Figure 63: IR spectra of pure phenyl-PMO coatings and sulfonated ones as well as ciprofloxacin (CFX) loaded. All spectra give only a hint for successful modifications.

In conclusion, the IR measurements gave only hints for a successful modification with sulfonic acid and loading with CFX in the phenyl-PMO coatings. On this occasion, Kr sorption measurements of functionalised phenyl-PMO coatings were performed, as shown in Figure 64. Looking at the isotherms, it is obvious that by modification with sulfonic acid groups, loading with ciprofloxacin and both modifications together the specific surface area and the pore volume decreased. The more the phenyl-PMO coating is modified and the more the porous network takes up larger molecules, the lower the specific surface area. As gathered in Table 12, the values for the sulfonated and CFX-loaded phenyl-PMO are nearly halved to those of the pure phenyl-PMO. Thus, the Kr

sorption measurements provide the evidence of a successful modification and loading with CFX of the phenyl-PMO.

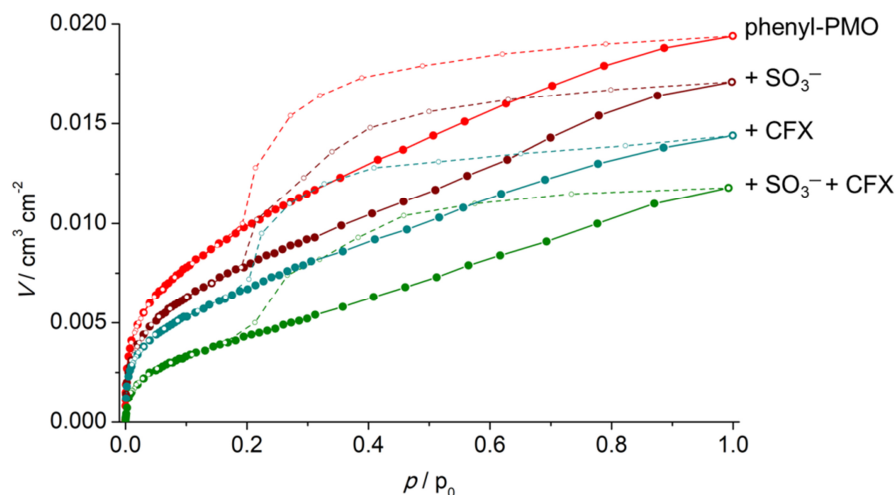


Figure 64: Krypton sorption measurements of functionalised phenyl-PMO coatings. Due to the modification with sulfonic acid groups or loading with CFX, the specific surface area of the phenyl-PMO films and the pore volume decrease.

Table 12: Specific surface area values and pore volumes of pure phenyl-PMO coating and the different modifications.

	$S_{\text{BET}} / \text{cm}^2 \cdot \text{cm}^{-2}$	pore volume / $\text{cm}^3 \cdot \text{cm}^{-2}$
phenyl-PMO	460	$2.80 \cdot 10^{-5}$
+ SO_3^-	380	$2.46 \cdot 10^{-5}$
+ CFX	360	$2.03 \cdot 10^{-5}$
+ SO_3^- + CFX	220	$1.69 \cdot 10^{-5}$

5.3.2 Release of Ciprofloxacin

In order to examine the release ability of the different coatings and modifications, ciprofloxacin release profiles were recorded. Figure 65 shows the released CFX amounts cumulated with respect to the macroscopic surface of the layers. The molecules of the antibiotic ciprofloxacin diffuse ideally into the pores of the PMO layers and are stored there.

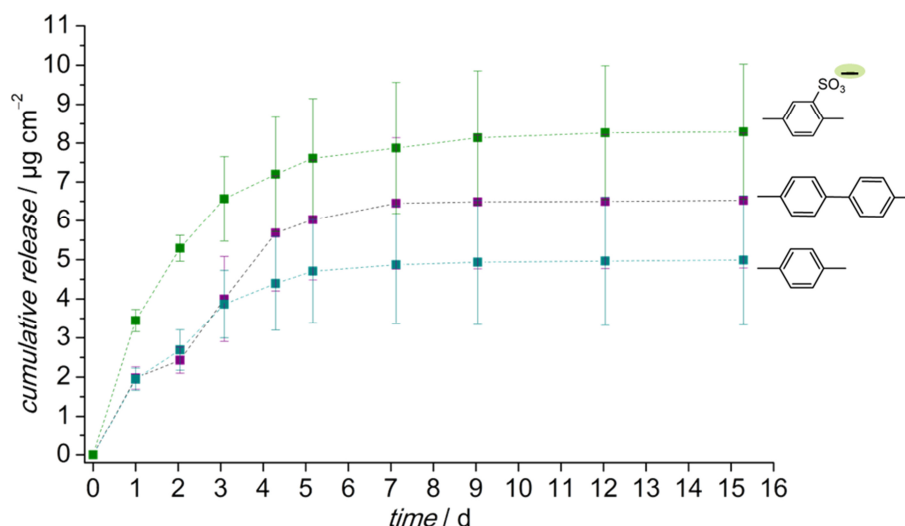


Figure 65: Cumulative release profiles of ciprofloxacin released from phenyl-PMO coatings, biphenyl-PMO coatings and previously-sulfonated phenyl-PMO coatings.

The reason for the modification with sulfonic acid groups was that these negatively-charged functionalities were able to attract more positively-charged ciprofloxacin by electrostatic interactions.^[3,251] In order to characterise the release behaviour of the mesoporous films, they were washed properly after storage in the ciprofloxacin solution. Subsequently, the samples were stored in PBS for a certain time, after which the PBS supernatants were collected and replaced by fresh PBS to simulate the dynamic flow conditions that can be found in the human body. Afterwards, UV-Vis photometric analysis of the PBS supernatants with released ciprofloxacin was performed.

The unmodified native phenyl-PMO film already released $5.0 \mu\text{g} \cdot \text{cm}^{-2}$ of ciprofloxacin after 15 days. After the modification with sulfonic acid groups, the value of released CFX was increased up to $8.3 \mu\text{g} \cdot \text{cm}^{-2}$. The biphenyl-PMO coating released $6.5 \mu\text{g} \cdot \text{cm}^{-2}$ of CFX after 15 days, thus lying in-between the native and sulfonated phenyl-PMO. The totally-loaded amount of the ciprofloxacin in the coatings was determined by dissolving the coatings in sodium hydroxide solution (0.1 M). In order to exclude an interference of the CFX and NaOH signal, the absorption intensity of 0.1 M NaOH, NaOH treated glass, phenyl-PMO and CFX-loaded phenyl-PMO were measured in the UV-Vis in a wave length range between 200 and 350 nm. In Figure 66, these UV-Vis measurements are displayed, showing that only the CFX-loaded samples have an absorption maximum at 275 nm. The other samples treated with NaOH demonstrated no higher absorption intensity at this wave length. Hence, the dissolution of the CFX-

loaded phenyl-PMO coatings in NaOH is a suitable method for determining the CFX amount in the coatings before and after release experiments.

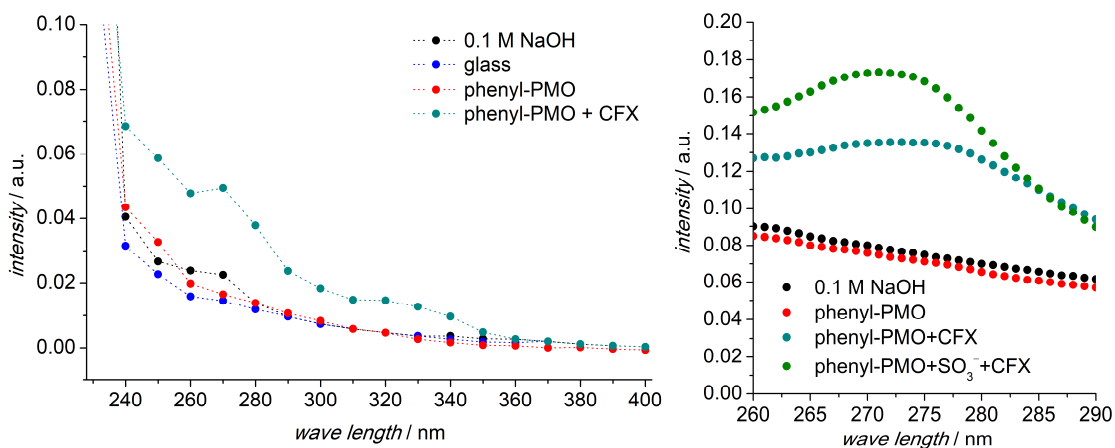


Figure 66: UV-Vis measurements of 0.1 M NaOH and NaOH treated glass, phenyl-PMO, sulfonated and CFX modified phenyl-PMO. In both graphs, a clear absorption maximum is seen for the CFX-loaded samples and no absorption is determined for other samples at 275 nm.

For CFX-loaded phenyl-PMO coatings, the totally loaded amount of CFX was $7.7 \mu\text{g} \cdot \text{cm}^{-2}$, which revealed 28% of unreleased CFX considering the release values ($5.0 \mu\text{g} \cdot \text{cm}^{-2}$). The sulfonated coatings loaded $9.1 \mu\text{g} \cdot \text{cm}^{-2}$ of CFX and thus 9% of CFX was not released ($8.3 \mu\text{g} \cdot \text{cm}^{-2}$). The biphenyl-PMO coatings could take up a total amount of $10.3 \mu\text{g} \cdot \text{cm}^{-2}$ of ciprofloxacin and thus presented 37% of unreleased CFX ($6.5 \mu\text{g} \cdot \text{cm}^{-2}$). Hence, in all cases a part of the CFX was not released within the first 15 days.

It is possible that the CFX molecules more strongly attach to the PMOs due to the electrostatic and π - π interactions. This is the initial reason why the phenylene and biphenylene linker are chosen. They have a similar chemical nature to some drugs, which mainly also have aromatic groups. Due to the aromatic system in the phenyl-PMO, it can already store nearly three times more CFX than mesoporous silica coatings (about $2 \mu\text{g} \cdot \text{cm}^{-2}$), as reported by EHLERT *et al.*^[200] One reason is the aromatic system of the drug ciprofloxacin, which interacts by π - π transfer with the phenylene unit. The biphenyl-PMO has a more elongated aromatic system with one phenylene ring more and thus more attraction to CFX, as reflected in the release results. Another interesting finding is the higher loading capacity of biphenyl-PMO compared to phenyl-PMO

coatings. As investigated by Kr sorption measurements, the specific surface of biphenyl-PMO coatings was about twice as small (section 5.2.2), still these coatings loaded more CFX. This confirms the theory of good interactions between the non-polar coatings and the drug. Through modifying phenyl-PMO with sulfonic acid groups, a further enhanced loading with ciprofloxacin could be achieved. CFX is positively charged in aqueous solution and interacts by electrostatic forces with the negatively-charged sulfonate group. Interestingly, the loaded CFX on sulfonated phenyl-PMO is released almost completely. The sulfonate groups probably detach and elute from the coating during the release experiments. Due to the electrostatic and π - π interactions, a part of CFX remains in the PMO material but probably can be released during a longer-lasting release experiment. Particularly regarding the loss of the structure of the PMO coatings after a certain time (chapter 5.2.7) they dissolve after a prolonged time, thus releasing the remaining drug.

Regarding the release kinetics of CFX, it could be observed that ciprofloxacin is already released on the first day in a high amount, namely one-third of the loaded CFX amount, from all coating types. A reason can be the adsorbed CFX molecules on the sample surfaces and the accumulation in the pore entries that are released or desorbed at first. The release was steady until the fifth day, but after eight days the release curves clearly flattened and a plateau developed in the subsequent days, although the changing intervals of the PBS solution were extended. Here, a first-order release kinetic can be observed, which is assigned to concentration-controlled release of the drug. After 15 days, the release experiment was interrupted as no significant amount of CFX could be detected. The modification with the sulfonate groups showed no influence on the release behaviour; rather, it only caused an enhanced amount of the loaded ciprofloxacin. In the first three days, the biphenyl-PMO showed the same values as the phenyl-PMO, but during the next four days it released more CFX until the curve flattened. The release profiles ranged between a burst release that was certainly found on the first day and a controlled release that followed on the next days.^[16] Nevertheless, the load and release of ciprofloxacin in PMO coatings could be increased several times compared to the results of mesoporous silica films presented by EHLERT *et al.*^[3] The higher CFX amounts in the coatings can be explained by the higher film thickness and a larger porous system of the PMO coatings. Furthermore, the hydrophobic character of the

PMOs is favourable for incorporating the antibiotic ciprofloxacin. The strong burst release of the silica coatings could be improved by the changed material chemistry.

The release experiments in PBS are only models displaying a part of the whole drug-release mechanism in the body. In order to examine whether the loading and release experiments with the drug ciprofloxacin were successful, antibacterial tests were performed with *Pseudomonas aeruginosa*, as described in chapter 5.4.

5.3.3 Examination of Ciprofloxacin Release by Foerster Resonance Energy Transfer

Foerster resonance energy transfer (FRET) method can monitor the release of drugs directly by measuring the extent of interactions between the host material and the drug to be released. Thus, the residual amount of the loaded molecules can be determined by measuring the fluorescence of the loaded samples. Release of the drug causes a decrease in the fluorescence. Furthermore, it should be possible to detect whether some drug molecules remain in the material after the release.

For the application of FRET, the spectroscopic properties of the coatings have to be analyzed first. Therefore, the fluorescence of the unloaded PMO coatings was analyzed. As discussed by Mandy Jahns in her master thesis,^[252] the absorption maxima of the samples were not constant at one value but scattered in a range of approximately 7 nm. These little differences can be explained by the slightly varying chemical surrounding of the chromophores in the coatings. For example, it is possible that some SDA residues remain in the pores after the calcination process; also, the calcination procedure influences the number of the silanol groups which influences the electronic structure of the material. As silanol groups or hydroxyl groups have a bathochromic effect, which means a red shift, the reduction in their number leads to the opposite effect.

In Figure 67, three curves are displayed showing the emission of a phenyl-PMO film, the extinction of solid ciprofloxacin and the emission of a ciprofloxacin loaded phenyl-PMO film. In theory, the more the emission curve of a donator and the extinction curve of an acceptor overlap, the better the electron transfer between these two. The phenyl-PMO film was excited with a wavelength of 270 nm. Its emission curve has one maximum at 327 nm. The excitation curve of ciprofloxacin has two maxima; the highest one is at 385 nm with a shoulder at 310 nm (excitation wavelength of 444 nm). The

CFX-loaded phenyl-PMO film was excited at a wavelength of 280 nm. Its emission curve has two maxima, one at 325 nm and the other one at 437 nm. These signals were caused by Foerster energy transfer, as an excitation of ciprofloxacin at the wavelength of 280 nm would not lead to any signal due to the higher excitation wavelength of CFX. Hence, the phenyl-PMO acting as a donor is responsible for the signal at 437 nm due to the FRET effect.

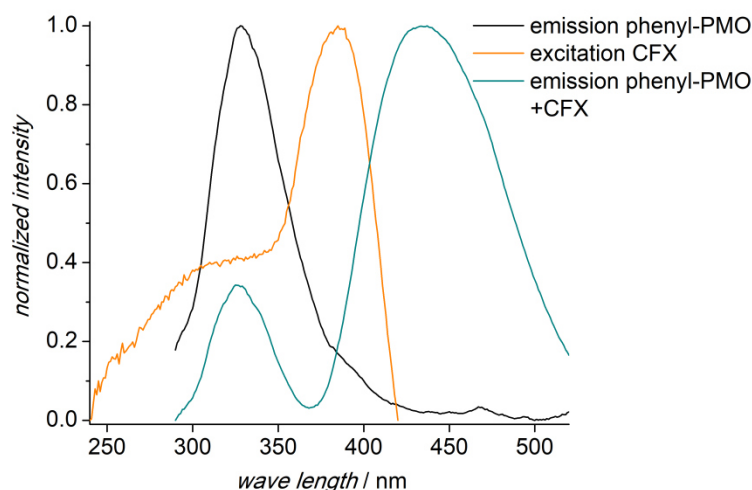


Figure 67: Comparison between the emission spectrum of a phenyl-PMO film (excitation at 280 nm), the excitation spectrum of ciprofloxacin (excitation at 444 nm) and the emission spectrum of a ciprofloxacin-loaded phenyl-PMO film (excitation at 270 nm). For better comparison the intensities are normalised.

Figure 68 shows the corresponding curves as Figure 67 for the samples based on biphenyl-PMO coatings. The maximum of the emission curve of the biphenyl-PMO film lies at 366 nm (excitation at 315 nm), while the maximum of the excitation curve of the CFX is the same as above (385 nm). However, both maxima are located very close to each other. The maximum of the emission at 441 nm of the CFX-loaded biphenyl-PMO film (excitation at 315 nm) lies close to that of the biphenyl-PMO. Furthermore, a slight shoulder is recognisable at 371 nm. Here, the FRET effect is also responsible for the emission of the CFX-loaded film.

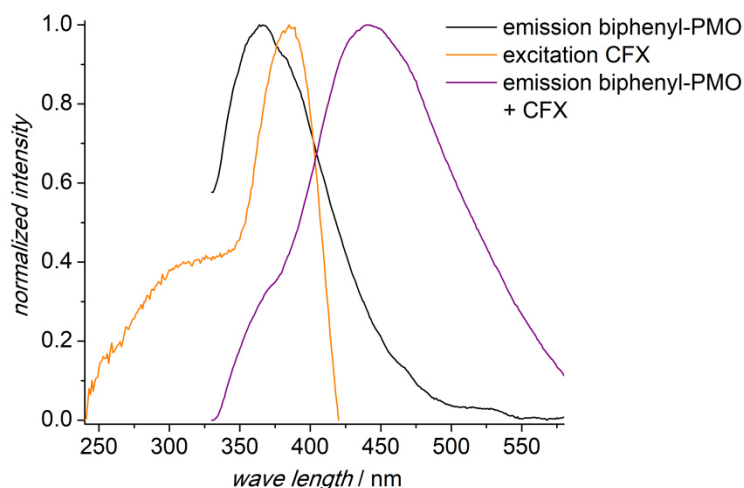


Figure 68: Comparison between the emission curve of a biphenyl-PMO film (excitation at 315 nm), the excitation curve of ciprofloxacin (excitation at 444 nm) and the emission curve of ciprofloxacin-loaded biphenyl-PMO film (excitation at 315 nm). For better comparison, the intensities are normalised.

After the existence of the FRET effect on ciprofloxacin-loaded PMO samples was proven, it was tested whether this effect can be used to determine CFX amounts in PMO and thus to study the release kinetics of the loaded PMO coatings. Therefore, phenyl-PMO films were loaded with different concentrations of ciprofloxacin, namely $0.01 - 0.06 \text{ g} \cdot \text{ml}^{-1}$. Comparing the FRET curves of CFX-loaded phenyl-PMO (Figure 69, top) and the emission curves of the pure substances (Figure 69, bottom), it becomes obvious that the maxima of the loaded samples can be assigned to a phenyl-PMO signal (300 – 375 nm) and a CFX signal (375 – 525 nm). Figure 69 shows a clear relation between the CFX concentration and the fluorescence intensity of the CFX signal. The higher the concentration of ciprofloxacin, the higher is also the intensity of the fluorescence. Inspection of the phenyl-PMO signal shows that its intensity does not depend on the CFX concentration.

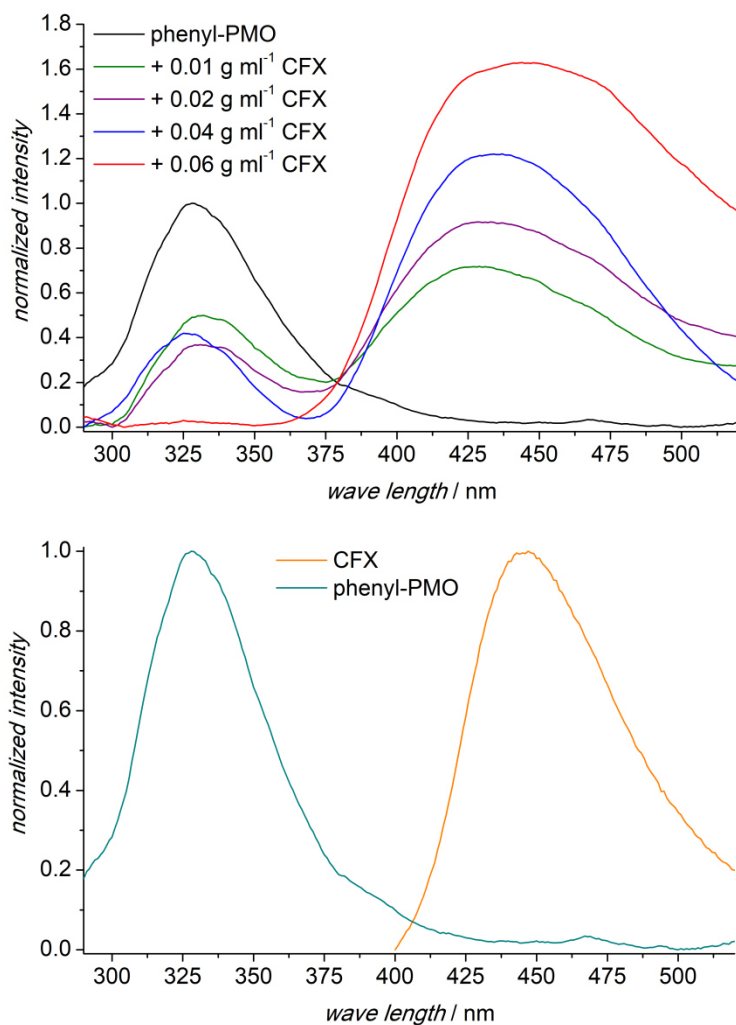


Figure 69: Ciprofloxacin-loaded phenyl-PMO coatings. With increasing concentration of the CFX solution used during loading, the phenyl-PMO film shows increasing emission intensities between 375 and 525 nm (excitation at 270 nm).

In parallel to the determination of the released CFX amounts by UV-Vis spectroscopy of the supernatants (compare chapter 5.3.2.), the releasing medium itself – namely the PMO coating – was examined by measuring the FRET effect. The amounts of ciprofloxacin remaining in the coatings after different release times were monitored by changes in the fluorescence intensities. In Figure 70, the release of ciprofloxacin is displayed for the sample which was prepared with the highest CFX concentration during loading ($0.06 \text{ g} \cdot \text{ml}^{-1}$) in phenyl-PMO coatings. FRET release profiles of samples prepared with lower concentrations can be found in the supporting information. Figure 71 presents the CFX release curve measured using UV-Vis spectroscopy on the supernatants.

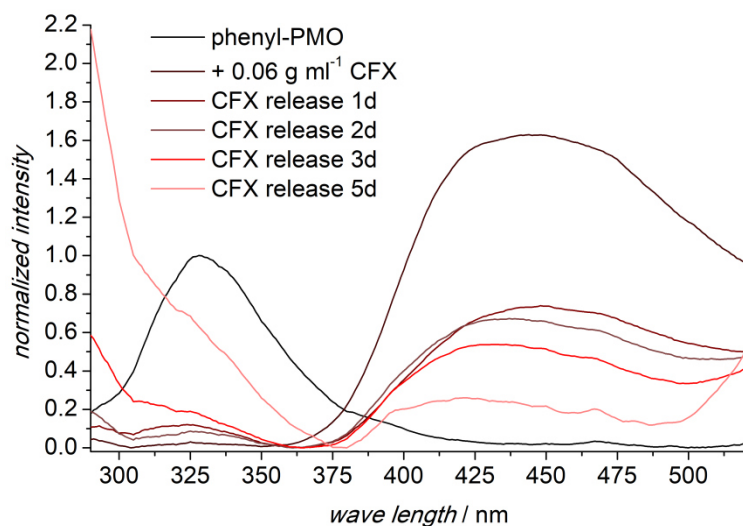


Figure 70: FRET-based study of the release of the antibiotic ciprofloxacin from loaded phenyl-PMO coatings. The sample studied was loaded using a solution with a CFX concentration of $0.06 \text{ g} \cdot \text{ml}^{-1}$. The release was monitored by the measurement of the fluorescence spectra of the test specimens every day after changing the supernatant. Due to the release of CFX, the emission peak at 437 nm decreases whereas the peak at 325 nm, assigned to the PMO emission, increases.

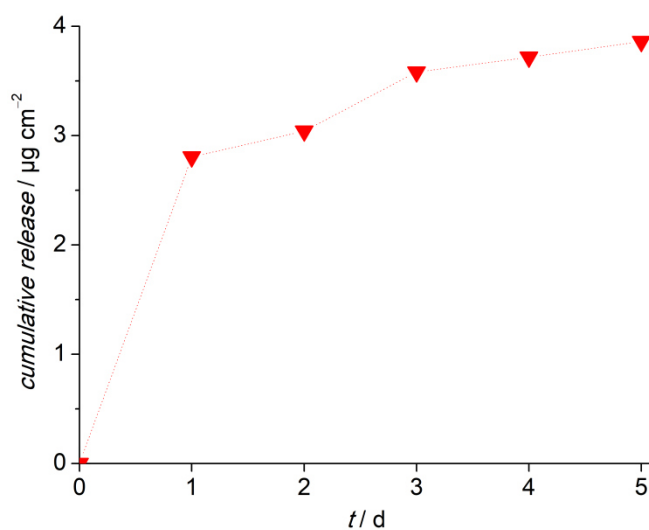


Figure 71: Results of the UV-Vis spectroscopic determination of the release of CFX from phenyl-PMO coating. The measurements were performed on the supernatants produced during the release of the samples used in the FRET study.

As expected, the amount of ciprofloxacin in the PMO coatings decreased day by day as can be easily pursued by the declining fluorescence intensity of the CFX signal (Figure 70, 375 - 525 nm). This direct monitoring of the CFX release from the releasing medium, the phenyl-PMO coatings, can be easily associated with the released CFX

amounts in the supernatants, measured by UV-Vis (Figure 71). On the first day, a very high amount of CFX is released from the coating as evidenced by the high absorption in the UV-Vis measurements and a strong decrease of the CFX fluorescence in the FRET measurements. During the following days, only low amounts of ciprofloxacin were released, resulting in a flat slope of the UV-Vis release curve on the second to fifth day. Also in the FRET measurements, these small amounts released could be pursued as the fluorescence intensity decreased in a modest way. Hence, with the CFX signal of the FRET curves the release of CFX also could be monitored due to the decreasing fluorescence intensities. Though, the FRET analysis of CFX release is not as accurate as the UV-Vis measurements.

It was expected that upon removal of the CFX from the phenyl-PMO coating, the emission signal of the PMO would rise (compare Figure 70, 300 – 375 nm) when the CFX emission signal decrease (375 – 500 nm). However, during the release experiments of CFX, it was found that both signals – phenyl-PMO and CFX – decreased. The phenyl-PMO film did not show the same high intensity as the pure film (Figure 70, black curve). This can be due to the restructuring of the PMO film in the aqueous PBS solution.

Regarding the CFX-loaded biphenyl-PMO film, a similar situation and release performance is recognisable. Figure 72 (top) shows the emission spectrum of the biphenyl-PMO coatings loaded with different concentrations of ciprofloxacin (excitation wavelength 315 nm). Compared to the lower picture where the emission curve of the pure biphenyl-PMO film and the excitation curve of ciprofloxacin are displayed, in the emission spectrum of CFX-loaded biphenyl-PMO the maxima for both FRET partners can be found. The biphenyl PMO signal is located at 340 – 390 nm, whereas the CFX signal is between 390 – 575 nm. Here, a clear differentiation of the native substances is difficult due to the close peak maxima.

The signal of the biphenyl-PMO is more like a shoulder and merges at low concentrations of ciprofloxacin to one broad curve. A clear dependence of the intensities due to the different CFX concentrations is not recognisable. The CFX signal maximum seems to shift to lower wavelengths with decreasing CFX concentrations. These effects can be explained by the extended π -system of the biphenylene group,

leading to a merging of both curves and resulting in a broad FRET curve with difficulties in interpreting the FRET results.

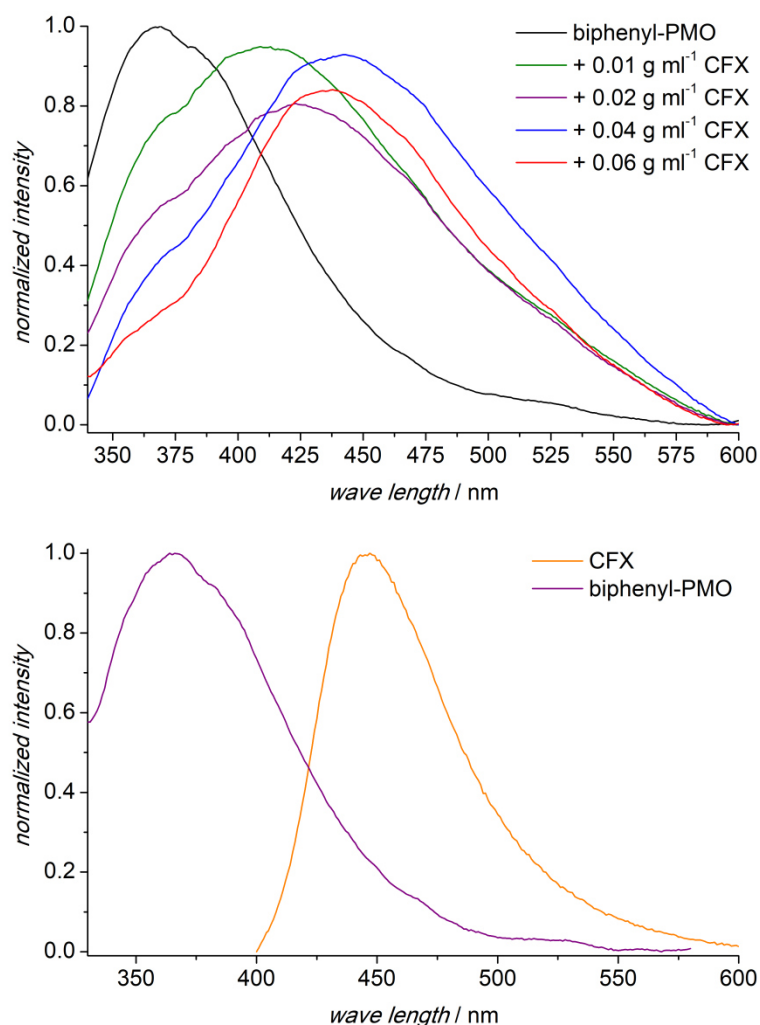


Figure 72: Ciprofloxacin loaded biphenyl-PMO coatings. With increasing concentration of the CFX solution used during loading, the biphenyl-PMO film shows decreasing emission intensities between 340 and 385 nm (excitation at 315 nm).

The release of ciprofloxacin from the biphenyl-PMO coating was also monitored with both techniques in parallel. By FRET technique the releasing samples were monitored (Figure 73), whereas the supernatants were measured by UV-Vis (Figure 74). Looking at the FRET release curves of the samples loaded in the highest CFX concentrations, the decreasing amount of CFX in the biphenyl-PMO coating can be well pursued. Starting with a clear CFX signal with a small biphenyl-PMO shoulder, the shift of the signal maximum and rise on the biphenyl-PMO site is considerably evident (Figure 73).

Nevertheless, the effect of overlapping signals is still strong, as on the second release day only a broad FRET curve can be measured.

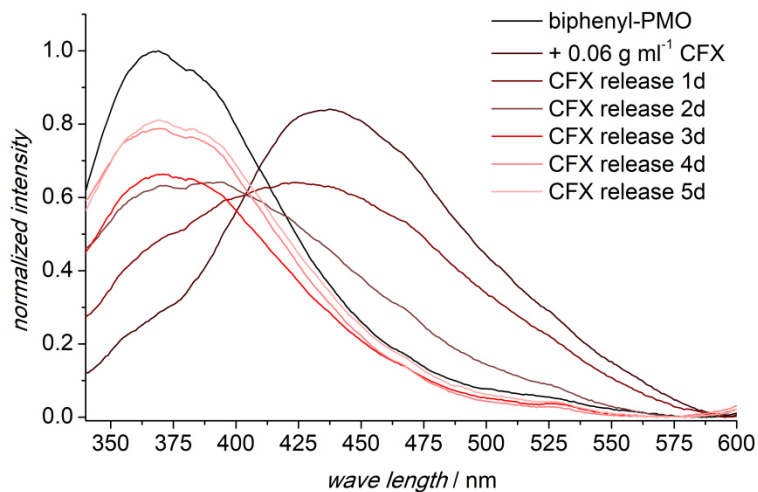


Figure 73: FRET-based study of the release of the antibiotic ciprofloxacin from loaded biphenyl-PMO coatings. The sample studied was loaded using a solution with a CFX concentration of $0.06 \text{ g} \cdot \text{ml}^{-1}$. The release was monitored by the measurement of the fluorescence spectra of the test specimens every day after changing the supernatant. Due to the release of CFX, the emission peak at 450 nm decreases whereas the peak at 360 nm, assigned to the PMO emission, increases.

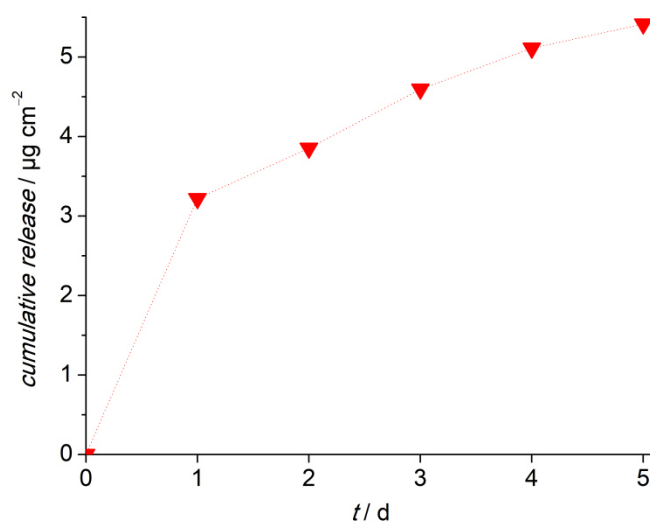


Figure 74: Results of the UV-Vis spectroscopic determination of the release of CFX from biphenyl-PMO coating. The measurements were performed on the supernatants produced during the release of the samples used in the FRET study.

The CFX release from biphenyl-PMO coating can be compared to the CFX release from phenyl-PMO. A burst release occurs on the first day followed by smaller amounts of released CFX (Figure 74). Comparing both monitoring methods in parallel, the results of the FRET and UV-Vis measurements correlate with each other. The tendency of decreased intensity of the biphenyl-PMO signal due to higher concentrations of CFX stored in the biphenyl-PMO coating is recognisable. The changes in the intensity and the shift of the CFX signal maxima during the release experiments can be pursued. Although, due to the close signal maxima of CFX and biphenyl-PMO this is difficult.

Summarising, FRET is a direct, non-destructive technique to monitor the release of substances from the releasing medium itself. The examination of the releasing medium – the PMO coatings – by the FRET method is an interesting tool to study the release kinetics. If the concentrations are high enough, the drug release can be monitored well. Nevertheless, the results obtained above show that the FRET method is not as precise as the UV-Vis measurements. Especially, the CFX release from the biphenyl-PMO film was difficult to pursue because of the close maxima of the biphenyl-PMO emission curve and CFX excitation curve. Another disadvantage is the restructuring of the PMO coatings due to the influence of the aqueous environment of the medium PBS.

However, the direct monitoring of drug release by FRET technique warrants further studies to fully understand the release kinetics in PMO coatings. This real-time monitoring technique has already been successfully applied *in vitro* to detect the release of drugs from mesoporous silica nanoparticles into HeLa cells^[253]. *In-vivo* polymer nanoparticles loaded with a dye and injected onto mice were proven to show a direct uptake of the nanoparticles in the cells, which was verified by the FRET effect due to the released dye.^[254] Therefore, such biosensing and real-time monitoring is conceivable with drug-loaded PMO coatings, as shown in this study.

5.3.4 Release of Rolipram

As the release properties with ciprofloxacin of both aromatic PMOs were promising, another substance – rolipram – was loaded in the coatings. Moreover, with this drug the release ability of the coatings was examined. The supernatants were exchanged every 24 hours.

Rolipram release tests are displayed in Figure 75. The release profiles started with a slight burst release on the first day. Subsequently, the released rolipram amounts from the phenyl-PMO decreased and the curve rose only slightly until the ninth day and clearly flattened during the following 20 days, with small remarkable amounts of the released drug. The biphenyl-PMO showed similar rolipram release behaviour, with the difference that the released amounts were higher than those of the phenyl-PMO coating. Although the slope of the curve decreased after the first nine days, at no time it revealed such a low slope like the phenyl-PMO. Overall, the phenyl-PMO coating released a cumulative amount of rolipram of $8.0 \mu\text{g} \cdot \text{cm}^{-2}$ and the biphenyl-PMO released $16.3 \mu\text{g} \cdot \text{cm}^{-2}$, twice as much. Compared to the released ciprofloxacin amounts (Figure 65), the determined amounts of rolipram were nearly twice as high. A possible reason is the smaller rolipram molecule that can more easily diffuse into the porous network. Hence, more molecules can be stored and released from the PMO coatings. Consequently, PMO coatings can be a sufficient medium for storing the neuroprotective drug rolipram.

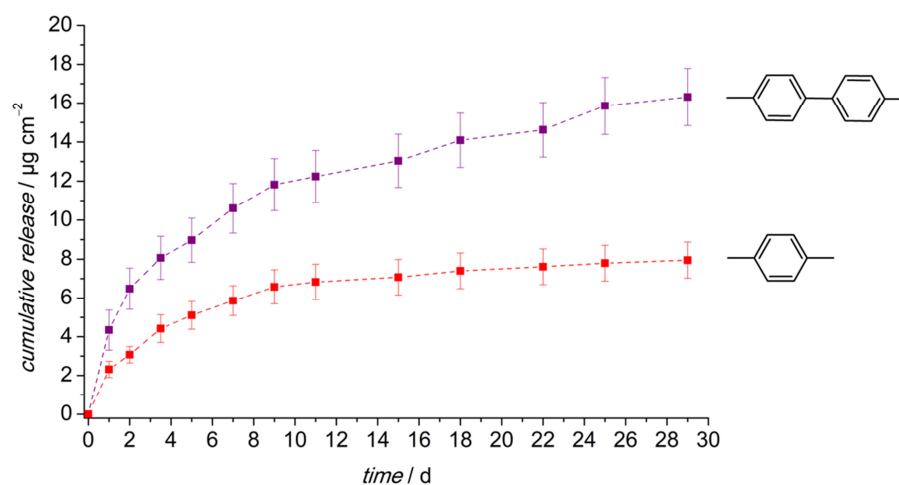


Figure 75: Cumulative release profiles of rolipram released from phenyl-PMO and biphenyl-PMO coatings over 29 days.

Summarising, it is obvious that biphenyl-PMO coatings can load and release a higher amount of rolipram than phenyl-PMO coatings. The reason may be the more non-polar nature of the biphenylene unit, which can attract more rolipram.

Due to the auto-fluorescence of the PMO coatings at a similar wavelength like the rolipram, it was not possible to determine the whole stored amount of rolipram in the coatings by dissolving them in NaOH. Furthermore, the self-dissolving of the coating in the PBS during the release experiments can be a source of faults determining the released rolipram amounts. Although pure PMO coatings in PBS were investigated parallel to the loaded ones and served as reference values while UV-Vis measurements, fault values cannot be excluded. In order to investigate the positive influence of rolipram on neurons, cell culture tests with spiral ganglion neurons were performed. These cell tests are described in section 5.5.3.

5.4 Antibacterial Activity of Ciprofloxacin-Loaded Phenyl-PMO Coatings

The antibacterial tests were performed by Dr. MUHAMMAD IMRAN RAHIM at the Helmholtz Centre for Infection Research, Braunschweig, Germany. These tests should evaluate the efficacy of the ciprofloxacin release from the phenyl-PMO coatings on a bioluminescent laboratory strain of *Pseudomonas aeruginosa* (PA01 CTX::lux). These bacteria exhibit luminescence when alive. The luminescence intensity correlates with the number of living bacteria. A time-dependent release of ciprofloxacin was performed by incubating the samples in PBS, collecting the supernatants every 24 h and replacing them with fresh PBS for 14 days, thus simulating a dynamic fluid environment. Hence, the same release times were chosen as in the CFX release experiments shown above (chapter 5.3.2). The supernatants were tested for their antibacterial activity on the *Pseudomonas aeruginosa* bacteria suspension by measuring the luminescence after zero and 6 hours after mixing. The results are summarised in Figure 76. The cleaned glass slides – which were used as a reference – as well as the native unmodified PMO coatings did not show any antibacterial activity. The values of the living bacteria were high and within the accuracy range (Figure 76 glass and A). The sulfonated PMO coatings exhibited a surprising result, showing an antibacterial efficacy in the first seven days (Figure 76 B). Measurements of the pH value of the supernatants during these first seven days revealed no changes of the pH value, which could have effects on the bacterial growth. The measured pH values ranged between 7.2 and 7.5. The antibacterial effect of the sulfonated phenyl-PMO coatings decreased day by day, which

can be traced possible residues of the modification chemicals that were not washed off properly or dissolution of the sulfonated phenyl-PMO coating.

When surfaces are functionalised with sulfonate groups, their antibacterial effect is not caused by the negative charge; rather, it is their influence on the adsorption of fibronectin and its effects on the proliferation and adherence of bacteria. The antibacterial activity of sulfonate groups can be found in PMMA research, grafting it with COO^- and SO_3^- groups. The carboxylic acid and sulfonate-modified PMMA supposed to show a highly antibacterial surface. In particular, the heparin-binding domains of the adsorbed fibronectin are decisive for the adhesion of bacterial cells.^[255–257] Sulfonate groups inhibit parts of the fibronectin signaling way, resulting in deviated adhesion of bacteria and leading to a bacteriostatic effect, i.e. the bacterial growth is stopped. Nevertheless, these modifications do not affect the adhesion and growth of other cells like osteoblasts.^[258] In the presence of sulfonate groups, osteoblasts can proliferate in a normal way without inhibition.^[259] Thus, no negative effects on the following cell compatibility examinations are expected due to sulfonation.

As expected, the CFX-loaded phenyl-PMO coatings indicated a very good antibacterial activity in the first seven days, which correlates with a sufficient amount of CFX to kill nearly the whole bacteria (Figure 76 C). On the following days 8 to 15, the activity progressively decreased, resulting in the same antibacterial values as the unmodified PMO coatings. To conclude, most of the ciprofloxacin is released during the first seven days and smaller amounts on the days thereafter. This confirms the results yielded from the controlled release profiles of ciprofloxacin (compare Figure 65). Moreover, the antibacterial activity of the released ciprofloxacin from the sulfonated PMO coatings is very high on the first eight days (Figure 76 D) and decreases in the following seven days, reaching comparable values as the PMO coatings. Nonetheless, the maximum bacterial amounts on days 12 to 15 are lower compared to those of the unsulfonated CFX-loaded coatings (Figure 76 C). However, clearly-enhanced efficacy of the sulfonated and CFX-loaded PMO samples cannot be observed in the antibacterial tests. Hence, the advantage of sulfonate modification is questionable. The following cell compatibility tests have to confirm and facilitate the decision concerning whether a sulfonate modification is necessary at all, as it has a low impact on the antibacterial activity of the coatings.

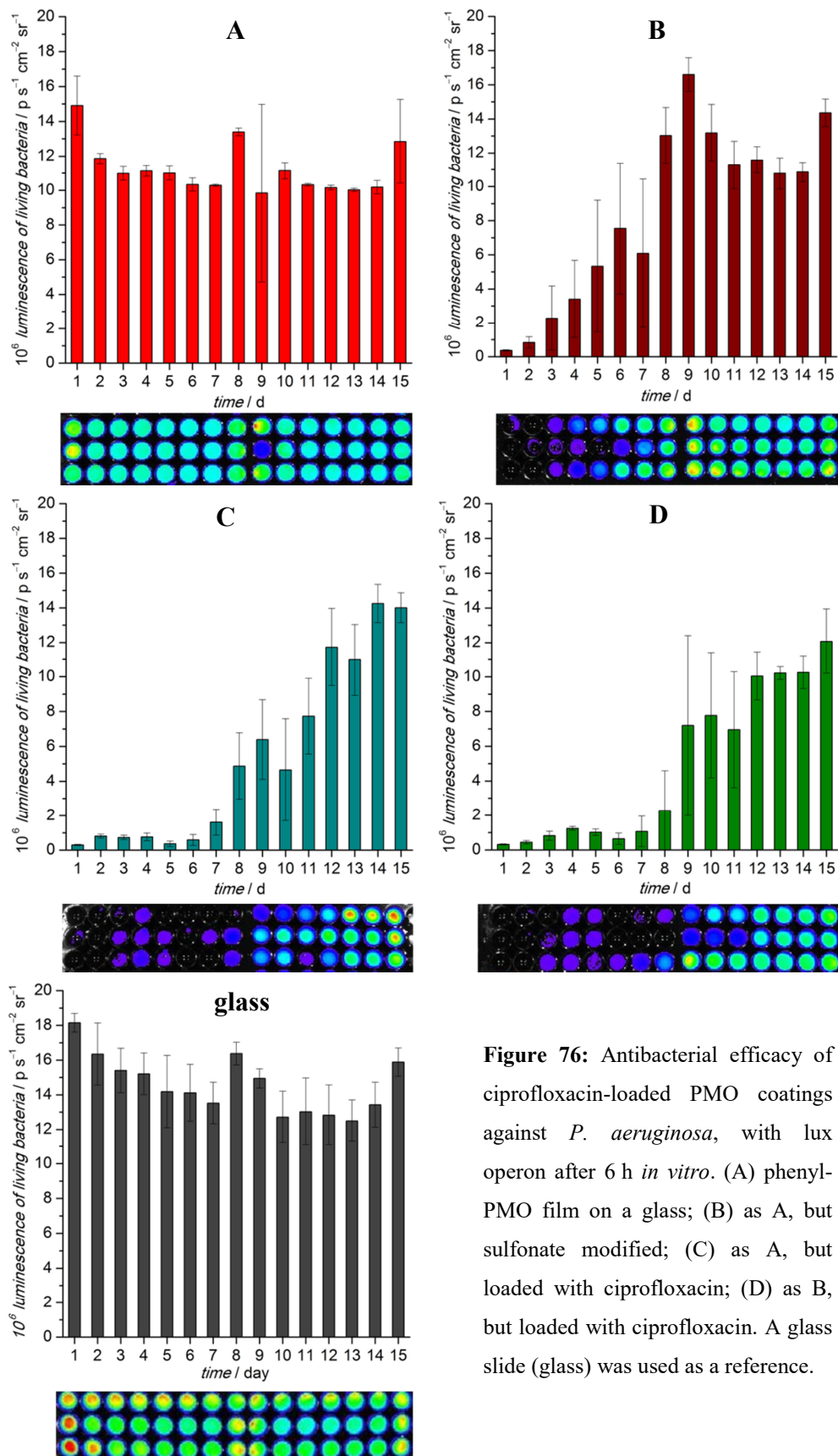


Figure 76: Antibacterial efficacy of ciprofloxacin-loaded PMO coatings against *P. aeruginosa*, with lux operon after 6 h *in vitro*. (A) phenyl-PMO film on a glass; (B) as A, but sulfonate modified; (C) as A, but loaded with ciprofloxacin; (D) as B, but loaded with ciprofloxacin. A glass slide (glass) was used as a reference.

These investigations indicate that it is possible to suppress bacterial proliferation very effectively during the first seven days, as well as reducing the number of bacteria during the following days by releasing ciprofloxacin from un- and modified phenyl-PMO coatings. The native phenyl-PMO coating already releases sufficient amounts of CFX, which correlates with a high antibacterial activity. A modification with sulfonic acid groups do not offer an obvious advantage compared to the pure phenyl-PMO coatings. Presumably, the sulfonation is not necessary to achieve a good suppression of bacterial growth. Hence, these coatings represent a practical approach for applications on implants for the human body. The ciprofloxacin-loaded phenyl-PMO coatings can suppress bacterial inflammation after an implantation locally without stress for the whole body through systemic medication with an antibiotic. Since a high amount of antibiotics immediately after an implantation is desirable, a burst release in the first days is not a disadvantage.

5.5 Cell Culture Tests on PMO Coatings

For a further approach, cell compatibility tests were necessary to estimate whether the PMO coatings are biocompatible at all. Therefore, cell culture tests with fibroblasts and HUVECs were performed on the un- and modified PMO coatings. It was fundamental that the coatings were biocompatible for further work, as the goal was an application of the PMO coatings on implant materials and use in the human body.

5.5.1 Cytocompatibility Tests of PMO Coatings

Testing of Fibroblasts and HUVECs on Different Types of Phenyl-PMO Coatings

The presented cell culture tests were performed by Dr. SABRINA SCHLIE-WOLTER from the Laser Zentrum Hannover e. V., Hannover, Germany.

The cytocompatibility of the phenyl-PMO coatings was tested by seeding the samples with two cell lines: first, human fibroblasts; and second, human umbilical vein endothelial cells (HUVEC). Both cell lines belong to standard cell lines for examining biocompatibility. The vitality of the cells on different phenyl-PMO sample types is shown in Figure 77. In comparison to the glass slides used as controls, no significant increase of dead cells could be detected. The fibroblasts (Figure 77 left) as well as the

5. Results and Discussion I

HUVECs (Figure 77 right) showed a high vitality of about 92% on all investigated materials.

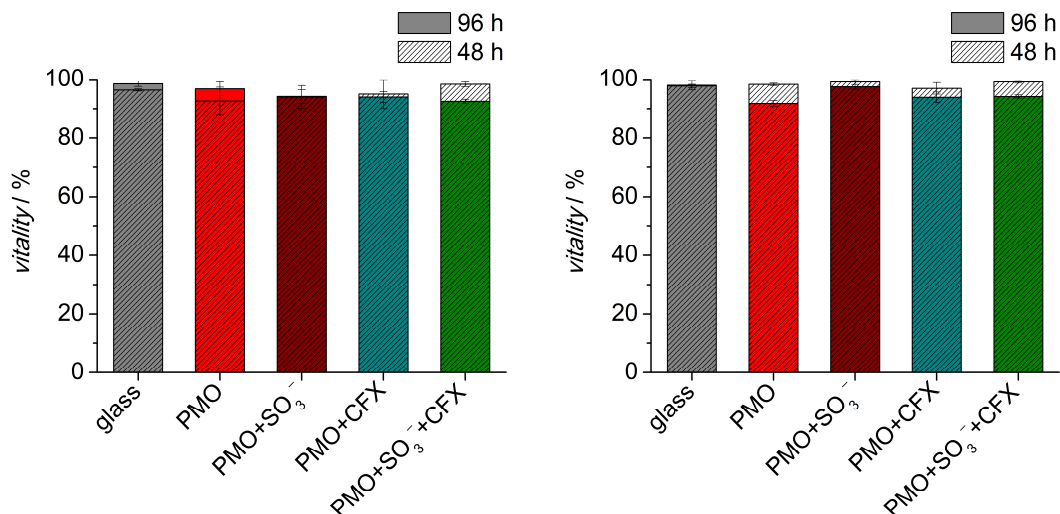


Figure 77: Vitality of (left) fibroblasts and (right) HUVECs on the different modified phenyl-PMO samples inoculated for 48 h and 96 h at 37 °C. Cleaned glass slides were used as a control.

As shown in Figure 78, the actin filaments of the cells were well organised and stretched over the whole surface across all investigated sample types compared to bare glass slides. It seems that the number of fibroblasts on the sulfonated coating and partly on the CFX-loaded ones is lower compared to the other samples. However, this can also be an occasional observation of a small part of the tested samples, as the vitality and proliferation numbers are not suppressed, compared to the other modified phenyl-PMO films.

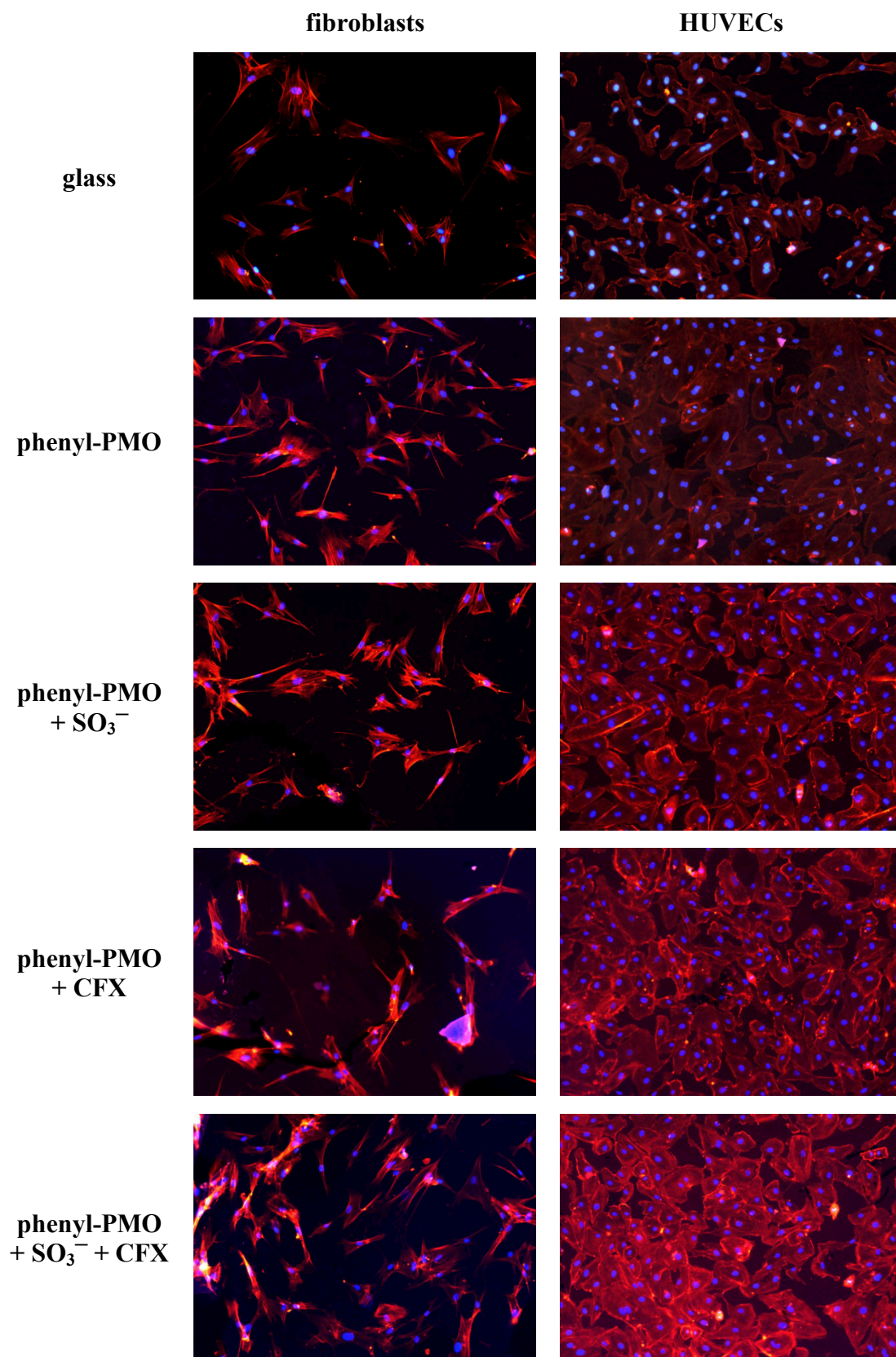


Figure 78: Fluorescence images of fibroblasts and HUVECs of the different samples after 24 h of cultivation time. The images of the red actin filaments and blue nuclei were combined by ImageJ.

To gain more insights into cell shape, cell elongation was quantified by the ratio of cell length and width (Figure 79). On the control glass slide, fibroblasts had a ratio of 4.98 and HUVECs of 2.41. Both cell lines were less elongated on the phenyl-PMO films and the sulfonated ones. This reduction was significant for both cell lines on phenyl-PMO films and significant for HUVECs on the sulfonated ones. Ciprofloxacin-loaded phenyl-PMO coatings increased the elongation of fibroblasts, albeit not significantly. Concerning HUVECs, the ratio on ciprofloxacin-loaded PMO film was comparable with the control treatment. The phenyl-PMO coatings modified with sulfonic acid groups and loaded with ciprofloxacin slightly increased cell elongation of both cell lines, albeit not significantly. It can be supposed that the enhanced elongation is related to the presence of CFX, since phenyl-PMO films and sulfonated phenyl-PMO films alone caused a higher amount of rounded cells, and only ciprofloxacin caused a higher amount of elongated cells.

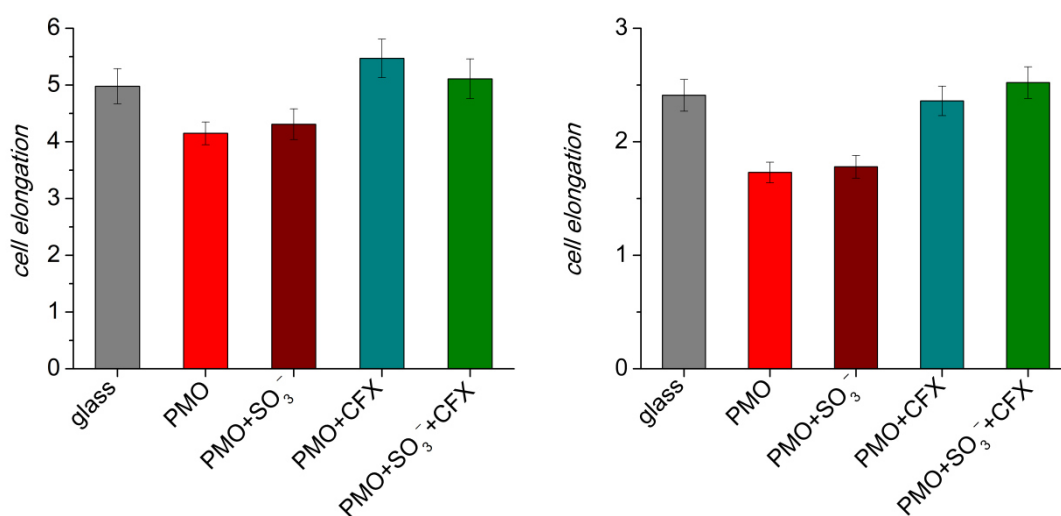


Figure 79: Quantification of cell ratios (equals cell length divided by cell width) of fibroblasts (**left**) and HUVECs (**right**) on the different samples.

Since all phenyl-PMO materials presented a high green auto-fluorescence, further staining of molecular adhesion components could not be performed. Therefore, no quantification of cell adhesion could be carried out with this procedure. However, the fluorescence staining also revealed insights in a specific form of cell attachment of the cells on the substrates. In contact with the cell culture media, it could be observed that the coating partially detached. Via enhancing the contrast of the fluorescence images,

this detachment could be visualised (Figure 80). This could be due to high thickness of the PMO coatings, where the coatings crack by contact with cell culture medium and drying afterwards.

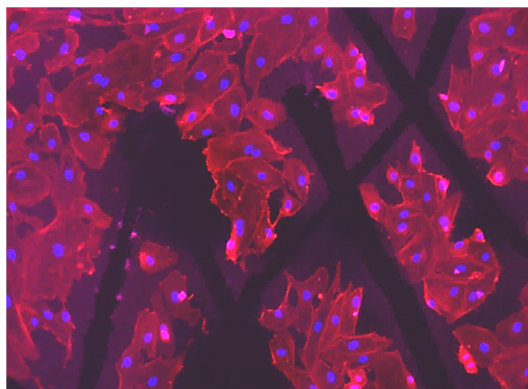


Figure 80: Visualised detached PMO coating exemplarily shown for HUVECs.

Due to the auto-fluorescence, the remaining coating shone slightly red, while the areas without coating were black. Interestingly, the cells only attached to the substrate that was still coated (“red”). Since the cells also attached to the uncoated control glass slides, it can be supposed that the so-called black substrate area was probably not comparable with glass. It was possible that certain chemicals that were needed for the specific coatings or other debris remained on the black substrate area. Such fragments inhibited cell attachment. With respect to the vitality results (Figure 78), it can further be concluded that the fragments and detached coatings were not cytotoxic to the cells.

The cell compatibility of the materials was also analysed with respect to cell proliferation over 48 h and 96 h cultivation time (Figure 81). Cell specific effects were observed by comparing the proliferation of fibroblasts (Figure 81 left) and HUVECs (Figure 81 right).

Concerning fibroblasts, phenyl-PMO and sulfonated coatings decelerated cell growth after 48 h when compared with the control. After 96 h, cell growths were enhanced on phenyl-PMO and sulfonated films alone, while all substrates containing ciprofloxacin displayed declining cell numbers. On CFX-loaded phenyl-PMO coatings alone, this reduction was significant. By contrast, the cell growth of HUVECs was not negatively affected by these materials after 48 h. In this case, a small but not significant increase on CFX-loaded phenyl-PMO film was quantified. After 96 h, the growth rate of

HUVECs on the control and CFX-loaded phenyl-PMO coatings was similar, while it was further reduced on unmodified, sulfonated and both sulfonated and CFX-loaded phenyl-PMO coatings. The reduction on sulfonated and CFX-loaded phenyl-PMO is probably related to the PMO coating and/or sulfonated PMO coating, since the ciprofloxacin-loaded PMO layer alone enhanced the growth of HUVECs. Thus, all coatings can be considered cell compatible, although the proliferation seems to depend on the cell type.

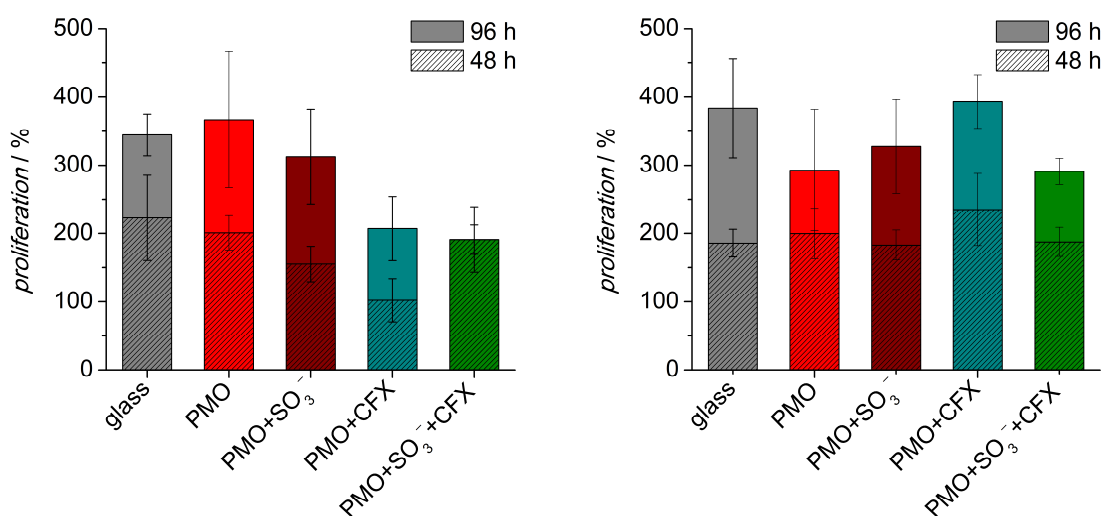


Figure 81: Cell proliferation of (left) fibroblasts and (right) HUVECs on the different modified phenyl-PMO specimens.

In order to understand the selective control of CFX-loaded materials, further investigation is necessary. Since the materials are neither cytotoxic nor do they seem to inhibit cell attachment, other aspects have to be responsible. BUJOR *et al.*^[260] confirmed that CFX inhibits the growth of fibroblasts. They demonstrated that CFX causes antifibrotic effects in an ERK 1 / 2- dependent manner, which involves the down-regulation of Dnmt1 and upregulation of Fli1. Concerning HUVECs, no details are known thus far.

Cell Compatibility Tests with Fibroblasts on Both PMO Coatings

These cell culture tests were performed by JENNIFER SCHULZE at the Hannover Medical School (MHH, Hannover, Germany), Department of Otorhinolaryngology.

Different modified phenyl-PMO coatings tested in a previous cell culture test showed good cytocompatibility. The proliferation of NIH3T3 mouse fibroblasts on pure phenyl-PMO coatings exhibited excellent results. Hence, the biocompatibility of the biphenyl-PMO coatings should also be tested. Therefore, the standard cell line of NIH3T3 fibroblasts was used to evaluate the cell compatibility. The compatibility of glass (as reference), phenyl- and biphenyl-PMO coatings was compared and is displayed in Figure 82. The vitality of the fibroblasts was examined using the neutral red uptake (NRU) staining, which marked the viable cells to differ them from the dead ones. The vitality of fibroblasts on glass was set as a reference. The vitality on the biphenyl-PMO coating was excellent and exhibited nearly the same values as the reference, whereby the standard error of mean was slightly higher. In comparison, the vitality on the phenyl-PMO coatings was almost 15% lower, which was difficult to explain, as the chemistry or rather the surface hydrophoby are almost the same. The difference between the two coatings is the porosity of the film surface. Phenyl-PMO coating surfaces seem to be more structured. Another possible explanation could be preparation failures.

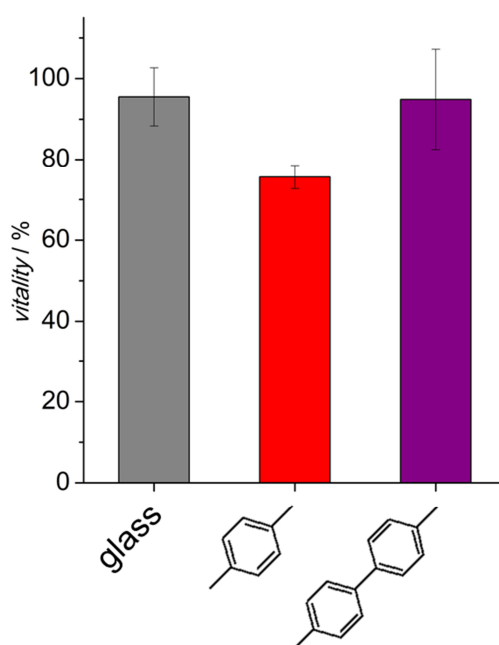


Figure 82: Vitality of fibroblasts on phenyl-PMO and biphenyl-PMO coatings inoculated for 96 h. Cleaned glass slides were used as a control and reference.

Regarding the microscopic pictures of the fibroblasts on the different surfaces after 96 h (Figure 83), most cells adhere well on the specimens and are elongated, which reflects a good proliferation. On all samples, a dense cell layer can be determined with only few rounded or detached cells. Regarding these pictures, small differences of the cell layers are observed depending on the substrate. The cells on the phenyl-PMO coating (Figure 83 b) look slightly smaller. Overall, a good vitality of cells on all tested surfaces could be stated, which was a good starting point for further compatibility tests with NIH3T3 fibroblasts that were gene-modified for production of BDNF.

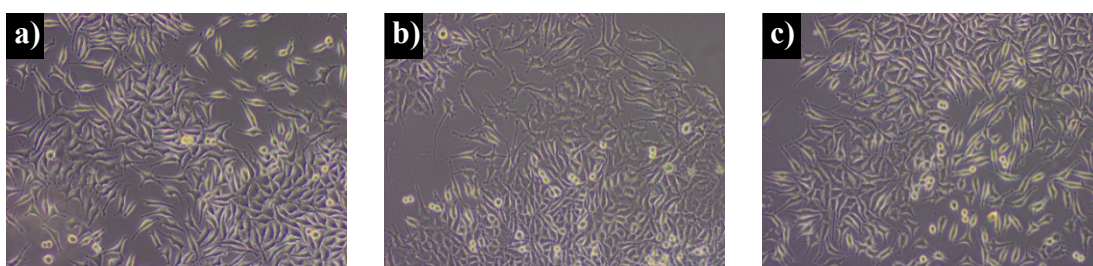


Figure 83: Images of adhered fibroblasts on different specimens recorded after 96 h. The cells look elongated and proliferate well on all surfaces: a) glass, b) phenyl-PMO and c) biphenyl-PMO coatings.

5.5.2 Examination of Brain-Derived Neurotrophic Factor Producing Cells on Phenyl-PMO Coating

These cell culture tests were performed by JENNIFER SCHULZE at the Hannover Medical School (MHH, Hannover, Germany), Department of Otorhinolaryngology.

Fibroblasts exhibited good vitality and proliferation on phenyl-PMOs, as described above. Hence, in a further step the production of brain-derived neurotrophic factor (BDNF) from gene-modified fibroblasts was examined. BDNF is crucial for the protection and growth of neurons and synapses. It is one of the most active neurotrophins. The lack of BDNF is responsible for many diseases concerning the peripheral nervous system and the brain, such as depression, dementia or epilepsy.^[168]

Our cooperation partners from the Medical School of Hannover had generated the above-mentioned BDNF-producing fibroblasts, but experienced difficulties when trying to attach these to the surface of cochlea implants. Correspondingly, the idea of the present investigation was to evaluate whether a PMO coating could serve as a favourable substrate for the growth of these fibroblasts and for their BDNF production.

Due to the chemical similarity of the silicone (as part of the cochlea implant) and PMO, it appeared feasible to generate such coatings on cochlea electrodes. In the same vein, the PMO coatings were also tested with spiral ganglion neurons (SGNs, see section 5.5.3 Spiral Ganglion Cell Culture Investigations of PMO Coatings Loaded with Bioactive Molecules), the decisive neural cell type addressed by cochlea implant stimulation.

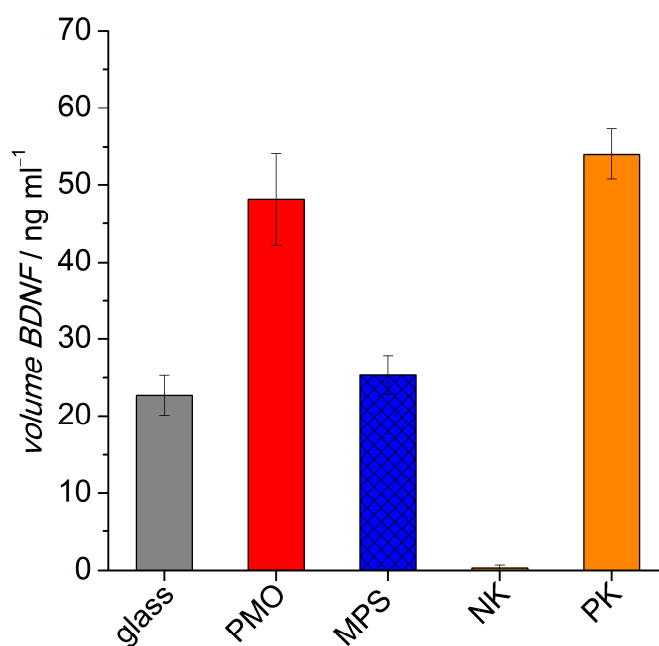


Figure 84: Production of BDNF (brain-derived neurotrophic factor) by modified fibroblasts proliferating on different surfaces. The phenyl-PMO was tested (PMO) and compared to mesoporous silica coating (MSP). Normal fibroblast (without expression of BDNF) served as a negative control (NK) and cell culture plastic served as a positive control (PK).

Figure 84 displays the released amounts of BDNF from gene-modified fibroblasts proliferating on different surfaces. The produced BDNF volume by the fibroblasts tested on glass samples and mesoporous silica coatings – which had a similar structure as the phenyl-PMO coatings – was the lowest. On both surfaces, the fibroblasts liberated an amount of about $25 \text{ ng} \cdot \text{mL}^{-1}$ of BDNF. However, on the phenyl-PMO coatings, the fibroblasts produced about $50 \text{ ng} \cdot \text{mL}^{-1}$ of BDNF a value almost as high as on the positive control (cell culture plastic) with $55 \text{ ng} \cdot \text{mL}^{-1}$. For a positive

influence or rather protection of SGNs, an amount of $50 \text{ ng} \cdot \text{mL}^{-1}$ BDNF is needed to achieve a good survival rate of the spiral ganglion neurons.^[56,261,262]

These results were supported by the images taken by a fluorescence microscope (Figure 85). The cell layers on phenyl-PMO coating and cell culture plastic (positive control, PK) appeared denser compared to those on glass and mesoporous silica coating (MPS). Thus, it is conceivable that these denser cell layers also produce a higher volume of BDNF. For a positive influence or rather protection of SGNs, an amount of $50 \text{ ng} \cdot \text{mL}^{-1}$ BDNF is needed to achieve a good survival rate of the spiral ganglion neurons.^[56,261,262]

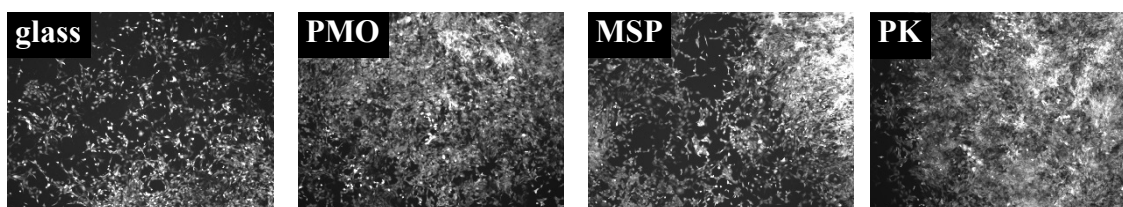


Figure 85: Images of gene-modified fibroblasts producing BDNF proliferating on different surfaces after 96 h: glass and cell culture plastic (positive control, PK) served as reference to phenyl-PMO (PMO) and mesoporous silica (MSP) coatings.

5.5.3 Spiral Ganglion Cell Culture Investigations of PMO Coatings Loaded with Bioactive Molecules

These cell culture tests were performed by JENNIFER SCHULZE at the Hannover Medical School (MHH, Hannover, Germany), Department of Otorhinolaryngology.

In order to further evaluate PMO coatings for possible applications, especially in the inner ear, cell culture studies were carried out spiral ganglion cells (SGCs). The SGCs used were freshly-isolated primary cells from the cochleae of neonatal rats. Such a spiral ganglion cell culture contains spiral ganglion neurons as the primary nerve cells as well as supporting glia cells and fibroblasts.^[56] Although this preparation method is well established, the quality of the cells is highly dependent on the preparation technique and the individual animals. Moreover, it has to be noted that SGCs are much more sensitive to their environment than e.g. fibroblasts. The SGCs were then seeded on the different samples: modified pure phenyl- and biphenyl-PMO surfaces, such surfaces loaded with rolipram ones, BDNF supplemented, and concurrent modified with rolipram and BDNF. KRANZ *et al.* reported that the combination of rolipram and BDNF

led to a higher survival rate of SGNs compared to a separate influence of rolipram or BDNF.^[56]

The results of the SGNs surviving tests are summarised in Figure 86.

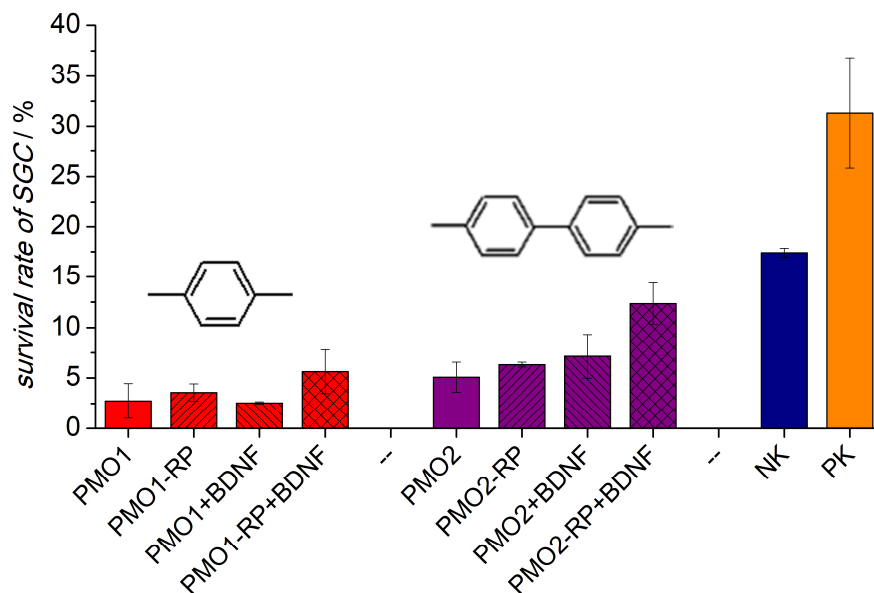


Figure 86: Survival rates of spiral ganglion neurons on different surfaces. Phenyl-PMO (PMO1) showed the lowest survival rates, independent of additions. The survival rates on biphenyl-PMO (PMO2) were higher, although still not as high as on the pure cell culture plastic (negative control, NK) or the CCP with added BDNF (positive control, PK).

As displayed, both controls – CCP as a negative and BDNF-supplemented medium CCP as a positive control – display higher surviving rates of the SGNs compared to both PMO coatings. This is slightly misleading as native CCP was used as a negative control. However, cells always adhere and proliferate on CCP better than on other substrates, e.g. PMO coatings, as shown in previous tests. Nevertheless, a few trends can be recognised. First, the native PMO coatings exhibit the lowest survival rate, 2.8% for phenyl-PMO (PMO1) and 5.1% for biphenyl-PMO (PMO2). The survival rate can be enhanced by loading them with rolipram, which leads to an improvement of nearly 1.5% for both. By adding of BDNF to the phenyl-PMO coating, the SGNs survival rate does not change and remains at about 2.5%. The addition of BDNF to the biphenyl-PMO coating leads to a higher rate of 7.1%. The highest impact is found for the loading with rolipram and simultaneous addition of BDNF, the survival rates increases up to 5.6% for phenyl-PMO and twice as high (12.4%) for biphenyl-PMO. These range at the

same level as the negative control. Thus, for an effective impact on the SGNs, both rolipram and BDNF should be present, as was also shown by KRANZ and co-workers. In the presented test, only the positive control reached the number of 30% of survived SGNs, which could be compared with the rates achieved in the study of KRANZ *et al.*^[56] Nevertheless, these findings support the previous tests with fibroblasts, where the fibroblasts have shown better vitality on the biphenyl-PMO coating compared to the phenyl-PMO coating (see section 5.5.1). Furthermore, the biphenyl-PMO films can load and release more rolipram (chapter 5.3.4), which plays a major role in the protection of SNGs.

The microscopic images taken of the cell culture tests after 48 h are displayed in Figure 87. For this purpose, the SGNs were stained by a neurospecific dye and subsequently treated with an Elite ABC Kit and visualised by peroxidase diaminobenzidine substrate. The pictures qualitatively confirm the quantitative survival rates presented in Figure 86. The same trends regarding loading with rolipram and addition of BDNF can be seen. The samples concurrently modified with both supplements have the highest SGN numbers and the longest dendrites. The number of SGNs on both controls is higher and they also exhibit longer dendrites. The length and the number of branches of the dendrites are important for bridging the distance between the cochlea electrode and the cochlea itself. The distance between the electrode and the cochlea can range between 0.3 – 2.3 mm.^[46] The transfer of the electrical impulses on the dendrites is crucial for the audio impression with a cochlea implant.

As these are the first *in-vitro* tests for the effect of PMO coatings on spiral ganglion neurons, they have to be repeated to evaluate the results. For instance, another negative control – e.g. silicone – can be chosen to neglect the positive influence of the cell culture plastic on the cell growth. Furthermore, these experiments are sensitive towards the preparation technique and the quality of the cells derived from the animals.

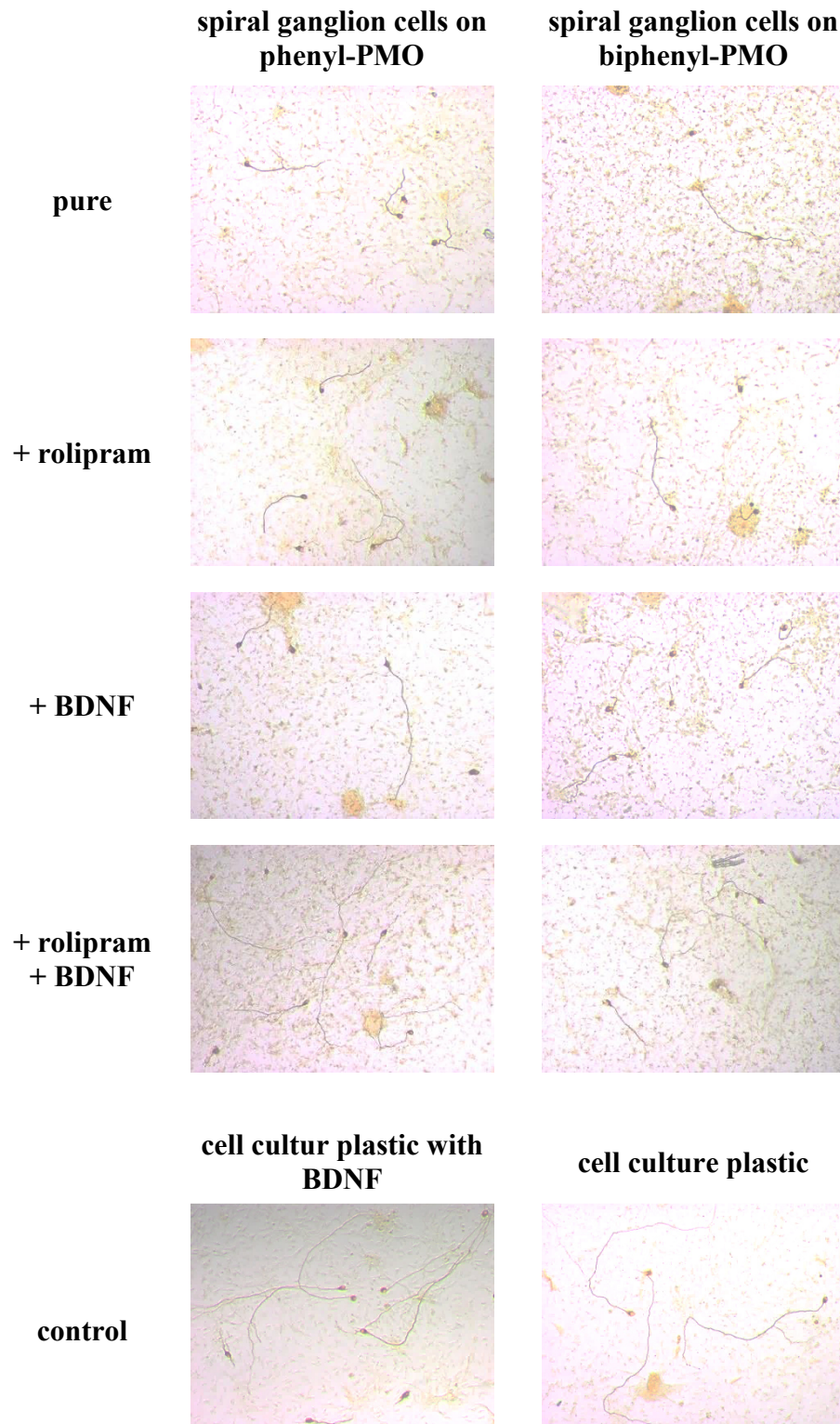


Figure 87: Microscopic images of the spiral ganglion cells on different surfaces. The SGNs were stained with a neurospecific dye and visualised with peroxidase diaminobenzidine. The number of SGNs is higher and the cell protrusions are longer on BDNF-containing samples. Overall, the controls show more SGNs compared to PMO coatings.

All cell culture tests performed displayed good or even excellent results in cytocompatibility. The phenyl-PMO coatings showed high vitality and proliferation rates in tests with fibroblasts and HUVECs, while the fibroblasts on biphenyl-PMO expressed an even better vitality. Overall, the cells seem to proliferate better on biphenyl-PMO coatings. The reason for this finding could be the less porous structure and thus smoother surface of the biphenyl-PMO film or even the higher hydrophobicity due to a less polar surface. Various studies have reported different findings on this topic. DOWLING *et al.*^[263] showed in a test series that a moderate surface roughness and a contact angle of about 64° led to the best cell adhesion and proliferation. Deviations in both directions impaired the results. Similar findings could be confirmed by other studies.^[264,265] Hence, regarding these characteristics, biphenyl-PMO coatings should provide better proliferation and adhesion of cells as they are more hydrophobic with little surface roughness.

5.6 Summary and Outlook

This work has presented new insights into the preparation, characterisation and application of periodic mesoporous organosilicas, especially phenyl- and biphenyl-PMO coatings on implant materials. PMOs are an effective alternative to nanoporous silicas as either nanoparticles or thin coatings. Due to their chemical structure, the PMOs already possess a first modification in the pore walls, namely the organic bridges. Their hydrophilicity is reduced compared to the mesoporous silica coatings, and thus polar drugs can be more easily loaded.

The primary objective of the study was to develop thin periodic mesoporous organosilica coatings on different substrates. This is the first study to examine the biocompatibility and bioactivity of PMO coatings as well as the loading of these coatings with different drugs. Overall, there are only few studies reported on the cell compatibility or the active uptake of bio-substances by PMOs. Most reports deal with ethylene-bridged PMOs or complex heterocyclic aromatic bridges and their applications in cancer cell therapy.^[133,134]

The preparation of novel coatings for biomedical applications based on phenyl- and biphenyl-PMOs with a uniform mesoporous structure was successful. The films produced with Pluronic® F-127 exhibited a well-ordered structure and high specific surface areas as well as high pore volume. Both properties are favourable for loading with substances. After the successful synthesis of PMO films on glass slides, these coatings were characterised by various methods. An overview and a comparison between characteristic data of phenyl-, biphenyl-PMO and mesoporous silica coatings is given in Table 13.

By means of thermogravimetric analysis, the thermic stability of phenyl- and biphenyl-PMOs was determined and the most appropriate calcination temperature (350 °C) for the decomposition of the SDA Pluronic® F-127 was obtained. The local chemical structure of PMOs was investigated by IR measurements. The latter indicated that the chemical structure of both PMOs remained largely undamaged during the annealing. Moreover, the chemical modification with sulfonic acid groups and the loading with the antibiotic ciprofloxacin could be proven by IR measurements. The TGA as well as IR measurements were performed partly on PMO powders.

Table 13: Comparison of properties between phenyl-, biphenyl-PMO and mesoporous silica coatings.

	phenyl-PMO	biphenyl-PMO	mesoporous silica
thermal stability / °C	< 550	< 455	< 700
film thickness / nm	360	270	150 ^[3]
S _{BET} / cm ² · cm ⁻²	460	160	11 ^[3]
pore volume / cm ³ · cm ⁻²	2.8 · 10 ⁻⁵	1.3 · 10 ⁻⁵	—
Young's modulus / GPa	6.6	3.3	18
contact angle / °	25	43	5
cumulative CFX release / μg · cm ⁻²	5.0 ^(*)	6.5	0.2 ^(*) ^[3]
cumulative rolipram release / μg · cm ⁻²	8.0	16.3	—
cell compatibility	good	good	good
BDNF production / ng · mL ⁻¹	50	—	25

(*) sulfonated phenyl-PMO 8.3 μg · cm⁻², sulfonated mesoporous silica 1.9 μg · cm⁻²^[3]

According to the X-ray diffraction measurements, the phenyl-PMO coatings had a periodic ordered mesoporous structure while biphenyl-PMO films showed no ordered porosity. One possible reason is the greater flexibility of the organic biphenylene linker along the longitudinal direction, leading to rotations or changes of the bond angles between the aromatic rings.

In SEM pictures, phenyl-PMO films demonstrated a porous surface. Cross-section images of the phenyl-PMO coatings displayed pores (pore diameters 9 – 10 nm) lying perpendicular to the film surface. The film thickness determined by TEM was 360 nm and was later confirmed by the ellipsometric measurements. TEM images of the scraped-off material approved the ordered porous structure of the phenyl-PMO. Furthermore, they depicted no regularity in the pore structure of the scraped-off biphenyl-PMO films. In order to comprehensively characterise the pore system of the PMO coatings, krypton sorption measurements were performed. For both coatings, they revealed high specific surface areas and a large pore volume. Nevertheless, the biphenyl-PMO film expressed three times lower values than the phenyl-PMO film, as summarised in Table 13. The shapes of both isotherms indicated bottle-neck pores. Like

the SBA-15 materials,^[237–239] the PMOs exhibited a bimodal pore width distribution. Furthermore, the sulfonation and loading with the antibiotic ciprofloxacin could be pursued by Kr sorption measurements, showing the expected decrease of the specific surface area and pore volume.

The initial plan was to apply PMO coatings on flexible silicone. The idea behind this was that the PMOs have flexible linkages. Thus, the coatings might be more flexible as compared to the brittle silica. In order to evaluate this idea, nanoindenter measurements were performed. They revealed that the PMO coatings had a lower Young's modulus than the mesoporous silica films, but not sufficiently low for flexible implants.

One of the most important properties of the PMOs investigated within this work is their ability to store and release active substances. This feature was analysed by loading both types of PMO coatings with the antibiotic ciprofloxacin and the neuroprotective drug rolipram. CFX was loaded in the pure and sulfonated phenyl-PMO film and into the biphenyl-PMO film. The sulfonated phenyl-PMO coating released the highest cumulated amount of CFX, followed by pure biphenyl- and the phenyl-PMO. This order can be explained by the polarity of the organic linker and electrostatic interactions between the sulfonic acid groups and ciprofloxacin. The release of rolipram demonstrated similar trends. Nearly twice as much rolipram was released from the biphenyl-PMO than from the phenyl-PMO. The biological efficacy of CFX-loaded coating was tested regarding their antibacterial activity versus *Pseudomonas aeruginosa*. In line with the release experiments, the different coatings showed similar antibacterial activity.

As an alternative characterisation method for drug-release experiments, FRET was employed. Here, the releasing medium – i.e. the PMO coatings – is directly examined by monitoring the fluorescence during the release phase. The PMO coatings acted as a donor, transferring electrons to the loaded acceptor ciprofloxacin. Due to changing FRET curves, the release of the drug from the coatings could be observed. The obtained values correlated perfectly with the conventional release experiments performed in parallel, providing an interesting method for *in-situ* monitoring of drug release.

Several cell culture studies stated an excellent cell compatibility of the PMO coatings towards NIH3T3 mouse fibroblasts and HUVECs. The cells proliferated well on the native PMO coatings. The fibroblasts showed a slightly reduced proliferation on the

CFX-loaded surfaces due to the growth inhibiting effect of CFX on fibroblasts, as described in other studies.^[260] The phenyl-PMO surface positively influenced the BDNF production from gene-modified fibroblasts, leading to liberated BDNF amounts comparable to those on cell culture plastic. Finally, the protective effect of rolipram-loaded PMO coatings on SGNs was examined. It was demonstrated that the phenyl-PMO exhibits the lowest protective effect on the SGNs, even with both supplements, rolipram and BDNF. By contrast, the biphenyl-PMO coatings revealed a considerably stronger protective effect. However, when compared to cell culture plastic, both PMO coatings showed less protective effects, even in the presence of the additives rolipram and BDNF. PMO coatings present a viable alternative to the well-characterised nanoporous silica bioactive films and can – due to their good biocompatibility – be further developed as a novel biomaterial.

Based on different PMO precursors, it is possible to adjust varying chemical properties, like pore size or hydrophobicity. In addition, the phenylene and biphenylene units as organic linkers offer interesting opportunities for further functionalisation, which can be useful for the binding of proteins or in drug-release applications. As all tests were performed on glass slides, the adhesion of the PMO coatings on various implant materials should be examined for future applications. Especially in the field of otolaryngology, such materials as metal alloys and silicone are widely used and should be tested for their compatibility with PMOs. XPS (X-ray photoelectron spectroscopy) would be helpful to prove whether some Si–C bonds are cleaved during the calcination. In particular, water sorption measurements should be performed to examine the hydrophilic character of the pores of the coatings for a better evaluation of interactions between the PMOs and drugs. A reproducible and simple test procedure has to be installed to determine quickly the loaded amount of drugs and thus predict their release time. The FRET technique is probably a suitable method for continuously monitoring drug release as it can provide results *in situ* from the releasing medium itself. The first experiments in this regard were promising. As the PMO coatings cannot be applied on flexible and soft materials like silicone rubber, the incorporation of PMO particles would be a promising way to combine the advantages of both materials. However, this field is new and fundamental research has to be performed here.

6. Results and Discussion II

Improving the Biocompatibility of PEEK by Coating with Thin Titania Films

Different titania films were produced by dip-coating to improve the bioactivity of PEEK implants. In the following, the samples investigated are designated as follows:

Sample type A: cleaned PEEK

Sample type B: plain titania film on PEEK substrate

Sample type C: titania film with added TiO₂ nanoparticles on PEEK substrate

Sample type D: titania film with TiO₂ nanoparticles formed *in situ* on PEEK substrate

6.1 Characterisation of Thin Titania Films on PEEK

Surface Morphology of Titania Films

The surface morphologies of cleaned and coated PEEK samples were investigated by means of SEM. The surfaces of cleaned PEEK samples – which appeared smooth and homogeneous on the macroscopic scale – showed scratches and bumps on the micrometre scale (Figure 88), which could have occurred during the production and cleaning steps.

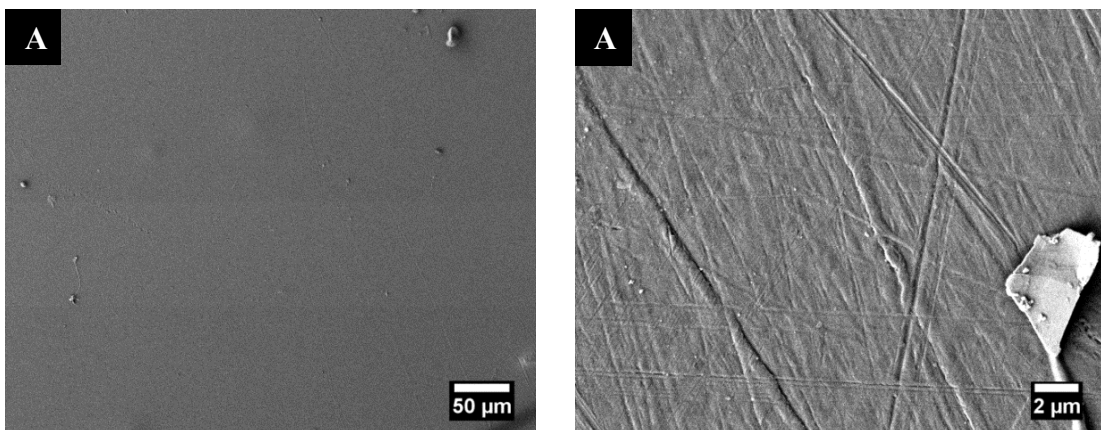


Figure 88: SEM images of a cleaned PEEK surface (type A) showing a smooth surface on the macroscopic scale and slightly structured on the microscopic scale.

SEM pictures of PEEK samples coated with a dense titania film (Figure 89) appeared very similar. Macroscopically and microscopically, the films showed no

inhomogeneities and had a dense structure without any cracks. Furthermore, the dense titania film seemed to imitate the surface topology of the cleaned PEEK, as the same scratched structure was visible (compare Figure 89 to Figure 88). Since the dense titania films were very thin (30 nm, estimated by ellipsometry), the polymer surface structures were directly transferred.

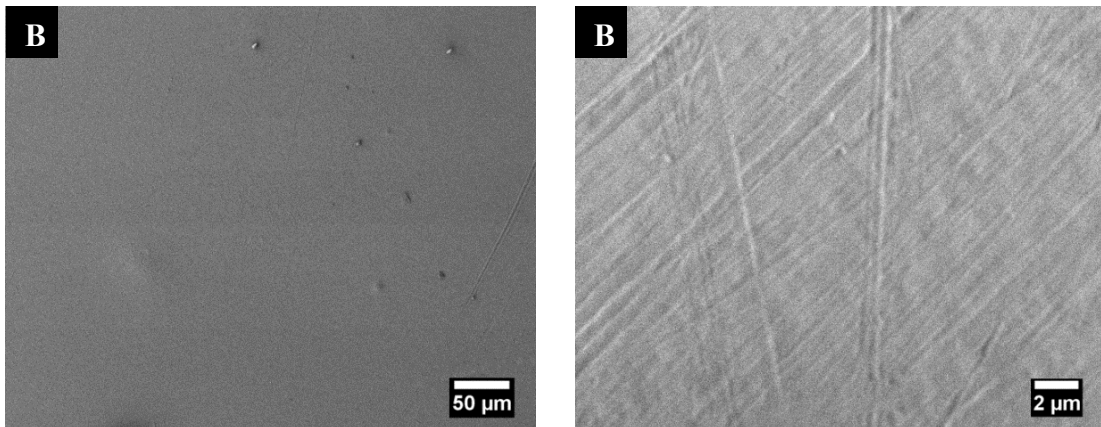


Figure 89: SEM images of a titania-coated PEEK surface (type B) imitating perfectly the cleaned PEEK surface.

The morphology of a dense titania film with added nanoparticles is presented in Figure 90. The small nanoparticles (size ranging from 10 to 20 nm) were mostly agglomerated. They formed nanoparticle heaps with sizes up to 2 μm . These agglomerates were homogeneously distributed in the film. In contrast to the film prepared without the nanoparticles, small cracks were visible within these coatings. Nevertheless, the adhesion between the film and the substrate was very good, whereby no chipped-off particles could be observed. The film thickness could not be measured by ellipsometry, presumably due to the inhomogeneous morphology of the coating. Comparing further SEM images of samples type C to the cleaned PEEK substrate, it can be assumed by analogy that the film thickness was in the same range as for the dense titania coatings (around 30 nm).

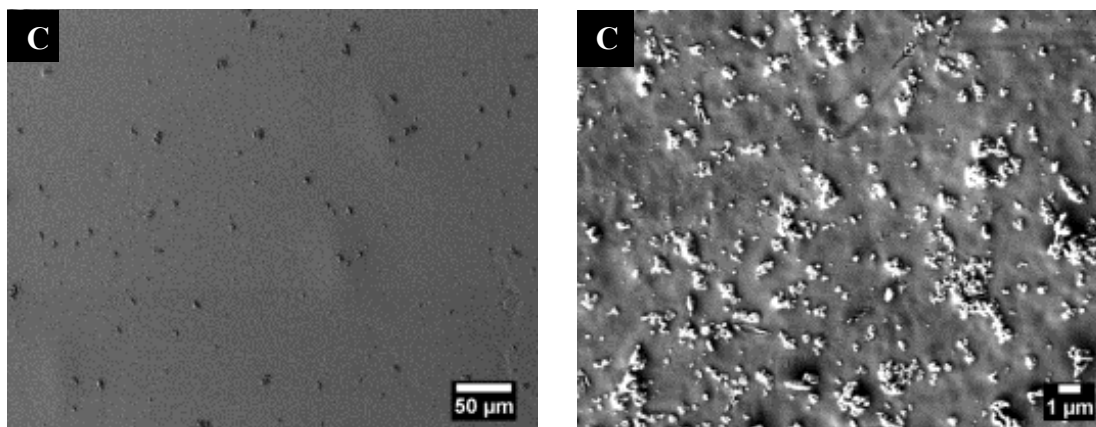


Figure 90: SEM images of titania-coated PEEK substrate with added TiO₂ particles (type C).

The titania films that were produced using the additives DEA and acac contained small nanoparticles produced *in situ*. The former exhibited macroscopically a smooth surface, while microscopically the films exposed a heterogeneous topology of the surface (Figure 91). The whole surface was covered by a film and small nano-sized particles were evenly distributed all over it. There were also knob-like agglomerates which were much smaller than the added titania particles, compared to sample type C. Thus, the nanoparticles must have been formed during the synthesis. The formation of the microstructures was controlled by the additives DEA and acac according to the mechanism described elsewhere.^[194] Notably, after the drying step no cracks could be observed. Hence, the thickness of the films could be determined by ellipsometry to be ca. 50 nm. Both coatings C and D showed promising topology for a good cell-substrate interaction due to their enhanced surface roughness.^[187]

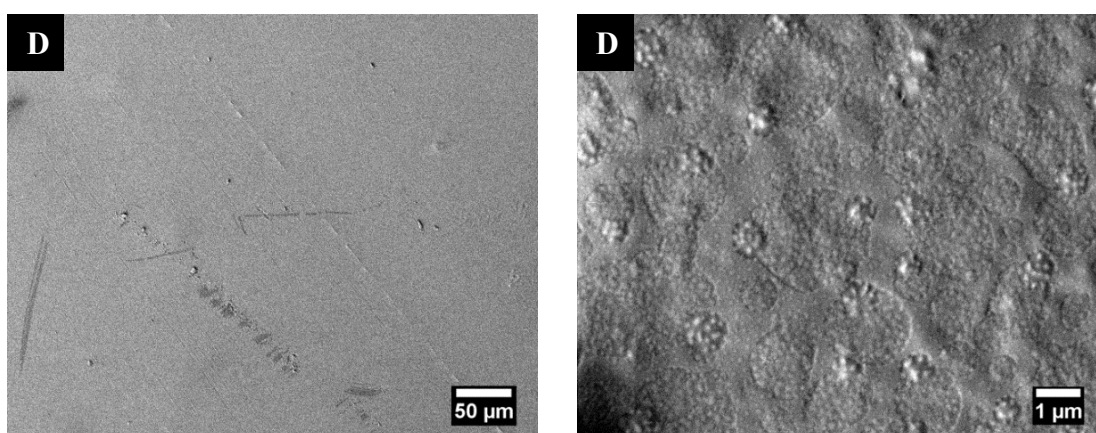


Figure 91: SEM image of a titania-coated PEEK sample with nanoparticles formed *in situ* (type D).

The thickness of the titania thin films ranged between 30 to 50 nm and was thus nearly five times thicker compared to the spontaneously-formed native oxide films on pure titanium. These are amorphous at room temperature and have a thickness of 2-6 nm.^[266] The native oxide films are known to be highly biocompatible enhancing the growth of cells on the coated implant surfaces.^[267–269] The process parameters had been chosen so that the titania oxide layers were as thin as possible, trying to imitate the native titania oxide films.

X-Ray Diffraction Analysis of Titania Films

The X-ray diffraction pattern shown in Figure 92 displayed several broad reflections, corresponding to the partially crystalline character of the PEEK substrates.^[270] The degree of crystallinity of PEEK varies depending on the thermal processing during manufacturing.^[64] All PEEK substrates carrying a titania coating showed the same XRD pattern (Figure 92), whereby no further reflections could be found for titania.

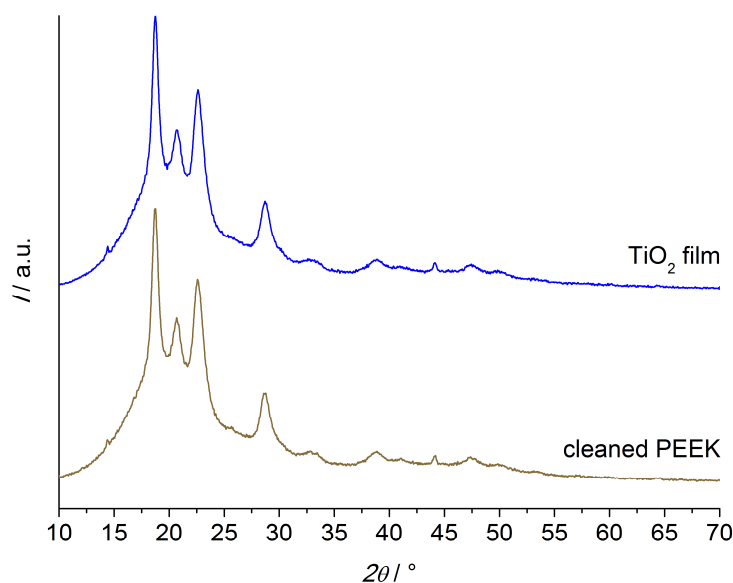


Figure 92: XRD patterns of cleaned PEEK, and a titania film on PEEK.

One possible reason for the absence of additional reflections was the low film thickness, while another was the amorphous morphology of the titania films. Both characteristics would be similar to the native titania films formed on blank titanium materials.^[266] Due to the post-synthetic treatment at low temperatures, an amorphous morphology of the

titania films was assumed. A higher annealing temperature of above 300 °C would be necessary to form thin titania films exhibiting a crystalline structure.^[271] Although nanoparticles had been added to the synthesis batch for film C, no corresponding signal could be detected in the XRD. This can be assigned to either the small volume fraction of the nanoparticles in the film or the large width of the reflections due to the small crystallite size.

Water Contact Angle Measurements on Titania Films

In order to investigate the changes in the surface properties of the coated samples, contact angle measurements were performed. The static contact angles of water were measured on uncoated PEEK samples and titania-coated ones (Figure 93 and Figure 94).

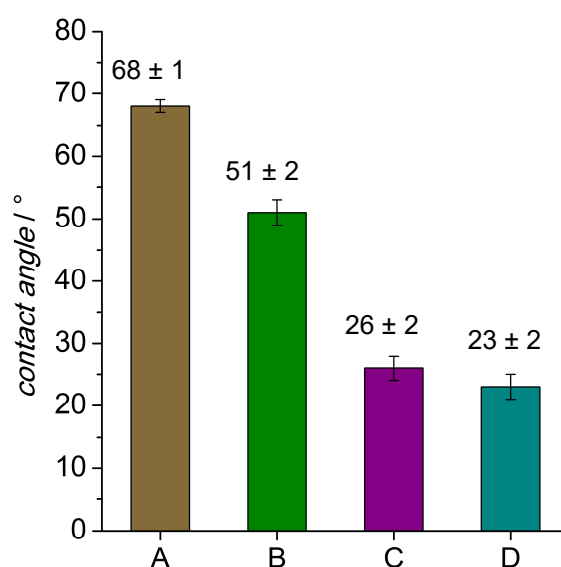


Figure 93: Results of static contact angle measurements with water. The statistical data of the measurements display the highest value for cleaned PEEK (A) and the lowest values for the samples with nanoparticles (C, D). The contact angle for plain titania coating (B) is between these two.

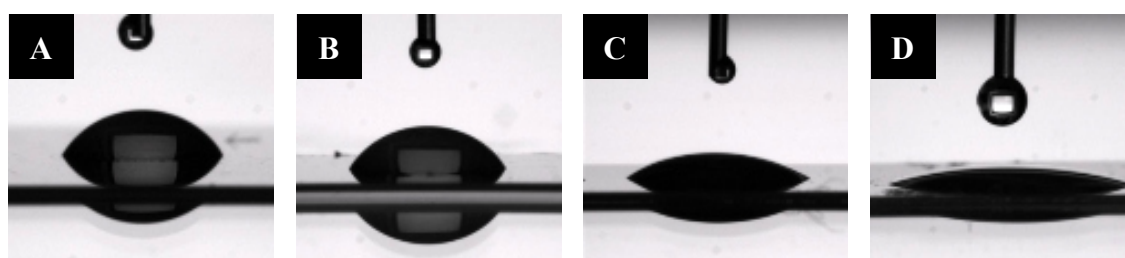


Figure 94: Images of the water contact angle measurements for all four types.

The uncoated cleaned PEEK surface had a water contact angle of $68^\circ \pm 1^\circ$. The water contact angle of the dense titania film on PEEK was $51^\circ \pm 2^\circ$ and thus more hydrophilic than the uncoated PEEK surface. This can be assigned to the oxidic character of the surface presenting hydroxyl groups. As no calcination was performed, the density of hydroxyl groups was expected to be high. Native as well as synthesised metal oxide films usually form hydroxyl groups on their surface, whereby the process has been previously investigated.^[272] The polarity of the surface has a strong influence on the adsorption of amino acids, proteins and other organic molecules that are included in body fluids. In addition, the interactions of physiologically important ions like calcium and phosphate with the surface of an implant are influenced by hydroxyl groups.^[273,274] Therefore, the increased density of the polar groups on the implant surface could intensify the strength of the cell interactions.

The presence of titania nanoparticles in the films had a strong influence on the water contact angle. The film with the additional nanoparticles had a water contact angle of $26^\circ \pm 2^\circ$. The titania film with particles formed *in situ* exhibited a contact angle of $23^\circ \pm 2^\circ$. These decreases can be ascribed to the increased surface roughness and increased surface area caused by the (partially agglomerated) titania nanoparticles. Thus, the surface topology had a direct effect on the wettability of the samples. Surface nanostructures and surface roughness on the micrometre scale can directly influence the hydrophilicity of a surface and its wettability.^[194,247,275]

6.2 Mechanical Stability Studies of Titania Films

In order to characterise the mechanical adhesion stability of the titania films to PEEK surfaces, adhesive tape tests were performed. The tape was pressed onto the sample with one kilogram for 2 hours and subsequently pulled off. In Figure 95, SEM pictures taken after this experiment are shown.

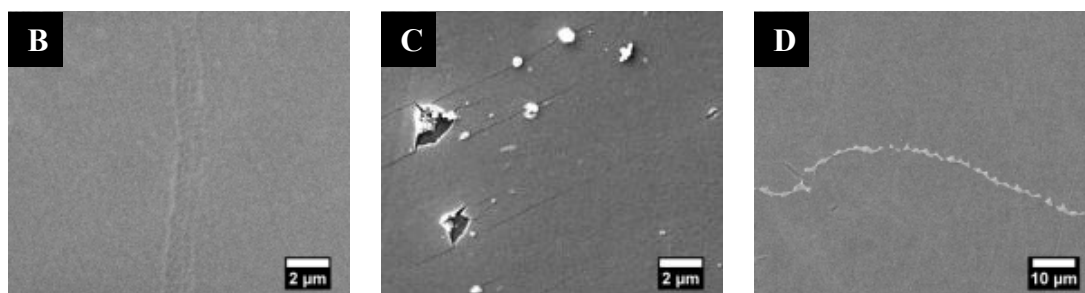


Figure 95: SEM images taken after the adhesive tape test. The adhesive tape was peeled off after 2 hours of loading with a mass of one kilogram. Only the titania film with the embedded nanoparticles (B) showed some spots that had been peeled off.

The dense titania film (Figure 95 B) did not display any damage or defects, suggesting a very strong adherence on the PEEK surface. By contrast, the titania film (Figure 95 C) with additional nanoparticles showed defects after pulling off the tape. Judging from the size and arrangement of the defects, it is obvious that the large agglomerates of nanoparticles are responsible for these defects and that especially the spots where the agglomerated nanoparticles were positioned peeled off. As already shown in Figure 1, these films also revealed some cracks after the drying step. The titania film produced in the presence of additives – which contained homogeneously-distributed nanoparticles and only small agglomerates – survived the tape test without defect (Figure 95 D), whereby only a small residue of the adhesive glue of the tape remained on the film surface.

These results refer to a strong adhesion of the amorphous titania films on PEEK substrates and can be taken as an indication for a good resistance under mechanical stress; for example, during the handling of a coated implant. The mechanical stability should be further investigated by adhesion tests with measurable adhesion forces like a scratch test.^[196]

6.3 Chemical Stability Studies of Titania Films

The titania coatings were also tested for their chemical stability by exposing them to PBS and ethanol. The amount of titanium ions released into a solution of solvent after certain time – a measure for the dissolution of the titania coating – was determined by using chromotropic acid, which forms a violet-coloured complex with Ti^{4+} ions. By means of a calibration procedure, the smallest detectable concentration of Ti^{4+} ions in

PBS was found to be $4 \cdot 10^{-7} \text{ mol} \cdot \text{l}^{-1}$ and for ethanol $5 \cdot 10^{-6} \text{ mol} \cdot \text{l}^{-1}$. For all tested periods of time – 24 h, 48 h and one week – all chromotropic acid tests were negative. More precisely, the concentration values were below the detection limit. These results indicate that the titania films – independent of their actual morphology – are stable in PBS and ethanol or rather show only a solubility below the detectable concentration. Contact angle measurements after sample storage for one week in PBS are presented in Figure 96. In Figure 97, SEM images taken after incubation of the samples in PBS for one week are displayed.

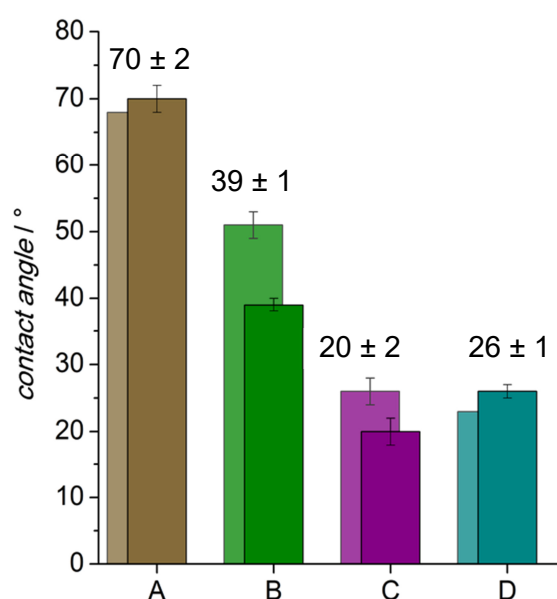


Figure 96: Contact angle measurements of PEEK and titania films after incubation in PBS for one week.

The contact angle of the cleaned PEEK samples (Figure 96 A) did not change after treatment in the PBS solution, while the SEM images also showed an unchanged surface (Figure 97 A). The contact angle of the dense titania film decreased by $10^\circ \pm 1^\circ$ (Figure 96 B), presumably due to the raised hydroxyl groups on the film after storage in PBS. The SEM images (Figure 97 B) revealed no changes of the sample surface. The hydroxyl groups are generated on the titania after storage in aqueous media due to tensioned Ti-O-Ti groups on the film surface. These are cleaved into Ti-OH...OH-Ti groups, resulting in a higher hydrophilic character of the coating. The contact angle of the film with the added particles decreased by $6^\circ \pm 2^\circ$ (Figure 96 C), but the SEM image (Figure 97 C) showed some cracks in the coating after the storage and drying step. Here,

it seems that the added particles act as starting points for the cracks. The film with particles formed *in situ* showed no changes of the contact angle and no changes of the surface (Figure 96 and Figure 97 D).

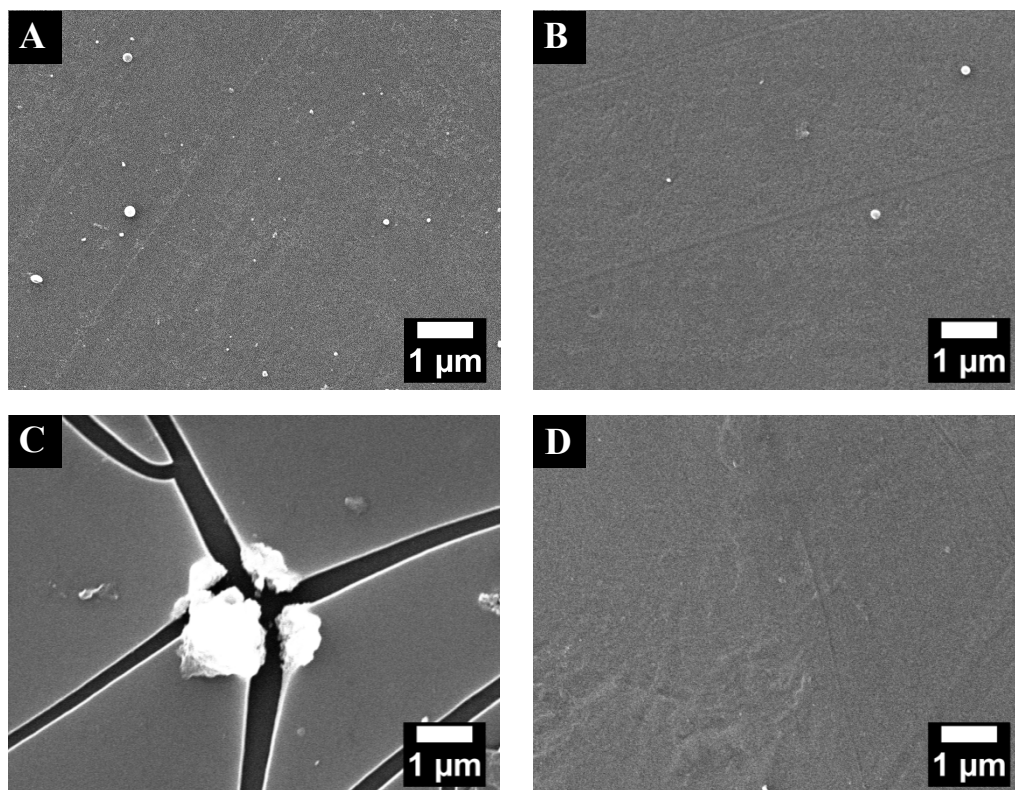


Figure 97: SEM images taken after incubation of the samples in PBS for one week. The titania film with the embedded nanoparticles showed cracked titania coating (D). Other surfaces showed little changes of the surfaces compared to those before incubation.

It seemed that the treatment with PBS had no effect on the coating, probably due to the presence of the stabilising agents during the synthesis such as diethanolamine and acetylaceton. The contact angle measurements revealed a slightly increase of the hydrophilic properties of the titania coatings after storage in PBS. Probably, due to generated hydroxyl groups. In SEM images, no changes of the coatings surface structure could be found.

6.4 Cytocompatibility Tests of Titania-Coated PEEK

DR. BUSHRA RAIS at the Helmholtz Centre for Infection Research Braunschweig performed the cytocompatibility tests for titania coated PEEK samples.

6. Results and Discussion II

These cell culture tests were carried out using mouse fibroblasts (NIH3T3) and a human osteoblast-like cell line (MG63 osteosarcoma) to examine the cytocompatibility of the titania coatings on PEEK substrates. The cells were grown on the cleaned PEEK surface as well as titania-coated PEEK samples. This cell growth was compared to that on the cell culture plastic, which is an ideal substrate for cell growth. The cells were labelled by a cell membrane permeable non-fluorescent compound (CFSE) to visualise viable cells. In the cell membrane of living cells, this compound is cleaved by intracellular esterases, resulting in a fluorescent dye. Subsequently, viable cells on different PEEK surfaces were imaged using a UV fluorescence detection microscope. The cell numbers are gathered in Figure 98, while fluorescence pictures of the single cell tests on different surfaces are displayed in Figure 99 and Figure 100.

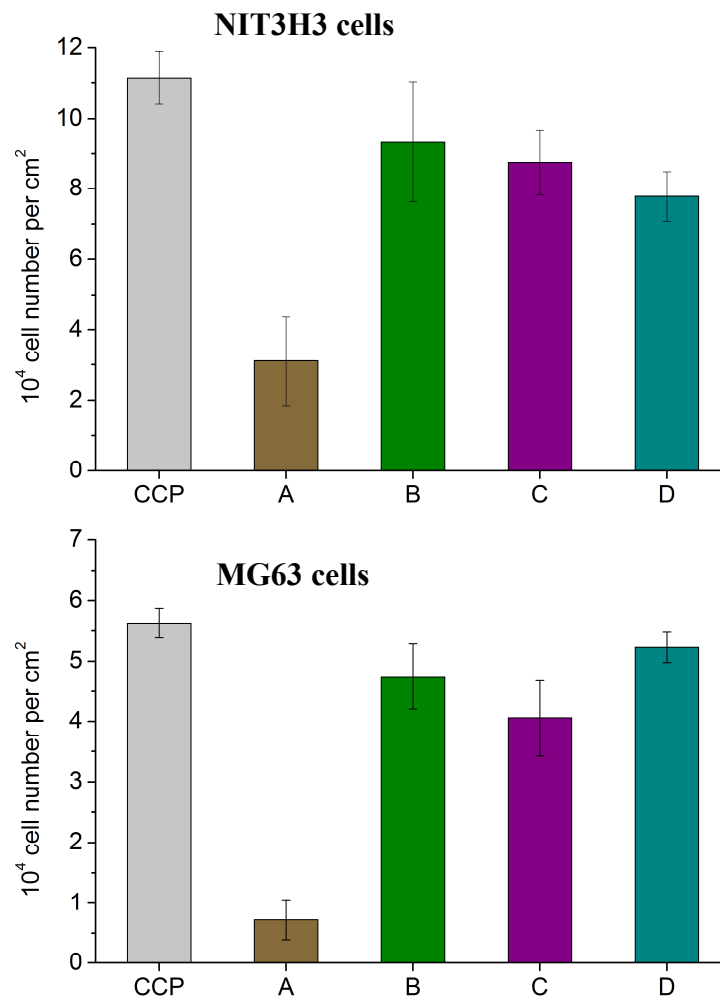


Figure 98: Results from cell culture tests using the **top)** NIH3T3 cell line, and **bottom)** MG63 cell line: Quantitative evaluation of cell densities.

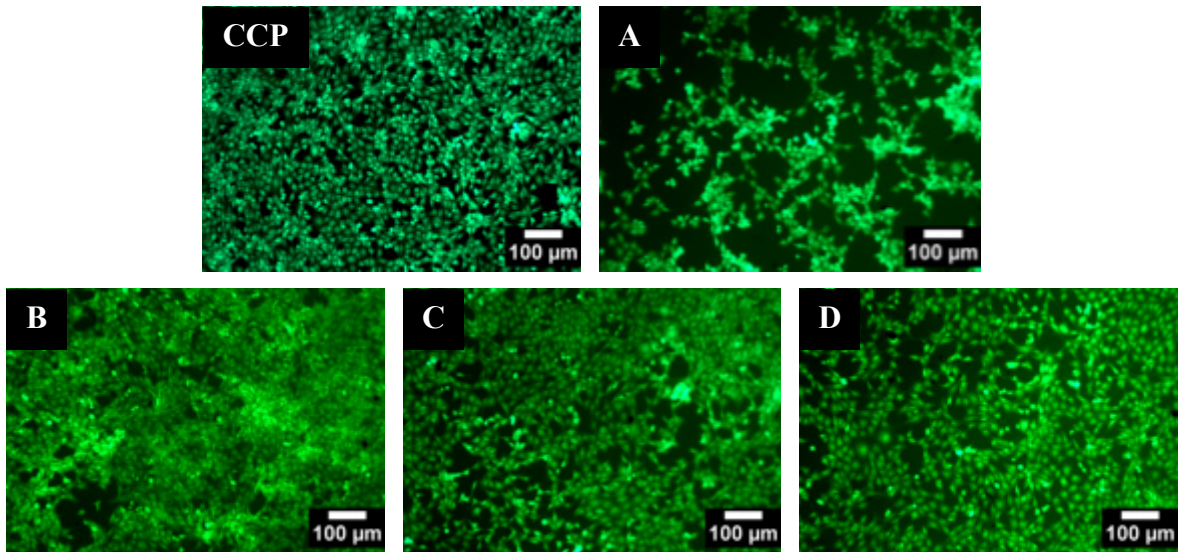


Figure 99: Results obtained from the cell culture tests using NIH3T3 cell line. Qualitatively, the cell densities on the coated PEEK samples (B-D) are higher compared to the cleaned PEEK sample (A), and comparable to the cell growth on the cell culture plate (CCP).

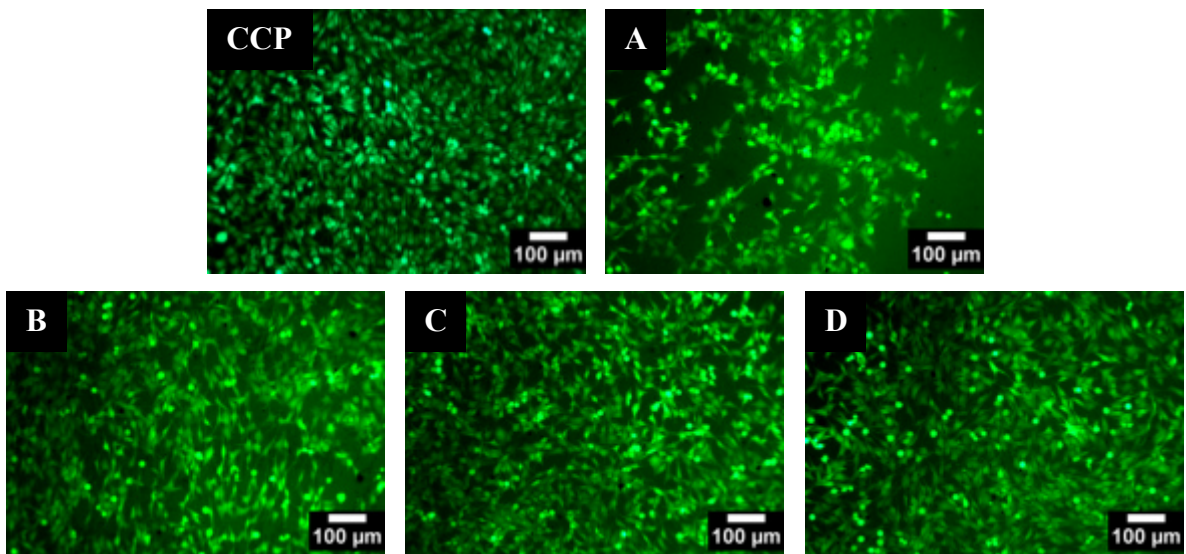


Figure 100: Results obtained from the cell culture tests using MG63 cell line. The results are comparable to those of the NIH3T3 cell culture tests. The cells proliferate better on the coated PEEK samples (B-D) in contrast to the cleaned PEEK sample (A).

After 48 hours of incubation, the cell density of fibroblasts and of osteosarcoma cells grown on titania coatings were almost as high as the cell density on cell culture-optimised plastic and significantly larger than on pure PEEK surfaces (Figure 98). The fibroblasts as well as the osteosarcoma cells adhered only poorly on the cleaned PEEK surface, while the cell density on these samples was also low (Figure 99 A and Figure

100 A). By contrast, both cell lines showed an excellent adherence and cell density on all titania-coated PEEK samples (Figure 99 B, C, D and Figure 100 B, C, D). The densities of the osteoblast-like cells on titania coatings were more than five times higher than those achieved on PEEK surfaces. These results indicated that the cytocompatibility of PEEK implants could unequivocally be improved by titania coatings. The bone-derived osteosarcoma cells proliferated preferentially on the titania coatings. This could improve the implant interactions with bony tissue.

It has been documented that there are at least four crucial characteristics of the implant surfaces that influence the interaction with cells and tissue, namely surface composition, roughness, topography and energy.^[276,277] The interactions of cells with surfaces influence not only the cell proliferation rate but also the cell morphology. A limited cell adhesion correlates with rounded cells. Optimal surface features allow cells to stretch or spread out on the surface and adhere better. In this case, it was shown that cells on pure PEEK surfaces formed clusters and did not spread out. This was consistent with the notion that the chemical inertness and hydrophobic character may offer fewer possibilities for interactions with cell adhesion proteins.^[278]

The results obtained from the cell culture experiments have provided clear evidence that the cytocompatibility and the bioactivity of PEEK can be considerably enhanced by coating with a titania film. The type of the film – whether a plain one or one containing nanoparticles – only plays a minor role. For both cell types, the bare PEEK samples showed the lowest cytocompatibility. The cells appeared round and not elongated in shape and formed cell clusters instead of spreading over the surface. The reasons are smoothness, the chemically-inert character and the hydrophobicity of the plain PEEK surface, which offers less attractive interaction points for cell adhesion.^[278]

At first sight, the surface of the PEEK samples coated with the plain titania film shows similar characteristics as it has a smooth surface (compare Figure 88 B) and is also rather hydrophobic (contact angle of 51°). However, the cells were elongated and spread over the whole surface of the sample. This can be explained by the fact that the oxidic surface imparted by titania film is covered with –OH groups, which are partially deprotonated in aqueous solutions (considering the isoelectronic point = 6 of titania), so that the surface is negatively charged. Several *in-vitro* studies^[106,276] postulated that positively-charged Ca²⁺ ions – present, for example, in SBF solution – bind to

negatively-charged groups on titania surfaces. These Ca^{2+} ions combine with negatively-charged phosphate ions and form amorphous calcium phosphate. In the body environment, this calcium phosphate transforms spontaneously into apatite.

The presence of the nanoparticles – in either larger agglomerates in sample type C or more even distribution in sample type D – increases the hydrophilicity and the surface roughness. These properties affect the cell adhesion in a crucial way. Many studies [187,266,267,276] have shown that structured surfaces enhance the surface area and promote cellular adherence. In this study, this effect was not observed for the structured samples C and D. Neither the addition of nanoparticles nor the *in-situ* formation of nanoparticles during the synthesis led to increased cell numbers for both cell lines. However, both samples C and D still exhibited a much better cytocompatibility than the uncoated PEEK. Obviously, the properties of samples C and D are mainly governed by those parts of the surface that are covered by the plain titania film, with only minor influence of the nanoparticles. In sum, titania-coated PEEK samples clearly showed better results in the cell culture tests compared to the uncoated PEEK. Taking the simple fabrication process of the plain titania coating and its mechanical and chemical stability into account, the application of plain titania coatings is a promising way to improve the biocompatibility and bioactivity of PEEK.

6.5 Summary and Outlook

The purpose of this study was to increase the biocompatibility and bioactivity of PEEK, whereby titania coatings on PEEK substrates were prepared and investigated for biomedical applications and compared to uncoated PEEK. Surface-covering titania films were produced by dip-coating, a simple and facile technique that can also be applied to complex implant shapes. Titania was chosen due to its known positive interaction with the surrounding body tissue in the orthopaedic field. Three different titania films were investigated: plain titania films, titania films with added preformed titania particles and titania films with titania nanoparticles formed during the synthesis.

The films differed in their surface properties like topology and wettability. The plain titania film showed a smooth and plain surface that adopted very well to those of the substrate with a wettability that was slightly decreased compared to the blank PEEK substrates. Both other coatings with the incorporated particles were much rougher compared to the plain one. The titania film with the added particles showed a layer with larger agglomerates of the titania particles that were more edgy and distinct in the titania layer. The coating with the particles formed *in situ* were also rougher compared to the plain titania film, although the particles were smoother than the added ones. Both coatings with particles had low contact angles in the same range. All coatings had a good mechanical stability investigated by the tape test. Only the titania film with added particles displayed some spalling in the regions with particle agglomerates, where probably the added particles acted as starting points for the spalling.

No degradation of the titania films was observed in aqueous solutions or in ethanol. After one week of storage in PBS, the coatings even showed a smaller contact angle, probably due to additionally formed hydroxyl groups on the coating surfaces. This fact may influence the cell culture tests. As expected, the cell culture tests performed with mouse fibroblasts NIH3T3 and the human osteosarcoma MG63 confirmed the poor cytocompatibility of the inert PEEK surface, while the all titania films demonstrated a good adherence and proliferation of the cells. Whereas the cell numbers ranged at a similar level for all samples, the plain titania film revealed the best results. Hence, titania coatings can decisively improve the biocompatibility and bioactivity of PEEK. Among the different titania coatings investigated, the plain titania film offers the best prospects.

For titania-coated PEEK samples, further mechanic stability studies have to be performed, e.g. a scratch tests to confirm good adherence of the titania films on PEEK surfaces. Moreover, the stability of the coating in simulated body fluids over longer time periods has to be repeated to determine the point when the titania film dissolves or undergoes spalling. Finally, cytocompatibility tests should be carried out with other cells and further cell culture studies should involve functional cells like osteoblasts or mesenchymal stem cells.

7. Conclusions

The goal of this thesis was to develop bioactive coatings based on titania and periodic mesoporous organosilica coatings. Both types of coatings were synthesised in sol-gel processes and applied onto substrates by dip-coating. The coatings had to fulfil several crucial requirements like bioactivity, excellent cytocompatibility, inhibited bacterial growth and mechanical stability on the substrate. In addition to the basic physicochemical characterisation, these properties were evaluated for the two different types of coatings. Furthermore, the coatings were also evaluated for their antibacterial efficacy.

In the first approach, we were able to establish novel coatings for biomedical applications based on phenyl- and biphenyl-PMO with a uniform mesoporous structure in which the organic linkers are embedded in the walls of the silica network. They possess a high surface area with a high pore volume, which is very favourable for incorporation of drugs. Furthermore, the hydrophilicity is reduced compared to the mesoporous silica coatings, so polar drugs can be loaded more effectively. Drugs carrying a charge in physiological solutions can be bound by electrostatic forces to attaching positive or negative groups to the organosilica framework, like in our case the sulfonic acid group. The PMO coatings were more flexible than their pure silica counterparts. The calcined, the sulfonate-functionalised as well as the drug-loaded PMO coatings showed a good biocompatibility in cell culture experiments, which was the most crucial factor for developing a biomaterial. Drug loading of the phenyl-PMO layers with the antibiotic ciprofloxacin was successful, as could be demonstrated in sorption as well as drug-release experiments. The antibacterial efficacy tests with pathogenic bacteria confirmed the drug-release results, where in the first eight days the bacteria were killed completely with a weaker efficacy in the following seven days independent from the modification of the layers. PMO coatings present a viable alternative to the well-characterised nanoporous silica bioactive films and – due to their good biocompatibility – can be further developed as a novel biomaterial. Based on different PMO precursors, it should be possible to adjust varying chemical properties, like pore size or hydrophobicity. In addition, the benzene and biphenylene units in the organic linkers offer interesting opportunities for further functionalisation, which can be useful for binding of proteins or in drug-release applications.

In the second approach, the purpose was to increase the biocompatibility and bioactivity of polyether ether ketone (PEEK), as this material is bioinert by its chemical nature. Therefore, we have prepared and examined titania coatings on PEEK substrates for biomedical applications and compared them to uncoated PEEK. Surface-covering titania films were produced by dip-coating, a simple and facile technique that can also be applied for complex implant shapes. Cell culture tests confirmed the poor cytocompatibility of the inert PEEK surface, whereas the titania films all demonstrated a good adherence and proliferation of the cells. Thus, it was shown that titania coatings can improve the biocompatibility and bioactivity of PEEK decisively. Titania-coated PEEK implants have to be further developed for applications in the biomedical field, especially for the use in osteogenesis. Among the different titania coatings investigated, the plain titania film offers the best prospects.

Summarising, the present thesis has shown that different types of implant materials can be equipped with bioactive coatings via simple sol-gel-based dip-coating processes. They can influence the bioactivity positively and – when nanoporous coating materials are used – supply a reservoir for drug delivery. In this context, the PMO-based coatings appear most promising as a novel implant coating material.

8. References

- [1] B. G. X. Zhang, D. E. Myers, G. G. Wallace, M. Brandt, P. F. M. Choong, *Int. J. Mol. Sci.* **2014**, *15*, 11878.
- [2] C. X. Lin, S. Z. Qiao, C. Z. Yu, S. Ismadji, G. Q. Lu, *Microporous Mesoporous Mater.* **2009**, *117*, 213.
- [3] N. Ehlert, M. Badar, A. Christel, S. J. Lohmeier, T. Luessenhop, M. Stieve, T. Lenarz, P. P. Mueller, P. Behrens, *J. Mater. Chem.* **2010**, *21*, 752.
- [4] N. Ehlert, P. P. Mueller, M. Stieve, T. Lenarz, P. Behrens, *Chem. Soc. Rev.* **2013**, *42*, 3847.
- [5] C. Turck, G. Brandes, I. Krueger, P. Behrens, H. Mojallal, T. Lenarz, M. Stieve, *Acta Oto-Laryngol.* **2007**, *127*, 801.
- [6] N. Ehlert, A. Hoffmann, T. Luessenhop, G. Gross, P. P. Mueller, M. Stieve, T. Lenarz, P. Behrens, *Acta Biomater.* **2011**, *7*, 1772.
- [7] N. Ehlert, P. P. Müller, M. Stieve, P. Behrens, *Microporous Mesoporous Mater.* **2010**, *131*, 51.
- [8] F. Hoffmann, M. Cornelius, J. Morell, M. Fröba, *Angew. Chem. Int. Ed.* **2006**, *45*, 3216.
- [9] P. van der Voort, D. Esquivel, E. de Canck, F. Goethals, I. van Driessche, F. J. Romero-Salguero, *Chem. Soc. Rev.* **2013**, *42*, 3913.
- [10] S. Inagaki, S. Guan, T. Ohsuna, O. Terasaki, *Nature* **2002**, *416*, 304.
- [11] G. A. Ozin, T. Asefa, M. J. MacLachlan, N. Coombs, *Nature* **1999**, *402*, 867.
- [12] W. J. Hunkeler, G. A. Ozin, *J. Mater. Chem.* **2005**, *15*, 3716.
- [13] F. Hoffmann, M. Fröba, *Chem. Soc. Rev.* **2011**, *40*, 608.
- [14] W. Wang, D. Faulkner, J. Moir, G. Ozin, *Sci. China Chem.* **2011**, *54*, 1920.
- [15] M. Seino, W. Wang, J. E. Lofgreen, D. P. Puzzo, T. Manabe, G. A. Ozin, *J. Am. Chem. Soc.* **2011**, *133*, 18082.
- [16] M. Vallet-Regí, F. Balas, D. Arcos, *Angew. Chem. Int. Ed. Engl.* **2007**, *46*, 7548.
- [17] T. Lenarz, H.-G. Boenninghaus, *Hals-Nasen-Ohren-Heilkunde*, Springer-Verlag Berlin Heidelberg, Heidelberg, Germany **2012**.
- [18] T. Heemeier, *Biomaterialien für Implantate im Ohrbereich*, Hannover **2016**.
- [19] T. Lenarz, *Cochlea-Implantat: Ein praktischer Leitfaden für die Versorgung von Kindern und Erwachsenen*, Springer Berlin Heidelberg, Berlin, Heidelberg **1998**.
- [20] R. F. Schmidt, F. Lang, M. Heckmann, *Physiologie des Menschen: Mit Pathophysiologie*, Springer-Verlag Berlin Heidelberg, Berlin, Heidelberg **2011**.

-
- [21] H. Lippert, *Lehrbuch Anatomie: 184 Tabellen*, Urban & Fischer, München [u.a.] **2002**.
- [22] R. F. Schmidt, H.-G. Schaible, *Neuro-und sinnesphysiologie*, Springer, Berlin **2006**.
- [23] MED-EL Elektromedizinische Geräte Gesellschaft m.b.H., *Hearing Solutions* **2017**, <http://www.medel.com/int/>.
- [24] G. Stange, *Laryngorhinootologie* **1989**, *68*, 653.
- [25] N. Ehlert, *Chemical and biochemical functionalization of middle ear implants*, Hannover **2009**.
- [26] UC Irvine Department of Head & Neck Surgery, *Cholesteatoma* **2017**, <http://www.ent.uci.edu/learning-center/blog/causes-and-treatments-cholesteatomas.asp>.
- [27] Spiggle & Theis Medizintechnik, *Middle Ear Implants* **2017**, <http://www.spiggle-theis.com/en/products/otology/middle-ear-implants>.
- [28] D. Beutner, K.-B. Hüttenbrink, *GMS Curr. Top. Otorhinolaryngol Head Neck Surg.* **2011**, *8*, Doc09.
- [29] S. Koscielny, E. Beleites, *HNO* **2001**, *49*, 367.
- [30] M. Hoffstetter, K.-H. Ebert, M. Schaumann, E. Wintermantel, in *World Congress on Medical Physics and Biomedical Engineering*, **2009** *25*, 49.
- [31] SFB 599, *Veröffentlichungen Teilprojekt D1 - Funktionalisierte Mittelohrprothese* **2016**, http://sfb599.de/index.php?id=publikationen_teilprojekt_d1.
- [32] J.-M. Seitz, M. Durisin, J. Goldman, J. W. Drelich, *Adv. Healthc. Mater.* **2015**, *4*, 1915.
- [33] J. Huang, Y. Ren, Y. Jiang, B. Zhang, K. Yang, *Front. Mater. Sci. China.* **2007**, *1*, 405.
- [34] R. Lensing, P. Behrens, P. P. Muller, T. Lenarz, M. Stieve, *J. Biomater. Appl.* **2014**, *28*, 688.
- [35] F. Duda, S. Bradel, A. Bleich, P. Abendroth, T. Heemeier, N. Ehlert, P. Behrens, K.-H. Esser, T. Lenarz, G. Brandes, N. K. Prenzler, *J. Biomater. Appl.* **2015**, *30*, 17.
- [36] N. Ehlert, T. Lüßenhop, I. Krueger, A. Feldhoff, M. Badar, P. P. Mueller, M. Stieve, T. Lenarz, P. Behrens, *BioNanoMaterials* **2013**, *14*.
- [37] D. Hesse, N. Ehlert, T. Lüßenhop, A. Smoczek, S. Glage, P. Behrens, P. P. Müller, K.-H. Esser, T. Lenarz, M. Stieve, A. Bleich, N. K. Prenzler, *Otol. Neurotol.* **2013**, *34*, 1138.
- [38] R. Lensing, A. Bleich, A. Smoczek, S. Glage, N. Ehlert, T. Luessenhop, P. Behrens, P. P. Müller, M. Kietzmann, M. Stieve, *Acta Biomater.* **2013**, *9*, 4815.

8. References

- [39] J. C. Vogt, G. Brandes, N. Ehlert, P. Behrens, I. Nolte, P. P. Mueller, T. Lenarz, M. Stieve, *J. Biomater. Appl.* **2009**, *24*, 175.
- [40] J. C. Vogt, G. Brandes, I. Krüger, P. Behrens, I. Nolte, T. Lenarz, M. Stieve, *J. Mater. Sci. Mater. Med.* **2008**, *19*, 2629.
- [41] F. Duda, M. Kieke, F. Waltz, M. E. Schweinefuss, M. Badar, P. P. Müller, K.-H. Esser, T. Lenarz, P. Behrens, N. K. Prenzler, *J. Mater. Sci. Mater. Med.* **2015**, *26*, 5334.
- [42] D. Hesse, M. Badar, A. Bleich, A. Smoczek, S. Glage, M. Kieke, P. Behrens, P. P. Müller, K.-H. Esser, M. Stieve, N. K. Prenzler, *J. Mater. Sci. Mater. Med.* **2013**, *24*, 129.
- [43] CochleaTM, *Chochla Implantate* **2017**, <http://www.cochlear.com/wps/wcm/connect/de/startseite/hoeren-und-hoerverlust/hoeren-und-hoerverlust/behandlungsmoeglichkeiten/cochlea-implantate>.
- [44] Department of Otolaryngology, *Cochlea Implant*, <https://www.mh-hannover.de/18120.html>.
- [45] Hearing4all, *Publikationen Hearing4all* **2017**, <http://hearing4all.eu/DE/Publikationen/publikationen.html>.
- [46] O. Stakhovskaya, D. Sridhar, B. H. Bonham, P. A. Leake, *J. Assoc. Res. Otolaryngol.* **2007**, *8*, 220.
- [47] J. H. Goldwyn, S. M. Bierer, J. Arenberg Bierer, *Hear. Res.* **2010**, *268*, 93.
- [48] J. Stieghorst, K. Tegtmeier, P. Aliuos, H. Zernetsch, B. Glasmacher, T. Doll, *Phys. Status Solidi A* **2014**, *211*, 1455.
- [49] J. Stieghorst, B. N. Tran, S. Hadelers, D. Beckmann, T. Doll, in *Proc. Eng. Proceedings Eurosensors Conference 2016*, Vol. 168, p. 1529.
- [50] J. Stieghorst, T. Doll, *IEEE Trans. Biomed. Eng.* **2016**, *63*, 2294.
- [51] U. Reich, E. Fadeeva, A. Warnecke, G. Paasche, P. Müller, B. Chichkov, T. Stöver, T. Lenarz, G. Reuter, *J. Biomed. Mater. Res. Part B Appl. Biomater.* **2012**, *100*, 940.
- [52] U. Reich, P. P. Mueller, E. Fadeeva, B. N. Chichkov, T. Stöver, T. Fabian, T. Lenarz, G. Reuter, *J. Biomed. Mater. Res. Part B Appl. Biomater.* **2008**, *87*, 146.
- [53] U. Reich, P. P. Mueller, E. Fadeeva, B. N. Chichkov, T. Stöver, T. Fabian, T. Lenarz, G. Reuter, *J. Biomed. Mater. Res.* **2008**, *87B*, 598.
- [54] N. Burbliès, J. Schulze, H.-C. Schwarz, K. Kranz, D. Motz, C. Vogt, T. Lenarz, A. Warnecke, P. Behrens, *PLoS ONE* **2016**, *11*, e0158571.
- [55] A. Warnecke, S. Sasse, G. I. Wenzel, A. Hoffmann, G. Gross, G. Paasche, V. Scheper, U. Reich, K.-H. Esser, T. Lenarz, T. Stöver, K. Wissel, *Hear. Res.* **2012**, *289*, 86.

-
- [56] K. Kranz, A. Warnecke, T. Lenarz, M. Durisin, V. Scheper, *PLoS ONE* **2014**, *9*, e92157.
- [57] F. Dencker, L. Dreyer, D. Müller, H. Zernetsch, G. Paasche, R. Sindelar, B. Glasmacher, *J. Biomed. Mater. Res. Part B Appl. Biomater.* **2017**, *105*, 2574.
- [58] M. Wilk, R. Hessler, K. Mugridge, C. Jolly, M. Fehr, T. Lenarz, V. Scheper, *PLoS ONE* **2016**, *11*, e0147552.
- [59] H. Planck, *Kunststoffe und Elastomere in der Medizin*, Verlag W. Kohlhammer, Stuttgart **1993**.
- [60] N. A. Peppas, R. Langer, *Science* **1994**, *263*, 1715.
- [61] S. P. Massia, J. A. Hubbell, *Cytotechnology* **1992**, *10*, 189.
- [62] A. Ballara, J. P. Trotignon, J. Verdu, *J. Mater. Sci. Lett.* **1986**, *5*, 706–708.
- [63] T. E. Attwood, P. C. Dawson, J. L. Freeman, L. R. J. Hoy, J. B. Rose, P. A. Staniland, *Polymer* **1981**, *22*, 1096.
- [64] S. M. Kurtz, J. N. Devine, *Biomaterials* **2007**, *28*, 4845–4869.
- [65] Ilona Kallage, *Bewertung des Belastungs- und Verformungsverhaltens ausgewählter PEEK-Compounds für zahnärztliche Anwendungen*, Berlin **2015**.
- [66] D. Kemmish, *Update on the Technology and Applications of Polyaryletherketones*, Smithers Rapra Technology **2010**.
- [67] M. Knebel, *elements* **2011**, *34*, 30–34.
- [68] A. Godara, D. Raabe, S. Green, *Acta Biomater.* **2007**, *3*, 209.
- [69] S. M. Kurtz, *Peek biomaterials handbook*, William Andrew, Kidlington **2012**.
- [70] K. B. Sagomyants, M. L. Jarman-Smith, J. N. Devine, M. S. Aronow, G. A. Gronowicz, *Biomaterials* **2008**, *29*, 1563–1572.
- [71] X. Jin, M. T. Bishop, T. S. Ellis, F. E. Karasz, *Brit. Polym. J.* **1985**, *17*, 4.
- [72] R. J. Karcha, R. S. Porter, *J. Macromol. Sci. A* **1995**, *32*, 957.
- [73] P. Bongardt, *Kunststoffe in der Medizintechnik: Trends beim Kunststoffeinsatz in der modernen Medizintechnik*, Tuttlingen **2006**.
- [74] A. Wang, R. Lin, C. Stark, J.H. Dumbleton, *Wear* **1999**, *225-229*, 724.
- [75] Y. Yamamoto, M. Hashimoto, *Wear* **2004**, *257*, 181.
- [76] H. B. Skinner, *Clinical Orthopaedics and Related Research* **1988**,
<http://www.scopus.com/inward/record.url?eid=2-s2.0-0023741286&partnerID=40&md5=cc4933f8162de918c8cec47446dfdaf>.
- [77] L. M. Wenz, K. Merritt, S. A. Brown, A. Moet, A. D. Steffee, *J. Biomed. Mater. Res.* **1990**, *24*, 207–215.
- [78] S. M. Kurtz, in *PEEK Biomaterials Handbook*, Elsevier **2012**, p. 1.

- [79] *PEEK dental*, <http://www.dtz-ma.de/materialien-cat255.html>.
- [80] *cranial plate*, http://www.xilloc.com/products_services/patient-specific-implants/examples/.
- [81] *interface screws*, <http://www.innotronics.sk/ifix>.
- [82] D. F. Williams, A. McNamara, R. M. Turner, *J. Mater. Sci. Lett.* **1987**, *6*, 188–190.
- [83] E. Wintermantel, S.-W. Ha, *Medizintechnik: Life science engineering Interdisziplinarität, Biokompatibilität, Technologien, Implantate, Diagnostik, Werkstoffe, Zertifizierung, Business*, Springer, Berlin **2009**.
- [84] A. Hunter, C. W. Archer, P. S. Walker, G. W. Blunn, *Biomaterials* **1995**, *16*, 287.
- [85] K. A. Jockisch, S. A. Brown, T. W. Bauer, K. Merritt, *J. Biomed. Mater. Res.* **1992**, *26*, 133–146.
- [86] T. W. Lin, A. A. Corvelli, C. G. Frondoza, J. C. Roberts, D. S. Hungerford, *J. Biomed. Mater. Res.* **1997**, *36*, 137–144.
- [87] C. Morrison, R. Macnair, C. MacDonald, A. Wykman, I. Goldie, M. H. Grant, *Biomaterials* **1995**, *16*, 987–992.
- [88] O. Petillo, G. Peluso, L. Ambrosio, L. Nicolais, W. J. Kao, J. M. Anderson, *J. Biomed. Mater. Res.* **1994**, *28*, 635–646.
- [89] J. M. Toth, M. Wang, B. T. Estes, J. L. Scifert, H. B. Seim, A. S. Turner, *Biomaterials* **2006**, *27*, 324.
- [90] R. H. Khonsari, P. Berthier, T. Rouillon, J.-P. Perrin, P. Corre, *J. Oral Maxillofac. Surg. Med. Pathol.* **2014**, *26*, 477.
- [91] R. Ma, T. Tang, *International journal of molecular sciences* **2014**, *15*, 5426.
- [92] K. H. Tan, C. K. Chua, K. F. Leong, C. M. Cheah, P. Cheang, M. S. Abu Bakar, S. W. Cha, *Biomaterials* **2003**, *24*, 3115–3123.
- [93] L. Wang, L. Weng, S. Song, Z. Zhang, S. Tian, R. Ma, *Mater. Sci. Eng. C* **2011**, *528*, 3689.
- [94] N. Knör, R. Walter, F. Hauptert, *J. Thermoplast. Compos. Mater.* **2011**, *24*, 185–205.
- [95] Victrex, *Einsatz von PEEK-OPTIMA™ HA Enhanced Polymer von Invibio kann Wirbelkörperperfusion verbessern* **2017**, <https://www.victrex.com/de/news/2017/01/post-nass>.
- [96] D. Briem, S. Strametz, K. Schröder, N. M. Meenen, W. Lehmann, W. Linhart, A. Ohl, J. M. Rueger, *J. Mater. Sci. Mater. Med.* **2005**, *16*, 671–677.
- [97] K. Schröder, B. Finke, H. Jesswein, F. Lüthen, A. Diener, R. Ihrke, A. Ohl, K. -D. Weltmann, J. Rychly, J. B. Nebe, *J. Adhes. Sci. Technol.* **2010**, *24*, 905–923.
- [98] S. Zhang, F. Awaja, N. James, D. R. McKenzie, A. J. Ruys, *Colloids Surf. A* **2011**, *374*, 88–95.

-
- [99] S. Barkarmo, A. Wennerberg, M. Hoffman, P. Kjellin, K. Breeding, P. Handa, V. Stenport, *J. Biomed. Mater. Res.* **2013**, *101A*, 465.
- [100] G. M. Wu, W. D. Hsiao, S. F. Kung, *Surf. Coat. Technol.* **2009**, *203*, 2755.
- [101] S.-W. Ha, E. Wintermantel, G. Maier, *Biokompatible Polymere: Medizintechnik* **2009**.
- [102] A. A. El hadad, et al., *J. Phys. Conference Series* **2010**, *252*, 12007.
- [103] S. D. Cook, A. M. Rust-Dawicki, *J. Oral. Implantol.* **1995**, *21*, 176–181.
- [104] H.-K. Tsou, P.-Y. Hsieh, C.-J. Chung, C.-H. Tang, T.-W. Shyr, J.-L. He, *Surf. Coat. Technol.* **2009**, *204*, 1121.
- [105] H. K. Tsou, P. Y. Hsieh, M. H. Chi, Y. W. Hung, C. J. Chung, J. L. He, *Key Eng. Mater.* **2011**, *479*, 98.
- [106] H.-K. Tsou, P.-Y. Hsieh, M.-H. Chi, C.-J. Chung, J.-L. He, *J. Biomed. Mater. Res.* **2012**, *100A*, 2787.
- [107] T. Shimizu, S. Fujibayashi, S. Yamaguchi, K. Yamamoto, B. Otsuki, M. Takemoto, M. Tsukanaka, T. Kizuki, T. Matsushita, T. Kokubo, S. Matsuda, *Acta Biomater.* **2016**, *35*, 305.
- [108] L. Sommer, *Fresenius J. Anal. Chem.* **1958**, *163*, 412–414.
- [109] K. Healy, P. Ducheyne, *Biomaterials* **1992**, *13*, 553.
- [110] J.-X. Liu, D.-Z. Yang, F. Shi, Y.-J. Cai, *Thin Solid Films* **2003**, *429*, 225–230.
- [111] T. Fu, B. Liu, Y. Zhou, X. Wu, *J. Sol-Gel Sci. Technol.* **2011**, *58*, 307.
- [112] C. T. Kresge, M. E. Leonowicz, W. J. Roth, J. C. Vartuli, J. S. Beck, *Nature* **1992**, *359*, 710.
- [113] J. S. Beck, J. C. Vartuli, W. J. Roth, M. E. Leonowicz, C. T. Kresge, K. D. Schmitt, C. T. W. Chu, D. H. Olson, E. W. Sheppard, S. B. McCullen, J. B. Higgins, J. L. Schlenker, *J. Am. Chem. Soc.* **1992**, *114*, 10834.
- [114] H. Fullriede, P. Abendroth, N. Ehlert, K. Doll, J. Schäske, A. Winkel, S. N. Stumpp, M. Stiesch, P. Behrens, *BioNanoMaterials* **2016**, *17*, 10460.
- [115] A. Neumann, A. Christel, C. Kasper, P. Behrens, *RSC Adv.* **2013**, *3*, 24222.
- [116] S. Williams, A. Neumann, I. Bremer, Y. Su, G. Dräger, C. Kasper, P. Behrens, *J. Mater. Sci. Mater. Med.* **2015**, *26*, 125.
- [117] C. T. Kresge, W. J. Roth, *Chem. Soc. Rev.* **2013**, *42*, 3663.
- [118] G. S. Attard, J. C. Glyde, C. G. Göltner, *Nature* **1995**, *378*, 366.
- [119] A. Monnier, F. Schüth, Q. Huo, D. Kumar, D. Margolese, R. S. Maxwell, G. D. Stucky, M. Krishnamurty, P. Petroff, A. Firouzi, M. Janicke, B. F. Chmelka, *Science* **1993**, *261*, 1299.

8. References

- [120] D. Ghosh, A. K. Pradhan, S. Mondal, N. A. Begum, D. Mandal, *Phys. Chem. Chem. Phys.* **2014**, *16*, 8594.
- [121] D. A. Chiappetta, G. Facorro, E. R. de Celis, A. Sosnik, *Nanomedicine* **2011**, *7*, 624.
- [122] R. Basak, R. Bandyopadhyay, *Langmuir* **2013**, *29*, 4350.
- [123] D. A. Loy, K. J. Shea, *Chem. Rev.* **1995**, *95*, 1431.
- [124] S. Inagaki, S. Guan, Y. Fukushima, T. Ohsuna, O. Terasaki, *J. Am. Chem. Soc.* **1999**, *121*, 9611.
- [125] B. J. Melde, B. T. Holland, C. F. Blanford, A. Stein, *Chem. Mater.* **1999**, *11*, 3302.
- [126] C. Yoshina-Ishii, T. Asefa, N. Coombs, M. J. MacLachlan, G. A. Ozin, *Chem. Commun.* **1999**.
- [127] M. P. Kapoor, Q. Yang, S. Inagaki, *J. Am. Chem. Soc.* **2002**, *124*, 15176.
- [128] J. Morell, C. V. Teixeira, M. Cornelius, V. Rebbin, M. Tiemann, H. Amenitsch, M. Fröba, M. Lindén, *Chem. Mater.* **2004**, *16*, 5564.
- [129] O. Muth, C. Schellbach, M. Fröba, *Chem. Commun.* **2001**.
- [130] Y. Goto, S. Inagaki, *Chem. Commun.* **2002**, *121*, 2410.
- [131] S. S. Park, M. Santha Moorthy, C.-S. Ha, *NPG Asia Mater.* **2014**, *6*, e96.
- [132] E. de Canck, C. Vercaemst, F. Verpoort, P. van der Voort, in *Stud. Surf. Sci. Catal.*, Vol. 175, p. 365.
- [133] D. Esquivel, P. van der Voort, F. J. Romero-Salguero, *AIMS Mater. Sci.* **2014**, *1*, 70.
- [134] M. A. Wahab, J. N. Beltramini, *RSC Adv.* **2015**, *5*, 79129.
- [135] S. Hudson, E. Magner, J. Cooney, B. K. Hodnett, *J. Phys. Chem. B* **2005**, *109*, 19496.
- [136] M. Park, S. S. Park, M. Selvaraj, D. Zhao, C.-S. Ha, *Microporous Mesoporous Mater.* **2009**, *124*, 76.
- [137] X. Wang, D. Lu, R. Austin, A. Agarwal, L. J. Mueller, Z. Liu, J. Wu, P. Feng, *Langmuir* **2007**, *23*, 5735.
- [138] H.-M. Kao, C.-H. Chung, D. Saikia, S.-H. Liao, P.-Y. Chao, Y.-H. Chen, K. C.-W. Wu, *Chem. Asian J.* **2012**, *7*, 2111.
- [139] M. S. Moorthy, M.-J. Kim, J.-H. Bae, S. S. Park, N. Saravanan, S.-H. Kim, C.-S. Ha, *Eur. J. Inorg. Chem.* **2013**, *2013*, 3028.
- [140] B. Guan, Y. Cui, Z. Ren, Z.-a. Qiao, L. Wang, Y. Liu, Q. Huo, *Nanoscale* **2012**, *4*, 6588.

-
- [141] J. Croissant, D. Salles, M. Maynadier, O. Mongin, V. Hugues, M. Blanchard-Desce, X. Cattoën, Wong Chi Man, Michel, A. Gallud, M. Garcia, M. Gary-Bobo, L. Raehm, J.-O. Durand, *Chem. Mater.* **2014**, *26*, 7214.
- [142] N. S. Kehr, H.-J. Galla, K. Riehemann, H. Fuchs, *RSC Adv.* **2015**, *5*, 5704.
- [143] X. Qian, W. Wang, W. Kong, Y. Chen, *J. Nanomater.* **2014**, *2014*, 1.
- [144] TyrionL, *Sol-Gel-Schicht* **2008**, <https://de.wikipedia.org/wiki/Sol-Gel-Schicht>.
- [145] D. Grosso, *J. Mater. Chem.* **2011**, *21*, 17033.
- [146] C. J. Brinker, *MRS Bull.* **2004**, *29*, 631.
- [147] D. Grosso, F. Cagnol, G. J. d. A. A. Soler-Illia, E. L. Crepaldi, H. Amenitsch, A. Brunet-Bruneau, A. Bourgeois, C. Sanchez, *Adv. Funct. Mater.* **2004**, *14*, 309.
- [148] G. J. A. A. Soler-Illia, P. C. Angelomé, M. C. Fuertes, A. Calvo, A. Wolosiuk, A. Zelcer, M. G. Bellino, E. D. Martínez, *J. Sol-Gel Sci. Technol.* **2011**, *57*, 299.
- [149] M. Faustini, B. Louis, P. A. Albouy, M. Kuemmel, D. Grosso, *J. Phys. Chem. C* **2010**, *114*, 7637.
- [150] H.-R. Brodt, Brodt-Groll-Just-Nübling, A. H. Groll, G. Just-Nübling, W. Stille, *Antibiotika-Therapie: Klinik und Praxis der antiinfektiösen Behandlung*, Schattauer, Stuttgart **2006**.
- [151] H. W. Doerr, U. Theuretzbacher, B. Wiedemann, *Mikrobiologie im klinischen Alltag: Erreger, Diagnostik, Therapie*, Kohlhammer, Stuttgart **2004**.
- [152] C. Simon, W. Stille, *Antibiotika-Therapie in Klinik und Praxis: Mit 102 Tabellen*, Schattauer, Stuttgart [u.a.] **2001**.
- [153] P. C. Sharma, A. Jain, S. Jain, R. Pahwa, M. S. Yar, *J. Enzyme. Inhib. Med. Chem.* **2010**, *25*, 577.
- [154] P. C. Appelbaum, P. A. Hunter, *Int. J. Antimicrob. Agents.* **2000**, *16*, 5.
- [155] National Institutes of Health, *Chemistry Data Base*, <https://pubchem.ncbi.nlm.nih.gov/>.
- [156] C. Herold, M. Ocker, M. Ganslmayer, H. Gerauer, E. G. Hahn, D. Schuppan, *Br. J. Cancer* **2002**, *86*, 443.
- [157] O. Aranha, D. P. Wood, F. H. Sarkar, *Clin. Cancer Res.* **2000**, *6*, 891.
- [158] O. Aranha, R. Grignon, N. Fernandes, T. McDonnell, D. Wood, F. Sarkar, *Int. J. Oncol.* **2003**.
- [159] E. Haron, K. V. I. Rolston, C. Cunningham, F. Holmes, T. Umsawasdi, G. P. Bodey, *J. Antimicrob. Chemother.* **1989**, *24*, 955.
- [160] M. A. Kohanski, D. J. Dwyer, J. J. Collins, *Nature Rev. Microbiol.* **2010**, *8*, 423.
- [161] R. Davis, A. Markham, J. A. Balfour, *Drugs* **1996**, *51*, 1019.

8. References

- [162] S. Esposito, G. D'Errico, C. Montanaro, *Arch. Otolaryngol. Head. Neck Surg.* **1990**, *116*, 557.
- [163] K. Ramakrishnan, R. A. Sparks, W. E. Berryhill, *Am. Fam. Physician.* **2007**, *76*, 1650.
- [164] Facharztwissen @ Medicoconsult, *Neuroprotektion*, <http://www.medicoconsult.de/neuroprotektion/>.
- [165] D. W. Brann, K. Dhandapani, C. Wakade, V. B. Mahesh, M. M. Khan, *Steroids* **2007**, *72*, 381.
- [166] J. W. Simpkins, J. A. Dykens, *Brain Res. Rev.* **2008**, *57*, 421.
- [167] A. E. Autry, L. M. Monteggia, *Pharmacol. Rev.* **2012**, *64*, 238.
- [168] D. K. Binder, H. E. Scharfman, *Growth Factors* **2004**, *22*, 123.
- [169] R. Levi-Montalcini, *Harvey Lect.* **1966**, *60*, 217.
- [170] Y. A. Barde, D. Edgar, H. Thoenen, *EMBO J.* **1982**, *1*, 549.
- [171] P. C. Maisonpierre, L. Belluscio, S. Squinto, N. Y. Ip, M. E. Furth, R. M. Lindsay, G. D. Yancopoulos, *Science* **1990**, *247*, 1446.
- [172] F. Hallböök, C. F. Ibáñez, H. Persson, *Neuron* **1991**, *6*, 845.
- [173] V. Lessmann, K. Gottmann, M. Malcangio, *Prog. Neurobiol.* **2003**, *69*, 341.
- [174] T. Numakawa, S. Suzuki, E. Kumamaru, N. Adachi, M. Richards, H. Kunugi, *Histol. Histopathol.* **2010**, *25*, 237.
- [175] K. Marosi, M. P. Mattson, *Trends Endocrinol. Metab.* **2014**, *25*, 89.
- [176] Protein Data Bank, *BDNF*, <https://www.rcsb.org/pdb/home/home.do>.
- [177] C. Normann, M. Berger, *Eur. Arch. Psychiatry Clin. Neurosci.* **2008**, *258*, 110.
- [178] J. Zhu, E. Mix, B. Winblad, *CNS Drug Rev.* **2001**, *7*, 387.
- [179] L. Yang, N. Y. Calingasan, B. J. Lorenzo, M. F. Beal, *Exp. Neurol.* **2008**, *211*, 311.
- [180] Y.-F. Li, Y. Huang, S. L. Amsdell, L. Xiao, J. M. O'Donnell, H.-T. Zhang, *Neuropsychopharmacology* **2009**, *34*, 2404.
- [181] S. A. Hitchcock, L. D. Pennington, *J. Med. Chem.* **2006**, *49*, 7559.
- [182] H. Pajouhesh, G. R. Lenz, *NeuroRX* **2005**, *2*, 541.
- [183] N. Yamashita, M. Yamauchi, J. Baba, A. Sawa, *Eur. J. Pharmacol.* **1997**, *337*, 95.
- [184] Y. Zhong, Y. Zhu, T. He, W. Li, H. Yan, Y. Miao, *Neurosci. Lett.* **2016**, *610*, 171.
- [185] T. Itoh, M. Tokumura, K. Abe, *Eur. J. Pharmacol.* **2004**, *498*, 135.
- [186] C. Bharti, U. Nagaich, A. K. Pal, N. Gulati, *Int. J. Pharm. Investig.* **2015**, *5*, 124.

- [187] M. Jäger, C. Zilkens, K. Zanger, R. Krauspe, *J. Biomed. Biotechnol.* **2007**, 2007, 1.
- [188] H. Schweikl, R. Möller, C. Englert, K.-A. Hiller, R. Kujat, M. Nerlich, G. Schmalz, *J. Mater. Sci. Mater. Med.* **2007**, 18, 1895–1905.
- [189] G. Zhao, Z. Schwartz, M. Wieland, F. Rupp, J. Geis-Gerstorfer, D. L. Cochran, B. D. Boyan, *J. Biomed. Mater. Res. Part B Appl. Biomater.* **2005**, 74, 49.
- [190] M. Ardhaoui, M. Naciri, T. Mullen, C. Brugha, A. K. Keenan, M. Al-Rubeai, D. P. Dowling, *J. Adhes. Sci. Technol.* **2010**, 24, 889.
- [191] M. Arnold, E. A. Cavalcanti-Adam, R. Glass, J. Blümmel, W. Eck, M. Kantlehner, H. Kessler, J. P. Spatz, *ChemPhysChem* **2004**, 5, 383.
- [192] S. Phadke, J. D. Sorge, S. Hachtmann, I. D. P.I. Birnie, *Thin Solid Films* **2010**, 518, 5467–5470.
- [193] A. Eshaghi, R. Mozaffarinia, M. Pakshir, A. Eshaghi, *Ceram. Int.* **2011**, 37, 327.
- [194] W. Huang, W. Deng, M. Lei, H. Huang, *Appl. Surf. Sci.* **2011**, 257, 4774–4780.
- [195] P. A. Steinmann, *J. Vac. Sci. Technol. A* **1989**, 7, 2267.
- [196] A. A. Volinsky, N. R. Moody, W. W. Gerberich, *Acta Mater.* **2002**, 50, 441.
- [197] A. von Endrédy, F. Brugger, *Z. Anorg. Allg. Chem.* **1942**, 249, 263–277.
- [198] H. Kurtenacker, *Fresenius J. Anal. Chem.* **1954**, 143, 52.
- [199] N. Hao, Y. Yang, H. Wang, P. A. Webley, D. Zhao, *J. Colloid Interface Sci.* **2010**, 346, 429.
- [200] N. Ehlert, M. Badar, A. Christel, S. J. Lohmeier, T. Luessenhop, M. Stieve, T. Lenarz, P. P. Mueller, P. Behrens, *J. Mater. Chem.* **2011**, 21, 752.
- [201] P. Ghosh, S. C. Chadha, Mukherjee A. R., S. R. Palit, *J. Polym. Sci. A Polym. Chem.* **1964**.
- [202] M. Thommes, K. Kaneko, A. V. Neimark, J. P. Olivier, F. Rodriguez-Reinoso, J. Rouquerol, K. S.W. Sing, *Pure Appl. Chem.* **2015**, 87, 1051.
- [203] K.S.W. Sing, R.A.W. Haul, L. Mouscou, R. A. Pierotti, J. Rouquerol, T. Siemieniowska, *Pure Appl. Chem.* **1985**, 57.
- [204] E. P. Barrett, L. G. Joyner, P. P. Halenda, *J. Am. Chem. Soc.* **1951**, 73, 373.
- [205] M. Thommes, N. Nishiyama, S. Tanaka, in *Stud. Surf. Sci. Catal.*, Vol. 165, p. 551.
- [206] K. M. Krause, M. Thommes, M. J. Brett, *Microporous Mesoporous Mater.* **2011**, 143, 166.
- [207] M. Thommes, *Quantachrome Instruments Powder Tech Note* **2006**, 39, 1.
- [208] H. G. Tompkins, E. A. Irene, *Handbook of ellipsometry*, William Andrew Pub; Springer, Norwich, NY, Heidelberg, Germany **2005**.

8. References

- [209] School of Physics, *Ellipsometry* **2012**,
<https://www.tcd.ie/Physics/Surfaces/ellipsometry2.php>.
- [210] Daniel Faltermeier, *Ellipsometrie an organischen Dünnschichten und Einkristallen zur Bestimmung der optischen und strukturellen Eigenschaften*, Stuttgart **2007**.
- [211] M. F. Doerner, W. D. Nix, *J. Mater. Res.* **1986**, *1*, 601.
- [212] G. M. Pharr, W. C. Oliver, *MRS Bull.* **1992**, *17*, 28.
- [213] J. A. Broussard, B. Rappaz, D. J. Webb, C. M. Brown, *Nat. Protoc.* **2013**, *8*, 265.
- [214] B. Valeur, *Molecular fluorescence: Principles and applications*, Wiley-VCH, New York **2001**.
- [215] Northwestern University, *Förster Resonance Energy Transfer* **2011**,
<https://cam.facilities.northwestern.edu/588-2/fluorescence-resonance-energy-transfer/>.
- [216] J. R. Lakowicz, *Principles of Fluorescence Spectroscopy*, Springer Science+Business Media, LLC, Boston, MA **2006**.
- [217] W. Massa, *Kristallstrukturbestimmung*, Vieweg+Teubner Verlag, Wiesbaden, Germany **2007**.
- [218] *Biologie in unserer Zeit* **2009**, *39*, 234.
- [219] G. Repetto, A. del Peso, J. L. Zurita, *Nat. Protoc.* **2008**, *3*, 1125.
- [220] A. Becher, H. P. Schweizer, *Biotechniques* **2000**, *29*, 948-50, 952.
- [221] M. P. Fletcher, S. P. Diggle, M. Camara, P. Williams, *Nat. Protoc.* **2007**, *2*, 1254.
- [222] U. Kahler, *Darstellung, Charakterisierung und Oberflächenmodifizierung von Siliziumnanopartikeln in Silica*, Halle-Wittenberg **2001**.
- [223] M. Hesse, H. Meier, B. Zeeh, *Spektroskopische Methoden in der organischen Chemie*, Thieme, Stuttgart **2011**.
- [224] H. Günzler, H.-U. Gremlich, *IR-Spektroskopie: Eine Einführung*, Wiley-VCH, Weinheim **2003**.
- [225] F. Hoffmann, M. Gungerich, P. J. Klar, M. Froba, *J. Phys. Chem. C* **2007**, *111*, 5648.
- [226] Philip J. Launer, Barry Arkles, *Silicon Compounds: Silanes & Silicones* **2013**.
- [227] B. D. Hatton, K. Landskron, W. Whitnall, D. D. Perovic, G. A. Ozin, *Advanced Functional Materials* **2005**, *15*, 823.
- [228] M. Seino, W. Wang, J. E. Lofgreen, D. P. Puzzo, T. Manabe, G. A. Ozin, *J. Am. Chem. Soc.* **2011**, *133*, 18082.

-
- [229] M. Kuroki, T. Asefa, W. Whitnal, M. Kruk, C. Yoshina-Ishii, M. Jaroniec, G. A. Ozin, *J. Am. Chem. Soc.* **2002**, *124*, 13886.
- [230] D. Esquivel, C. Jiménez-Sanchidrián, F. J. Romero-Salguero, *J. Mater. Chem.* **2011**, *21*, 724.
- [231] T. Asefa, M. J. MacLachlan, H. Grondley, N. Coombs, G. A. Ozin, *Angew. Chem. Int. Ed.* **2000**, *39*, 1808.
- [232] D. Kuang, T. Brezesinski, B. Smarsly, *J. Am. Chem. Soc.* **2004**, *126*, 10534.
- [233] P.-H. Liu, K.-J. Chao, X.-J. Guo, K.-Y. Huang, Y.-R. Lee, C.-W. Cheng, M.-S. Chiu, S.-L. Chang, *J. Appl. Crystallogr.* **2005**, *38*, 211.
- [234] K.-J. Chao, P.-H. Liu, K.-Y. Huang, *C. R. Chim.* **2005**, *8*, 727.
- [235] P. Behrens, A. Glaue, C. Haggemüller, G. Schechner, *Solid State Ion.* **1997**, *101-103*, 255.
- [236] M. Thommes, in *Nanoporous Materials: Science and Engineering*, **2004**, *4*, 317.
- [237] C. Jo, K. Kim, R. Ryoo, *Microporous Mesoporous Mater.* **2009**, *124*, 45.
- [238] M. Kruk, M. Jaroniec, C. H. Ko, R. Ryoo, *Chem. Mater.* **2000**, *12*, 1961.
- [239] Z. Liu, O. Terasaki, T. Ohsuna, K. Hiraga, H. J. Shin, R. Ryoo, *ChemPhysChem* **2001**, *2*, 229.
- [240] L. Hatch, *Sol-Gel Coating Process: Dip Coating* **2010**, <http://exoplanets.astro.yale.edu/instrumentation/sol-gel.php>.
- [241] Y. Li, *Periodic mesoporous organosilicas with functional chromophores*, München **2012**.
- [242] F. Goethals, *Periodic Mesoporous Organosilicas for Application as low-k Dielectric Materials*, Gent, Belgien **2012**.
- [243] M. A. Wahab, C. He, *Langmuir* **2009**, *25*, 832.
- [244] N. Chemin, M. Klotz, V. Rouessac, A. Ayrat, E. Barthel, *Thin Solid Films* **2006**, *495*, 210.
- [245] H. Föll, *Elastizitätsmodul in Zahlen: MaWi 1 Skript*, https://www.tf.uni-kiel.de/matwis/amat/mw1_ge/kap_7/illustr/t7_1_2.html.
- [246] F. Heinroth, R. Münnekhoff, C. Panz, R. Schmoll, J. Behnisch, P. Behrens, *Microporous Mesoporous Mater.* **2008**, *116*, 95.
- [247] M. Järn, F. J. Brieler, M. Kuemmel, D. Grosso, M. Lindén, *Chem. Mater.* **2008**, *20*, 1476.
- [248] W. Wang, D. Grozea, S. Kohli, D. D. Perovic, G. A. Ozin, *ACS Nano* **2011**, *5*, 1267.

8. References

- [249] A. Grunenwald, A. Ayrat, P.-A. Albouy, C. Licitra, P. Gergaud, D. Quemener, A. Deratani, V. Rouessac, A. Zenasni, V. Jousseume, *Microporous Mesoporous Mater.* **2012**, *150*, 64.
- [250] F. Goethals, E. Levrau, E. de Canck, M. Baklanov, C. Detavernier, I. van Driessche, P. van der Voort, *Materials* **2013**, *6*, 570.
- [251] M. Manzano, V. Aina, C. O. Areán, F. Balas, V. Cauda, M. Colilla, M. R. Delgado, M. Vallet-Regí, *Chem. Eng. J.* **2008**, *137*, 30.
- [252] M. Jahns, *Untersuchungen zum Förster-Resonanz-Energietransfer an beladenen periodisch-mesoporösen Organosilica-Beschichtungen*, Hannover **2015**.
- [253] J. Lai, B. P. Shah, E. Garfunkel, K.-B. Lee, *ACS Nano* **2013**, *7*, 2741.
- [254] P. Zou, H. Chen, H. J. Paholak, D. Sun, *Mol. Pharm.* **2013**, *10*, 4185.
- [255] C. Latz, G. Pavon-Djavid, G. Hélarý, M. D. M. Evans, V. Migonney, *Biomacromolecules* **2003**, *4*, 766.
- [256] S. Berlot, Z. Aissaoui, G. Pavon-Djavid, J. Belleney, M. Jozefowicz, G. Hélarý, V. Migonney, *Biomacromolecules* **2002**, *3*, 63.
- [257] F. El Khadali, G. Hélarý, G. Pavon-Djavid, V. Migonney, *Biomacromolecules* **2002**, *3*, 51.
- [258] S. Kerner, V. Migonney, G. Pavon-Djavid, G. Helary, L. Sedel, F. Anagnostou, *J. Mater. Sci. Mater. Med.* **2010**, *21*, 707.
- [259] F. Anagnostou, A. Debet, G. Pavon-Djavid, Z. Goudaby, G. Hélarý, V. Migonney, *Biomaterials* **2006**, *27*, 3912.
- [260] A. M. Bujor, P. Haines, C. Padilla, R. B. Christmann, M. Junie, P. D. Sampaio-Barros, R. Lafyatis, M. Trojanowska, *Int. J. Mol. Med.* **2012**, *30*, 1473.
- [261] P. A. Leake, G. T. Hradek, A. M. Hetherington, O. Stakhovskaya, *J. Comp. Neurol.* **2011**, *519*, 1526.
- [262] D. Rejali, V. A. Lee, K. A. Abrashkin, N. Houmayun, D. L. Swiderski, Y. Raphael, *Hear. Res.* **2007**, *228*, 180.
- [263] D. P. Dowling, I. S. Miller, M. Ardhaoui, W. M. Gallagher, *J. Biomater. Appl.* **2011**, *26*, 327.
- [264] Y. Arima, H. Iwata, *Biomaterials* **2007**, *28*, 3074.
- [265] M. Lampin, R. Warocquier-Clérout, C. Legris, M. Degrange, M. F. Sigot-Luizard, *J. Biomed. Mater. Res.* **1997**, *36*, 99.
- [266] A. Cimpean, S. Popescu, C. M. Ciofrangeanu, A. N. Gleizes, *Mater. Chem. Phys.* **2011**, *125*, 485.
- [267] C. Larsson, L. Emanuelsson, P. Thomsen, L. E. Ericson, B.-O. Aronsson, B. Kasemo, J. Lausmaa, LAUSMAA, J., *J. Mater. Sci. Mater. Med.* **1997**, *8*, 721.
- [268] J. Takebe, S. Itoh, J. Okada, K. Ishibashi, *J. Biomed. Mater. Res.* **2000**, *51*, 398.

- [269] J. C. Keller, C. M. Stanford, J. P. Wightman, R. A. Draughn, R. Zaharias, *J. Biomed. Mater. Res.* **1994**, *28*, 939.
- [270] C.-M. Han, E.-J. Lee, H.-E. Kim, Y.-H. Koh, K. N. Kim, Y. Ha, S.-U. Kuh, *Biomaterials* **2010**, *31*, 3465.
- [271] R. M. Almeida, E. E. Christensen, *J. Sol-Gel Sci. Technol.* **1997**, *8*, 409.
- [272] H. Tamura, K. Mita, A. Tanaka, M. Ito, *J. Colloid Interface Sci.* **2001**, *243*, 202.
- [273] Y. Tanaka, E. Kobayashi, S. Hiromoto, K. Asami, H. Imai, T. Hanawa, *J. Mater. Sci. Mater. Med.* **2007**, *18*, 797.
- [274] Y. Tanaka, H. Saito, Y. Tsutsumi, H. Doi, H. Imai, T. Hanawa, *Mater. Trans.* **2008**, *49*, 805.
- [275] X. J. Feng, L. Jiang, *Adv. Mater.* **2006**, *18*, 3063.
- [276] L. Ponsonnet, K. Reybier, N. Jaffrezic, V. Comte, C. Lagneau, M. Lissac, C. Martelet, *Mater. Sci. Eng. C Mater. Biol. Appl.* **2003**, *23*, 551.
- [277] Z. Schwartz, B. D. Boyan, *J. Cell. Biochem.* **1994**, *56*, 340.
- [278] J. F. Mano, R. A. Sousa, L. F. Boesel, N. M. Neves, R. L. Reis, *Compos. Sci. Technol.* **2004**, *64*, 789.

9. Supporting Information

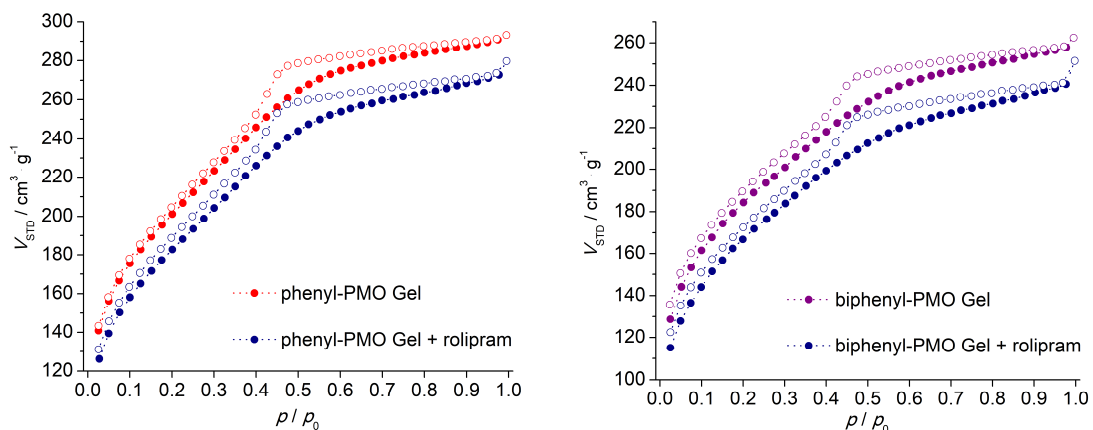


Figure 101: Nitrogen sorption measurements of **(left)** phenyl-PMO gel and additional loaded with rolipram, **(right)** sorption curves of biphenyl-PMO gel. Due to loading with rolipram, the specific surface area is decreased.

Table 14: Values of the specific surface area and pore volume of PMO powders.

material	$S_{\text{BET}} / \text{m}^2 \cdot \text{g}^{-1}$	pore volume / $\text{cm}^3 \cdot \text{g}^{-1}$
phenyl-PMO gel	720	0.45
biphenyl-PMO gel	670	0.40

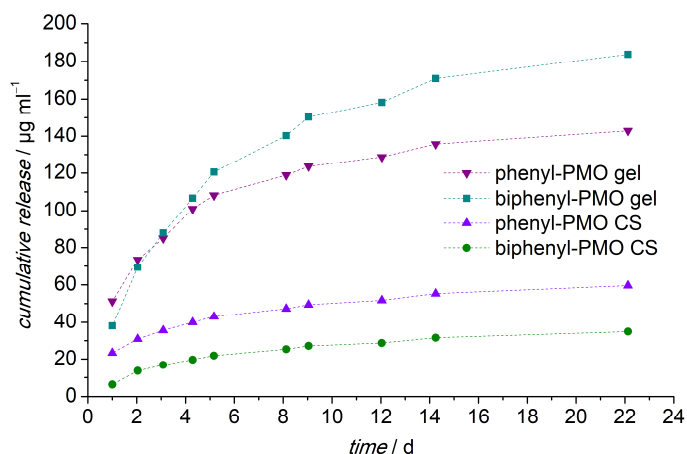


Figure 102: Release of rolipram from PMO particles synthesized by drying and calcining the dipping solution (referring as gel) and synthesized in a classic way by precipitation (CS).

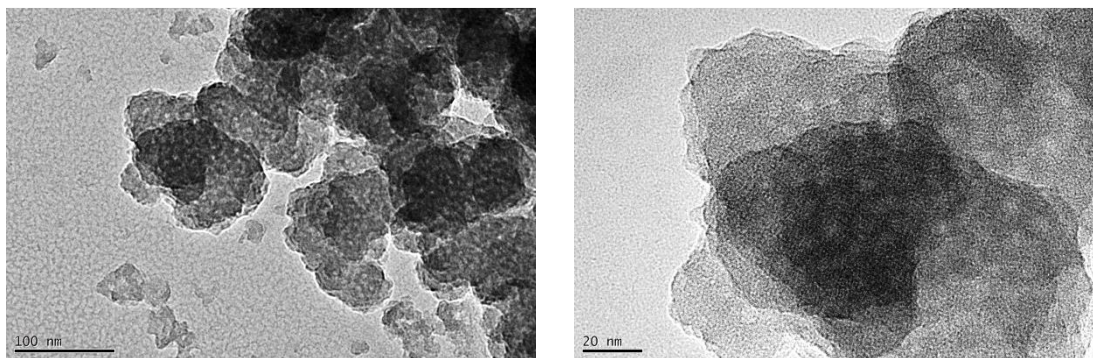


Figure 103: TEM images of porous phenyl-PMO particles.

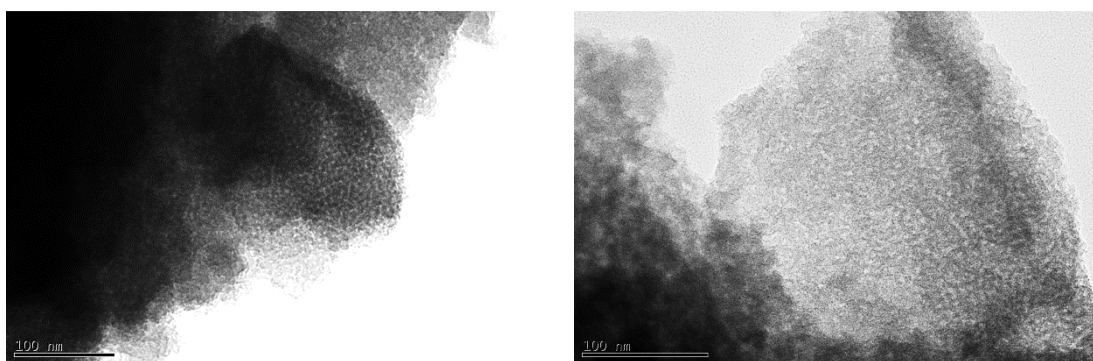


Figure 104: TEM images of porous biphenyl-PMO particles.

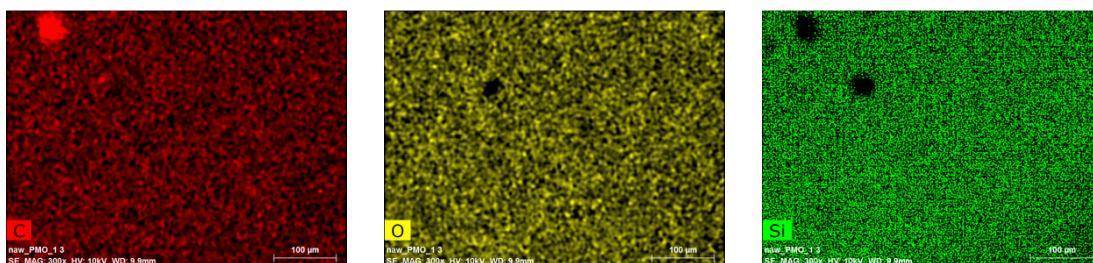


Figure 105: EDX measurements of phenyl-PMO coatings, elements distribution of carbon, oxygen and silicone.

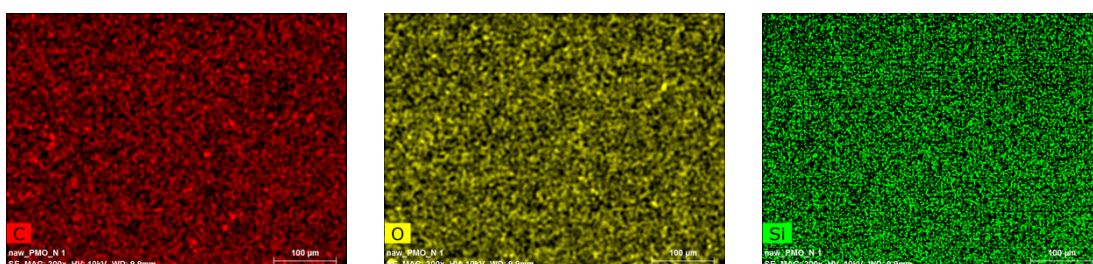


Figure 106: EDX measurements of biphenyl-PMO coatings, elements distribution of carbon, oxygen and silicone.

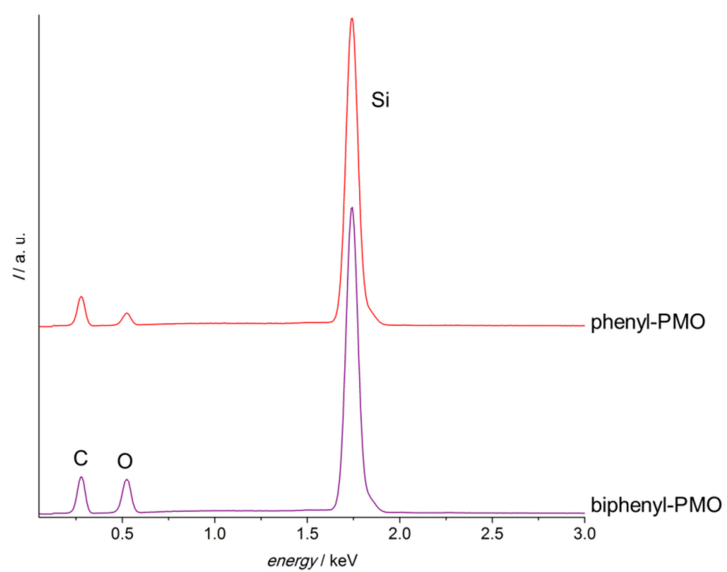


Figure 107: EDX spectra of phenyl- and biphenyl-PMOs. Due to different intensities of the carbon and oxygen peaks, it was obvious that the biphenyl-PMO film contains more carbon compared to the phenyl-PMO sample.

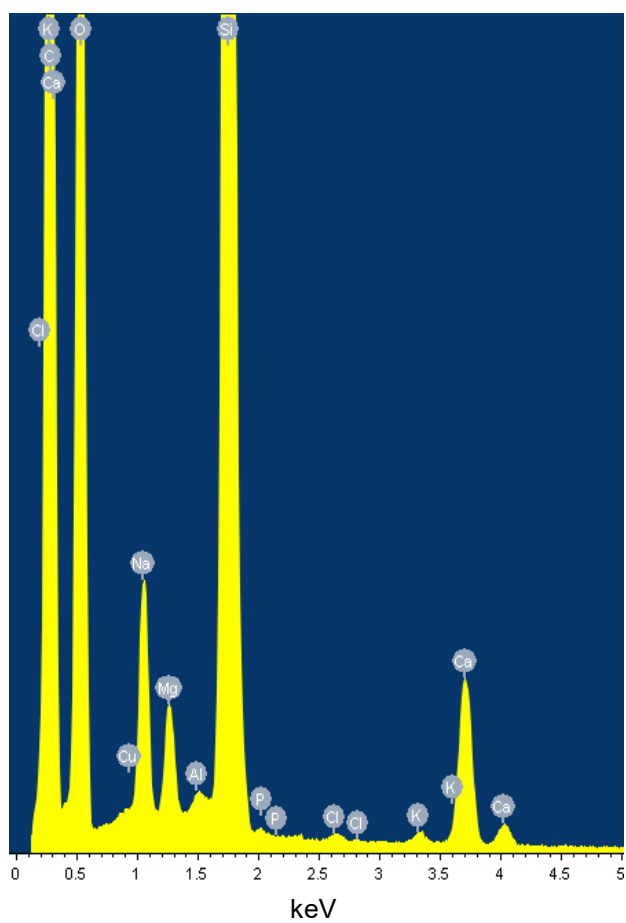


Figure 108: EDX spectrum of the investigated cross-section phenyl-PMO TEM sample.

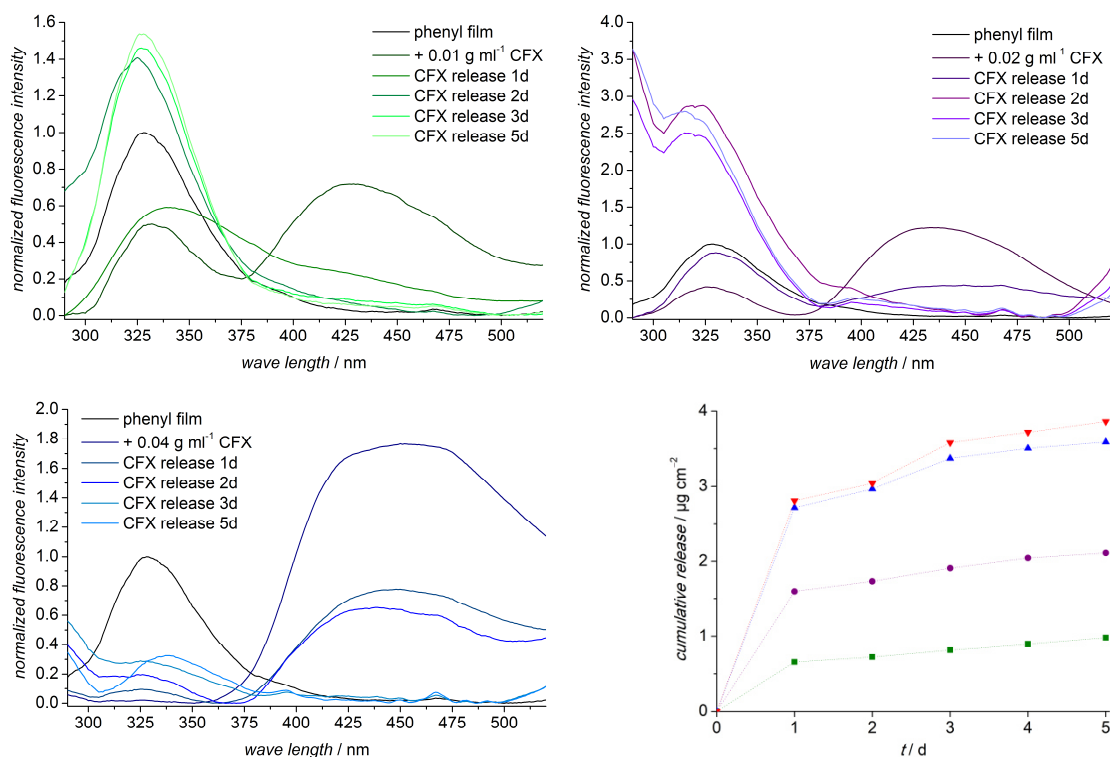


Figure 109: Phenyl-PMO coatings loaded with 0.01, 0.02 and 0.04 $\text{g} \cdot \text{ml}^{-1}$ ciprofloxacin. The CFX release was monitored by FRET. The supernatants were renewed every day. In parallel, the supernatants measured by UV-Vis.

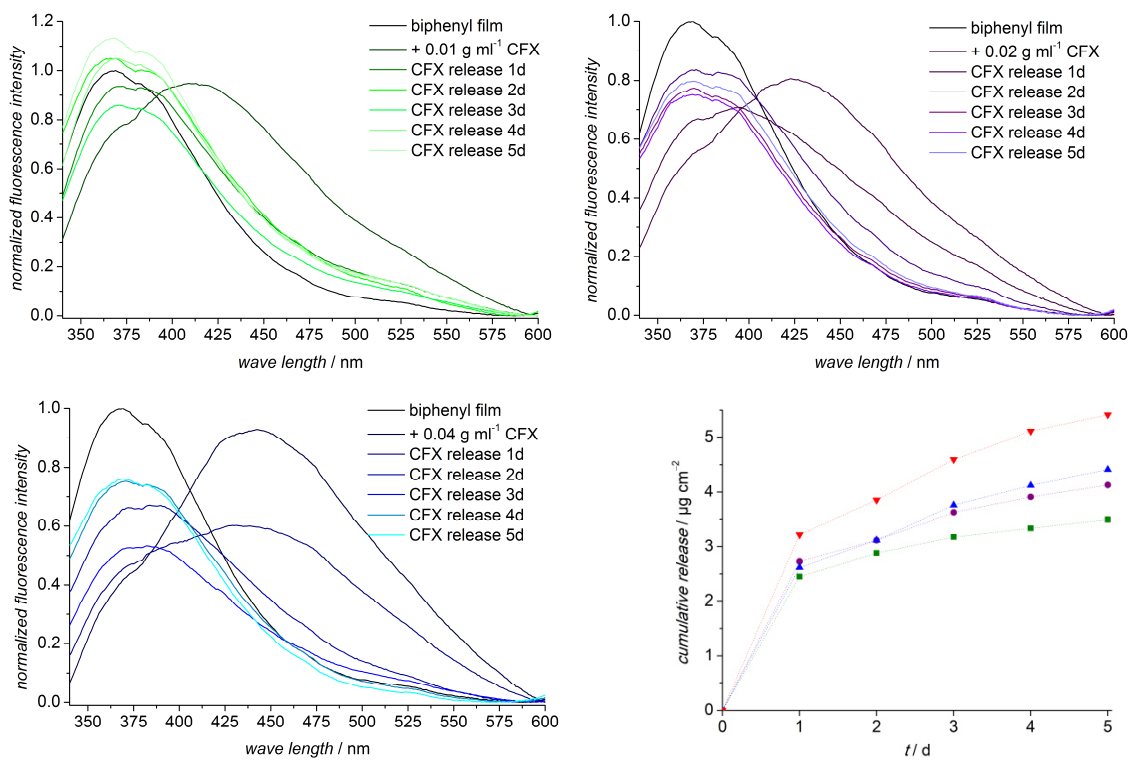


Figure 110: Biphenyl-PMO coatings loaded with 0.01, 0.02 and 0.04 $\text{g} \cdot \text{ml}^{-1}$ ciprofloxacin. The CFX release was monitored by FRET and UV-Vis in parallel.

9. Supporting Information

Exemplary protocol for an ellipsometric measurement of a phenyl-PMO film

Model

Number	Layer Name	Thickness [nm]	Refr. Index [632.8 nm]	Fitted
0	Air	-	1.000	no
1	Roughness	0.00	0.763	yes
2	phenyl-PMO	367.65	1.449	yes
3	Cau-SiO ₂ (therm.)	0.00	1.522	no
4	Si DUV-NIR	-	3.874	no

Fit parameter

Fit parameter	Fit result
[1,1] Roughness: Thickness [nm]	0,00
[1,2] Phenyl-PMO: Thickness [nm]	367,65
Phenyl-PMO: Eg(0)	5,1193
Phenyl-PMO: A(0)	17,086
Phenyl-PMO: E0(0)	5,9046
Phenyl-PMO: C(0)	1,3771
Phenyl-PMO: Eg(1)	4,6833
Phenyl-PMO: A(1)	13,872
Phenyl-PMO: E0(1)	5,7207
Phenyl-PMO: C(1)	0,0667
Phenyl-PMO: Eg(2)	5,8672
Phenyl-PMO: A(2)	0,368
Phenyl-PMO: E0(2)	6,1276
Phenyl-PMO: C(2)	0,2059
Phenyl-PMO: Eg(3)	3,4575
Phenyl-PMO: A(3)	4,343
Phenyl-PMO: E0(3)	7,2423
Phenyl-PMO: C(3)	0,3070
Phenyl-PMO: Eg(6)	7,0826
Phenyl-PMO: A(6)	141,134
Phenyl-PMO: E0(6)	12,0662
Phenyl-PMO: C(6)	39,2161

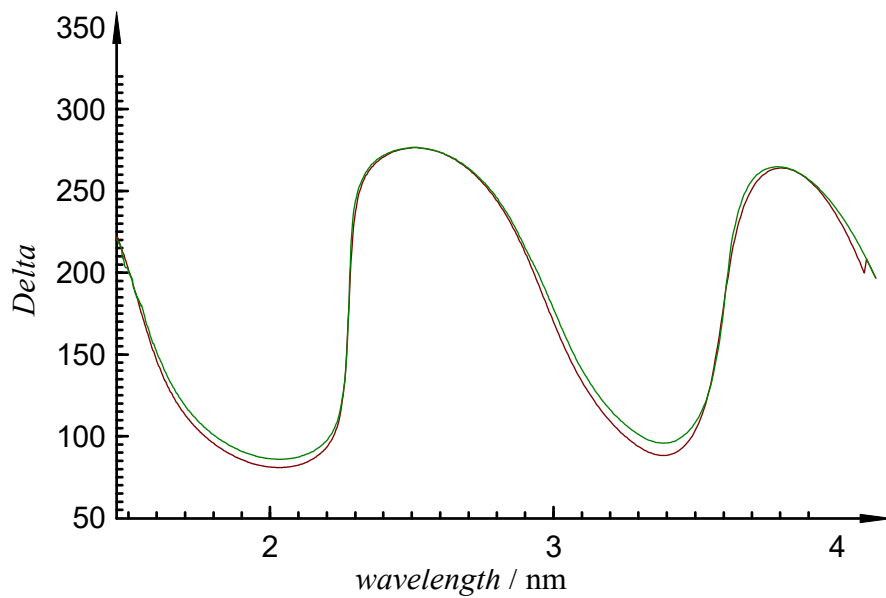
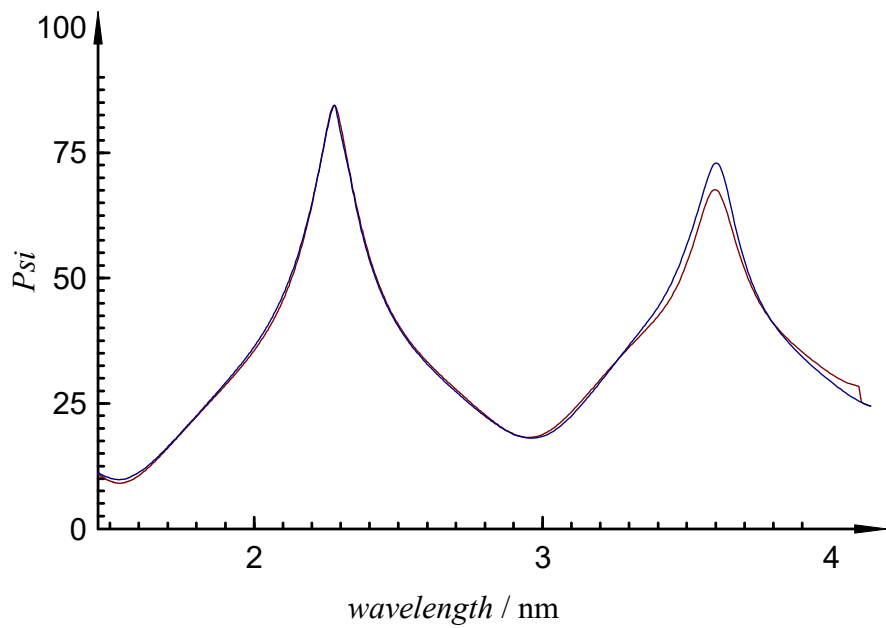
All parameter

Parameter	Value
[1] Sample rotation [°]	0,00
[1] Angle offset [°]	-0,01
[1] Wavelength Offset (nm)	0,00
[1] Wavelength Linear	1,00000
Roughness: Inclusion:Refr. index	1,000
Roughness: Inclusion:Absorption	0,000
[1,1] Roughness: Thickness [nm]	0,00
Roughness: Fraction of inclusion	0,500
[1,2] Phenyl-PMO: Thickness [nm]	367,65
Phenyl-PMO: e1(inf)	1,00000
Phenyl-PMO: Eg(0)	5,1193

Phenyl-PMO: A(0)	17,086
Phenyl-PMO: E0(0)	5,9046
Phenyl-PMO: C(0)	1,3771
Phenyl-PMO: Eg(1)	4,6833
Phenyl-PMO: A(1)	13,872
Phenyl-PMO: E0(1)	5,7207
Phenyl-PMO: C(1)	0,0667
Phenyl-PMO: Eg(2)	5,8672
Phenyl-PMO: A(2)	0,368
Phenyl-PMO: E0(2)	6,1276
Phenyl-PMO: C(2)	0,2059
Phenyl-PMO: Eg(3)	3,4575
Phenyl-PMO: A(3)	4,343
Phenyl-PMO: E0(3)	7,2423
Phenyl-PMO: C(3)	0,3070
Phenyl-PMO: Eg(6)	7,0826
Phenyl-PMO: A(6)	141,134
Phenyl-PMO: E0(6)	12,0662
Phenyl-PMO: C(6)	39,2161
[1,3] Cau-SiO2 (therm.): Thickness [nm]	0,00
Cau-SiO2 (therm.): N0	1,492
Cau-SiO2 (therm.): N1	121,8
Cau-SiO2 (therm.): N2	0,0
Cau-SiO2 (therm.): K0	0,000
Cau-SiO2 (therm.): K1	0,000
Cau-SiO2 (therm.): K2	0,000
Pola.Pos.	45,00
Pola.Offs.	0,00
Ret.Axis	0,00
Ret.Phase	90,00
Eta	1,00000
Ana.Offs.	0,00
Ana.Offs.Lin.	0,00
Ana.Offs.Quadr.	0,00
Psi Offs.	0,00
Psi Lin.	0,00
Psi Quadr.	0,00
Delta Offs.	0,00
Delta Lin.	0,00
Delta Quadr.	0,00
MSE	0,97170764

Measured Data

Psi, Delta / Spectral range: 1,459 eV - 4,137 eV / Angle of incidence: 70,0° /
08.05.2013



10. Appendix

Danksagung

Ich danke Prof. Dr. Peter Behrens für die Möglichkeit meine Dissertation in seinem Arbeitskreis anfertigen zu können. Vielen Dank für die gute Betreuung, anregende Diskussionen und die vielen Möglichkeiten diese Arbeit auf unterschiedlichen Konferenzen vorstellen zu dürfen. Da diese Arbeit innerhalb des Sonderforschungsbereichs 599 eingebunden war, waren viele bereichernde interdisziplinäre Kooperationen möglich.

Prof. Dr. Peter Paul Müller danke ich für die Übernahme des Korreferats und für die sehr gute Zusammenarbeit in dem Teilprojekt D1 innerhalb des SFB 599.

Allen Mitgliedern des Teilprojekts D1 innerhalb des SFB 599 danke ich für eine gute Kooperation, anregende Diskussionen und auch außerfachlichen Austausch während der Treffen. Dr. Mohammad Imran Rahim und Dr. Bushra Rais danke ich für die *in vitro* Untersuchungen der Materialien. Ebenso danke ich Jennifer Schulze und Dr. Katharina Kranz für die *in vitro* Untersuchungen im Hinblick auf die Biokompatibilität der Materialien Innenohr.

Dr. Daniel Gottschalk vom Institut für Kontinuumsmechanik danke ich für die Durchführung der Nanoindenteruntersuchungen und die Hilfe bei der Auswertung dieser mittels Excel.

Dem gesamten Arbeitskreis Behrens, vor allem auch den ehemaligen Mitgliedern, danke ich für die tolle Zeit und Atmosphäre, den vielen fachlichen Diskussionen und Hilfestellungen. Ihr alle habt die Zeit neben der Arbeit zu etwas Besonderem gemacht. Vor allem bedanke ich mich bei den LNQE Mädels in wechselnder Zusammensetzung Mandy Jahns, Kim Kreisköther, Dr. Nina Ehlert und Dr. Olga Kufelt. Ein besonderer Dank gilt meiner HiWine Mandy Jahns, die viele Proben hergestellt hat und mit mir zusammen das LNQE Labor des AK Behrens gehütet hat. Außerdem danke ich auch meiner HiWine Karen Beseke für ihre Hilfe bei der Probenherstellung.

Dem LNQE Team danke ich für die Bereitstellung der medialen Infrastruktur und der Mitbetreuung des Labors. Es war sehr schön durch das offene Konzept des Gebäudes viele interdisziplinäre Arbeitsgruppen kennenzulernen, was die Kenntnisse und die Arbeitsweise bereicherte. Dem Arbeitskreis Dr. Nadja C. Bigall vom Institut für

Physikalische Chemie danke ich für die Nutzung der Fluoreszenzgeräte und Patrick Adel für die Einweisung in diese, sowie die Hilfe bei der Interpretation der Ergebnisse.

Dr. Hans-Christoph Schwarz möchte ich für die Hilfestellungen bei den Foto-Aufnahmen danken. Dr. Gesa Zahn, Dr. Maria Schweinefuß und Katharine Nolte danke ich für die teilweise schwierigen REM Aufnahmen. Bastian Hoppe danke ich für das Anfertigen der EDX Aufnahmen. Prof. Dr. Armin Feldhoff und Frank Steinbach vom Institut für Physikalische Chemie danke ich für die Probenpräparation und Anfertigung der TEM Querschnittaufnahmen. Vielen Dank an Dr. Alexandra Satalov für die vielen TEM Bilder. Bei Katharina Nolte und Dr. Sergej Springer bedanke ich mich für die TG-Messungen.

Ich bedanke mich ganz herzlich bei den Korrektoren meiner Arbeit: Dr. Hendrik Fullriede und Dr. Hans-Christoph Schwarz, vor allem auch für die formalen Korrekturen. Großer Dank gilt Dr. Nina Ehlert, dass sie sich die Zeit genommen hat alle Teile durchzugehen. Ich möchte mich besonders bei Dr. Jenny Schneider bedanken für ihre Freundschaft und ihre Begleitung während unseres gemeinsamen Studiums, den vielen gemeinsamen Praktika und dem Lernen vor den Klausuren, sowie die vielen hilfreichen Korrekturen dieser Arbeit. Außerdem danke ich Mentorium für ein schnelles und hilfreiches Lektorat.

Abschließend danke ich meiner Familie, die mich immer unterstützt, viel abgelenkt und mir sehr geholfen hat diese Arbeit abzuschließen. Vielen Dank für die unendliche Unterstützung, Geduld und Liebe meiner Eltern, Schwiegereltern, meines Mannes Steffen Wendt und meiner geliebten Kinder.

List of Publications***Oral Presentations*****Improved Biocompatibility of Polyether Ether Ketone (PEEK) by Coating with Thin Titania Films**

N. Wendt, B. Rais, H. Fullriede, G. Zahn, P.P. Müller, P. Behrens
3rd Euro BioMAT, Weimar, **2015**

Periodic Mesoporous Organosilica (PMO) Coatings for Biomedical Applications

N. Wendt, S. Schlie-Wolter, B. Chichkov, I. Rahim, P.P. Müller, D. Gottschalk, P. Wriggers, P. Behrens
4th International Conference on Multifunctional, Hybrid and Nanomaterials, Sitges, **2015**

Improved Biocompatibility of Polyether Ether Ketone (PEEK) by Coating with Thin Titania Films

N. Wendt, B. Rais, P.P. Müller, P. Behrens
48th Annual Conference of Deutschen Gesellschaft für Biomedizinische Technik (DGBMT), Hannover, **2014**

Nanoporous Platinum Coatings for the Advance of Electrode Surfaces

K.D. Kreiskother, N. Ehlert, N. Wendt, H.-C. Schwarz, A. Warnecke, K. Kranz, P. Behrens
48th Annual Conference of Deutschen Gesellschaft für Biomedizinische Technik (DGBMT), Hannover, **2014**

Evaluating Periodic Mesoporous Organosilica (PMO) Coatings as a Novel Biomaterial

N. Wendt, N. Ehlert, S. Schlie-Wolter, B. Chichkov, P. Behrens
6th International Federation of European Zeolite Associations (FEZA) Conference, Leipzig, **2014**

Periodic Mesoporous Organosilica (PMO) Coatings for Biomedical Applications

N. Wendt, M. Jahns, N. Ehlert, S. Schlie, B. Chichkov, P. Behrens
26th European Conference on Biomaterials, Liverpool, **2014**

Evaluating Periodic Mesoporous Organosilica (PMO) Coatings as a Novel Biomaterial

N. Wendt, N. Ehlert, S. Schlie, B. Chichkov, P. Behrens
26. Deutsche Zeolith-Tagung (DZT), Paderborn, **2014**

Poster Presentations

Periodic Mesoporous Organosilica (PMO) Coatings for Biomedical Applications

N. Wendt, S. Schlie-Wolter, B. Chichkov, I. Rahim, P.P. Müller, D. Gottschalk, P. Wriggers, P. Behrens

3rd Euro BioMAT, Weimar, **2015**

Periodic Mesoporous Organosilica (PMO) Coatings for Biomedical Applications

N. Wendt, S. Schlie-Wolter, B. Chichkov, I. Rahim, P.P. Müller, D. Gottschalk, P. Wriggers, P. Behrens

Symposium Architected Biomaterials, Medical and Tissue Engineering, Berlin, **2014**

Periodic Mesoporous Organosilica (PMO) Coatings for Biomedical Applications

N. Wendt, N. Ehlert, K. Kurselis, A. Deiwick, B. Chichkov, P. Behrens

2nd Euro BioMAT, Weimar, **2013**

Periodic Mesoporous Organosilica (PMO) Coatings for Biomedical Applications

N. Wendt, N. Ehlert, K. Kurselis, A. Deiwick, B. Chichkov, P. Behrens

25. Deutsche Zeolith-Tagung (DZT), Hamburg, **2013**

Periodic Mesoporous Organosilica (PMO) Coatings for Biomedical Applications

N. Wendt, T. Lüßenhop, N. Ehlert, K. Kurselis, S. Schlie, B. Chichkov, P. Behrens

Jahrestagung der Deutschen Gesellschaft für Biomaterialien (DGBM), Hamburg, **2012**

Antibacterial Coatings Based on Quaternary Ammonium Salts

T. Lüßenhop, N. Wendt, M. Badar, P.P. Mueller, P. Behrens

Jahrestagung der Deutschen Gesellschaft für Biomaterialien (DGBM), Gießen, **2011**

Polymer-based antibacterial coatings for biomedical applications

O. Kufelt, T. Lüßenhop, N. Wendt, W. Heuer, A. Winkel, M. Badar, L. Ringenberg, M. Stiesch, P.P. Müller, P. Behrens

Jahrestagung der Deutschen Gesellschaft für Biomaterialien (DGBM), Tübingen, **2009**

*Articles***Porous Aerogels from Shape-Controlled Metal Nanoparticles Directly from Non-Polar Colloidal Solution**

S. Naskar, A. Freytag, J. Deutsch, N. Wendt, P. Behrens, N. Bigall, Chemistry of Materials, **2017**, *29*, 9208

Versatile Aerogel Fabrication by Freezing and Subsequent Freeze-Drying of Colloidal Nanoparticle Solutions

A. Freytag, S. Sánchez-Paradinas, S. Naskar, N. Wendt, M. Colombo, G. Pugliese, J. Poppe, C. Demirci, I. Kretschmer, D.W. Bahnemann, P. Behrens, N.C. Bigall, Angewandte Chemie Internationale Edition, **2016**, *55*, 1200.

Periodic Mesoporous Organosilica (PMO) Coatings for Biomedical Applications

N. Wendt, T. Lüßenhop, N. Ehlert, K. Kurselis, S. Schlie, B. Chichkov, P. Behrens, Bionanomaterials **2012**, *13*, 80.

Antibacterial Coatings Based on Quaternary Ammonium Salts

T. Lüßenhop, N. Wendt, M. Badar, P.P. Mueller, P. Behrens, Biomaterialien **2011**, *12*, 81.

Polymer-based antibacterial coatings for biomedical applications

O. Kufelt, T. Lüßenhop, N. Wendt, W. Heuer, A. Winkel, M. Badar, L. Ringenberg, M. Stiesch, P.P. Müller, P. Behrens, Biomaterialien **2009**, *10*, 123.

Curriculum Vitae

Wendt (née Mitjko), Natalja

Date of Birth 08.03.1986

Place of Birth Almaty, Kazakhstan

Nationality German

since 11/2011 **Dissertation**

Institute of Inorganic Chemistry at Leibniz University of Hanover
Topic: *“Bioactive Silica and Titania Coatings on Implant Materials”*

Member of Collaborative Research Center 599 *“Sustainable Bioresorbable and Permanent Implants of Metallic and Ceramic Materials”*

Student of Integrated Graduate College 599 *“Biomedical Engineering”*

Member of Cluster of Excellence *“Hearing4all”*

10/2009 – 10/2011 **Master of Science Materials and Nanochemistry**

Master Thesis at Institute of Inorganic Chemistry at Leibniz University of Hanover

Topic: *“Modification and Functionalization of Polyether Ether Ketons”*

10/2006 – 10/2009 **Bachelor of Science Chemistry**

Bachelor Thesis at Institute of Technical Chemistry at Leibniz University of Hanover

Topic: *„Aufbau und Charakterisierung eines Perfusionsbioreaktors für Tissue Engineering Anwendungen.“*

06/2006 **Abitur at Wilhelm-Raabe-Schule**